# Effective field theories in Higgs physics at higher orders

Zur Erlangung des akademischen Grades eines

## DOKTORS DER NATURWISSENSCHAFTEN

von der KIT-Fakultät für Physik
des Karlsruher Instituts für Technologie (KIT)

genehmigte

## DISSERTATION

von

## M.Sc. Jannis Lang

aus Würzburg

Referentin:     Prof. Dr. Gudrun Heinrich

Korreferent:    Prof. Dr. Matthias Steinhauser

Tag der mündlichen Prüfung:     09. Februar 2024

Eidesstattliche Versicherung gemäß § 13 Absatz 2 Ziffer 3 der Promotionsordnung des Karlsruher Instituts für Technologie (KIT) für die KIT-Fakultät für Physik:

1. Bei der eingereichten Dissertation zu dem Thema

**Effective field theories in Higgs physics at higher orders**

handelt es sich um meine eigenständig erbrachte Leistung.

2. Ich habe nur die angegebenen Quellen und Hilfsmittel benutzt und mich keiner unzulässigen Hilfe Dritter bedient. Insbesondere habe ich wörtlich oder sinngemäß aus anderen Werken übernommene Inhalte als solche kenntlich gemacht.

3. Die Arbeit oder Teile davon habe ich bislang nicht an einer Hochschule des In- oder Auslands als Bestandteil einer Prüfungs- oder Qualifikationsleistung vorgelegt.

4. Die Richtigkeit der vorstehenden Erklärungen bestätige ich.

5. Die Bedeutung der eidesstattlichen Versicherung und die strafrechtlichen Folgen einer unrichtigen oder unvollständigen eidesstattlichen Versicherung sind mir bekannt.

Ich versichere an Eides statt, dass ich nach bestem Wissen die reine Wahrheit erklärt und nichts verschwiegen habe.

**Karlsruhe, den 10. Januar 2024**


............................................
(Full name)

# List of Publications

## Articles (published or under review) that became part of this thesis

- G. Heinrich and J. Lang, "Combining chromomagnetic and four-fermion operators with leading SMEFT operators for $gg \to hh$ at NLO QCD," [arXiv:2311.15004]

- S. Di Noi, R. Gröber, G. Heinrich, J. Lang and M. Vitti, "On $\gamma_5$ schemes and the interplay of SMEFT operators in the Higgs-gluon coupling," [arXiv:2310.18221]

- L. Alasfar, L. Cadamuro, C. Dimitriadi, A. Ferrari, R. Gröber, G. Heinrich, T. Ingebretsen Carlson, J. Lang, S. Ördek, L. Pereira Sánchez, L. Scyboz and J. Sjölin, "Effective Field Theory descriptions of Higgs boson pair production," [arXiv:2304.01968]

- G. Heinrich, J. Lang and L. Scyboz, "SMEFT predictions for $gg \to hh$ at full NLO QCD and truncation uncertainties," *JHEP* **08** (2022), 079

## Research works that are not presented in this thesis

- B. Agarwal, G. Heinrich, S. P. Jones, M. Kerner, S. Y. Klein, J. Lang, V. Magerya and A. Olsson, "Two-loop amplitudes for ttH production: the quark-initiated Nf-part," [arXiv:2402.03301]

- J. Lang, S. Liebler, H. Schäfer-Siebert and D. Zeppenfeld, "Effective field theory versus UV-complete model: vector boson scattering as a case study," *Eur. Phys. J. C* **81** (2021) no.7, 659

## Conference proceedings

- J. Lang, "Precise SMEFT predictions for di-Higgs production," *PoS* **LHCP2023** (2024), 192

- G. Heinrich, J. Lang and L. Scyboz, "Two Higgs bosons, two loops, x+2 operators," *PoS* **RADCOR2023** (2024), 002

- G. Heinrich and J. Lang, "SMEFT truncation effects in Higgs boson pair production at NLO QCD," *J. Phys. Conf. Ser.* **2438** (2023) no.1, 012153

- G. Heinrich, J. Lang and L. Scyboz, "Beyond dimension six in SM Effective Field Theory: a case study in Higgs pair production at NLO QCD," *PoS* **LL2022** (2022), 009

# Abstract

So far, the Standard Model of particle physics has been proven well compatible with data obtained from collider experiments. The discovery of a Higgs boson at the Large Hadron Collider about 10 years ago represents the last big milestone of this remarkable success story, but also marked the beginning of the precision era in Higgs physics for the measurement of all its properties and couplings in order to identify potential inconsistencies between prediction and experiment. These searches are well motivated, since there are several hints for the incompleteness of the Standard Model as the full theory up to arbitrary high energies. Especially the Higgs channels provide a testing ground for sectors of the Standard Model that are yet to be precisely explored, for which the structure of the Higgs potential is a prime example.

The absence of prominent signals in the data sets suggests that a significant scale separation between the relevant energies of collider experiments and the new physics sector persists. This would be a scenario in which new physics effects are consistently described in a model agnostic way by an effective field theory approach. In order to provide reliable predictions of deviations from purely Standard Model behaviour, higher orders in perturbative calculations also in the effective field theory extensions of the Standard Model are imperative. This thesis aims to clarify some aspects in the application of effective field theory extensions of the Standard Model for high precision predictions, thereby presenting calculations in the dominant channel of single- and di-Higgs production at a proton-proton collider, the gluon fusion channel. Moreover, the phenomenology of these theories in di-Higgs production is investigated.

Necessary theoretical techniques for perturbative calculations are briefly recapitulated and the main features of the two prevalent extensions of linear (SMEFT) and non-linear (HEFT) effective field theory together with their power counting are introduced. Subsequently, the relevant calculational steps of di-Higgs production at full NLO QCD for the leading contributions of HEFT and SMEFT are presented. The phenomenology of the two theories is contrasted at the level of total cross section and distributions, and the effect of different truncation options for dimension-6 operator insertions in the SMEFT is investigated. As calculations at higher loop orders almost exclusively employ dimensional regularisation schemes, we study the structure of two different, well-defined schemes for the continuation of $\gamma_5$ to $D$ dimensions in the SMEFT for the single-Higgs production process. Consistency of physical predictions then leads to the derivation of relations between parameters in the SMEFT that can be used to translate parameter values in different $\gamma_5$ scheme choices. Having understood this structure, the subleading SMEFT contribution to di-Higgs production of the chromomagnetic and 4-top operators is calculated in the two $\gamma_5$ schemes. The relevance of the corresponding Wilson coefficients is investigated and compared with the leading contribution of SMEFT. The impact of different $\gamma_5$ scheme choices on a naive single Wilson coefficient variation is exemplified, highlighting the importance of being inclusive enough in the parameter space in order to derive scheme independent results.

# Zusammenfassung

Bis zum heutigen Tag hat sich das Standardmodell der Teilchenphysik als gut vereinbar mit den Messungen an Teilchenbeschleunigern erwiesen. Die Entdeckung eines Higgs-Bosons am Large Hadron Collider vor etwa 10 Jahren stellt den letzten großen Meilenstein dieser Erfolgsgeschichte dar, was zugleich den Startpunkt für die Präzisionsära in der Physik des Higgs-Bosons markiert, um all seine Eigenschaften und Kopplungen zu erforschen und potentielle

Unvereinbarkeiten zwischen Vorhersage und Experiment zu finden. Diese Untersuchungen sind gut begründet, da es einige Hinweise auf die Unvollständigkeit des Standardmodells als komplette Theorie für beliebig hohe Energien gibt. Die Kanäle der Higgs-Produktion bieten hierfür ein Testgelände für Sektoren des Standardmodells, welche bisher nicht präzise bestimmt wurden, worunter insbesondere das Higgs-Potential fällt.

Das Fehlen von direkten Signalen in den Datensätzen deutet darauf hin, dass eine deutliche Skalenseparation zwischen den relevanten Energien der Beschleunigerexperimente und dem Sektor der neuen Physik vorherrscht. Dies würde ein Szenario darstellen, in welchem Effekte von neuer Physik konsistent und modellunabhängig mit den Methoden von effektiven Feldtheorien beschrieben werden können. Um verlässliche Vorhersagen für Abweichungen vom reinen Standardmodell Verhalten zu beschreiben, sind Rechnungen in höheren Ordnungen der perturbativen Entwicklung auch für Erweiterungen des Standardmodells in effektiver Feldtheorie vonnöten. Diese Arbeit zielt darauf ab, einige Aspekte der Anwendung von effektiven Feldtheorien des Standardmodells für die Vorhersage bei hoher Präzision anhand von Rechnungen für den dominanten Produktionskanal der Gluon-Fusion für Higgs-Boson- und Higgs-Paarerzeugung an einem Proton-Proton Teilchenbeschleuniger zu klären. Darüber hinaus wird die Phänomenologie dieser Theorien für Higgs-Paarproduktion erforscht.

Die notwendigen theoretischen Methoden der Störungsrechnung werden kurz rekapituliert und die Haupteigenschaften der zwei vorherrschenden Erweiterungen der linearen (SMEFT) und nichtlinearen (HEFT) effektiven Feldtheorie zusammen mit deren Vorschrift zum Ordnen der Operatorstrukturen eingeführt. Anschließend werden die relevanten Schritte zur vollen NLO QCD Berechnung von Higgs-Paarproduktion für den dominanten Beitrag der HEFT und SMEFT präsentiert. Die Phänomenologie der beiden Theorien wird für den totalen Wirkungsquerschnitt und in Verteilungen gegenübergestellt und der Effekt von verschiedenen Arten der Trunkierung der Beiträge von SMEFT Operatoren der Dimension-6 untersucht. Da höhere Schleifenordnungen fast ausschließlich in Vorschriften der dimensionalen Regularisierung berechnet werden, untersuchen wir die Struktur von zwei wohldefinierten Vorschriften für die Fortsetzung von $\gamma_5$ in $D$-dimensionaler Raumzeit in SMEFT für den Prozess der Higgs-Boson Erzeugung. Aus der Konsistenz physikalischer Vorhersagen werden Relationen zwischen den Parametern der SMEFT hergeleitet, welche für eine Übersetzung von Parameterwerten bei unterschiedlichen Vorschriften für $\gamma_5$ genutzt werden können. Mit dem daraus abgeleiteten Wissen wird der subdominante Beitrag der SMEFT zur Higgs-Paarproduktion durch den chromomagnetischen Operator und 4-Top Operatoren für zwei unterschiedliche Vorschriften für $\gamma_5$ berechnet. Die Bedeutung der zugehörigen Wilson Koeffizienten wird untersucht und mit dem dominanten Beitrag der SMEFT verglichen. Die Auswirkung von unterschiedlichen Wahlen der Vorschrift für $\gamma_5$ auf die naive Variation einzelner Wilson Koeffizienten wird veranschaulicht und dabei die Wichtigkeit für eine ausreichend inklusive Auswahl an Parametern für vorschriftsunabhängige Resultate hervorgehoben.

# Contents

# Introduction

The Standard Model of particle physics (SM) ranks high among the greatest scientific accomplishments of the last century. The discovery of a scalar particle at the Large Hadron Collider (LHC) [1,2] which very well fulfills the expected properties of the Higgs boson, the until then last missing constituent of the SM, just underpins the success. With only 19 free parameters, the theory of the SM is predictive after only very few measurements and the amount of self-consistency of SM predictions in comparison with various experiments is remarkable.

However, despite the tremendous achievements, it is a well known fact that the SM cannot be viewed as 'the theory of everything' of the quantum world. There are many observations and theoretical signs of incompleteness which the SM cannot address. Therefore, the SM should be regarded as an effective theory that is valid at currently measured energies and up to the observed precision so far, for which the extension, also called ultraviolet (UV) completion in the jargon of effective field theories (EFT), is yet to be found.

Absence of direct signals in form of bumps in measured distributions pushes the community to search for deviations on the precision frontier between SM calculations and experimental results. A necessary complement is then given by precision calculations considering effects beyond the SM (BSM) in order to measure potential deviations. As there is a plethora of potential realisations of BSM extensions, the pragmatic approach parameterises BSM effects in a generic, but consistent way, with the help of bottom-up EFTs. These EFTs are constructed only with minimal assumptions on the BSM physics and are equipped with a systematic expansion that allows to include effects up to arbitrary precision.[1]

Within a bit more than 10 years after the announcement of the Higgs discovery, a lot of progress was made in the determination of the Higgs properties and measurement of interactions [3,4], however there are still some areas where potential BSM deviations could show up. A particular interesting showcase is given by di-Higgs production, as it provides direct insight to the Higgs self interaction.

Throughout this work, we express all formulas in natural units, i.e. we effectively set

$$\hbar = 1, \qquad c = 1, \qquad \epsilon_0 = 1 . \tag{1.1}$$

---

[1]It is important to stress, however, that there are potential BSM models that cannot adequately be described using EFTs. Therefore, we do not advocate to completely ignore the investigations of well motivated, concrete model realisations.

Therefore, the notion of time, length and energy is used interchangeably, in particular in the context of high energy, UV and short distance, and low energy, infrared (IR) and long distance physics we refer to the same scale separation.

The present document is divided into two parts. In Part I of the thesis, we briefly revisit the necessary theoretical concepts for precision applications of bottom-up EFTs at the LHC. Hence, Chapter 2 serves as a quick introduction to the relevant content of the SM also mentioning some shortcomings to highlight the need for a more general theory. In Chapter 3 the techniques used for higher order perturbative corrections of QCD induced processes are introduced and also the technical difficulties of chirality in dimensional regularisation are addressed. Moreover, in Chapter 4 we establish the basic concept of EFTs and the two canonical bottom-up EFTs in Higgs physics.

Part II of this thesis is dedicated to the concrete application of the introduced methods in Higgs pair production in the gluon fusion channel $gg \to hh$. Chapter 5 highlights the importance of Higgs pair production and the gluon channel in particular. In addition, an overview of the current theoretical status is presented. Subsequently, some recent results of the application of EFTs in precision calculation are reviewed.

In Chapter 6 the work of Ref. [5] is discussed which considers the effect of the leading contribution of the EFTs at full NLO QCD. The relevant formulas of the calculation in the two EFTs are presented and practical differences pointed out. After definition of different truncation options for the Standard Model effective field theory (SMEFT), the two EFT realisations are contrasted at the level of total cross section and distributions. Moreover, the effect of the different truncation options is investigated.

Afterwards, the intricacy of $\gamma_5$ scheme choices at higher orders in the context of EFTs is revisited for the example of single Higgs production in Chapter 6 following the work of Ref. [6]. Thereby, a subset of operators in the SMEFT framework is considered and the explicit scheme dependence of single Wilson coefficients is elaborated.

Having understood the structure of the $\gamma_5$ scheme in the presence of EFT operators, the knowledge is applied to the subleading SMEFT contribution in $gg \to hh$ including insertions of chromomagnetic and 4-top operators in Chapter 8. The potential sensitivity of the process on the considered Wilson coefficients is investigated. In addition, the effect of $\gamma_5$ scheme choices in naive observations of single Wilson coefficient contributions is demonstrated. Thus, the results point to the importance of being sufficiently inclusive in the selection of Wilson coefficients for parameter fits and bounds, as $\gamma_5$ scheme independent results are only obtained if operator combinations are considered. The discussion of the chapter follows closely the results in Ref. [7].

Finally, in Chapter 9 we derive conclusions and provide an outlook for further directions of research.

# Part I.

# Perturbation theory in the Standard Model and its effective field theory extensions

# The Standard Model of particle physics in a nutshell

As already highlighted in the introduction, the importance of the SM as the basis of modern particle physics cannot be stressed enough. Its development to the final version has a history of many significant contributions over a few decades. A few milestones are worth mentioning: the Brout-Englert-Higgs mechanism (Higgs mechanism in the following) [8–11] that describes the generation of mass terms in the SM, the Glashow-Salam-Weinberg theory of electroweak (EW) interactions [12–14] and the description of asymptotic freedom of quantum chromodynamics (QCD) [15, 16]. The following chapter provides a very brief overview about the relevant structure of the SM.

SM is a renormalisable quantum field theory (QFT) which is based on a chiral gauge theory. The SM fields enter in the scalar, vector and spinor representations of the Lorentz group $SO(3,1)$ and particles are considered as the quantised excitations of the associated fields. On top of their Lorentz representation, they are specified by their local transformation properties under the gauge group

$$\mathcal{G} = SU(3)_{QCD} \times SU(2)_L \times U(1)_Y \ . \tag{2.1}$$

$SU(3)_{QCD}$ is the gauge group of QCD and acts non-trivially on the 'coloured' fields of the SM. The $SU(2)_L \times U(1)_Y$ is the unified group of EW interactions, where subscript $L$ denotes that that the gauge group is chiral and only acts on the left-handed (LH) fermion fields whereas right-handed (RH) fermion fields are left invariant. The $U(1)_Y$ coupling is defined by the hypercharge $Y$ of the field.

The field content in interaction eigenstates and the respective representations is summarised in Table 2.1. $G^a$ are the gauge bosons of the $SU(3)_{QCD}$ gauge group of strong interactions, $W^i$ and $B$ are the EW gauge bosons of the $SU(2)_L$ and $U(1)_Y$ gauge group, respectively. The fermions are collected according to their transformation properties, where quarks are coloured and couple to the strong interactions, whereas leptons are only subject to EW interactions. The LH fermion fields are collected in pairs forming doublets under $SU(2)_L$ the RH fields are singlets of that gauge group. All fermion species enter with three copies of the same transformation properties, the so called quark and lepton families, but they differ according to their coupling to the Higgs doublet $\phi$ and hence their mass after EW symmetry breaking. The different kinds of quarks and leptons are also called flavours.

| Field | | Representation | | |
|:---:|:---:|:---:|:---:|:---:|
| Type | Symbol | $SU(3)_{QCD}$ | $SU(2)_L$ | $Y$ |
| Gauge bosons | | | | |
| Strong | $G^a$ | 8 | 1 | 0 |
| EW | $W^i$ | 1 | 3 | 0 |
| | $B$ | 1 | 1 | 0 |
| Fermions | | | | |
| Quarks | $q_L^i = \left\{ \begin{pmatrix} u_L \\ d_L \end{pmatrix}, \begin{pmatrix} c_L \\ s_L \end{pmatrix}, \begin{pmatrix} t_L \\ b_L \end{pmatrix} \right\}$ | 3 | 2 | 1/6 |
| | $u_R^i = \{u_R, c_R, t_R\}$ | 3 | 1 | 2/3 |
| | $d_R^i = \{d_R, s_R, b_R\}$ | 3 | 1 | $-1/3$ |
| Leptons | $l_L^i = \left\{ \begin{pmatrix} \nu_e \\ e_L \end{pmatrix}, \begin{pmatrix} \nu_\mu \\ \mu_L \end{pmatrix}, \begin{pmatrix} \nu_\tau \\ \tau_L \end{pmatrix} \right\}$ | 1 | 2 | 1/2 |
| | $e_R^i = \{e_R, \mu_R, \tau_R\}$ | 1 | 1 | 1 |
| Scalar | | | | |
| Higgs | $\phi$ | 1 | 2 | 1/2 |

**Table 2.1.:** Field content of the SM with its representations.

For the covariant derivative, the sign convention

$$D_\mu = \partial_\mu - ig_s G_\mu^a T^a - ig_1 W_\mu^i \frac{\tau^i}{2} - ig_2 B_\mu Y \ , \tag{2.2}$$

is employed throughout the thesis. $T^a$ are the generators of $SU(3)_{QCD}$, $\dfrac{\tau^i}{2}$ are the generators of $SU(2)_L$ given by the Pauli matrices $\tau^i$ and $Y$ is the hypercharge associated to $U(1)_Y$. Since we refer to different colour factors throughout the thesis, we briefly introduce the relevant combinations of the $SU(3)_{QCD}$ colour algebra:

$$\begin{aligned} T_F \delta^{ab} &= \text{Tr}\left[T^a T^b\right] \\ c_F \delta_{ij} &= (T^a T^a)_{ij} \\ c_A \delta^{ab} &= f^{acd} f^{bcd} \ , \end{aligned} \tag{2.3}$$

with

$$[T^a, T^b] = i f^{abc} T^c \ . \tag{2.4}$$

The specifications of gauge group and field content already define our theory and the classical SM Lagrangian is obtained writing down the all renormalisable terms obeying the gauge symmetry condition up to canonical dimension-4[2]

$$
\begin{aligned}
\mathcal{L}_{\mathrm{SM}} = & -\frac{1}{4} G^a_{\mu\nu} G^{a\mu\nu} - \frac{1}{4} W^i_{\mu\nu} W^{i\mu\nu} - \frac{1}{4} B_{\mu\nu} B^{\mu\nu} \\
& + \bar{q}_L i\slashed{D} q_L + \bar{u}_R i\slashed{D} u_R + \bar{d}_R i\slashed{D} d_R + \bar{l}_L i\slashed{D} l_L + \bar{e}_R i\slashed{D} e_R \\
& + (D_\mu \phi)^\dagger (D^\mu \phi) - V(|\phi|^2) \\
& + \left( \bar{q}_L \hat{Y}_u u_R \tilde{\phi} + \bar{q}_L \hat{Y}_d d_R \phi + \bar{l}_L \hat{Y}_e e_R \phi + \mathrm{H.c.} \right) \; .
\end{aligned}
\tag{2.5}
$$

$\tilde{\phi} = \varepsilon \phi^*$ is the charge conjugate of the Higgs doublet. The first two lines of Eq. (2.5) contain ingredients of a massless gauge theory, with the gauge kinetic terms of pure Yang-Mills theory in the first line and fermion kinetic terms with gauge interaction in the second. The third line contains the Higgs sector with kinetic term and Higgs potential $V(|\phi|^2)$. The last line describes Yukawa interactions with the fermions of the theory except neutrinos. The Yukawa couplings $\hat{Y}_i$ are given by matrices, as the Yukawa interactions a priori cannot be expected to be diagonal in the interaction eigenstates of the fermions. The Higgs sector and Yukawa interactions lead to mass terms of the particles at low energies which is described in the following subsection.

## 2.1. Symmetry breaking and Higgs physics in the Standard Model

Spontaneous symmetry breaking is an important cornerstone of the SM. It provides the mechanism that is responsible for the generation of mass terms of the SM fields, whilst preserving gauge invariance of the chiral gauge group in the Lagrangian. The crux of the Higgs mechanism [8–11] in the SM is that the scalar doublet $\phi$ acquires a non-vanishing vacuum expectation value (vev) $v$ below the symmetry breaking scale. The new ground state is obtained by a minimisation condition of the Higgs potential

$$
V\left(|\phi|^2\right) = -\hat{\mu}^2 |\phi|^2 + \lambda |\phi|^4 \; ,
\tag{2.6}
$$

which leads to $\dfrac{v^2}{2} := |\phi_0|^2 = \dfrac{\hat{\mu}^2}{2\lambda}$ at leading order.

Below the symmetry breaking scale the Higgs doublet is typically expanded around the vev and the components are arranged such that the vev appears in the real scalar component of the Higgs doublet, i.e.

$$
\phi = \begin{pmatrix} G^+ \\ \dfrac{h + v + iG^0}{\sqrt{2}} \end{pmatrix} \; .
\tag{2.7}
$$

While the theory itself is invariant under the full gauge group $SU(2)_L \times U(1)_Y$, the ground state defined by $v$ is only invariant under a $U(1)_Q$ subgroup which is identified with the gauge

---

[2]For the quantisation of non-abelian gauge theories, a gauge fixing condition is necessary. Standard $R_\xi$-gauge approach follows the trick introduced by Fadeev and Popov [17] which has been extended for broken gauge theories. It is based on the insertion of a unit into the path integral quantisation of a gauge theory in the form of

$$
1 = \int \mathcal{D}\alpha \, \det\left( \frac{\delta G(V^\alpha)}{\delta \alpha} \right) \delta\left( G(V^\alpha) - \omega(x) \right) \; ,
$$

with alpha being a gauge configuration, which is then pulled to the quantum action through an integration over $\omega(x)$ with Gaussian weight $\int \mathcal{D}\omega \, e^{-i \int d^d x \frac{\omega^2}{2}}$. The determinant part which is independent of the gauge configuration $\alpha$ for a linear gauge fixing condition is interpreted as a generalized differential operator that is expanded by integration over Grassmann fields (ghosts). As this is a standard procedure a more detailed description can be found in many modern textbooks, e.g. Ref. [18].

group of electromagnetism. According to the Goldstone theorem a breaking of continuous global symmetries leads to Goldstone bosons $G^+$, $G^-$ and $G^0$ for each broken symmetry degree of freedom, i.e. the number of Goldstone fields is given by the dimensionality of the coset $\mathcal{G}/\mathcal{H}$ with $\mathcal{H} = SU(3)_{QCD} \times U(1)_Q$ and $\mathcal{G}$ given in Eq. (2.1). In the presence of a local gauge symmetry, however, the resulting Goldstone fields are not physical and their degrees of freedom are absorbed in the mass generation of the gauge bosons related to the broken symmetry.

For the purpose of deriving the mass terms and couplings to the physical Higgs field, it is sufficient to work in unitary gauge which effectively removes the unphysical would-be Goldstone degrees of freedom. The covariant derivative on the Higgs doublet thus leads to

$$
\begin{aligned}
\left(D_\mu \phi\right)^\dagger \left(D^\mu \phi\right) &\to \frac{1}{2} \left(\partial_\mu h\right)^2 + \frac{1}{2} \left| \left(-i\frac{g_1}{2}\tau^i W_\mu^i - i\frac{g_2}{2}B_\mu\right) \begin{pmatrix} 0 \\ h+v \end{pmatrix} \right|^2 \\
&= \frac{1}{2} \left(\partial_\mu h\right)^2 + \left(m_W^2 W_\mu^+ W^{-\,\mu} + \frac{m_Z^2}{2} Z_\mu Z^\mu\right)\left(1 + \frac{h}{v}\right)^2 ,
\end{aligned}
\tag{2.8}
$$

where the second line is obtained after diagonalisation of the mass matrix with the definition for the fields

$$
W^\pm = \frac{1}{\sqrt{2}}\left(W^1 \mp iW^2\right) \qquad Z_\mu = \frac{1}{\sqrt{g_1^2 + g_2^2}}\left(-g_2 B + g_1 W^3\right) ,
\tag{2.9}
$$

and their mass parameters

$$
m_W^2 = v^2 \frac{g_1^2}{4} \qquad m_Z^2 = v^2 \frac{g_1^2 + g_2^2}{4} .
\tag{2.10}
$$

For the case of fermion mass generation, we consider the example of the up-type quarks. Thus, we have for the Yukawa interaction

$$
\begin{aligned}
\bar{q}_L \hat{Y}_u u_R \tilde{\phi} + \text{H.c.} &\to \frac{v}{\sqrt{2}}\left(\bar{u}_L \hat{Y}_u u_R + \bar{u}_R \hat{Y}_u^\dagger u_L\right)\left(1 + \frac{h}{v}\right) \\
&= \left(m_u \bar{u}u + m_c \bar{c}c + m_t \bar{t}t\right)\left(1 + \frac{h}{v}\right) ,
\end{aligned}
\tag{2.11}
$$

where in the second line the fermion fields have been redefined in order to diagonalise the mass term. Since we usually quantise the theory in the mass eigenstates, the diagonalisation in Eq. (2.11) leads to weak interactions with $W^\pm$ bosons that also couple between states of different fermion family in the mass basis. These family off-diagonal interactions are parameterised by the unitary Cabibbo-Kobayashi-Maskawa (CKM) matrix [19, 20]

$$
V_{CKM} = \begin{pmatrix} V_{ud} & V_{us} & V_{ub} \\ V_{cd} & V_{cs} & V_{cb} \\ V_{td} & V_{ts} & V_{tb} \end{pmatrix} ,
\tag{2.12}
$$

which translates between mass eigenstates and interaction eigenstates.

The Higgs potential reduces in unitary gauge to

$$
V\left(|\phi|^2\right) \to \frac{m_h^2}{2}h^2 + \frac{m_h^2}{2v}h^3 + \frac{m_h^2}{8v^2}h^4 ,
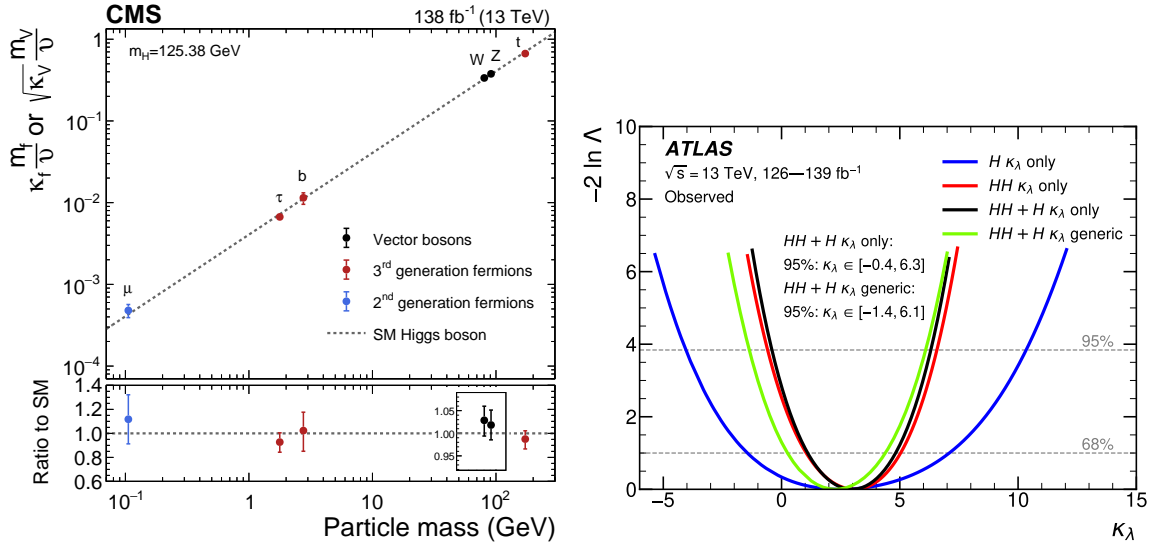\tag{2.13}
$$

**Figure 2.1.:** Diagrams demonstrating the measurements of Higgs couplings in comparison with the predicted mass relation of EW symmetry breaking in the $\kappa$-framework. Left: interaction with fermions and massive gauge bosons [3], right: trilinear Higgs self interaction [24].

where $m_h^2 = 2\lambda v^2$ defines the mass of the physical Higgs.

Through the structure of EW symmetry breaking, all fields couple to the physical Higgs directly related to their mass parameter, i.e. after measurement of the masses and one additional parameter, for instance the Fermi constant $G_F = \dfrac{1}{\sqrt{2}v^2}$, all couplings of the Higgs boson are completely defined.[3] The leading order relations between masses and couplings are demonstrated in Eqs. (2.8), (2.11) and (2.13).

After the Higgs boson discovery, a huge effort has been put into the precise measurement of the Higgs couplings in order to test if the structure predicted by EW symmetry breaking in the SM is sufficient. The common framework for these measurements is given by coupling modifiers in the so-called $\kappa$-framework which is described in Refs. [22,23]. Recent experimental results are shown in Fig. 2.1. The diagram on the left in Fig. 2.1 demonstrates that the couplings of gauge bosons and the fermions to the Higgs are very well compatible to the mass proportionality predicted by the SM. Measurements of the trilinear Higgs coupling, as presented on the right in Fig. 2.1, show that the structure of the Higgs potential is among the least explored parts of the SM, such that there is still the possibility for sizable deviations from the SM. The main process to gain more insight into the Higgs potential is given by Higgs pair production which is therefore the focus of the studies presented in Part II. However, as variations of single couplings are theoretically not well motivated and the $\kappa$-framework does not describe a consistent parameterisation of BSM effects, we consider the framework of bottom-up EFTs for which a basic introduction is given in Chapter 4.

## 2.2. Incompleteness of the SM

Before continuing with the other chapters, it may be instructive to remind ourselves why we need to take into account BSM extensions at all, since the SM has been proven to describe

---

[3]Depending on the EW input scheme, also other parameter measurements can be the starting point determining the other couplings. A detailed discussion about different input schemes can be found in the literature, e.g. in Ref. [21].

physics at collider experiments with great success. Yet, there are quite a few observations that are incompatible with our current understanding of the fundamental theory of nature.

- One example is the astronomical observation of strong hints for the existence of *Dark Matter* which provides an unknown gravitational source that does not interact with electromagnetism and therefore differs from visible matter made of Hadrons. These gravitational effects manifest in atypical distributions of velocity in the rotations of spiral arms of spiral galaxies, which cannot be described by visible matter alone. Also there are clusters of high mass density that lead to gravitational lensing effects, while the matter comprising the mass density is invisible.

- The visible universe, so far, appears to have a significant excess of matter over anti-matter. The necessary requirements on a mechanism to provide this asymmetry have been formalised by the Sakharov conditions [25]. However, if only the SM is taken into account as the sole microscopic theory of the universe, the condition of CP violation would not be provided in sufficient magnitude.

- Another observation closely related to particle physics are mass effects in neutrino physics. While neutrino masses are not part of the SM, oscillations of interaction eigenstates have been observed [26–28] which can only be explained if at least two of the neutrino flavours are massive.

Moreover, there are purely theoretical motivations to search for a BSM theory. These follow from the consideration of patterns among the parameters of the SM that appear not to be 'natural' if there is no mechanism in the background adjusting them. It is commonly argued, for instance, that the mass parameter of the Higgs doublet is not protected by a symmetry, such that higher order corrections from yet undiscovered, potentially very heavy fields could in principle lead to large higher order contributions. In addition, the arrangement of the flavour structure in the quark sector is quite peculiar, since the CKM matrix responsible for the translation of the mass eigenstates to the flavor eigenstates appears to be almost diagonal.

These indications motivated the theory community to construct a plethora of concrete models on the basis of intuition, symmetry and generalisations of the Higgs sector, with many of them increasing the spectrum of the field content. At the same time experiments are probing the microscopic theory of particles for potential signs of BSM physics. However, up to the current date, no direct observations in form of bumps in distributions have been found which would clearly signal the discovery of new particles. This leads to the current popularity of a more pragmatic approach in the search for deviations of the SM by means of bottom-up EFTs. An introduction into the framework of EFTs is presented in Chapter 4.

# Higher order calculations and QCD cross sections

In the aim for precise predictions in the framework of QFT, there are many technical difficulties that need a clever treatment. In this chapter we are going to touch some of these.

First we exemplify the issue of infinities that appear in the naive application of perturbation theory. Therefore, we have a look at a generic one-loop Feynman integral defined as follows[4]

$$
=: N_{0,D=4} = \int_{-\infty}^{\infty} \frac{\mathrm{d}^4 l}{(2\pi)^4} \frac{1}{D_0 \ldots D_{n-1}} \ . \tag{3.1}
$$

The integration domain of the loop momentum includes the complete Minkowski space, thus a potential source of problem is given by the boundary at infinity. In order to demonstrate this we switch to polar coordinates and just do a rough power counting of loop momentum in the integration.[5] Restricting only to the limit of large loop momentum, i.e. $|l| \to \infty$ in the integrand, the integration leads to

$$
N_{0,D=4}\bigg|_{\mathrm{UV}} \sim \int^{\infty} \mathrm{d}|l| \, \frac{|l|^3}{(|l|^2)^n} \ , \tag{3.2}
$$

which becomes divergent on the upper limit of the integration for $n \leq 2$. This is an example of an UV divergence at one-loop. Divergences that appear in the modes of low loop momentum of Feynman integrals are called IR divergences. A necessary requirement for these are massless interacting particles in the loop. We refrain from an explicit demonstration of their appearance in one-loop integrals and refer the interested reader to Ref. [30], which provides a comprehensive classification and evaluation of all divergent (UV and IR) one-loop master integrals.

---

[4]All Feynman diagrams throughout this thesis were generated using TIKZ-FEYNMAN [29].

[5]The switch to polar coordinates requires a Wick rotation.

Now we have established the appearance of divergences in the naive evaluation of Feynman integrals. This is, however, not the end of QFT (apparently). The main idea to deal with this kind of singularities is to employ a consistent deformation of the integrals, that parameterises the divergence as a certain limit of the introduced so-called regulator. A straight forward choice for UV divergences would be given by an upper cutoff of the loop integral in Eq. (3.1). Such a cutoff does not preserve Poincaré invariance in intermediate steps of the calculations, and, therefore, turns out to be quite cumbersome in calculations within the SM. Hence, a more convenient choice is given by dimensional regularisation (DimReg) that became the standard nowadays. The basic principles of DimReg is presented in Sec. 3.1.

Once a particular regulator has been chosen, it then has to be carried through the calculation until all necessary contributions to physical observables are taken into account, such that the parameterised divergences cancel out and the limit to remove the deformation can be taken. In Sec. 3.2 we introduce the main principle of renormalisation, that turns out to be sufficient to remove all UV divergences on the level of scattering amplitudes, but also introduces insight in the scaling behaviour of parameters and Green's functions. The treatment of IR divergences is described in Sec. 3.3. We briefly describe the necessary factorisation formula of QCD in Sec. 3.4, that allows us to still apply the techniques of perturbation theory for proton collisions at the LHC. Subsequently, we mention the steps to calculate general scattering amplitudes and the particular toolchain relevant for the presented work. Finally, the issue of chirality in DimReg and the continuation of $\gamma_5$ in $D$ dimensions is reviewed in Sec. 3.6.

## 3.1. Dimensional regularisation

In the introduction of the chapter we got to know regularisation as a tool to deform integrals and parameterise the infinities appearing at intermediate steps of the calculation. The basic idea of DimReg is the deformation of the spacetime dimension, which can be understood as an analytic continuation from 4 to (quasi) $D$ dimensions. Formally, the Lorentz representations of vectors and tensors become infinite dimensional, as $D$ can be an arbitrary complex number. The covariant metric tensor, however, is defined such that the index contraction leads to $\eta^{\mu\nu}\eta_{\mu\nu} = D$. The spacetime defined by these metric tensors is therefore called quasi $D$-dimensional spacetime which has the original 4-dimensional spacetime as subspace [31]. The formal definition of Feynman integrals in $D$ dimensions using axioms [32], constructive prescription and proofs of their properties can be found in the literature, e.g. in Refs. [31, 33]. The UV and IR divergences are now represented by pole singularities in $D$. For a 4-dimensional theory they are obtained for $D = 4 - 2\epsilon$ such that negative powers of $\epsilon$ represent poles, whereas positive powers can be safely set to 0 after all UV and IR divergences are removed.

Consistency of the regularisation requires that not only the Feynman diagrams are performed to $D$ dimensions, but also the full theory has to be promoted to a regularised version. Therefore, the action of the theory is expressed as a $D$-dimensional integration over the Lagrangian, i.e. $S = \int \mathrm{d}^d x\, \mathcal{L}$, such that the dimension of the fields and the couplings of the theory diverge from their value at 4 dimensions. In order to restore the usual dimensionality of the couplings, a dimensionful scale $\mu$ is extracted in the renormalisation procedure, as is described in the subsequent section.

There are different schemes for DimReg which differ by their treatment of polarisations of vector fields. For non-supersymmetric theories, the most common choices are 't Hooft-Veltman scheme and conventional DimReg. In the 't Hooft-Veltman scheme, external polarisations are treated in 4-dimensions and polarisations of loop particles are extended to $D$ dimensions, whereas in conventional DimReg all polarisations are considered in $D$ dimensions. A more

detailed overview of different schemes of DimReg, but also of non-dimensional regulators, can be found in Refs. [34].

## 3.2. UV divergences, renormalisation and renormalisation group equation

We have observed in the introduction of this chapter an explicit example of an UV divergence at one-loop. These divergences, once expressed parametrically using an adequate regularisation prescription, can be actually absorbed if a reparameterisation of the Lagrangian parameters and fields is performed. This procedure is called renormalisation.

One main requirement for a consistent renormalisation procedure is that the regularised UV divergences are local, such that they consist of polynomials of external momenta and mass parameters. This has indeed been proven to be the case, when divergences of subdiagrams are already taken care of [33, 35–40]. Therefore, it is possible to absorb the infinities in local counter terms of the Lagrangian.

If the the Lagrangian already includes all non-redundant terms allowed by the underlying symmetry, the local counter terms can be constructed from an expansion of the original (bare) parameters and fields of the theory. In order to clarify this point, it is important to understand that the Lagrangian of the theory itself is nothing measurable. Thus, there is a freedom to redefine its bare parameters in renormalised, UV finite parts and counter terms that are constructed order by order in perturbation theory. The renormalised parameters then resemble quantities that can be experimentally determined, i.e. masses of the fields and couplings. In the following, we denote bare parameters and fields with a superscript $b$. The renormalisation can then be represented by a multiplicative constant which is expanded order by order. Working in DimReg we may write for a bare coupling $g^b$, bare mass $m^b$ and bare field $\phi^b$

$$
\begin{aligned}
g^b &= \mu^\epsilon Z_g g = \mu^\epsilon \left( 1 + \delta_{Z_g}^{(1)} + \dots \right) g \\
m^b &= Z_m m = m + \delta_m^{(1)} + \dots \\
\phi^b &= \sqrt{Z_\phi}\phi = \left( 1 + \frac{1}{2}\delta_{Z_\phi}^{(1)} + \dots \right) \phi \,,
\end{aligned}
\tag{3.3}
$$

where a factor including the renormalisation scale $\mu$ is extracted from $g$ in order to remove the dimensionality of the coupling introduced by the regulator. After the expansion of the form Eq. (3.3) we are left to define the counter terms $\delta_i$ with an adequate renormalisation prescription. The basic condition is that the $\delta_i$ absorb all the UV poles, however, there is also a freedom to include additional finite pieces.

In modern perturbative calculations, there are two common prescriptions which we also apply in the subsequent work:

$\overline{\text{MS}}$ **scheme:** The modified minimal subtraction ($\overline{\text{MS}}$) scheme [41] is based on the minimal subtraction (MS) scheme [38]. The counter terms are defined such that they remove only the UV divergences together with the constant combination $\log(4\pi) - \gamma_E$, with $\gamma_E$ being the Euler-Mascheroni constant, that appears in DimReg. Therefore, a typical counter term has the polynomial form

$$
\delta_i^{(l)} = \sum_{j=1}^{l} c_j \frac{(4\pi e^{-\gamma_E})^l}{\epsilon^{n_j}} \,,
\tag{3.4}
$$

where $l$ denotes the perturbative order, i.e. $l = 1$ for NLO.

**OS scheme:** In the on-shell (OS) scheme the renormalisation constants for fields and masses are chosen such that the renormalised mass parameter has precisely the value of the pole of the resummed propagator and its residue is set to $i$. This is formalised in two conditions on the full self energy $\hat{\Sigma}(\not{p})$ (including counter terms)

$$\mathrm{Re}\left(\hat{\Sigma}(\not{p})\right)u(p)\Big|_{p^2\to m^2}=0\,,\qquad\frac{i}{\not{p}-m}\mathrm{Re}\left(\hat{\Sigma}(\not{p})\right)u(p)\Big|_{p^2\to m}=0\,,\qquad(3.5)$$

where Eq. (3.5) only describes the fermionic case, as we apply it to the top-quark.

If we were able to calculate in arbitrary precision, the different choices of shifting finite pieces should not affect the calculation of observables as the full theory does not know about the regularisation and renormalisation schemes. Yet working at finite order we encounter differences between the schemes. This is however not only a downside, since it can give some qualitative idea on the convergence of the perturbative expansion, when different well-motivated renormalisation prescriptions are compared at the same order. For $\overline{\mathrm{MS}}$ this is usually done in a variation of the renormalisation scale $\mu$ and the resulting differences are called scale uncertainty. The size of the scale uncertainty in practical calculations has been demonstrated to shrink when higher order effects are taken into account. However, the perturbative expansion of predictions may not be at a convergent order such that the scale uncertainty without knowledge of higher order effects cannot really be interpreted as an 'uncertainty'.

It is also possible to change the perspective and try to get some insight on the scaling behaviour of the theory considering that bare quantities should be independent on the choice of regulator and renormalisation. The renormalisation procedure introduces a dependence of the renormalised quantities on a scale, in $\overline{\mathrm{MS}}$ the scale $\mu$, which the original bare quantities do not have. Applying a derivative w.r.t. the regulator, $\mu\partial/\partial_\mu$ for $\overline{\mathrm{MS}}$, on observables, bare $n$-point functions or parameters leads to differential equations, the so-called renormalisation group equation (RGE), which resemble the energy scaling behaviour. This is an important relation since all parameters are always determined at a specific energy scale. Thus the predictions of observables is much improved if we know how to transport (run) the parameters to the scale relevant for the process. We exemplify this for the strong coupling $\alpha_s=g_s^2/(4\pi)$ in the following.

The renormalised strong coupling is defined as

$$\alpha_s^b=\mu^{2\epsilon}Z_{\alpha_s}\alpha_s\,.\qquad(3.6)$$

Considering $\mu\dfrac{\partial}{\partial_\mu}\alpha_s^b=0$, we find

$$\mu\frac{\partial}{\partial\mu}\alpha_s=-2\epsilon\alpha_s-Z_{\alpha_s}^{-1}\mu\frac{\partial}{\partial\mu}Z_{\alpha_s}\alpha_s\to-\beta_0\frac{\alpha_s^2}{2\pi}+\mathcal{O}\left(\alpha_s^3\right)\,,\qquad(3.7)$$

where $\beta_0=\dfrac{11}{3}c_A-\dfrac{4}{3}T_Fn_l$, with $n_l$ being the number of active quark flavours contributing to the running. We take the limit $\epsilon\to0$ in the expanded expression on the right hand side of Eq. (3.7). The solution of the one-loop RGE for the running from the input scale $\mu_0$ to the renormalisation scale $\mu$ can be written as

$$\alpha_s(\mu)=\frac{\alpha_s(\mu_0)}{1+\frac{\beta_0}{2\pi}\log\frac{\mu}{\mu_0}}\,.\qquad(3.8)$$

Since $\beta_0>0$ for QCD in the SM, Eq. (3.8) describes a decrease of QCD coupling strength if the scale $\mu$ is increased (which remains valid at higher perturbative orders). This asymptotic
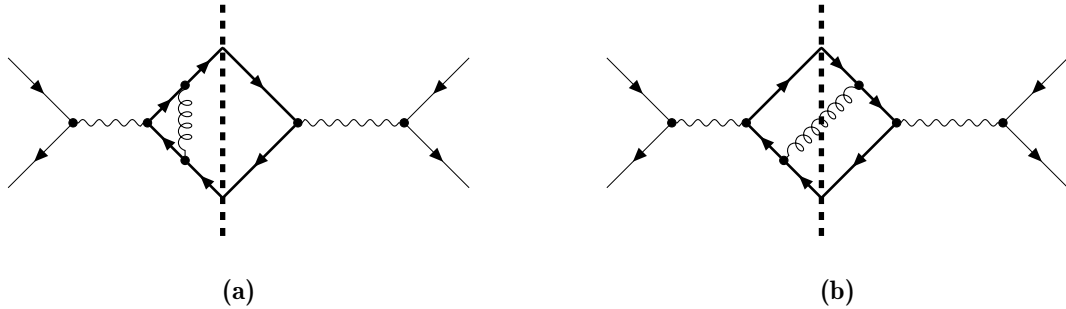
**(a)**            **(b)**

**Figure 3.1.:** Visualisation of virtual correction (a) and real radiation (b) which need to be taken into account in order to reach an IR finite result at NLO QCD for the case of $e^+e^- \to \bar{q}q$ at parton level. The diagrams resemble the cut diagram version of $\mathcal{M}_1\mathcal{M}_2^*$.

freedom is an important property of QCD, as it implies that QCD in the high energy regime can be treated in perturbation theory. On the other hand, the denominator of Eq. (3.8) vanishes for some energy scale $\Lambda_{\mathrm{QCD}} < \mu_0$, the so-called Landau pole of QCD. If the energy scale approaches $\Lambda_{\mathrm{QCD}}$ the coupling strength increases until perturbation theory breaks down.

We can try to get a qualitative picture what happens in the low energy regime of QCD. Starting in the high energy regime in which QCD behaves perturbatively, interacting particles of QCD, the quarks and gluons, are subject to an increasing interaction strength for decreasing energy scale or, likewise, increasing distance between partices. If the distance between the particles is sufficiently increased, the associated QCD potential grows large enough to produce particles and antiparticles out of the interacting vacuum, which after complete separation of the particles leads to very complicated, non-perturbative multi-parton bound states, so-called hadrons. Even if their existence can be understood by the principles of perturbative QCD, these bound states cannot be described in a perturbative way. That we are still able to apply the methods of perturbative QCD for the calculation of proton collisions at the LHC is subject of Sec. 3.4.

## 3.3. Infrared structure and subtraction

We encountered the notion of IR divergences already in the introduction of this chapter in the integration region of vanishing loop momentum of loop integrals. The IR divergent loop diagrams have a counter part in diagrams with additional radiation of massless particles that also lead to IR divergences in some regions of the phase space integration, and their combination to observables can indeed lead to IR finite results. This will be clarified with the example of $e^+e^- \to \bar{q}q$ with $m_e = m_q = 0$.

In Fig. 3.1 (a) we show an example diagram for the virtual contribution to the process at NLO which leads to an IR divergence (and UV divergence, which we assume to be treated by appropriate renormalisation). The diagram is represented in the form of a cut diagram that resembles already the interference between LO matrix element $\mathcal{M}_{\mathrm{B}}$ and NLO matrix element $\mathcal{M}_{\mathrm{V}}$, i.e. $\mathcal{M}_{\mathrm{V}}\mathcal{M}_{\mathrm{B}}^*$, which has the overall order in the strong coupling $\mathcal{O}(\alpha_s)$. However, the virtual corrections are just one part of the expansion of the cross sections $\sigma \sim |\mathcal{M}|^2$ at $\mathcal{O}(\alpha_s)$, as the squared tree level amplitude including the radiation of an additional gluon, $e^+e^- \to \bar{q}qg$, contributes at the same order. The diagram in Fig. 3.1 (b) depicts such a real radiation contribution, which in the cut diagram representation makes the counting apparent. The real radiation contributions exhibit IR divergences in the phase-space integration. If both, virtual and real corrections, are evaluated with the same regulator and all contributions to the cross section at the same order after integration over the phase space are considered, the final result turns out to be finite.

Qualitatively, this can be understood as follows. The final states of an interacting theory are not well separated from multi-particle states including soft (infinitesimal energy) and collinear (same direction) radiation of massless particles. As the additional radiation in these regions cannot be resolved by experiment, they have to be included order by order in a consistent definition of an observable. Since the collinear and soft regions are precisely the ones responsible for the IR divergence of the real radiation, such an inclusive observable will always be finite. A formal proof of this behaviour is given by the KLN-theorem, named after Kinoshita, Lee and Nauenberg [42, 43]. (Although for interactions with initial state QCD partons the KLN-theorem requires also to be inclusive for multi-initial states, this is not necessary when initial state partons are massless.)

In mathematical language, we may write the expansion of the partonic cross section in the perturbative regime in the form

$$\sigma = \sigma_{\text{LO}} + \sigma_{\text{NLO}} + \dots \tag{3.9}$$

where the NLO cross section is split into virtual and real radiation contribution as

$$\sigma_{\text{LO}} = \int_n \mathrm{d}\sigma_B$$
$$\sigma_{\text{NLO}} = \int_n \mathrm{d}\sigma_V + \int_{n+1} \mathrm{d}\sigma_R \ . \tag{3.10}$$

We introduced the short-hand notation $\int_n$ for an integration over $n$-particle phase space volume, $\mathrm{d}\sigma_B$ for the Born integrand, $\mathrm{d}\sigma_V$ for the integrand of the virtual contribution and $\mathrm{d}\sigma_R$ for the integrand of the real radiation. Even though the definition for $\sigma_{\text{NLO}}$ in Eq. (3.10) leads to an analytically finite result, it is fairly impractical if we want to compute cross sections numerically since the divergences have to cancel over different dimensional phase-space integrals. Working in DimReg that means only after integration the limit $\epsilon \to 0$ can be used. A remedy for this issue has been developed in the form of IR subtraction procedures which introduces additional terms into Eq. (3.10) that cancel the IR divergences of virtual and real contributions individually on integrand level. For NLO calculations several versions have been developed. We follow the notation of the dipole subtraction by Catani and Seymour [44–46] and briefly summarize the main principle.

A subtraction term $\mathrm{d}\sigma_A$ is chosen such that it approximates the real radiation in the divergent regions. If its structure is appropriately organised, the combination to the NLO cross section

$$\sigma_{\text{NLO}} = \int_n \left[ \mathrm{d}\sigma_V + \int_1 \mathrm{d}\sigma_A \right] + \int_{n+1} \left[ \mathrm{d}\sigma_R - \mathrm{d}\sigma_A \right] \ , \tag{3.11}$$

leads to a separately IR finite expression for the subtracted real radiation and in the integrand of the subtracted virtual contribution. Therefore, already before performing the integral the limit $\epsilon \to 0$ can be taken which makes the numerical evaluation feasible. In the Catani-Seymour formalism, the subtraction term is constructed with the definition of universal dipole operators that are applied to the Born integrand. Integrating the dipole operator over the one-particle phase space associated with the radiation, the IR subtracted virtual contribution leads to

$$\left[ \mathrm{d}\sigma_V + \int_1 \mathrm{d}\sigma_A \right] = \mathrm{d}\Phi_n \left( 2\mathrm{Re} \left( \langle \mathcal{M}_{\text{LO}} | \mathcal{M}_{\text{NLO}} \rangle \right) + \langle \mathcal{M}_{\text{LO}} | \mathbf{I} | \mathcal{M}_{\text{LO}} \rangle \right) \ , \tag{3.12}$$

where $\Phi_n$ is the $n$-particle phase space, $\mathbf{I}$ is the Catani Seymour $\mathbf{I}$ operator and $|\mathcal{M}_{\text{(N)LO}}\rangle$ denotes the matrix element expressed as a vector in colour space according to the formalism

in Refs. [44–46]. $|\mathcal{M}_{(\text{N})\text{LO}}\rangle$ is therefore constructed as a linear combination of its independent colour structures and [46]

$$
\begin{aligned}
\mathbf{I} = -\frac{\alpha_s}{2\pi}\frac{(4\pi)^\epsilon}{\Gamma(1-\epsilon)} \sum_j \frac{1}{\mathbf{T}_j^2} \sum_{k \neq j} \mathbf{T}_j \cdot \mathbf{T}_k \\
\times \left[ \mathbf{T}_j^2 \left( \frac{\mu^2}{2p_j \cdot p_k} \right)^\epsilon \left( \mathcal{V}_j - \frac{\pi^2}{3} \right) + \Gamma_j + \gamma_j \log \frac{\mu^2}{2p_j \cdot p_k} + \gamma_j + K_j + \mathcal{O}\left( \epsilon \right) \right] \,,
\end{aligned}
\tag{3.13}
$$

where we suppressed the arguments of $\mathcal{V}_j$ and $\Gamma_j$. The sum in $j$, $k$ denotes all external coloured partons and $\mathbf{T}_{j/k}$ are the generators of the respective $SU(3)_{QCD}$ representation which can be evaluated as a matrix in the colour space defined by the independent colour structures of $|\mathcal{M}_{(\text{N})\text{LO}}\rangle$. The expressions for $\mathcal{V}_j$, $\Gamma_j$, $\gamma_j$ and $K_j$ can be found in Ref. [46].

There has been much progress in the generalisation of IR schemes to the higher order case, but there is no general and efficient procedure available yet [47]. The pole structure of IR divergences at NNLO QCD, however, has been derived a while ago [48–54]. The complete factor that generalises the IR pole structure of the $\mathbf{I}$ operator of Eq. (3.13) to NNLO QCD can be found in Ref. [53]. This procedure at NNLO QCD did not enter the work of the present thesis, but has been applied in Ref. [55] in order to derive the IR poles for a cross check of the two-loop virtual contribution.

## 3.4. Factorisation and evaluation of hadronic cross sections

Up to this point, we were only discussing how to work with QCD in the regime where perturbation theory is possible. However, proton-proton colliders, like the LHC, are based on the collision of non-perturbative QCD bound states, hence their cross sections cannot directly be calculated with the tools established so far in this work. Yet, considering that there are very different energy scales at play we expect the hard physics of the highest energy collision and the soft physics of the non-perturbative proton dynamics to effectively decouple. The time scale of the hard scattering between the partonic states is expected to be much shorter than the typical reaction time of the non-perturbative dynamics such that there is basically no interference.

This principle has been formalised in the QCD factorisation theorems [56] which allow to split the non-perturbative soft physics from the hard scattering process. Within the hard process the partons are approximated as free states that enter the perturbative calculation. The relevant QCD factorisation for cross sections of proton-proton collisions $\sigma(P_1, P_2)$ can be expressed as a convolution of parton distribution functions (PDF) with the hard partonic cross section of the form[6]

$$
\sigma(P_1, P_2) = \sum_{a,b} \int \mathrm{d}x_1 \int \mathrm{d}x_2 f_{a|p}\left( x_1, \mu_F^2 \right) f_{b|p}\left( x_2, \mu_F^2 \right) \hat{\sigma}_{(a,b)}\left( x_1 P_1, x_2 P_2; \mu_F^2 \right) \,.
\tag{3.14}
$$

where the sum in $a$ and $b$ runs over all parton types of the proton and $\hat{\sigma}_{(a,b)}$ is the respective partonic cross section of the hard process. $x_1$ ($x_2$) can be understood as the fraction of the proton momentum $P_1$ ($P_2$) that is transferred to parton $a$ ($b$), however, the parton momentum has to be mapped to a massless on-shell state. The PDF $f_{a|p}$ ($f_{b|p}$) describes the probability to find a free parton $a$ ($b$) within the parent proton that carries the momentum fraction $x_1$ ($x_2$) of the proton. The PDF themselves inherit the non-perturbative dynamics of the proton

---

[6]In principle, there are corrections of $\mathcal{O}\left( \Lambda_{QCD}/Q \right)$ on the right hand side of Eq. (3.14) with $Q$ being characteristic energy scale of the process. These corrections are called higher twist contributions. In collider experiments at high energies they become negligible and Eq. (3.14) represents a sufficient description.

and are therefore not calculable, but they represent a universal property. Hence, they can be measured by a limited number of experiments and then reused for predictions of arbitrarily many observables.

Eq. (3.14) also introduces the factorisation scale $\mu_F$, which can be seen as the energy scale at which the partons are resolved. Note that the hard and soft physics are decorrelated, such that Eq. (3.14) describes a multiplication of probabilities.

More information about perturbative QCD and factorisation can be found in Ref. [57] which provides a broad introduction to the topic.

## 3.5. General procedure for the evaluation of fixed order amplitudes and computational tools

In this section, we briefly describe the general structure of evaluating higher order matrix elements. We also specify the tools used throughout this work.

At one-loop level, all Feynman integrals can be expressed in terms of a finite set of master integrals for which the structure is well understood. A common procedure of this reduction and representation of master integrals (Passarino-Veltman integrals) was developed by t'Hooft, Passarino and Veltman [58, 59]. Tensor integrals are expressed in terms of form factors of combinations of the metric and external momenta, which are related to the master integrals through a system of linear equations obtained by contraction with metric and momenta. In the notation of Passarino-Veltman integrals, the master integrals are given by tadpoles ($A_0$), bubbles ($B_0$), triangles ($C_0$) and boxes ($D_0$). Note that Feynman integrals of $n$-point functions with $n > 4$ can in principle be reduced to maximally box-type integrals, with the caveat that for some momentum configuration the denominators of the prefactors involving inverse Gram-determinants could vanish. The analytic expressions of loop amplitudes later in this thesis are expressed in terms of these Passarino-Veltman integrals in the convention of FEYNCALC [60–62] (which is equivalent to the LOOPTOOLS [63] convention), thus keeping the loop factors explicit.

For the analytic calculations, we use QGRAF [64] in order to generate the relevant diagrams and FEYNCALC for algebraic manipulations. In addition, the one-loop numerical evaluation of the real radiation in Chapter 6 is done with the one-loop matrix element provider GOSAM [65, 66]. In the employed setup, GOSAM relies on QGRAF, FORM [67] and SPINNEY [68] for the amplitude construction and GOLEM95C [69–71] or NINJA [72,73] for the reduction and integral evaluation.

Starting at the two-loop level, the evaluation procedure gets more involved. One reason being the possible combinations of scalar products of momenta in the numerator of Feynman integrals which outnumber the denominator structures such that the reduction is more involved. In addition, exact evaluation of master integrals can be quite tedious and is in cases with many scales or loops even impossible with current day techniques.

The genuine two-loop calculations relevant for this work have been performed based on two toolchains which follow a similar pattern. The first one uses the framework of GOSAM-Xloop, which is a private extension building on GOSAM, the second one is organised by ALIBRARY [74]. In both cases, the structure can be crudely summarized in three steps:

**Projection onto form factors** The relevant diagrams are generated with QGRAF, the amplitude is projected onto form factors using FORM and the Feynman integrals are identified.

**Reduction to master integrals** The reduction of the Feynman integrals is based on Laporta's algorithm [75]. GoSam-Xloop invokes Reduze [76] for the reduction, Alibrary uses an interface to Kira [77, 78].

**Numerical evaluation** In both cases the master integrals are evaluated numerically using pySecDec [79–82].

## 3.6. Chirality in dimensional regularisation and $\gamma_5$ schemes

The concept of chirality is intimately connected to the 4-dimensional nature of space time, since it is a direct consequence of two irreducible spinor representations of $SO(3,1)$ which we denote as LH and RH (Weyl-) spinors. This poses, however, some trouble with DimReg, as this relies on the definition of the theory in $D$ dimensions to parameterise divergences at intermediate steps of the calculation. The technical consequences of this formal incompatibility and possible attempts for a proper treatment is the topic of this section.

As a first step we show how chirality is mathematically represented in practical calculations in terms of $\bar{\gamma}_5$.[7] Then the main features of the Dirac algebra and the properties of $\bar{\gamma}_5$ in 4-dimensions are briefly recapitulated. Afterwards, the extension to $D$ dimensions of the Dirac algebra is discussed and the difficulty for a continuation of $\bar{\gamma}_5$ is pointed out. Then possible attempts to consistently treat $\bar{\gamma}_5$ in $D$ dimensions are discussed and two common prescriptions are introduced in Secs. 3.6.1 and 3.6.2.

In the SM massive fermionic fields acquire their mass after symmetry breaking in form of a Dirac mass term. Hence, it is convenient to represent fermion fields in their mass eigenstate in terms of Dirac spinors (which are a reducible combination of LH and RH representations) in practical calculations. However, since the SM is a chiral gauge theory, the interaction acts on the chiral substructure which can be represented using projection operators

$$\psi_{L/R} = \mathbb{P}_{L/R}\psi \, , \tag{3.15}$$

where

$$\mathbb{P}_{L/R} = \frac{1}{2}\left(\mathbb{1} \mp \bar{\gamma}_5\right) \, . \tag{3.16}$$

In the Dirac representation of fermions, the 4-dimensional nature of chirality is therefore expressed in terms of the 4-dimensional object $\bar{\gamma}_5$. Thus, a proper treatment of chirality in dimensional regularisation is shifted towards a consistent prescription of the extension of $\bar{\gamma}_5$ to $D$ spacetime dimensions.

Let us briefly introduce the Dirac algebra (which given by the Clifford algebra $\mathrm{Cl}_{1,3}(\mathbb{R})$) in 4-dimensions. For 4-dimensional gamma matrices $\bar{\gamma}^\mu$ and metric $\bar{\eta}^{\mu\nu}$ the main property of the Dirac algebra is the anticommutation relation

$$\{\bar{\gamma}^\mu, \bar{\gamma}^\nu\} = 2\bar{\eta}^{\mu\nu} \, , \tag{3.17}$$

where the indices can have values $\mu, \nu \in \{0, 1, 2, 3\}$. In addition to those four $\bar{\gamma}$-matrices comprising the algebra in Eq. (3.17), we define an additional matrix, that has to fulfill

$$\{\bar{\gamma}^\mu, \bar{\gamma}_5\} = 0 \, , \quad \bar{\gamma}_5^2 = \mathbb{1} \, . \tag{3.18}$$

It is easy to proof that this object exists in 4-dimension, as the explicit constructive definition

$$\bar{\gamma}_5 := i\bar{\gamma}^0\bar{\gamma}^1\bar{\gamma}^2\bar{\gamma}^3 = -\frac{i}{4!}\bar{\epsilon}^{\mu_1\mu_2\mu_3\mu_4}\bar{\gamma}_{\mu_1}\bar{\gamma}_{\mu_2}\bar{\gamma}_{\mu_3}\bar{\gamma}_{\mu_4} \, , \tag{3.19}$$

---

[7]In this section, we clearly discriminate between the 4-dimensional (constructively defined) $\bar{\gamma}_5$ and the $D$-dimensional (algebraic) extension $\gamma_5$.

satisfies Eq. (3.18). The definition on the right side of Eq. (3.19) uses the 4-dimensional, fully antisymmetric Levi-Civita symbol $\bar{\epsilon}^{\mu_1\mu_2\mu_3\mu_4}$ with convention $\bar{\epsilon}^{0123} = 1$. Another feature of $\bar{\gamma}_5$ is the trace identity

$$\text{Tr}\left[\bar{\gamma}^{\mu_1}\bar{\gamma}^{\mu_2}\bar{\gamma}^{\mu_3}\bar{\gamma}^{\mu_4}\bar{\gamma}_5\right] = -4i\bar{\epsilon}^{\mu_1\mu_2\mu_3\mu_4} \ , \tag{3.20}$$

which is obvious when the definition in Eq. (3.19) in terms of $\bar{\epsilon}^{\mu_1\mu_2\mu_3\mu_4}$ is considered.

It is important to note that both properties of $\bar{\gamma}_5$, the anticommutation relation of Eq. (3.17) and the trace identity Eq. (3.20), have important physical consequences. The anticommutation relation is necessary for the preservation of symmetry relations between Green's functions that are dictated by the gauge symmetry of the theory, i.e. Ward-Takahashi identities [83, 84] and Slavnov-Taylor identities [85, 86]. The $\bar{\gamma}_5$ trace relation is responsible for the Adler-Bell-Jackiv anomaly [87, 88]. Thus, if we are aiming for higher order calculations involving chiral vertices, a continuation scheme of $\bar{\gamma}_5$ to $D$-dimension has to consistently respect both in the limit $D \to 4$.

The usual property of the Dirac algebra Eq. (3.17) can be unambiguously extended $D$-dimensions which then takes the form

$$\{\gamma^\mu, \gamma^\nu\} = 2\eta^{\mu\nu} \ , \tag{3.21}$$

where unbarred $\gamma^\mu$ and $\eta^{\mu\nu}$ are now Dirac matrix and metric of quasi $D$-dimensional spacetime. It is impossible, however, to find a $D$-dimensional representation $\gamma_5$ that consistently fulfills the following three identities (that are simultaneously valid in strictly 4-dimensions):

(1) $\qquad \{\gamma^\mu, \gamma_5\} = 0$

(2) $\qquad \text{Tr}\left[\Gamma_1\Gamma_2\gamma_5\right] = \text{Tr}\left[\Gamma_2\gamma_5\Gamma_1\right] \quad$ for arbitrary strings of $\gamma$ matrices $\Gamma_1$ and $\Gamma_2$ $\quad$ (3.22)

(3) $\qquad \text{Tr}\left[\gamma^{\mu_1}\gamma^{\mu_2}\gamma^{\mu_3}\gamma^{\mu_4}\gamma_5\right] = -4i\bar{\epsilon}^{\mu_1\mu_2\mu_3\mu_4}$

This can be easily demonstrated [89]: Assume we have a representation of $\gamma_5$ following (1) and (2). Then

$$\begin{aligned}
0 &= \text{Tr}\left[\gamma_\alpha\gamma^\alpha\gamma^{\mu_1}\gamma^{\mu_2}\gamma^{\mu_3}\gamma^{\mu_4}\gamma_5\right] - \text{Tr}\left[\gamma^\alpha\gamma^{\mu_1}\gamma^{\mu_2}\gamma^{\mu_3}\gamma^{\mu_4}\gamma_5\gamma_\alpha\right] \\
&= 2\left(D - 4\right)\text{Tr}\left[\gamma^{\mu_1}\gamma^{\mu_2}\gamma^{\mu_3}\gamma^{\mu_4}\gamma_5\right] \ ,
\end{aligned} \tag{3.23}$$

leads to a contradiction of (3): If $D \neq 4$ then Eq. (3.23) requires the trace to vanish. Interpreting dimensional regularisation as analytic continuation, complex analysis now requires the trace to vanish for all values of $D$, including $D = 4$, which is in clear contradiction of requirement (3).

We have to conclude that in $D$-dimensions, one of the properties has to be violated in a way that it is restored in the limit $D \to 4$ for physical observables. Different approaches have been developed in the attempt to achieve this. We focus in this work only on two versions, the naive dimensional regularisation (NDR) [90] scheme and the Breitenlohner-Maison-'t Hooft-Veltman (BMHV) [91, 92] scheme. These are introduced in the following subsections and they are contrasted in the SMEFT calculation of single Higgs production in Chapter 7.

### 3.6.1. Naive Dimensional Regularisation

In the NDR [90] scheme $\gamma_5$ is defined by the algebraic property (1) of Eq. (3.22). This scheme is a convenient choice for single Dirac lines and for Dirac traces with an even number of $\gamma_5$, as it automatically preserves the Ward identities, is computationally straight forward and leads to consistent results [90, 93–95]. The case for an odd number of $\gamma_5$ in the traces, however, needs an additional prescription. There are different flavours of NDR for these traces: On the one hand, Ref. [89] proposes to assume cyclicity of the trace and fix the ambiguous terms

using relations between tensor form factors derived by explicitly demanding the necessary symmetry relations, like Bose symmetry and current conservation. On the other hand, the approach by Refs. [96, 97] dismisses the cyclicity of traces with odd $\gamma_5$ in favor of the trace relation (3) of Eq. (3.22), such that these anomalous traces are understood as a functional instead of a 'proper trace'. This modification then requires a reading point prescription to be applied consistently for well defined results. Recent results of the singlet axial-current operator [98] suggest, however, that a modified version of the scheme in Refs. [96, 97] might become necessary at higher loop order.

### 3.6.2. Breitenlohner-Maison-'t Hooft-Veltman Scheme

The BMHV [91, 92] scheme defines $\bar{\gamma}_5$ constructively with the 4-dimensional definition of Eq. (3.19). Hence, the 4-dimensional subspace and the quasi $(D - 4)$-dimensional subspace are separated in the process.[8] We therefore introduce the metric $\hat{\eta}$ that projects on the $(D - 4)$-dimensional subspace and $\hat{\gamma}$ the gamma matrix of the $D - 4$ indices. We identify the following relations

$$\{\bar{\gamma}^\mu, \bar{\gamma}_5\} = 0 \,, \qquad [\hat{\gamma}^\mu, \bar{\gamma}_5] = 0 \,. \tag{3.24}$$

This necessarily introduces a violation of symmetry relations in a chiral theory [31]: In principle, DimReg allows the freedom to choose different $D$-dimensional extensions of the interaction Lagrangian which may differ by evanescent contributions, as long as the limit $D \to 4$ restores the original Lagrangian. The regularisation of loop integrals with fermions, however, necessitates a Dirac representation of the fermion fields and the derivative of the kinetic term has to be fully promoted to a $D$-dimensional version. As the chiral symmetry is constructed with the 4-dimensional version of $\bar{\gamma}_5$, the evanescent part of the fermion kinetic term in the regularised Lagrangian violates chiral symmetry transformations. These violations of Ward identities then have to be restored by symmetry restoring counterterms order by order in perturbation theory.

The BMHV scheme has been proven to be self consistent [92] and in fact it is up to date the only scheme for which this is the case. However, the procedure of splitting dimensions and the need for symmetry restoring counterterms make calculations computationally involved.[9]

For the chiral vertices appearing in subsequent chapters, we apply the symmetrised $D$-dimensional extension

$$\bar{\gamma}^\mu \, \mathbb{P}_{L/R} \to \mathbb{P}_{R/L} \, \gamma^\mu \, \mathbb{P}_{L/R} \,, \tag{3.25}$$

which fully resembles the chirality of the interacting fields in the Lagrangian. In addition, this choice leads to the simplest expressions in intermediate stages of explicit calculations (see e.g. Refs. [31, 100, 101]).

---

[8]Although it is not strictly required, the BMHV scheme for $\bar{\gamma}_5$ naturally combines with the 't Hooft-Veltman scheme for DimReg, as in both cases the 4-dimensional and $(D - 4)$-dimensional parts are split.

[9]The scheme developed by Larin [99] for the purpose of higher order calculations in QCD and QED is a special case of the BMHV scheme that avoids the explicit splitting of $D$ into 4- and $(D - 4)$-dimensions with the introduction of a quasi $D$-dimensional version of the Levi-Civita symbol in the definition of Eq. (3.19) and a manual adjustment for the axial current into a Hermitian form. Nevertheless, symmetry restoration at each higher order is still required and the scheme can lead to inconsistencies when more than two Levi-Civita symbols appear in the evaluation of amplitudes [31].

Effective field theories

In this work, we rely on Effective field theories (EFT) for the description of deviations from pure SM behavior in processes observed at colliders. This chapter is devoted to the introduction of the general concept of EFTs and their application as a bottom-up extension of the SM. The first part is intended to give a motivation for the EFT approach and an overview. The following introduction to the topic and Sec. 4.1 greatly profited from the recent reviews of Refs. [102–104], which provide not only a much more detailed resource about the Standard Model effective field theory (SMEFT), but also EFTs in QFT in general.

Effective field theories are a tool to formalise the general notion that phenomena which appear at very separate scales decouple from each other. Thus, their application allows to retain only the relevant degrees of freedom for the studied scale supplemented with an expansion procedure to systematically include effects of the decoupling physics up to arbitrary precision.

In order to clarify this approach we briefly discuss a practical example from classical electrodynamics in the following. The Green's function for the potential of a point charge in electrodynamics has the well known form $G(\vec{r}, \vec{R}) \sim |\vec{r} - \vec{R}|^{-1}$. Using the Green's function it is in principle possible to write down the formal solution for Poisson's equation of electrostatics with a general charge distribution (neglecting surface terms). However, if the charge distribution is localised in a limited area and the potential $V$ for an observer far away at the position $\vec{R}$ is to be described, it is much more convenient to do a multipole expansion of the form [105]

$$V\left(\vec{R}\right) = \int_V d^3r \frac{\rho\left(\vec{r}\right)}{4\pi|\vec{R} - \vec{r}|} = \frac{1}{R} \sum_{l=0}^{\infty} \sum_{m=-l}^{l} C_{lm} \left(\frac{d}{R}\right)^l Y^{lm}\left(\Omega\right) \tag{4.1}$$

where the typical length scale of the charge distribution $d$ is extracted from the expansion coefficients in order to have dimensionless coefficients $C_{lm}$. The terms in Eq. (4.1) are naturally ordered by importance since subsequent orders in $l$ are suppressed by higher powers of $(d/R)^l$. Therefore, already a finite number of coefficients $C_{lm}$ for the first moments suffices for an accurate description of the potential if the scale hierarchy fulfills $d \ll R$. For a better prediction higher order terms can be included to systematically improve the precision.

The expansion in Eq. (4.1) can be used in two ways. On the one hand, if a charge distribution at *short distance* is known, the leading moments $C_{lm}$ can be calculated to derive an effective

description of the potential $V$. On the other hand, if a charge distribution is unknown, the coefficients[10] $\bar{C}_{lm} = C_{lm}d^l$ can be determined at *long distance* by measurement of the potential.

The two possibilities for the usage of the multipole expansion reflect the two directions of applications of EFTs in general, which are called *top-down* and *bottom-up* approach. The two EFT approaches shall be briefly described:

**Top-down:** Assume a high energy theory is well known, but should be used to predict low energy observables such that a large hierarchy of scales exist. The full theory could in principle be directly applied in perturbative calculations of observables. However, the scale separation could introduce large logarithms with bad numerical stability. Therefore, matching the UV theory to an EFT representation retaining only the relevant degrees of freedom for the low energy process can be much more predictive with the possibility to include as many terms in the expansion as necessary for the desired precision.

**Bottom-up:** In the bottom-up scenario there is a well established theory valid at low energies which is to be probed for effects of unknown new physics at higher energies. Since the systematics of an EFT expansion are universal, it can be used to describe potential deviations from the low energy theory as would be induced by arbitrary new physics scenarios under generic assumptions, while being ignorant about a concrete model realisation. In the optimal scenario, a pattern in the parameter space describing the deviation would point to new physics scenarios to which the physics community could point their attention to look for concrete models.

EFTs in QFT have a long history and their usage is widespread nowadays. The first instances of an EFT operator in a QFT was the invention of Fermi's theory of weak interaction [106]. It provided a very successful description for the low energy limit of weak interactions even if the concepts necessary for a consistent definition of an EFT had not yet been developed. A seminal step in the direction towards formalising EFTs was made by the decoupling theorem [107, 108].

The theorem demonstrated, that Green's functions involving only legs of light degrees of freedom in the presence of heavy fields lead to corrections that are suppressed by powers of the heavy mass in addition to contributions to the renormalisation of the low energy parameters. With this we can conclude that the heavy particles decouple when their mass parameters are taken to infinity, if the coupling does not diverge as the mass approaches the limit. This generalises the standard notion that physics at different scales should not affect each other in decoupling scenarios to the context of QFTs. Hence, for a sufficient separation of scales a decent approximation is obtained if much lower scales are set to 0 and much higher scales are set to infinity. As the contributions in the Green's functions with higher suppression of the mass are local, they can be treated as perturbations of the low energy theory and expressed in terms of higher order EFT operators.

After the necessary understanding was achieved in the physics community, several quantum EFTs have been developed in order to investigate different energy scales relevant for particle physics and beyond. In the following, we focus on the bottom-up extensions of the SM, that will be used in Part II. Therefore, in Sec. 4.1 and Sec. 4.2, the relevant systematics for the linear and non-linear bottom-up EFT of the SM are established. Subsequently, in Sec. 4.3 we specify additional assumptions and our power counting defining the version of SMEFT we apply.

---

[10]Note that the scale of the distribution $d$ cannot be directly measured by this observer. This is in analogy to the procedure in SMEFT of Sec. 4.1 where the energy scale of new physics $\Lambda$ is commonly extracted from the Wilson coefficients to make the order of the expansion manifest.

## 4.1. Standard Model effective field theory

The SMEFT relies on the SM field content and is built under the assumption that the SM symmetries are respected and the fields are coupled to a sufficiently separated and decoupling new physics sector. Then the low energy effects of the new physics can be expressed in terms of the exact SMEFT Lagrangian

$$\mathcal{L}_{\text{SMEFT}} = \mathcal{L}_{\text{SM}} + \sum_{d=5}^{\infty} \sum_{i} \frac{\mathcal{C}_i^{(d)}}{\Lambda^{d-4}} \mathcal{O}_i^{(d)} \,, \tag{4.2}$$

where the higher order operators $\mathcal{O}_i^{(d)}$ are constructed from SM fields and grouped by their canonical dimension $d$. The accompanying Wilson coefficients $\mathcal{C}_i^{(d)}/\Lambda^{d-4}$ contain the full information on the new physics structure which can be considered to result from integrating out the heavy degrees of freedom. As is customary, we explicitly extract powers of the scale of new physics $\Lambda$ from the Wilson coefficients in order to have dimensionless coefficients $\mathcal{C}_i^{(d)}$ and make the power counting manifest.

Each insertion of a Wilson coefficient in scattering amplitudes then scales as $\mathcal{C}_i^{(d)} E^{d-4}/\Lambda^{d-4}$ where $E \sim v$ is a typical energy scale of the process. Therefore, for a large separation of scales, i.e. $E \ll \Lambda$, it is apparent that the first non-trivial orders in $d$ of Eq. (4.2) suffice for an effective low energy representation of new physics effects. For a consistent application of this finite order approximation the order of truncation has to be applied at the level of observables (or at least at the level of matrix elements). In that case, even though a finite sum in Eq. (4.2) represents a classically non-renormalisable Lagrangian, higher order calculations with a consistent truncation are well defined and renormalisable without introducing additional operators.

At dimension-5 level there is only one operator class, the so-called Weinberg operator [109], which provides a Majorana mass for neutrinos after the Higgs doublet acquires its vev. However, this operator introduces lepton number ($L$) violation and the Wilson coefficients has to very small due to the smallness of neutrino masses.

Hence, the relevant contribution for our investigation is given by the dimension-6 operators. A first complete list was originally classified in Ref. [110], but it included redundant operators. Using such an overcomplete operator set in calculations can become ambiguous, hence it is important to work with a complete set without redundancy, a so-called on-shell operator basis. The first operator basis at dimension-6, commonly referred to as Warsaw basis, was constructed by Ref. [111]. Their strategy to remove redundant operators is as follows:

**Integration by parts** Integration by parts (IBP) relations in the Lagrangian leave the action of the theory invariant up to topological terms, such that on-shell scattering amplitudes in perturbation theory are not affected.

**Field redefinitions** Field redefinitions do not change amplitudes as long as the one-particle on-shell states are preserved. In the reduction of sets of EFT operators, a perturbative field redefinition is chosen, such that redundant operators are removed up to differences at higher order in the canonical dimension. Working only up to dimension-6, field redefinitions are equivalent to the application of the classical equation of motion of the dimensional-4 Lagrangian on dimension-6 operators in order to find relations between them. A detailed account on field redefinitions in EFTs can be found in Ref. [112].

**Fierz identities and reduction of Dirac structures** The 4-dimensional Dirac algebra is sufficient to determine independent operator structures for on-shell bases, in particular the 4-dimensional Fierz identity can be applied. However, if an operator should be

translated to another one using identities of the 4-dimensional Dirac algebra, evanescent structures need to be considered for calculations at loop order [94, 113, 114]. In addition, relations between generators of the symmetry groups can be applied for the reduction of operators.

The procedure to count the number of independent operators and construct an operator basis at arbitrary higher dimension has been developed [115–120] and lead to the construction of a complete SMEFT basis up to dimension-12 [121–124]. Recently, a tool for an automated on-shell basis construction for a broad range of quantum EFTs was developed [125].

Even though the Lagrangians at higher canonical dimension are available, the consistent inclusion of higher orders in $\Lambda$ in the calculation of observables is in general quite cumbersome. For global measurements their inclusion is likely not feasible [126], however their contribution could be relevant in the determination of an uncertainty related to the truncation of the EFT series [127]. One approach for inclusion of higher orders in $\Lambda$ is based on organising the contributions according to the field geometric structure of the Lagrangian, named GeoSMEFT [128], which has been successfully applied for processes of low multiplicity of external particles in Refs. [129–133]. Also the importance of subsets of dimension-8 EFT operators have been assessed for specific models [134, 135]. For the general case it is common to use a subset of the dimension-8 effects from dimension-6 operators only as a proxy [126] which for the case of Higgs pair production is going to be discussed in Chapter 6.

## 4.2. Higgs effective field theory

The Higgs effective field theory (HEFT) [136–141] is another possibility to construct an EFT extension of the SM. It derives its alternative name, EW chiral Lagrangian (EW$\chi$L), from similarities to the construction of chiral perturbation theory of pions [142, 143]. In the case of HEFT the physical Higgs field does not originate from a doublet field after symmetry breaking anymore, but rather is an EW singlet by definition that couples, together with the Goldstone fields, to the possibly strongly interacting new physics sector which lives above the dynamical symmetry breaking scale $\Lambda$. Since this theory is not fully decoupling in the limit $\Lambda \to \infty$ anymore, the power counting is not adequately described by a counting of canonical dimension.

The construction of the HEFT will be described shortly, but first it is instructive to recast the SM Lagrangian of Eq. (2.5) after symmetry breaking in order to better understand the following notation. We define the Goldstone matrix

$$U = \exp\left(i\sigma^i \pi^i / v\right) \ , \tag{4.3}$$

where $\pi^i := \pi^i(x)$ are the Goldstone modes in the exponential representation. The Goldstone matrix transforms linearly under the SM gauge group according to

$$D_\mu U = \partial_\mu U - i\frac{g_1}{2} W_\mu^i \sigma^i U + i\frac{g_2}{2} B_\mu U \sigma^3 \ , \tag{4.4}$$

thus, the fields $\pi^i$ themselves transform non-linearly (this property defines the notion of non-linear Lagrangian). The SM Higgs doublet then takes the form $\phi = (h + v) U (0, \ 1)^T / \sqrt{2}$. Since the SM Higgs sector can also be described in terms of a bidoublet $\Phi = (\tilde{\phi}, \ \phi)^T / \sqrt{2}$ as

$$\mathcal{L}_{\text{Higgs}} = \text{Tr}\left[D_\mu \Phi^\dagger D^\mu \Phi\right] + \frac{\hat{\mu}^2}{2} \text{Tr}\left[\Phi^\dagger \Phi\right] - \frac{\lambda}{4} \text{Tr}\left[\Phi^\dagger \Phi\right] \ , \tag{4.5}$$

it is possible to rewrite Eq. (2.5) in the form

$$
\begin{aligned}
\mathcal{L}_{\text{SM}} = &- \frac{1}{4} G_{\mu\nu}^a G^{a\,\mu\nu} - \frac{1}{4} W_{\mu\nu}^i W^{i\,\mu\nu} - \frac{1}{4} B_{\mu\nu} B^{\mu\nu} + \sum_\psi \bar{\psi} i \slashed{D} \psi \\
&+ \frac{v^2}{4} \text{Tr} \left[ D_\mu U^\dagger D^\mu U \right] \left( 1 + \frac{h}{v} \right)^2 + \frac{1}{2} \partial_\mu h \partial^\mu h - V(h) \\
&- v \left[ \bar{q}_L Y_u U P_+ q_R \left( 1 + \frac{h}{v} \right) + \bar{q}_L Y_d U P_- q_R \left( 1 + \frac{h}{v} \right) \right. \\
&\left. \quad + \bar{l}_L Y_e U P_- l_R \left( 1 + \frac{h}{v} \right) + \text{H.c.} \right] ,
\end{aligned}
\tag{4.6}
$$

where the short-hand notation $P_\pm = (1 \pm \sigma^3)/2$ is introduced, and the right-handed fermion singlet fields are collected in $q_R = (u_R,\ d_R)^T$ and $l_R = (0,\ e_R)^T$ to compactify the expression. In Eq. (4.6) the origin of the physical Higgs field $h$ as being part of a doublet is now obscured, but the information is still available in the polynomial structure of the terms in the Lagrangian, i.e. $(1 + h/v)$, $(1 + h/v)^2$ and $V(h)$. The generalisation of the polynomial structure will then lead to the leading order HEFT Lagrangian, as will be explained in the following.

Basically, the HEFT is based upon an expansion in the scale hierarchy $f^2/\Lambda^2 \sim (16\pi^2)^{-1}$, where $f \approx v$ is the typical energy scale at which the Lagrangian is valid (cf. the pion decay constant in chiral perturbation theory) and $\Lambda$ is the new physics scale of possibly dynamical symmetry breaking in a strongly interacting sector. Hence, the power counting in HEFT can be understood as a loop counting. The operator classification can be equivalently performed in terms of chiral dimensions $d_\chi$ [142, 144, 145] with the definition

$$
\begin{aligned}
{[\partial_\mu]}_{d_\chi} = 2 [\psi]_{d_\chi} = [g]_{d_\chi} = [y]_{d_\chi} = \frac{1}{2} [\lambda]_{d_\chi} = 1 \, , \\
[\varphi]_{d_\chi} = [A_\mu]_{d_\chi} = 0 \, ,
\end{aligned}
\tag{4.7}
$$

where $g$ ($y$) denotes a general gauge (Yukawa) coupling, $\psi$, $\varphi$ and $A_\mu$ are general spinor, scalar and vector fields, respectively. The full expansion of the HEFT Lagrangian therefore takes the form

$$
\mathcal{L}_{\text{HEFT}} = \mathcal{L}_{d_\chi=2} + \sum_{L=1}^\infty \sum_i \left( \frac{1}{16\pi^2} \right)^L c_i^{(L)} O_i^{(L)} \, ,
\tag{4.8}
$$

with the identification $d_\chi = 2L + 2$.

The full LO HEFT Lagrangian is given by

$$
\begin{aligned}
\mathcal{L}_{d_\chi=2} = &- \frac{1}{4} G_{\mu\nu}^a G^{a\,\mu\nu} - \frac{1}{4} W_{\mu\nu}^i W^{i\,\mu\nu} - \frac{1}{4} B_{\mu\nu} B^{\mu\nu} + \sum_\psi \bar{\psi} i \slashed{D} \psi \\
&+ \frac{v^2}{4} \text{Tr} \left[ D_\mu U^\dagger D^\mu U \right] (1 + F_U(h)) + \frac{1}{2} \partial_\mu h \partial^\mu h - V(h) \\
&- v \left[ \bar{q}_L \left( Y_u + F_{Y_u}(h) \right) U P_+ q_R + \bar{q}_L \left( Y_d + F_{Y_d}(h) \right) U P_- q_R \right. \\
&\left. \quad + \bar{l}_L \left( Y_e + F_{Y_e}(h) \right) U P_- l_R + \text{H.c.} \right] ,
\end{aligned}
\tag{4.9}
$$

which has general polynomials $F_U(h)$, $V(h)$, $F_{Y_u}(h)$, $F_{Y_d}(h)$ and $F_{Y_e}(h)$ with a priori infinite number of parameters of $\mathcal{O}(1)$, as the Goldstone fields and the singlet Higgs are coupled to the potentially strong dynamics. This LO Lagrangian is already non-renormalisable in the classical sense, hence operators of higher loop order naturally have to be included in general higher order calculations. The full NLO Lagrangian has been obtained in Ref. [141]. For the

application in the phenomenology of Higgs physics, however, the HEFT Lagrangian Eq. (4.8) can still be quite predictive, since only a limited number of coupling parameters are necessary at a given order. The application of the HEFT theory for Higgs pair production in gluon fusion will be described in Chapter 6.

## 4.3. SMEFT power counting and operator selection

Up to now the SMEFT in Sec. 4.1 has been introduced as a theory that obeys an expansion of canonical dimension alone. In this section, we augment this classification and consider approaches to associate a systematic hierarchy of expected importance of Wilson coefficients that are based on generic assumptions about the UV theory SMEFT should describe. In particular, since the canonical expansion of SMEFT is combined with the loop perturbative expansion involving SM couplings in precision predictions, these expansions are getting intertwined.

In order to structure this combined expansion, there are two viable approaches that can be considered: The first one attempts to be as agnostic about UV completions as possible, since being agnostic is the purpose of the bottom-up EFT after all. In this case, a priori only the pure canonical counting in $\Lambda$ decides about the importance of Wilson coefficients, that is a posteriori further refined based on experimental observations leading to parameter constraints like flavour assumptions. However, the choice of using SMEFT (as opposed to the non-linear HEFT theory) already makes at least *some* assumptions for possible UV extensions, and the complete agnostic approach could lead to misclassification of importance in particular contributions [146, 147]. In addition, the number of parameters of a complete basis at canonical dimension-6 in the SMEFT is already at 2499 (though usually the set that contributes to a process is more confined), it is an immense task to get enough data to achieve a predictive theory. Feeding in additional assumptions allows to concentrate more on the parameters with expected leading impact, thus leading to potential higher precision in their determination. Therefore, the second approach is based on a pre-classification of the expected impact of Wilson coefficients which takes into account additional a priori generic assumptions about the UV theory. The latter approach is the one we follow in this work.

The SMEFT is considered to follow from integrating out some degrees of freedom of an unknown UV physics that lives at an energy scale beyond the cutoff scale $\Lambda$. In case the UV sector is based on a renormalisable QFT and is weakly coupling to the SM fields, some operators of the EFT can *potentially* follow from a tree-level matching whereas other operators are necessarily generated by loop diagrams due to the limited possibilities of vertex structures. Under these assumptions we naturally obtain a hierarchy of expected importance, which was originally described by Ref. [148] based on topological arguments. Similar to the HEFT theory in Sec. 4.2, this same classification can formally be achieved by the introduction of chiral dimension also for the SMEFT operators which has been demonstrated in Ref. [147], if the minimum number of weak couplings necessary to couple the fields composing the operator is carefully extracted. For UV completions with $\Lambda$ not too far away from the relevant energy scales $E$ of collider experiments, the expansion in loop factors can still be relevant compared to the canonical expansion, i.e. the hierarchy might be $(16\pi^2)^{-1} > E^2/\Lambda^2$ and not $(16\pi^2)^{-1} \gg E^2/\Lambda^2$. This would be a desirable configuration where deviations from the SM are potentially observable in the not too distant future. An overview of such a discussion of importance has been done in Refs. [145, 149] for the SILH Lagrangian [149–151] following from an expansion of the HEFT using the parameter $\xi = v/f$.

We acknowledge that the tree-loop classification is controversial. A discussion about this from a very critical perspective can be found for instance in Ref. [103] which highlights potential misconceptions. Nevertheless, we evaluate the derived power counting to be very useful in

practical applications, but agree that the assumptions have to be described properly and cannot represent the general case. We mention some of the valid counter arguments at the end of this section and present our perspective on the matter.

In the following, we fully define the systematics about the SMEFT expansion we apply throughout this work. Using the SMEFT we already limit ourselves to the SM degrees of freedom and the SM gauge group, so we are left to specify the underlying symmetries and the application of the power counting.

Due to strong experimental constraints, Baryon number ($B$) and $L$ violating operators are omitted and we want to consider only $CP$-even coefficients. In addition, we constrain the flavour structure of the quark sector to exactly fulfill

$$\mathcal{G}_{\text{flavour}} = U(2)_q \times U(2)_u \times U(3)_d \ . \tag{4.10}$$

This flavour choice prohibits chirality flipping fermion bilinears involving light quarks (including $b$-quark) and right-handed charged currents [152–154]. Effectively we set the CKM matrix diagonal and remove the quark masses and Yukawa interactions except for the top-quark. Therefore, this choice is compatible with a five-flavour scheme of QCD on which our NLO QCD calculations rely. In addition, the flavour assumption highlights the importance of the heavy top-quark in many potential BSM extensions, and it could serve as a baseline scenario for a future spurion expansion in the form of Minimal Flavour Violation (MFV) [155].[11]

Following the considerations of renormalisable and weakly coupling UV completion of SMEFT, it is instructive to express the Wilson coefficients by dimensionless parameters of equal (expected) magnitude that are multiplied by powers of $\Lambda^{-1}$ based on their canonical dimension (this is common practice) and powers of $\mathbf{L} = (16\pi^2)^{-1}$ depending on chiral dimension (which is the additional tree-loop classification). This leads to the expansion of a generic Wilson coefficient $C_i$ into[12]

$$\mathcal{C}_i \times \Lambda^{-(d_c-4)} \sim C_i \times \Lambda^{-(d_c-4)} \times \mathbf{L}^{l_i} \ , \tag{4.11}$$

with the canonical dimension $d_c = 6$ fixed for dimension-6 operators and $l_i = 0$ for potentially tree-induced and $l_i = 1$ for loop-suppressed operators. For the Warsaw basis, the operators that are loop-induced are precisely the ones involving field-strength tensors. In the calculation of matrix elements of physical processes, the counting of coefficient powers is combined with explicit loop-factors $(16\pi^2)^{-1}$ of the SM loop perturbative expansion. However, since QCD and EW corrections typically have different impact on the prediction of observables, we treat them separately in perturbative calculations and collect loop factors explicitly with associated strong coupling powers in $(g_s^2 L)$.

In order to classify the order in power counting of a contribution to the amplitude or the cross section, we use a specification of the form

$$\mathcal{O}\left(g_s^{n_{\text{tree}}}(g_s^2 L)^{l_{\text{QCD}}} \mathbf{L}^{l_{\text{weak}}} \Lambda^{-2n_6}\right) \ , \tag{4.12}$$

---

[11] The spurion expansion for the baseline scenario of Eq. (4.10) can be found in Ref. [152]. The Yukawa matrices are decomposed into parameters and non-dynamical auxiliary fields, so-called spurions, with formal transformation properties that allow the SM Yukawa interaction terms to be compatible with the baseline flavour symmetry. The original Yukawa couplings are recovered by background values of the spurions which lead to a breaking of the flavour symmetry. Assuming the flavour pattern to be respected in the UV physics as well, violation of flavour symmetry of higher order operators can be parameterised by the spurion fields which lead to a reduction of the number of independent Wilson coefficients and a suppression according to the smallness of the background value compared to the top-Yukawa coupling. The leading order approximation of such a spurion expansion is therefore given for vanishing spurions, thus only retaining terms compatible with the exact symmetry Eq. (4.10).

[12] The so-called SILH Lagrangian [149–151] is a version of the SMEFT that explicitly considers such an expansion. However, since the Warsaw basis [111] is so widely used, we rely on its conventions for the Wilson coefficients and only implicitly consider the described expansion for the classification of contributions into leading and subleading.
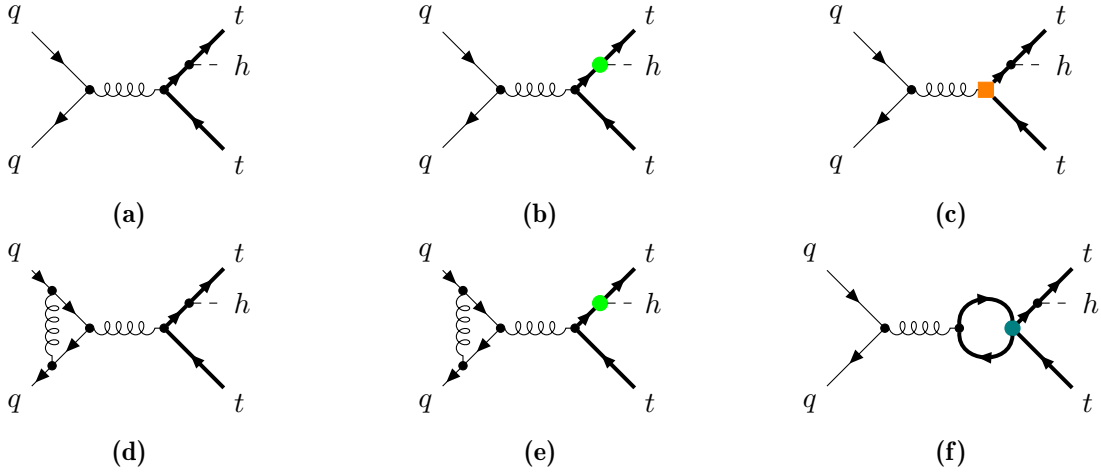
**Figure 4.1.:** Example diagrams for the application of the power counting in $\bar{q}q \to \bar{t}th$. Small black dots denote SM vertices, green dots denote insertions of $\mathcal{C}_{tH}$, orange boxes denote insertions of loop-suppressed $\mathcal{C}_{tG}$ and teal dots denote 4-top interactions.

where $n_{\text{tree}}$ is the number of strong couplings in the SM tree-level contribution (which is 0 if the process is loop induced), $l_{\text{QCD}}$ is the number of loops associated to a QCD correction and $n_6$ counts the insertions of dimension-6 operators. $l_{\text{EFT}}$ denotes the power of loop suppression of Wilson coefficients or loops involving weak couplings only (EW or pure SMEFT coupling). For each gluon field strength tensor in a SMEFT operator, a factor of $g_s$ will be associated to its Wilson coefficient for the power counting formula. A SMEFT contribution will then be called *leading* by our power counting, if it is the lowest non-trivial order in $\Lambda$ <u>and</u> the lowest order in **L**, and *subleading* if it follows from higher order in **L**. This notion will be used in parallel with the specification of LO QCD, which is the leading order in $(g_s^2 L)$, and NLO QCD, which is the next-to-leading order in $(g_s^2 L)$.

We will clarify this nomenclature with a specific example considering the amplitude for the partonic process $\bar{q}q \to \bar{t}th$, where $q$ ($\bar{q}$) denotes a light (anti-)quark. We therefore consider the SM in addition with the following operators of the Warsaw basis

$$
\begin{aligned}
\mathcal{L}_{\text{SMEFT}} \supset \mathcal{L}_{\text{SM}} &+ \frac{\mathcal{C}_{tH}}{\Lambda^2} \left( \left( \phi^\dagger \phi \right) \left( \bar{Q}_L t_R \tilde{\phi} \right) + \text{H.c.} \right) \\
&+ \frac{\mathcal{C}_{tG}}{\Lambda^2} \left( \left( \bar{Q}_L \sigma^{\mu\nu} T^a t_R \tilde{\phi} \right) G_{\mu\nu}^a + \text{H.c.} \right) + \frac{\mathcal{C}_{Qt}^{(1)}}{\Lambda^2} \left( \bar{Q}_L \gamma^\mu Q_L \right) \bar{t}_R \gamma_\mu t_R \, ,
\end{aligned}
\tag{4.13}
$$

with $\sigma^{\mu\nu} = \frac{i}{2} [\gamma^\mu, \gamma^\nu]$. $\mathcal{C}_{tH}$ modifies Yukawa-like interactions between scalars and the top-quark, $\mathcal{C}_{Qt}^{(1)}$ describes a 4-top interaction and $\mathcal{C}_{tG}$ is the coefficient of the chromomagnetic operator. Applying the expansion of Eq. (4.11) we find $\mathcal{C}_{tH} \sim \mathcal{O}(1)$, $\mathcal{C}_{Qt}^{(1)} \sim \mathcal{O}(1)$ and $\mathcal{C}_{tG} \sim \mathcal{O}(g_s \mathbf{L})$,[13] i.e. the chromomagnetic operator is necessarily loop induced whereas the other operators are potentially tree induced. Example diagrams for the contribution to $\bar{q}q \to \bar{t}th$ are demonstrated in Fig. 4.1. We denote with $\mathcal{A}_{(a\text{-}f)}$ the corresponding amplitude contribution in the following. Applying the aforementioned power counting, we find:

- $\mathcal{A}_{(a)} \sim \mathcal{O}(g_s^2)$ , which is a SM contribution at LO QCD,
- $\mathcal{A}_{(b)} \sim \mathcal{O}(g_s^2 \Lambda^{-2})$ , which is a leading SMEFT contribution at LO QCD,

---

[13] Even though there is one factor of $g_s$ extracted in the power counting of $\mathcal{C}_{tG}$, the loop factor cannot be considered to be of QCD origin. Since the chromomagnetic operator replaces a gauge interaction in the $\bar{t}tg(h)$ vertex it is not of higher order in $g_s$.

- $\mathcal{A}_{(c)} \sim \mathcal{O}\left(g_s^2 \mathbf{L} \Lambda^{-2}\right)$ , which is a subleading SMEFT contribution at LO QCD,

- $\mathcal{A}_{(d)} \sim \mathcal{O}\left(g_s^2(g_s^2 L)\right)$ , which is a SM contribution at NLO QCD,

- $\mathcal{A}_{(e)} \sim \mathcal{O}\left(g_s^2(g_s^2 L)\Lambda^{-2}\right)$ , which is a leading SMEFT contribution at NLO QCD,

- $\mathcal{A}_{(f)} \sim \mathcal{O}\left(g_s^2 \mathbf{L} \Lambda^{-2}\right)$ , which is a subleading SMEFT contribution at LO QCD.

We note that the chromomagnetic and 4-top operators appear at same order considering the UV assumptions of this section even though their diagrammatic order is different.

Finally, we want to address some valid counter arguments to the proposed power counting based on a tree-loop classification:

- This power counting fails to describe a strongly coupling BSM scenario: SMEFT necessarily requires the UV physics to completely decouple in the limit $\Lambda \to \infty$ which could be violated in a strongly interacting scenario. For instance, if the Higgs sector would couple strongly to the new physics, a HEFT like scenario as described in Sec. 4.2 would be the favoured choice [147], thus, SMEFT may not provide a valid description for this scenario.

- The UV physics present beyond the scale $\Lambda$ could be a non-renormalisable theory, as well: In the case of a non-renormalisable UV theory, the couplings of this effective theory would be further suppressed by a new scale $\Lambda' \gg \Lambda$ which likely overcompensates the violation of the tree-loop classification.

- *Potentially* tree-induced does not mean the operator is *necessarily* tree induced: This is true, but we find it still reasonable to pursue such an ordering in hierachy, as the method is supposed to determine the potentially most interesting Wilson coefficients for which the first investigation is most promising. It should, however, not be understood as a prejudice to completely remove parameters in subsequent studies, but rather serve as a complementary to the fully agnostic approach.

- The separation between potentially tree generated and loop generated operators does not persist considering the RGE of dimension-6 operators in full generality: This mixing only affects a mixing of operators of class $(\bar{L}R)(\bar{R}L)$ into $\psi^2 \phi X$ operators [156]. Since this particular contribution, in principle, is a one-loop effect induced by EW couplings it might not be too relevant for interesting UV configurations with $\Lambda$ not too far away from experiments, however, this needs to be tested in future studies. For the selection of operators based on the flavour assumption in Eq. (4.10), this mixing is not present since the operator of concern in the class $(\bar{L}R)(\bar{R}L)$ is not allowed. If the flavour assumption was loosened, the mixing would be still suppressed by $m_b/m_t$.

- The separation between potentially tree generated and loop generated operators is violated by field redefinitions: Indeed, the classification is performed on a specific basis choice and hence the results will necessarily be basis dependent. In Ref. [157] it is argued that a preferable choice of basis is selected under the requirement that loop induced operators are replaced by potentially tree induced operators whenever possible which is the case for the Warsaw basis [111]. Nevertheless, after results are obtained through measurement or analytic matching, the chiral dimension would be preserved if the powers of weak couplings in the equation of motion are considered.

## 4.4. Renormalisation in the SMEFT and the evolution of Wilson coefficients

In Sec. 3.2 we already had a look at the renormalisation of QCD and the induced RGE of the strong coupling $\alpha_s(\mu)$. The structure of the renormalisation procedure and the connection to

the RGE for the dimension-6 Wilson coefficients is a bit more tedious, since they mix among each other.

If the counter terms are derived for off-shell one-particle irreducible Green's functions, additional operators of a so-called Green's basis are needed at intermediate steps. After all Green's functions are made finite, these additional operators can be reduced applying the strategy mentioned in Sec. 4.1 in order to derive counter terms of the physical basis. Alternatively, the counter terms for a process can be derived considering all relevant on-shell matrix elements. The latter strategy will be used in Sec. 7.3.1.

Hence, divergences on the level of canonical dimension-6 lead in general to a renormalisation which mixes Wilson coefficients, i.e. the renormalisation of $\mathcal{C}_i^b$ in $\overline{\text{MS}}$ has the form

$$\mathcal{C}_i^b = \mu^{\kappa_i \epsilon} Z_{\mathcal{C}_i}^{\mathcal{C}_j} \mathcal{C}_j = \mu^{\kappa_i \epsilon} \left( \mathcal{C}_i + \delta_{\mathcal{C}_i}^{\mathcal{C}_j} \mathcal{C}_j + \dots \right) , \qquad (4.14)$$

where we restrict ourselves to only consider dimension-6 Wilson coefficients. $\mu^{\kappa_i \epsilon}$ was introduced in Eq. (4.14) such that the coefficients $\mathcal{C}_j$ have the mass dimension of the $D = 4$ dimensional theory. Note that the mass dimension of the bare coefficients depends on the field content of the operator. If we were to include dimension-8 contributions as well, there would be renormalisation terms mixing the square of dimension-6 Wilson coefficients into dimension-8 Wilson coefficients, in general.

From the condition, that the unrenormalised coefficient $\mathcal{C}_i^b$ is independent of the renormalisation scale $\mu$, we can derive[14]

$$\mu \frac{\partial \mathcal{C}_i}{\partial \mu} = - \left( Z^{-1} \right)_{\mathcal{C}_i}^{\mathcal{C}_j} \left( \kappa_j \epsilon Z_{\mathcal{C}_j}^{\mathcal{C}_k} + \mu \frac{\partial}{\partial \mu} Z_{\mathcal{C}_j}^{\mathcal{C}_k} \right) \mathcal{C}_k \rightarrow \underbrace{\left( -\kappa_i \epsilon \, \delta_{\mathcal{C}_i}^{\mathcal{C}_j} + \kappa_j \epsilon \, \delta_{\mathcal{C}_i}^{\mathcal{C}_j} + \mu \frac{\partial}{\partial \mu} \delta_{\mathcal{C}_i}^{\mathcal{C}_j} \right)}_{(16\pi^2)^{-1} \gamma_{\mathcal{C}_i, \mathcal{C}_j}} \mathcal{C}_j , \quad (4.15)$$

where the summation in $j$ and $k$ is implicit and the arrow denotes the expansion up to one-loop order. The full structure of the anomalous dimension matrix $\gamma_{\mathcal{C}_i, \mathcal{C}_j}$ of the Wilson coefficients in the Warsaw basis is presented in Refs. [156, 158, 159].

For a sufficiently small selection of relevant operators, the RGE can be solved analytically, see for instance Ref. [160].

---

[14]A more explicit formula connecting the counter terms for dimension-6 Wilson coefficients with the elements of the anomalous dimension matrix can be found in the appendix of Ref. [6].

# Part II.

# Effective field theories in gluon fusion Higgs processes

# Status of theoretical predictions in Higgs boson pair production at the LHC

Higgs boson pair ($hh$) production is an important class of processes at the LHC. It is the prime channel to shed light on the structure of the Higgs potential, since it gets contributions proportional to the trilinear Higgs self interaction already at leading order. As was highlighted in Sec. 2 the Higgs potential is among the parameters least explored in the SM.

In a collider experiment of protons, like the LHC, there are several partonic channels that contribute to $hh$ production. Their respective cross section as a function of the center-of-mass energy of the proton beam is shown in Fig. 5.1. Due to the large abundance of gluons
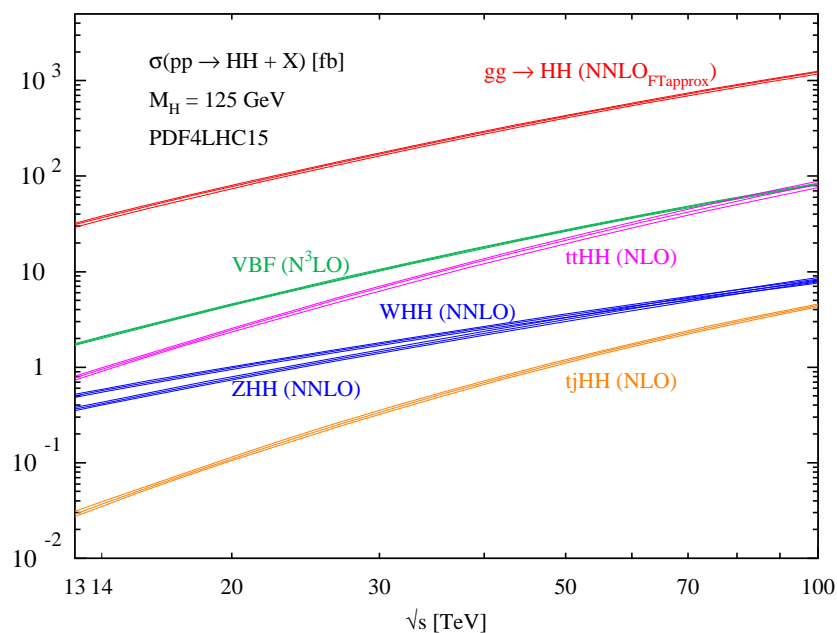


**Figure 5.1.:** $hh$ cross section at a $pp$ collider for different channels as a function of the center of mass energy $\sqrt{s}$. The diagram is taken from Ref. [161].

within the proton at the studied energies, as described by the PDF, the gluon fusion channel ($gg \rightarrow hh$) is expected to happen by at least one order of magnitude more frequently at

the LHC than the other channels. Therefore, the discussion of the subsequent research work focuses on the gluon fusion process.

The Feynman diagrams contributing to $gg \rightarrow hh$ can be structured into box-type and triangle-type contribution, the Born diagrams in the context of the SM are shown in Fig. 5.2. It is the
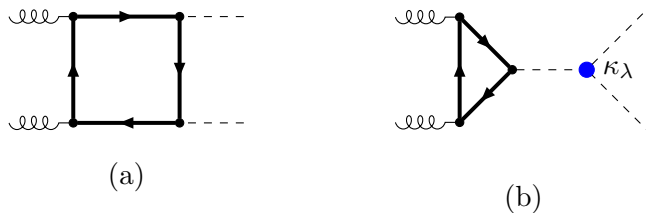


(a)

(b)

**Figure 5.2.:** SM Born topologies for $gg \rightarrow hh$. The trilinear Higgs coupling is highlighted by a blue dot together with the coupling modifier $\kappa_\lambda$.

triangle-type diagram that has the dependency on the trilinear coupling which is highlighted by a coupling modifier $\kappa_\lambda$. The full one-loop Born contribution was originally calculated in Ref. [162]. Since the differential cross section suffers from an intricate cancellation between box-type diagram and triangle-type diagrams in the low $m_{hh}$ region for the pure SM case, the process can become very sensitive to modifications of the trilinear coupling [163]. However, as such a single coupling modification is not satisfactory from the theory perspective, we will discuss in the subsequent chapters the BSM contributions to $gg \rightarrow hh$ in two full-fledged EFT scenarios.

In the following, we briefly address the current theoretical status of $gg \rightarrow hh$. There has been a huge progress in precision calculations for $hh$ production in the gluon fusion channel over the past few years, however, there are still some sources of theory uncertainties that remain. NLO QCD calculations accounting for the full $m_t$ dependence via numerical evaluation of the two-loop integrals are available in Refs. [164–167] and a combination with the high energy expansion for improved results in the high energy region has been performed in Ref. [168]. Equivalent results were obtained in calculations that combine only analytic expansions in different kinematic regions [169, 170]. Higher orders beyond NLO QCD have been achieved in the heavy top limit (HTL). The NLO HTL calculation was established a long time ago [171], NNLO HTL results were presented in Refs. [172–175] and a few years ago N3LO was reached [176]. Some of the numerical NLO QCD calculations with full $m_t$ dependence have been combined with higher order results in the HTL [177, 178]. This significantly improved the perturbative convergence and the missing top-mass effects of the HTL are sufficiently under control. The primary uncertainty in the SM is related to the treatment of the top-quark mass in different renormalisation schemes which has been investigated at full NLO QCD [170, 179]. There is also major progress in EW corrections. Partial calculations considering effects of Yukawa type interactions were performed in Refs. [180, 181], and the full EW corrections in the HTL are presented in Ref. [182]. Since very recently, numerical results of the full EW correction including complete mass effects are available in Ref. [183].

In the context of EFTs for the process $gg \rightarrow hh$, anomalous couplings have been investigated at NLO QCD in the Born-improved HTL for CP-conserving [184] and CP-violating [185] operators in the HEFT and SMEFT framework. NLO QCD corrections including full $m_t$-dependence have been considered for the HEFT in Ref. [186]. In Ref. [187] NNLO corrections have been calculated in the HTL for HEFT. State-of-the-art results in the HEFT for an approximate NNLO prediction (NNLO′) have been obtained in Ref. [188] which combines the calculation including full $m_t$ dependence up to NLO QCD of Ref. [186] with the NNLO HTL

results of Ref. [187]. Results for SMEFT are available at full NLO QCD for the leading operator contribution in Ref. [5] considering different truncation options. Additional subleading operator contributions, the chromomagnetic and 4-top operators, have been investigated in Ref. [7].

The content of the following chapters is as follows: In Chapter 6, the structure of the calculation leading to NLO QCD HEFT results in Ref. [186] and the implementation in the POWHEG-BOX-V2 code GGHH [163] is reviewed with subsequent description of necessary adjustments to comply with the SMEFT framework for the leading operator contribution. In addition, the phenomenological results of Ref. [5] highlighting the practical difference between HEFT and SMEFT and investigating truncation effects will be presented. In Chapter 7, we will elaborate on the effect of $\gamma_5$ scheme choices in DimReg for the calculation of gluon fusion processes in SMEFT on the example of the Higgs-gluon coupling, thereby following the work in [6]. Finally, Chapter 8 is dedicated to study the effect of the subleading operator contributions of the chromomagnetic and 4-top operators in $gg \to hh$ which was assessed in Ref. [7].

# Higgs pair production in gluon fusion at NLO QCD for the leading contribution of effective field theories

The previous chapter established the importance of Higgs pair production, especially in the gluon fusion channel, to scrutinize the trilinear Higgs coupling as the first component of the structure of the Higgs potential in precision tests. In the absence of new intermediate states in the production of Higgs pairs, the so-called non-resonant scenario, the effects of BSM physics are consistently described by EFTs.

In this chapter we use the two canonical bottom-up EFTs in Higgs physics, i.e. SMEFT and HEFT, for predictions in the process of Higgs pair production in gluon fusion ($gg \to hh$) at fixed order NLO QCD and describe the relevant calculational steps for the implementation in GGHH_SMEFT [5]. We thereby only consider operators of the leading contribution according to the power counting formula Eq. (4.12).

In Chapter 4 we made ourselves familiar with some of the different assumptions that make the two EFTs structurally different. In particular, the SMEFT series is an expansion in canonical dimension whereas HEFT is an expansion in loop orders. Yet, there are parameter configurations in which a translation between them is possible. In general, the full SMEFT expansion can be considered to be always translatable to HEFT, whereas the contrast is not true, hence the parameter space of HEFT less restricted. Considering the field representations of the two EFTs, it is obvious that the couplings of the physical Higgs field in the SMEFT originating from a doublet are correlated in the perturbative treatment of the expansion, which is not present in HEFT. There are more theoretical approaches to the difference of the Lagrangian structure in the full theories, which look for non-analyticities in the Higgs sector of a doublet scalar [189], make use of a field geometric interpretation in order to derive statements independent of field redefinitions [190, 191] or a combination of both [192, 193]. Proposals for future studies of these differences in the Lagrangian structure have been put forward in Refs. [194–196]. We will follow a more practical approach and make a naive comparison by an explicit parameter translation at a perturbative level of the two expansions, in order to highlight potential pitfalls. Even though this just demonstrates the expected behaviour, it

provides an instructive showcase to emphasize the importance to study both EFTs separately in practical applications.[15]

In addition, we want to address the uncertainty related to the truncation of the SMEFT expansion with our work. Working at finite order, an estimate of the uncertainty is vital for the interpretation of data. Hence, recently significant attention was brought to the topic [127, 132, 132, 134, 135, 153, 160, 197, 198], nevertheless no general recommendations were decided on [126]. Our calculation provides several options for truncations of the dimension-6 operator contributions to the cross section, which can be used as a proxy for the qualitative observation of the convergence.

In this chapter, we closely follow the outline of Ref. [5], but also refer to preceding calculations of $gg \to hh$ that were essential for our work. This entails, in particular, the evaluation of pure SM results in Refs. [164, 165, 199], the Higgs trilinear coupling variations of Ref. [163] and the HEFT implementation of Refs. [186, 200]. Furthermore, some results of Ref. [201] are included.

The outline is as follows: We first discuss the general structure of the $gg \to hh$ amplitude in Sec. 6.1. Subsequently, in Sec. 6.2 we review all relevant steps leading to the implementation of the HEFT code GGHH [200]. In Sec. 6.3, we relate the SMEFT setup and calculation to the outlined HEFT case and point out necessary adjustments for a consistent reuse of the established HEFT implementation. In addition, we define different truncation options for the dimension-6 contributions in the SMEFT formalism as they are implemented in the POWHEG-BOX-V2 [202–204] process files GGHH_SMEFT. Finally, in Sec. 6.4 benchmark points for specific shapes in the HEFT framework are investigated and a comparison between the two EFTs is drawn.

## 6.1. Setup and general structure of the amplitude

This section is devoted for a brief overview of the general structure of the amplitude. Following the original calculation of Ref. [162], the amplitude for $g(p_1)g(p_2) \to h(q_1)h(q_2)$ in a $CP$-even theory can be decomposed into two form factors $\mathcal{F}_1$ and $\mathcal{F}_2$ as

$$\mathcal{M} = \delta^{A_1 A_2} \epsilon_{\mu_1}(p_1) \epsilon_{\mu_2}(p_2) \left( T_1^{\mu_1 \mu_2} \mathcal{F}_1 + T_2^{\mu_1 \mu_2} \mathcal{F}_2 \right) , \tag{6.1}$$

where $A_1$ and $A_2$ are the color indices of the incoming gluons. A practical choice for the tensor structure is given by

$$T_1^{\mu_1 \mu_2} = \eta^{\mu_1 \mu_2} - \frac{p_1^{\mu_2} p_2^{\mu_1}}{p_1 \cdot p_2}$$

$$T_2^{\mu_1 \mu_2} = \eta^{\mu_1 \mu_2} + \frac{1}{p_T^2 (p_1 \cdot p_2)} \left[ m_h^2 p_1^{\mu_2} p_2^{\mu_1} - 2 (p_1 \cdot q_1) q_1^{\mu_2} p_2^{\mu_1} - 2 (p_2 \cdot q_1) q_1^{\mu_1} p_1^{\mu_2} + 2 (p_1 \cdot p_2) p_3^{\mu_1} p_3^{\mu_2} \right] ,$$
$$\tag{6.2}$$

with $p_T^2 = (\hat{u}\,\hat{t} - m_h^4)/\hat{s}$, since the two tensors ar orthogonal in 4-dimensions. $\hat{s}$, $\hat{t}$ and $\hat{u}$ denote the Mandelstam variables of the partonic system in the hard scattering process. The form factor $\mathcal{F}_1$ can be further decomposed into triangle-type contribution $\mathcal{F}_\triangle$ with an off-shell Higgs that decays into a Higgs pair and box-type contribution $\mathcal{F}_{1,\square}$ according to the topologies of

---

[15]This is indeed an important point to make, as measurements in $hh$ production are primarily available for the $\kappa$-framework or the HEFT. Our findings suggest that separate parameter determinations in the two EFT frameworks are in general not translatable at current experimental sensitivity.

the loop-diagrams. $\mathcal{F}_2$ only has a box-type contribution $\mathcal{F}_{2,\square}$. At LO in the HTL, the SM contribution completely cancels between triangle-type and box-type contributions [162]

$$
\begin{aligned}
\mathcal{F}_1 &= \mathcal{F}_\triangle + \mathcal{F}_{1,\square} = \mathcal{O}\left(\frac{\hat{s}}{m_t^2}\right) , \\
\mathcal{F}_2 &= \mathcal{F}_{2,\square} = \mathcal{O}\left(\frac{\hat{s}}{m_t^2}\right) ,
\end{aligned}
\tag{6.3}
$$

which leads to a large suppression at production threshold. We apply the splitting into triangle-type and box-type also on the level of the full SM amplitude

$$
\mathcal{M}_{\mathrm{SM}} = \mathcal{M}_\triangle + \mathcal{M}_\square ,
\tag{6.4}
$$

for later reference.

## 6.2. Structure of the calculation in the HEFT scenario

In this section we describe the operator selection for the HEFT scenario and the structure of contributions to the cross section as they are used in GGHH [200]. Therefore, we review the relevant steps and analytic expressions in Refs. [163–165, 199, 200] that lead to the implementation of the GGHH process files in the POWHEG-BOX-V2, in order to clarify the consistency with the SMEFT calculation presented in the subsequent section.

Even though the LO HEFT Lagrangian in Eq. (4.9) already has an infinite amount of parameters only a small selection of terms of the full HEFT Lagrangian enter in $gg \to hh$ at NLO QCD. We therefore only need to take into account the following set of terms [186][16]

$$
\Delta\mathcal{L}_{\mathrm{HEFT}} = -m_t\left(c_{tth}\frac{h}{v} + c_{tthh}\frac{h^2}{v^2}\right)\bar{t}\,t - c_{hhh}\frac{m_h^2}{2v}h^3 + \frac{\alpha_s}{8\pi}\left(c_{ggh}\frac{h}{v} + c_{gghh}\frac{h^2}{v^2}\right)G_{\mu\nu}^a G^{a,\mu\nu} ,
\tag{6.5}
$$

where $c_{tth}$, $c_{tthh}$ and $c_{hhh}$ are parameters of the LO Lagrangian in Eq. (4.9) and the Higgs-gluon couplings $c_{ggh}$ and $c_{gghh}$ are part of the NLO Lagrangian which is made apparent by extraction of the prefactor $\alpha_s/(8\pi)$. Notice that the prefactors are chosen such that the value of the HEFT parameters can naturally be of $\mathcal{O}(1)$ with $c_{hhh} = 1$, $c_{tth} = 1$, $= 0$, $c_{ggh} = 0$ and $c_{gghh} = 0$ resembling the SM configuration. Hence, the parameters work as a coupling modifier similar to the $\kappa$-framework at LO.

All couplings of Eq. (6.5) appear at the same order in $gg \to hh$ and form the diagrams of the Born contribution depicted in Fig. 6.1. The Born contribution consists of explicit loop diagrams with couplings of the LO Lagrangian given by Fig. 6.1 (a)–(c), and tree diagrams involving couplings of the NLO Lagrangian visible in Fig. 6.1 (d)–(e). Applying the power counting of the form in Eq. (4.12) they all contribute at $\mathcal{O}\left((g_s^2 L)\right)$.

### 6.2.1. NLO QCD virtual contribution

The NLO QCD contributions in the HEFT theory is also composed of higher orders in SM loops and operators of the NLO Lagrangian. Sample diagrams are presented in Fig. 6.2. Counting only in chiral dimension, also additional contributions of EW couplings or a chiral dimension 6 Higgs-gluon operator would contribute. However, as radiative corrections from QCD are known to be dominant in gluon fusion processes, we restrict ourselves to only include chiral dimension 6 contributions that come with a relative factor of $g_s^2$ which are of the

---

[16]A flavour assumption similar to Eq. (4.10) has been applied in order to remove the mass and Yukawa interaction of light quarks, which just by chiral dimension counting would be of same order.
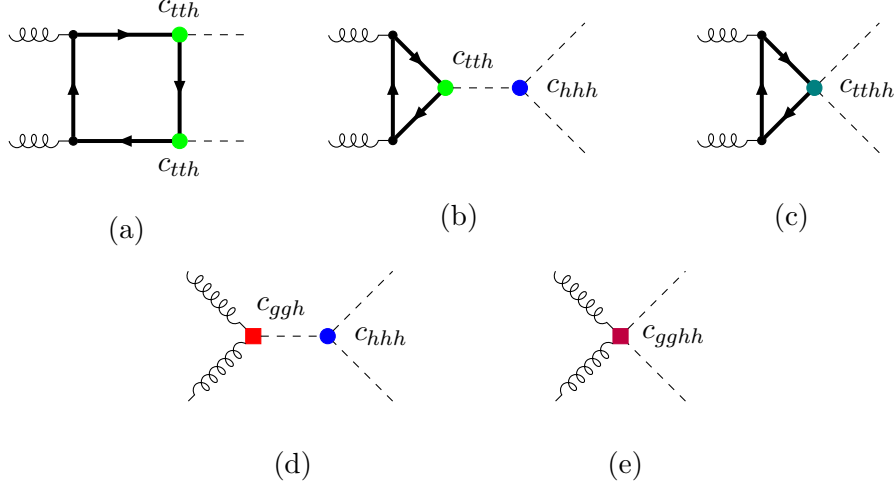
**Figure 6.1.:** Feynman diagrams of the Born contribution in the HEFT scenario. The dots denote vertices of the LO HEFT Lagrangian, the squares vertices of the NLO Lagrangian. The HEFT vertices are labeled with the associated parameter of the HEFT Lagrangian.

same order as the SM NLO QCD calculation. This can be consistently done including only the anomalous interactions of Eq. (6.5), since the Lagrangian is renormalisable for QCD corrections [186, 205]. Thus, all parts of the virtual NLO QCD contribution enter at $\mathcal{O}\left((g_s^2 L)^2\right)$ at amplitude level.

The renormalisation procedure is completely determined by a renormalisation of the SM parameters analogous to Ref. [164], i.e. the top mass $m_t$ is renormalised in the on-shell scheme and the QCD coupling $\alpha_s$ in the $\overline{\text{MS}}$ scheme for $n_l = 5$ active flavours. No additional renormalisation for the coupling parameters $c_{hhh}$, $c_{tth}$, $c_{tthh}$, $c_{ggh}$ and $c_{gghh}$ is necessary at the order we are investigating. The renormalisation constant for the strong coupling $\alpha_s^b = \mu^{2\epsilon}\alpha_s\left(1 + \frac{\alpha_s}{4\pi}\delta_{\alpha_s} + \mathcal{O}\left(\alpha_s^2\right)\right)$ is given by

$$\delta_{\alpha_s} = \frac{(4\pi e^{-\gamma_E})^\epsilon}{\epsilon}\left(-\beta_0 + \left(\frac{m_t^2}{\mu^2}\right)^{-\epsilon}\frac{4}{3}T_F\right) , \tag{6.6}$$

with $\beta_0 = \frac{11}{3}c_A - \frac{4}{3}T_F n_l$. The on-shell mass counter term for $m_t^b = m_t + \frac{\alpha_s}{4\pi}\delta_{m_t} + \mathcal{O}\left(\alpha_s^2\right)$ has the form

$$\delta_{m_t} = \left(4\pi e^{-\gamma_E}\right)^\epsilon \left(\frac{m_t^2}{\mu^2}\right)^{-\epsilon} m_t c_F \left(-\frac{3}{\epsilon} - 4\right) , \tag{6.7}$$

and the gluon field renormalisation has the form $Z_A = 1 + \frac{\alpha_s}{4\pi}\delta_{Z_A} + \mathcal{O}\left(\alpha_s^2\right)$ with

$$\delta_{Z_A} = \frac{(4\pi e^{-\gamma_E})^\epsilon}{\epsilon}\left(\frac{m_t^2}{\mu^2}\right)^{-\epsilon}\left(-\frac{4}{3}T_F\right) . \tag{6.8}$$

It is important to note that the genuine virtual two-loop diagrams are very similar to the SM, therefore the NLO QCD virtual contribution in the HEFT can be obtained by means of a reweighting which can be written as

$$\mathcal{M}_{\text{HEFT}}^{\text{NLO}} = \mathcal{M}_{\square}^{\text{NLO}}c_{tth}^2 + \mathcal{M}_{\triangle}^{\text{NLO}}\left(c_{tth}c_{hhh} + \frac{2}{3}\frac{\hat{s} - m_h^2}{m_h^2}c_{tthh}\right) \\ + \mathcal{M}_1^{\text{NLO}} + \mathcal{M}_0^{\text{NLO}} , \tag{6.9}$$
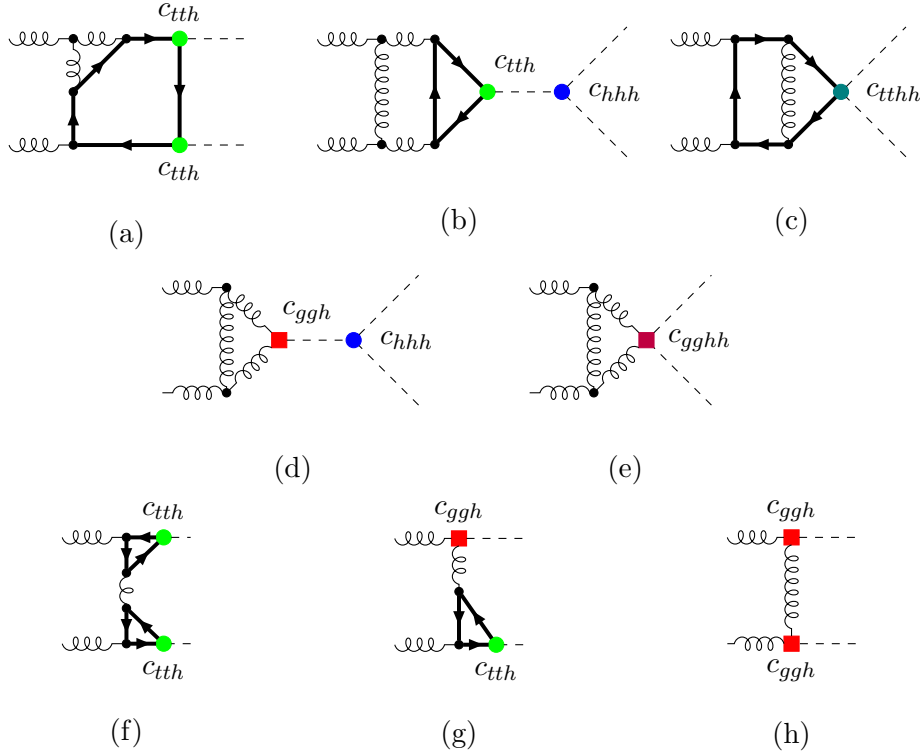
**Figure 6.2.:** Sample diagrams of the virtual contribution in the HEFT scenario. The dots denote vertices of the LO HEFT Lagrangian, the squares vertices of the NLO Lagrangian. The diagrams form genuine two-loop (upper and (f)), one-loop (middle and (g)) and tree-level (h) topologies.

where $\mathcal{M}_1^{\text{NLO}}$ are the one-loop contributions involving one insertion of $c_{ggh}$ or $c_{gghh}$ (cf. Fig. 6.2 (d), (e) and (g)) and $\mathcal{M}_0^{\text{NLO}}$ are the tree-level contributions involving two insertions of $c_{ggh}$ (cf. Fig. 6.2 (h)). $\mathcal{M}_\triangle^{\text{NLO}}$ and $\mathcal{M}_\square^{\text{NLO}}$ denote the decomposition of the NLO QCD SM amplitude according to Eq. (6.4). The explicit evaluation of the amplitude was performed in Refs. [186, 200] using the numerical values for the SM contributions of Refs. [164, 165] in combination with analytic expressions for the tree-level and one-loop contributions.

The subtraction term to remove the IR divergences of the virtual contribution is constructed applying the Catani-Seymour $\mathbf{I}$ operator on the Born amplitude. Since there is only a single colour structure in Eq. (6.1), the operator reduces to a scalar factor, i.e. Eq. (3.13) simplifies to

$$\mathbf{I}_{gg} = \frac{\alpha_s}{2\pi} \frac{(4\pi)^\epsilon}{\Gamma(1-\epsilon)} \left(\frac{\mu^2}{\hat{s}}\right)^\epsilon \left(c_A \frac{2}{\epsilon^2} + \frac{\beta_0}{\epsilon} - c_A \frac{2\pi^2}{3} + \beta_0 + 2K_g\right) . \tag{6.10}$$

In order to implement the finite virtual contribution into the framework of the POWHEG-BOX-V2 [202–204] the finite pieces of the subtraction defined by Eq. (6.10) need to be removed. This leads to the following conversion [199, 204, 206]

$$\begin{aligned}
\mathcal{V}_{\text{fin}}\left(\mu\right) = & \frac{2\pi}{\alpha_s(\mu)} \left(\mathcal{V}_b + \mathbf{I}_{gg} \cdot \mathcal{B}\right)(\mu) \\
& - \mathcal{B}\left(\mu\right) \left(c_A \log^2\left(\frac{\mu^2}{\hat{s}}\right) + \beta_0 \log \frac{\mu^2}{\hat{s}} - c_A \frac{2\pi^2}{3} + \beta_0 + 2K_g\right) ,
\end{aligned} \tag{6.11}$$

where $\mathcal{B}$ is the Born squared amplitude, $\mathcal{V}_b$ the UV renormalised virtual interference term, and $\mathcal{V}_{\text{fin}}$ is the finite virtual contribution that enters the code in the POWHEG-BOX-V2.

In the HEFT, $\mathcal{V}_{\text{fin}}$ can be parameterised in terms of a polynomial of all possible coupling combinations in the form [186]

$$
\begin{aligned}
\mathcal{V}_{\text{fin}}^{\text{HEFT}}(\mu_0) = {} & a_1 \cdot c_{tth}^4 + a_2 \cdot c_{tthh}^2 + a_3 \cdot c_{tth}^2 c_{hhh}^2 + a_4 \cdot c_{ggh}^2 c_{hhh}^2 + a_5 \cdot c_{gghh}^2 + a_6 \cdot c_{tthh} c_{tth}^2 \\
& + a_7 \cdot c_{tth}^3 c_{hhh} + a_8 \cdot c_{tthh} c_{tth} c_{hhh} + a_9 \cdot c_{tthh} c_{ggh} c_{hhh} + a_{10} \cdot c_{tthh} c_{gghh} \\
& + a_{11} \cdot c_{tth}^2 c_{ggh} c_{hhh} + a_{12} \cdot c_{tth}^2 c_{gghh} + a_{13} \cdot c_{tth} c_{hhh}^2 c_{ggh} + a_{14} \cdot c_{tth} c_{hhh} c_{gghh} \\
& + a_{15} \cdot c_{ggh} c_{hhh} c_{gghh} + a_{16} \cdot c_{tth}^3 c_{ggh} + a_{17} \cdot c_{tth} c_{tthh} c_{ggh} + a_{18} \cdot c_{tth} c_{ggh}^2 c_{hhh} \\
& + a_{19} \cdot c_{tth} c_{ggh} c_{gghh} + a_{20} \cdot c_{tth}^2 c_{ggh}^2 + a_{21} \cdot c_{tthh} c_{ggh}^2 \\
& + a_{22} \cdot c_{ggh}^3 c_{hhh} + a_{23} \cdot c_{ggh}^2 c_{gghh} \,,
\end{aligned}
\tag{6.12}
$$

where the $a_i$ are defined as the coefficients for each possible coupling combination. Within the implementation of GGHH, these coefficients are obtained by the combination of numerical grids with 23 linearly independent choices of coupling values which have been calculated for the scale $\mu_0 = m_{hh}/2$, with $m_{hh}$ being the invariant mass of the $hh$ system. The evaluation of $\mathcal{V}_{\text{fin}}^{\text{HEFT}}$ for an arbitrary scale choice $\mu$ is obtained by [199]

$$
\mathcal{V}_{\text{fin}}^{\text{HEFT}}(\mu) = \mathcal{V}_{\text{fin}}^{\text{HEFT}}(\mu_0) \left( \frac{\alpha_s(\mu)}{\alpha_s(\mu_0)} \right)^2 + c_A \mathcal{B}(\mu) \left( \log^2 \left( \frac{\mu_0^2}{\hat{s}} \right) - \log^2 \left( \frac{\mu^2}{\hat{s}} \right) \right) \,.
\tag{6.13}
$$

### 6.2.2. Real radiation

The real radiation involves an IR divergent $ggg$ channel and an IR finite $qqg$ channel that appear at the same order. Diagrams for the $ggg$ channel are obtained radiating a gluon off the Born diagrams in Fig. 6.1. The topologies of the $qqg$ channel diagrams are obtained when one of the initial gluons in Fig. 6.1 originates from a quark line that leads to a jet, the full $qqg$ channel then consists of all permutations of the external coloured particles. The matrix elements for the real radiation have been generated by GoSam [65, 66] in conjunction with a UFO [207, 208] model file. The evaluation of the the squared matrix element for the real radiation proceeds through an interface [209] to the POWHEG-BOX-V2.

## 6.3. Structure of the calculation in the SMEFT scenario

In this section we describe the calculation for a SMEFT scenario and relate all steps to their HEFT analogue of the previous section. This allows us to reuse the well established framework for the evaluation in the SMEFT after some additional modifications. Since SMEFT is based on different assumptions compared to HEFT, as was introduced in Chapter 4, the reader will be reminded when a relation has to be considered with care.

We begin with the relevant Lagrangian terms that follow from the flavour assumption of Eq. (4.10). In addition, we only consider the Wilson coefficients that comprise the leading SMEFT contribution to $gg \to hh$ applying the power counting explained in Sec. 4.3.[17] Thus, we retain the following set

$$
\begin{aligned}
\Delta \mathcal{L}_{\text{SMEFT}}^{\text{lead}} = {} & \frac{\mathcal{C}_{H\square}}{\Lambda^2} \left( \phi^\dagger \phi \right) \square \left( \phi^\dagger \phi \right) + \frac{\mathcal{C}_{HD}}{\Lambda^2} \left( \phi^\dagger D_\mu \phi \right)^* \left( \phi^\dagger D^\mu \phi \right) + \frac{\mathcal{C}_H}{\Lambda^2} \left( \phi^\dagger \phi \right)^3 \\
& + \frac{\mathcal{C}_{tH}}{\Lambda^2} \left( \left( \phi^\dagger \phi \right) \left( \bar{Q}_L t_R \tilde{\phi} \right) + \text{H.c.} \right) + \frac{\mathcal{C}_{HG}}{\Lambda^2} \phi^\dagger \phi \, G_{\mu\nu}^a G^{\mu\nu,a} \,,
\end{aligned}
\tag{6.14}
$$

where we are using the operator definition of the Warsaw basis [111]. The Wilson coefficients $\mathcal{C}_{H\square}, \mathcal{C}_{HD}, \mathcal{C}_H$ and $\mathcal{C}_{tH}$ are potentially tree induced, whereas $\mathcal{C}_{HG}$ is loop induced and therefore carries an implicit suppression of $\mathcal{C}_{HG} \sim \mathcal{O}\left( (g_s^2 L) \right)$.

---

[17]The discussion of the subleading SMEFT contribution is postponed to Chapter 8.

Since we are probing the theory in the EW broken phase, the Higgs doublet is expanded around its vev $v$, which in the presence of Eq. (6.14) also involves a higher order contribution in $\Lambda$. Moreover, other parameters of the dimension-4 Lagrangian get a higher order contribution, in particular we have for the full top-mass[18]

$$m_t = \frac{v}{\sqrt{2}} \left( y_t - \frac{v^2}{2} \frac{\mathcal{C}_{tH}}{\Lambda^2} \right) \, . \tag{6.15}$$

$\mathcal{C}_{H\square}$ and $\mathcal{C}_{HD}$ lead to non-canonical normalisation of the kinetic term for the physical Higgs field $h$ which can be adjusted by a field redefinition. Working in unitary gauge, a particular convenient choice is given by the gauge dependent field redefinition

$$h \rightarrow h + v^2 \frac{\mathcal{C}_{H;\,\mathrm{kin}}}{\Lambda^2} \left( h + \frac{h^2}{v} + \frac{h^3}{3v^2} \right) \, , \tag{6.16}$$

with the definition $\mathcal{C}_{H;\,\mathrm{kin}} := \mathcal{C}_{H\square} - \frac{1}{4} \mathcal{C}_{HD}$. This ensures that there are no vertices with derivatives on the Higgs field up to the order in canonical dimension we are interested in.

After the application of the field redefinition the relevant interaction parts of the Lagrangian now have precisely the form of Eq. (6.5) and we identify the relations listed in Table 6.1. Note that Table 6.1 is not to be considered as an exact translation between the theories,

| HEFT | Warsaw |
|---|---|
| $c_{hhh}$ | $1 + 3v^2 \dfrac{\mathcal{C}_{H;\,\mathrm{kin}}}{\Lambda^2} - 2\dfrac{v^4}{m_h^2} \dfrac{\mathcal{C}_H}{\Lambda^2}$ |
| $c_{tth}$ | $1 + v^2 \dfrac{\mathcal{C}_{H;\,\mathrm{kin}}}{\Lambda^2} - \dfrac{v^3}{\sqrt{2}m_t} \dfrac{\mathcal{C}_{tH}}{\Lambda^2}$ |
| $c_{tthh}$ | $v^2 \dfrac{\mathcal{C}_{H;\,\mathrm{kin}}}{\Lambda^2} - \dfrac{3v^3}{2\sqrt{2}m_t} \dfrac{\mathcal{C}_{tH}}{\Lambda^2}$ |
| $c_{ggh}$ | $\dfrac{8\pi v^2}{\alpha_s} \dfrac{\mathcal{C}_{HG}}{\Lambda^2}$ |
| $c_{gghh}$ | $\dfrac{4\pi v^2}{\alpha_s} \dfrac{\mathcal{C}_{HG}}{\Lambda^2}$ |

**Table 6.1.:** Translation at Lagrangian level between HEFT and SMEFT valid up to $\mathcal{O}\left(\Lambda^{-2}\right)$.

since HEFT and SMEFT are technically different. The HEFT expansion is based on a loop counting, such that the coefficients $c_i$ in Eq. (6.5) are a priori allowed to take arbitrary values of $\mathcal{O}(1)$. The SMEFT, however, is constructed around an expansion in $\Lambda$, such that for a typical energy scale $E$ the combination $\dfrac{E^2}{\Lambda^2}\mathcal{C}_i$ needs to be a small quantity. Therefore, the theoretically allowed HEFT parameter space allows for much larger deviations from the SM and a naive translation from a valid HEFT configuration to the truncated SMEFT can become inconsistent. This will be exemplified in Sec. 6.4.

Since the Lagrangian is now in a convenient form which resembles the HEFT structure we describe in the following the Born contribution to the amplitude. All diagrams that appear in the HEFT case of Fig. 6.1 contribute in the SMEFT case, as well. The SMEFT truncation,

---

[18]For the precise definition of physical quantities in SMEFT, we refer to Chapter 5 of Ref. [159].

however, requires that the full anomalous coupling cannot enter at each vertex. Therefore, we split the amplitude according to



$$\mathcal{M}_{\text{SMEFT}}^{\text{LO}} = \quad \cdots \quad + \quad \cdots \quad + \quad \cdots$$

$$+ \quad \cdots \quad + \quad \cdots$$
(6.17)

$$= \mathcal{M}_{\text{SM}}^{\text{LO}} + \mathcal{M}_{\text{dim6}}^{\text{LO}} + \mathcal{M}_{\text{dim6}^2}^{\text{LO}} \ ,$$

where the $\mathcal{C}_i/\Lambda^2$ pieces at the vertices denote the dimension-6 part of the anomalous coupling according to Table 6.1. The amplitude is split in SM contribution, single insertion of a dimension-6 operator $\mathcal{M}_{\text{dim6}}$ and double insertion of a dimension-6 operator $\mathcal{M}_{\text{dim6}^2}$. Retaining $\mathcal{M}_{\text{dim6}^2}$ but not including dimension-8 operator insertions (and higher dimension contributions induced by the field redefinition Eq. (6.16)) is not in line with the systematics of the SMEFT expansion. Nevertheless, we consider these contributions in some of the truncation options in order to gauge the importance of double insertions. Applying the power counting formula of Eq. (4.12), we have $\mathcal{M}_{\text{SM}} \sim \mathcal{O}\left((g_s^2 L)\right)$, $\mathcal{M}_{\text{dim6}} \sim \mathcal{O}\left((g_s^2 L)\Lambda^{-2}\right)$ and $\mathcal{M}_{\text{dim6}^2} \sim \mathcal{O}\left((g_s^2 L)\Lambda^{-4}\right)$, i.e. $\mathcal{M}_{\text{dim6}}$ forms the leading SMEFT contribution.

### 6.3.1. NLO QCD virtual contribution and truncation options

In the following we discuss the structure of the NLO QCD virtual corrections in an expansion of the form of Eq. (6.17). A priori we may consider all diagrams of the HEFT scenario in Sec. 6.2, but have to account for the SMEFT expansion according to Eq. (6.17). In a general SMEFT calculation, UV divergences of NLO diagrams with a double insertion of dimension-6 operators require a renormalisation of dimension-8 operators. This is, however, not the case at NLO QCD for the set of operators in Eq. (6.14), as they only renormalise themselves. Hence, in addition to the renormalisation of the SM parameters in Sec. 6.2 we also have to consider a renormalisation of $\mathcal{C}_{HG}^b = \mu^{2\epsilon}\left(1 + \delta_{\mathcal{C}_{HG}}^{\mathcal{C}_{HG}}\right)\mathcal{C}_{HG}$ and $\mathcal{C}_{tH}^b = \mu^{3\epsilon}\left(1 + \delta_{\mathcal{C}_{tH}}^{\mathcal{C}_{tH}}\right)\mathcal{C}_{tH}$, with counter terms [159]

$$\delta_{\mathcal{C}_{HG}}^{\mathcal{C}_{HG}} = \frac{\alpha_s}{4\pi}\delta_{\alpha_s}$$
$$\delta_{\mathcal{C}_{tH}}^{\mathcal{C}_{tH}} = \frac{\alpha_s}{4\pi}\left(\frac{\delta_{m_t}}{m_t} + c_F\left(4 + 3\log\left(\frac{\mu^2}{m_t^2}\right)\right)\right) \ ,$$
(6.18)

where $\delta_{\alpha_s}$ and $\delta_{m_t}$ are specified in the previous section. Since the renormalisation of the Wilson coefficients for QCD corrections resemble the structure of an $\overline{\text{MS}}$ renormalisation of $m_t$ and $\alpha_s$ (cf. Eqs. (6.6) and (6.7)), we are able to express the SMEFT NLO QCD amplitude in terms of the HEFT amplitude in Eq. (6.9) with application of Table 6.1. We are then left to adjust the renormalisation of $\mathcal{C}_{tH}$, since in HEFT all Yukawa-type interactions are renormalised for on-shell $m_t$. Schematically we obtain

$$\mathcal{M}_{\text{SMEFT}}^{\text{NLO}} = \mathcal{M}_{\text{HEFT}}^{\text{NLO}} + \Delta_{\text{ren}}\mathcal{M} \ ,$$
(6.19)

with

$$\Delta_{\text{ren}}\mathcal{M} = -\frac{v^3}{\sqrt{2}m_t}\frac{\alpha_s}{4\pi}c_F\left(4 + 3\log\left(\frac{\mu^2}{m_t^2}\right)\right)\frac{\mathcal{C}_{tH}}{\Lambda^2}$$
$$\times\left(2c_{tth}\mathcal{M}_{\square}^{\text{LO}} + \left(c_{hhh} + \frac{\hat{s} - m_h^2}{m_h^2}\right)\mathcal{M}_{\triangle}^{\text{LO}}\right). \tag{6.20}$$

The Catani-Seymour subtraction procedure is not affected by SMEFT, since the IR structure of the theory is not modified by higher order operators describing the UV physics, which is a defining principle of the bottom-up EFT. Hence, a combination of the form in Eq. (6.11) is still valid in the SMEFT scenario.

With the amplitude structure being settled, we specify the four considered possibilities of combinations of $|\mathcal{M}_{\text{SMEFT}}|^2$ with an amplitude expanded according to Eq. (6.17) that enter the cross section:

$$\sigma \simeq \begin{cases} \sigma_{\text{SM}} + \sigma_{\text{SM}\times\text{dim6}} & \text{(a)} \\ \sigma_{(\text{SM}+\text{dim6})\times(\text{SM}+\text{dim6})} & \text{(b)} \\ \sigma_{(\text{SM}+\text{dim6})\times(\text{SM}+\text{dim6})} + \sigma_{\text{SM}\times\text{dim6}^2} & \text{(c)} \\ \sigma_{(\text{SM}+\text{dim6}+\text{dim6}^2)\times(\text{SM}+\text{dim6}+\text{dim6}^2)} & \text{(d)}. \end{cases} \tag{6.21}$$

The options can be described as follows: Option (a) denotes the expansion of $\sigma \sim |\mathcal{M}_{\text{SMEFT}}|^2$ at $\mathcal{O}\left(\Lambda^{-2}\right)$ (linear dimension-6), (b) is the expansion of the amplitude $\mathcal{M}_{\text{SMEFT}}$ at $\mathcal{O}\left(\Lambda^{-2}\right)$ (linear+quadratic dimension-6). In case (c) all contributions of dimension-6 operator insertions up to $\mathcal{O}\left(\Lambda^{-4}\right)$ of the cross section are included which, however, lacks contributions of dimension-8 operators interfered with the SM and $\mathcal{O}\left(\Lambda^{-4}\right)$ terms of the field redefinition in Eq. (6.16). Option (d) (naive translation) corresponds to the full insertion of anomalous couplings in all vertices which equals the HEFT after using the translation of parameters according to Table 6.1 naively, up to differences due to the renormalisation of $\mathcal{C}_{tH}$ and scale dependence of $\alpha_s$ in Table 6.1.

As a reminder, neglecting dimension-8 operator contributions, only option (a) and (b) can be understood to be a consistent choice of the SMEFT expansion which is applicable in the derivation of bounds and fits. To be very strict, only option (a) would correspond to a consistent leading order expansion in $\Lambda^{-2}$ of the observable [127], as field redefinitions would introduce $\Lambda^{-4}$ ambiguities that are of the same order as the part $\sim |\mathcal{M}_{\text{dim6}}|^2$ that is retained in option (b). Option (b), however, is more practical in calculations and fits, since option (a) can lead to negative cross section if the parameter values are not very close to the SM configuration. Therefore, usually both, (a) and (b), are evaluated and compared which serves as a proxy to get a qualitative impression of the EFT convergence. Overall, usage and interpretation of truncation options and related uncertainties are an ongoing debate in the community [126].

As explained beforehand, options (c) and (d) are UV finite without introducing additional operators, hence they can be used to study the importance of double insertions in the amplitude.

In order to use the grid framework of the HEFT implementation we have to relate truncation options (a)–(d) to the selection of coefficients in Eq. (6.12). The final structure of the virtual contribution has the form

$$\mathcal{V}_{\text{fin}}^{\text{SMEFT}} = \mathcal{V}_{\text{fin}}^{\text{HEFT}} + \frac{2\pi}{\alpha_s(\mu)}2\text{Re}\left(\Delta_{\text{ren}}\mathcal{M}\cdot\left(\mathcal{M}_{\text{SMEFT}}^{\text{LO}}\right)^*\right) + \delta_{\mathcal{V}}^{\text{(b)}}, \tag{6.22}$$

where the translation of Table 6.1 and the truncation options of Eq. (6.21) are understood. The inclusion of $\delta_{\mathcal{V}}^{(b)}$ indicates, that for truncation option (b) additional care needs to be taken. This will be described in the following.

As was explained after Eq. (6.21), option (a) and (c) form a truncation on the level of cross section (or squared amplitude) and therefore the truncation in Eq. (6.22) is unambiguous. For option (d) no truncation is applied. Truncation (b), however, is defined on the level of the amplitude. Considering the different diagrams of Fig. 6.2, all topologies do contribute except for type (h). In case a coefficient $a_i$ of Eq. (6.12) has a contribution of diagram type (h) of Fig. 6.2, but also includes other combinations that would be allowed in truncation (b), this $a_i$ coefficient cannot fully be considered in the evaluation of the virtual contribution. As it turns out only combinations of maximally one-loop diagrams are affected, therefore $\delta_{\mathcal{V}}^{(b)}$ includes interference terms which have been implemented analytically in GGHH_SMEFT. More details about the implementation, in particular for the virtual amplitude, are found in App. B.

### 6.3.2. Real radiation

The diagrams of the real radiation contribution have not changed w.r.t. the HEFT case. However, since we consider truncation options defined in Eq. (6.21), a modification of the amplitude calculation is necessary. Therefore, a modified version of GoSam [65, 66] was developed that splits the amplitude according to Eq. (6.17) and combines the amplitude interference according to Eq. (6.21). The interface to the POWHEG-BOX-V2 has been adjusted to allow for the truncation setting.

## 6.4. Phenomenological results

In the following, we are going to discuss results which were generated with GGHH_SMEFT that has been implemented in the POWHEG-BOX-V2. More information about the implementation and usage can be found in App. B.

The results were produced for a proton-proton center-of-mass energy $\sqrt{s} = 13$ TeV. The parton distribution functions and corresponding value for $\alpha_s$ of PDF4LHC15_nlo_30_pdfas [210] were interfaced to our code via LHAPDF [211]. The generation of the virtual amplitude using the grids in Eq. (6.12) require the masses of the Higgs boson and the top-quark to be fixed to $m_h = 125$ GeV, $m_t = 173$ GeV. Decay widths of the particles have been set to zero. Jets are clustered with the anti-$k_T$ algorithm [212], as implemented in the FastJet package [213, 214], with jet radius $R = 0.4$ and a minimum transverse momentum $p_{T,\min}^{\text{jet}} = 20$ GeV. We set the renormalisation and factorisation scales to $\mu = \mu_F = m_{hh}/2$.

For the subsequent discussion on the level of total cross section and $m_{hh}$ distributions, we consider three benchmark points which are defined in Table 6.2. The benchmarks feature characteristic shapes in the $m_{hh}$ distribution at NLO QCD in the HEFT and were classified using unsupervised machine learning [215]. The benchmarks were originally derived in Ref. [215], and updated in Refs. [5, 201] in accordance with recent experimental bounds. In particular, measurements of Refs. [216, 217] require $0.83 \leq c_{tth} \leq 1.17$, and additionally $|c_{tthh}| < 0.05$ was chosen for benchmark 1. We consider the three shape types:

- benchmark 1: enhanced low $m_{hh}$ region

- benchmark 3: enhanced low $m_{hh}$ region and second local maximum above $m_{hh} \simeq 2m_t$

- benchmark 6: close by double peaks (shoulder left).

| benchmark | $c_{hhh}$ | $c_{tth}$ | $c_{tthh}$ | $c_{ggh}$ | $c_{gghh}$ | $\mathcal{C}_{H;\,\mathrm{kin}}$ | $\mathcal{C}_H$ | $\mathcal{C}_{tH}$ | $\mathcal{C}_{HG}$ |
|---|---|---|---|---|---|---|---|---|---|
| SM | 1 | 1 | 0 | 0 | 0 | 0 | 0 | 0 | 0 |
| 1 | 5.105 | 1.1 | 0 | 0 | 0 | 4.95 | $-6.81$ | 3.28 | 0 |
| 3 | 2.21 | 1.05 | $-\frac{1}{3}$ | 0.5 | $0.25^*$ | 13.5 | 2.64 | 12.6 | 0.0387 |
| 6 | $-0.684$ | 0.9 | $-\frac{1}{6}$ | 0.5 | 0.25 | 0.561 | 3.80 | 2.20 | 0.0387 |

**Table 6.2.:** The benchmark points used for the total cross section results in Table 6.3 and the invariant mass distributions in Figs. 6.4–6.6. The SMEFT Wilson coefficients are determined for $\Lambda = 1$ TeV, $\alpha_s(m_Z) = 0.118$ was used for the translation of $\mathcal{C}_{HG}$.

In order to test the behaviour of the SMEFT convergence when the Wilson coefficients of the benchmarks approach the SM configuration, we will explicitly set $\Lambda = 2$ TeV and $\Lambda = 4$ TeV while keeping the parameters $\mathcal{C}_i$ fixed. Let the reader be reminded, that the new physics scale $\Lambda$ of the Wilson coefficients is not a parameter that can be measured (in contrast to the full Wilson coefficient $\mathcal{C}_i/\Lambda^2$), but is rather a means of exemplifying the SMEFT expansion. Changing Wilson coefficients for explicit values of $\Lambda$ is still convenient as it intuitively allows the interpretation of a further decoupling of the UV physics.

### 6.4.1. Total cross section results

In this part we investigate the result on the level of total cross section. We first discuss total cross section values for the benchmark scenarios of Table 6.2. Subsequently, heat maps demonstrating the dependence on pairs of Wilson coefficients for different truncation options are shown.

In Table 6.3, we present the total cross section values for benchmarks 1, 3 and 6 at $\Lambda = 1, 2$ TeV. The SM values are also shown for reference. Truncation option (a) leads to unphysical, negative total cross section for benchmark 1 and the cross section value for $\Lambda = 2$ TeV is still very small in that case indicating the appearance of negative differential cross section in the Monte Carlo integration.

As the squared amplitude in Eq. (6.12) can be expanded in coefficients of different coupling combinations, so can the total cross section as well. Applying the translation of Table 6.1 and truncations of Eq. (6.21) the parameterisation can be reused for the SMEFT scenario if $\mathcal{C}_{HG} = 0$. This leads to the heatmaps in Fig. 6.3 which demonstrate the total cross section as a function of the Wilson coefficient pairs $\mathcal{C}_H$, $\mathcal{C}_{tH}$ and $\mathcal{C}_H$, $\mathcal{C}_{H;\,\mathrm{kin}}$ for truncation options (a), (b) and (c). The options lead to very different dependence of the cross section on the coefficient combination. As is obvious from the white areas in the upper panels, large areas of the parameter space lead to negative cross section values for option (a) (linear dimension-6). This can already occur for values of $\mathcal{C}_i \sim \mathcal{O}(1)$. Since option (a) corresponds to the linear interference with the SM only, there are extended flat directions. Choosing truncation option (b) (linear+quadratic dimension-6) leads to elliptic shapes which flat side resembles the flat directions of option (a). Non-trivial shapes are obtained for truncation option (d), where the elliptic iso-contours of (b) are deformed by higher polynomial orders in the Wilson coefficients.

| benchmark | $\sigma_{\text{NLO}}$ [fb] option (b) | K-factor option (b) | ratio to SM option (b) | $\sigma_{\text{NLO}}$ [fb] option (a) | $\sigma_{\text{NLO}}$ [fb] HEFT |
|:---:|:---:|:---:|:---:|:---:|:---:|
| SM | $27.94^{+13.7\%}_{-12.8\%}$ | 1.67 | 1 | - | - |
| $\Lambda = 1$ TeV | | | | | |
| 1 | $71.95^{+20.1\%}_{-15.7\%}$ | 2.06 | 2.58 | -57.64 | 91.62 |
| 3 | $68.69^{+9.4\%}_{-9.5\%}$ | 1.80 | 2.46 | 30.15 | 70.20 |
| 6 | $70.18^{+18.8\%}_{-15.5\%}$ | 1.83 | 2.51 | 50.82 | 87.9 |
| $\Lambda = 2$ TeV | | | | | |
| 1 | $14.53^{+12.6\%}_{-12.2\%}$ | 1.62 | 0.52 | 6.44 | - |
| 3 | $30.80^{+14.4\%}_{-13.6\%}$ | 1.71 | 1.10 | 28.41 | - |
| 6 | $34.80^{+16.8\%}_{-14.9\%}$ | 1.73 | 1.25 | 33.6 | - |

**Table 6.3.:** Total cross section results of $gg \to hh$ at NLO QCD for the SM and three benchmark points for truncation option (b), including scale uncertainties for a 3-point scale variation. The values are shown for $\Lambda = 1$ TeV and $\Lambda = 2$ TeV. Results for truncation option (a) are given to contrast with option (b). The HEFT cross sections are shown for reference, if applicable. The cross section for truncation option (a) with $\Lambda = 1$ TeV leads to a negative value for benchmark point 1, thus, it should not be considered a valid SMEFT configuration.
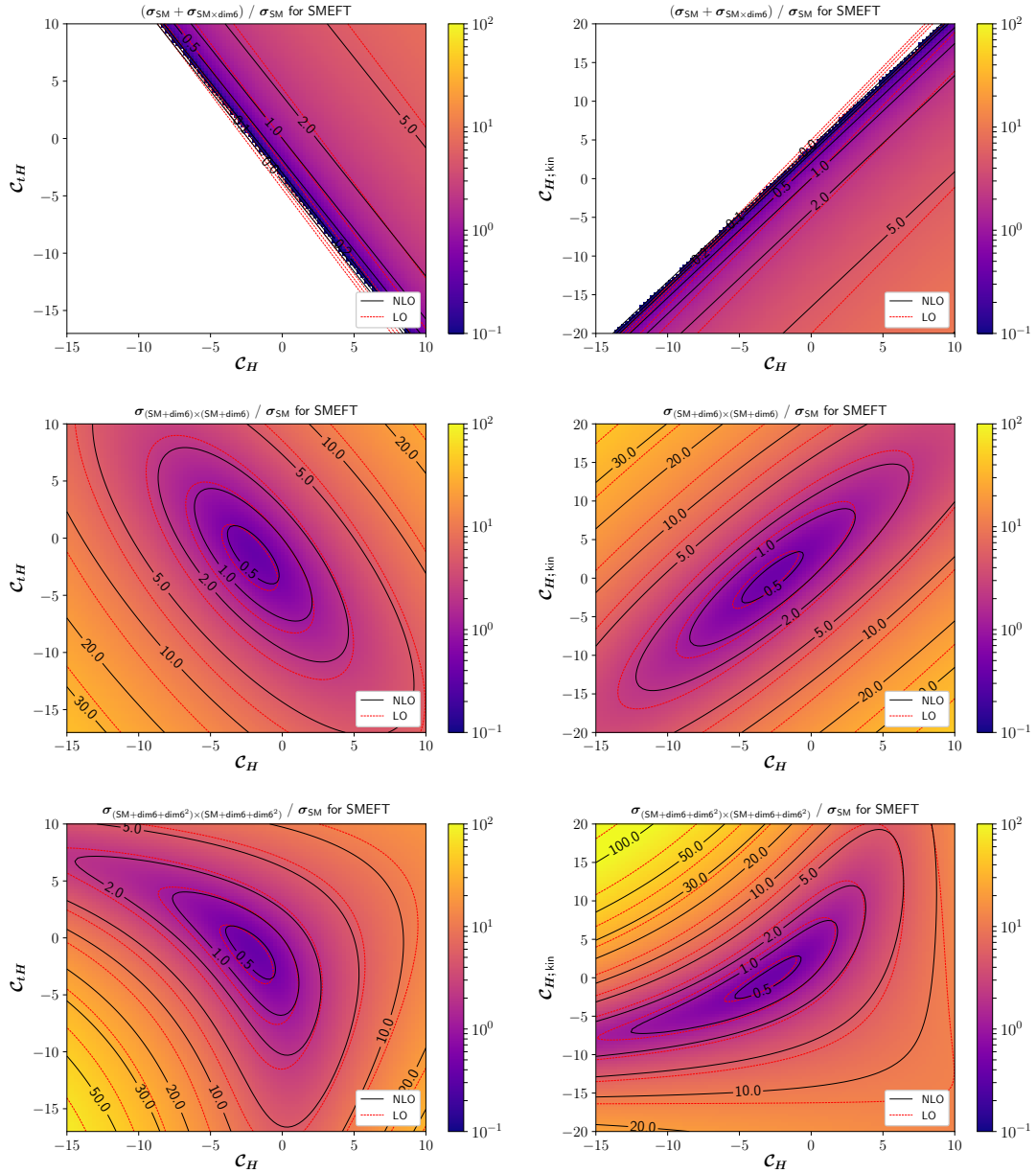
**Figure 6.3.:** Heat maps demonstrating the dependence of the total cross section on variations of $\mathcal{C}_H$, $\mathcal{C}_{tH}$ (left) and $\mathcal{C}_H$, $\mathcal{C}_{H;\mathrm{kin}}$ (right) over large ranges for $\Lambda = 1$ TeV. The cross section is normalised to the SM value. The results are shown for different truncation options defined in Eq. (6.21): Upper panels: option (a), middle panels: option (b), lower panels: option (d). White areas denote negative cross section values.

### 6.4.2. Higgs boson pair invariant mass distributions

In the following we observe the differential cross section in invariant mass distributions for the benchmarks of Table 6.2. In particular, we inspect the effect of different truncation options on the three scenarios. For truncation option (b) and the SM, we include a scale uncertainty band for a 3-point scale variation around the central scale of the form $\mu = \mu_F = c \cdot m_{hh}/2$, for $c \in \{1/2, 1, 2\}$. We verified for the SM and benchmark 1 that the 3-point already provides the envelope of a more general 7-point variation.

The distributions for benchmarks 1, 3 and 6 are presented in Figs. 6.4–6.6. The panels of each figure are arranged in the following order: The upper panels show distributions for $\Lambda = 1$ TeV, middle panels for $\Lambda = 2$ TeV and the lower panels for $\Lambda = 4$ TeV; the left panels demonstrate LO, the right panels NLO results. The original HEFT benchmark distributions are included in the upper panels in order to exemplify the naive application of Table 6.1 at $\Lambda = 1$ TeV.

In Fig. 6.4, the distributions for benchmark 1 are displayed. We observe negative cross section for a large $m_{hh}$ range for truncation option (a). This was already expected comparing with the total cross section values in Table 6.3. This is a clear demonstration, that the perfectly valid HEFT configuration of benchmark 1 can upon naive translation lead to a SMEFT scenario for which the expansion in $\Lambda^{-1}$ breaks down, i.e. this corresponds to an invalid configuration for the SMEFT expansion up to dimension-6 operators. The distributions of options (b), (c) and (d) are positive definite. The curves for (b) and (c) are very close, hence the interference of the amplitude with dimension-6 operator double insertions with the SM appears to be subdominant for parameter values of benchmark 1. Truncation (d) behaves almost identical to the HEFT case, the only difference is due to the correction of the renormalisation of $\mathcal{C}_{tH}$ in Eq. (6.20). For $\Lambda = 1$ TeV, all truncation options except for (a) qualitatively reproduce the shape of enhanced low $m_{hh}$ region.

For $\Lambda = 2$ TeV the distributions of options (b)–(d) coincide well with each other. Option (a), however, does not and still leads to an area of negative differential cross section values. The shapes of options (b)–(d) for $\Lambda = 2$ TeV now exhibit a second local maximum and therefore resemble the defining shape structure of benchmark 3.

Setting $\Lambda = 4$ TeV the distributions approach the SM, but there is still a significant deviation w.r.t. the SM curve beyond scale uncertainty in the low $m_{hh}$ region. All truncation options are very close to each other in this configuration, there is only a slight deviation at production threshold for option (a) with negative values.

Distributions for benchmark point 3 are presented in Fig. 6.5. At $\Lambda = 1$ TeV, options (a) and (c) exhibit negative cross section. Therefore, the interference term of the amplitude with double insertions entering option (c) leads to significant deviation from truncation (b) for benchmark 3. The difference between option (d) and the HEFT distribution is now more pronounced, which is due to the scale dependence of $\alpha_s(\mu)$ in the translation of Table 6.1. Overall, again truncation options (b)–(d) reproduce the characteristic shapes defining the HEFT benchmark scenario.

For $\Lambda = 2$ TeV the distributions approach the SM more closely than was the case for benchmark 1 in Fig. 6.4. The different truncation options coincide well except option (a) in the low $m_{hh}$ region.

At $\Lambda = 4$ TeV the distributions for all options are very close to the SM, only a slight damping of the cross section in the low $m_{hh}$ regime is visible.

Finally, in Fig. 6.6 we investigate the $m_{hh}$ distributions for benchmark point 6. In contrast to the two previous benchmark scenarios, we observe no negative cross section for benchmark

6. The distributions of truncation options (a) and (b) are relatively close to each other in the low $m_{hh}$ region with deviations beyond the scale uncertainty for $m_{hh} \gtrsim 520$ GeV. The truncation options in SMEFT fail to reproduce the close-by double peaks that define the HEFT benchmark except for the naive translation option (d). The distribution of option (c) lies in between the ones of options (b) and (d).

For $\Lambda = 2$ TeV, the curves approach the SM distribution already quite close. For $\Lambda = 4$ TeV the SMEFT scenario becomes indistinguishable compared to the SM, as the distributions remain within the scale uncertainty.
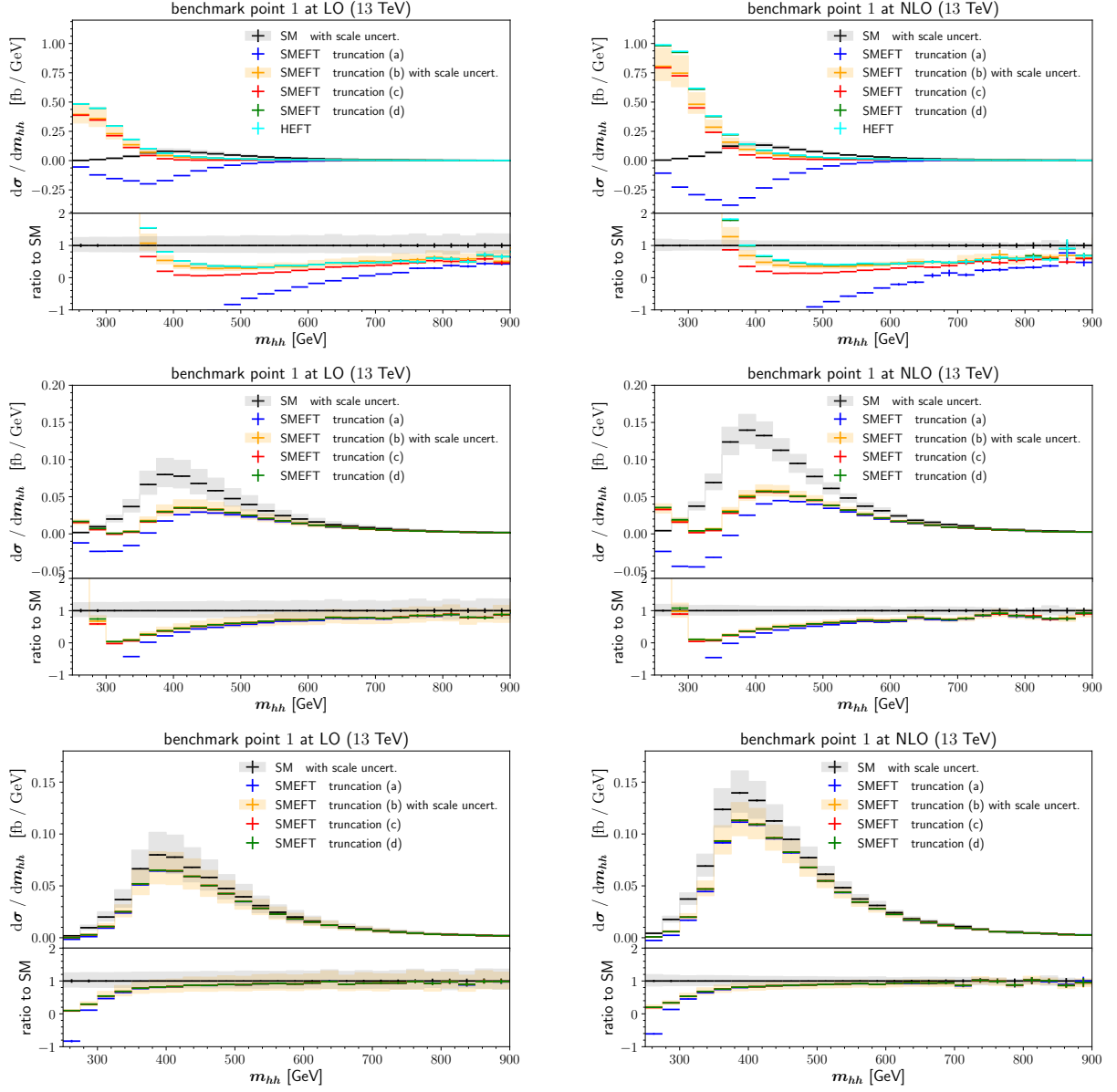
**Figure 6.4.:** Differential cross section distributions for the invariant mass $m_{hh}$ for benchmark point 1 of Table 6.2. Top row: $\Lambda = 1$ TeV, middle row: $\Lambda = 2$ TeV, bottom row: $\Lambda = 4$ TeV. Left: LO, right: NLO.
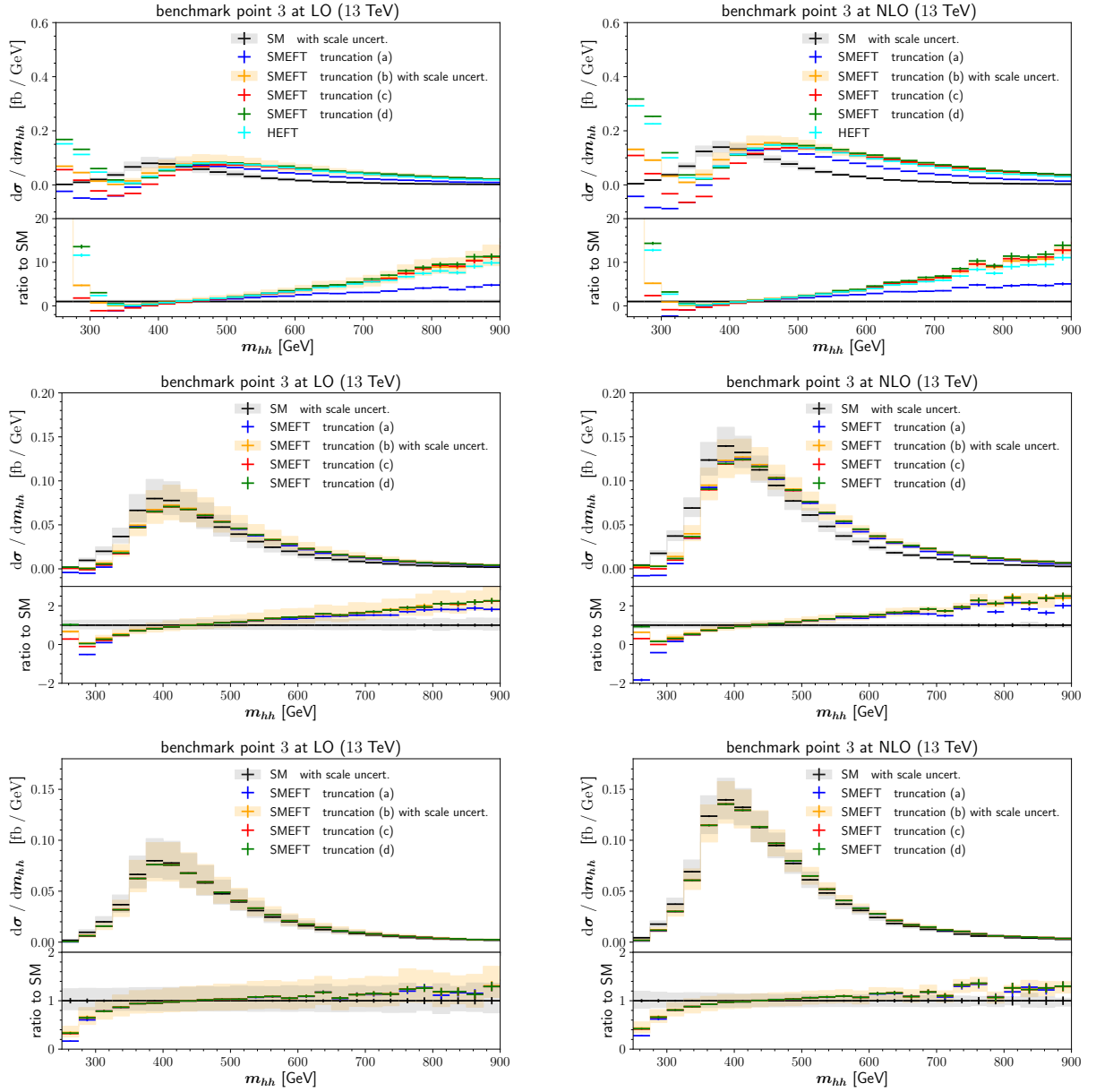
**Figure 6.5.:** Differential cross section distributions for the invariant mass $m_{hh}$ for benchmark point 3 of Table 6.2. Top row: $\Lambda = 1$ TeV, middle row: $\Lambda = 2$ TeV, bottom row: $\Lambda = 4$ TeV. Left: LO, right: NLO.
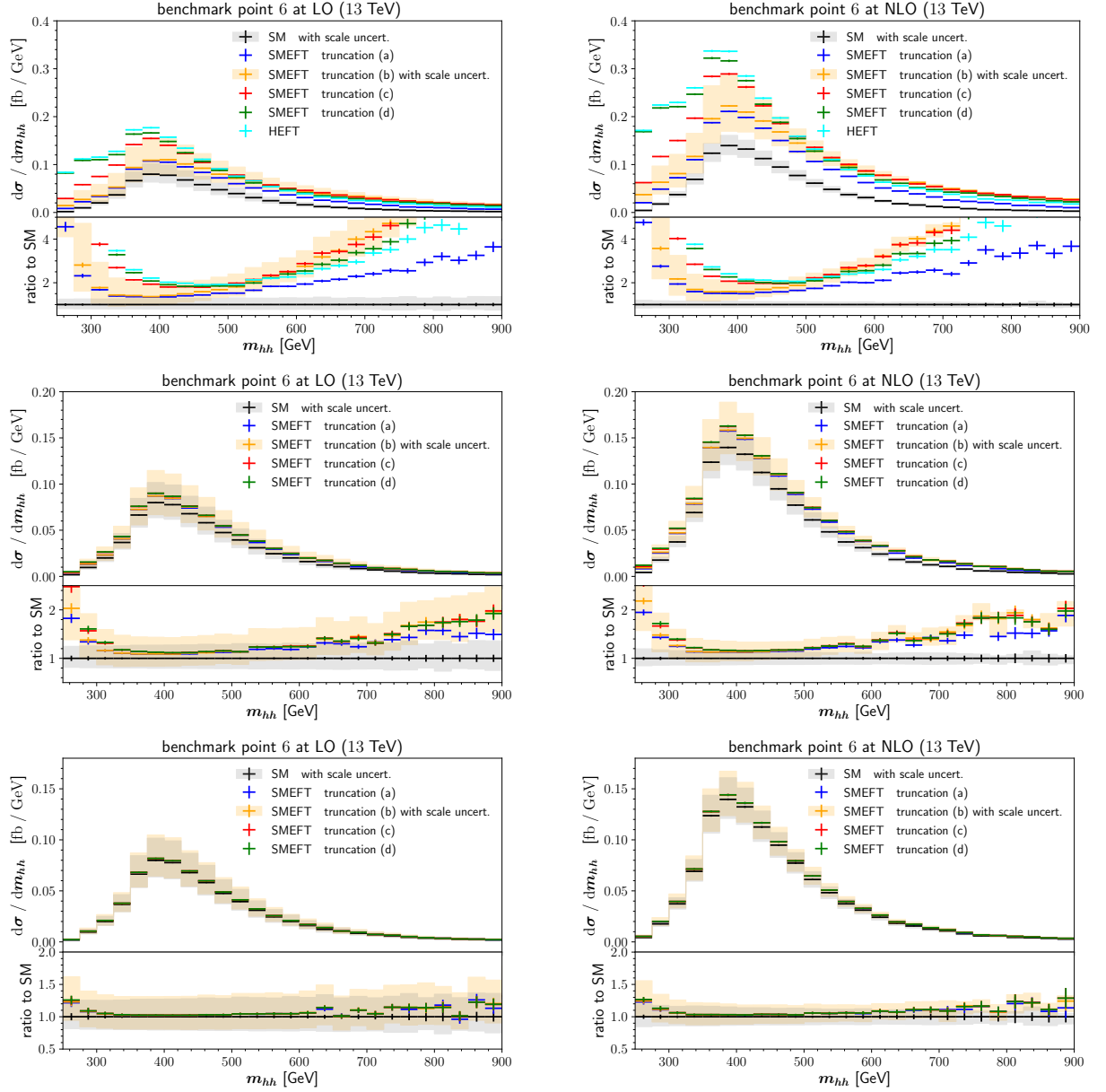
**Figure 6.6.:** Differential cross section distributions for the invariant mass $m_{hh}$ for benchmark point 6 of Table 6.2. Top row: $\Lambda = 1$ TeV, middle row: $\Lambda = 2$ TeV, bottom row: $\Lambda = 4$ TeV. Left: LO, right: NLO.

## 6.5. Uncertainty of the EFT predictions

After the formulas for the evaluation have been discussed and results presented, we need to clarify sources of theoretical uncertainty not yet addressed. There are few aspects that need to be considered and we follow the discussion in Ref. [201].

**SMEFT truncation** There is no quantitative prescription to specify uncertainty related to SMEFT truncation yet [126]. We provide a possibility to get a qualitative picture of the convergence when comparing different truncation options of the dimension-6 operator contributions. This, however, has to be assessed on a case by case basis.

**Scale uncertainty** The scale uncertainties are obtained by a variation of renormalisation and factorisation scale around the central choice, $\mu_0 = m_{hh}/2$. A 3-point variation of the form $\mu = \mu_F = c \cdot \mu_0$ with $c \in \{1/2, 1, 2\}$ has been assessed for the SM and benchmarks 1, 3 and 6 for truncation (b). On the level of differential distributions the resulting bands are presented in Figs. 6.4–6.6, for the total cross section the relative uncertainty is shown in Table 6.3. The scale uncertainty ranges vary depending on the benchmark configuration and can be asymmetric around the central scale prediction, with relative size of 10% for benchmark 3 and 15–20% for benchmarks 1 and 6 at $\Lambda = 1$ TeV. For $\Lambda = 2$ and 4 TeV the size is closer to the SM with 13–15% and equally symmetric. Scale uncertainties for HEFT have been investigated in Refs. [186, 200] and are in general equal in magnitude. An approximate version of NNLO QCD corrections, partially using the HTL, demonstrated a decrease of the scale uncertainty by a factor 2 to 3 [188].

**PDF+$\alpha_s$ uncertainty** The PDF+$\alpha_s$ uncertainty is estimated to $\pm 3\%$ for $\sqrt{s} = 13$ and 14 TeV [218] which has been obtained with a Born-improved approximation of NNLO using PDF4LHCNNLO [210]. The uncertainty appears to be quite robust for variations of $c_{hhh}$ [218], but could potentially differ for benchmark scenarios with enhanced tails.

**Top-quark mass renormalisation scheme** The choice of the $m_t$ renormalisation scheme and associated scale $\mu_m$ for the $\overline{\text{MS}}$ mass leads to significant differences in the cross section and distributions. It has been estimated in the SM with $\overline{\text{MS}}$ renormalisation of $m_t$ for the NLO cross section, where the envelope between the scale choices $\mu_m = m_t$, $m_{hh}$ and $m_{hh}/4$ defines the range. At $\sqrt{s} = 13$ TeV this leads to $^{+4\%}_{-18\%}$ w.r.t. the on-shell scheme [179]. In the SM this is the dominant source of uncertainty, since the usual scale uncertainty is reduced by the approximate NNLO results [177]. An investigation of the mass scheme uncertainty in off-shell single Higgs production at NNLO with a soft-virtual approximation for the real radiation [219] indicates that the scheme uncertainty potentially reduces at higher orders in QCD, and that the on-shell renormalisation could be more stable with regards to higher order contributions in some regions of phase space. It has been demonstrated that the $m_t$ scheme uncertainty is sensitive to the choice of $c_{hhh}$ [170, 179]. This indicates that it would be necessary to assess the uncertainty for each EFT parameter configuration separately.

**EW corrections** Recently the full EW corrections in the SM have been computed [183]. The result leads to $\mathcal{K} = 0.958$ relative to the LO total cross section for $\mu = \mu_F = m_{hh}/2$. For the $m_{hh}$ distributions there are $+10\%$ deviations at production threshold and up to $-10\%$ in the tails beyond $m_{hh} \sim 600$ GeV. The result, however, is not translatable to EW corrections in an EFT scenario, since at this order, i.e. $\mathcal{O}\left((g_s^2 L)\mathbf{L}\Lambda^{-2}\right)$, more operators would need to be considered, a part of which are studied in Chapter 8.

**Numerical evaluation of the NLO QCD virtual corrections** As described in Eq. (6.12), the NLO virtual corrections $\mathcal{V}_{\text{fin}}$ are obtained by means of a combination of grids, that are

interpolated for an evaluation of each phase space point [199]. The original grids for the two-loop amplitude have been sampled in order to have an overall statistical accuracy up to $\lesssim 2\%$ in the binning of the differential cross section for the $m_{hh}$ distribution of the SM. This leads to some regions where the grid points are only sparsely populated, e.g. the low $m_{hh}$ region or large $m_{hh}$ tails. The structure of the EFT contribution, however, can be vastly different leading to enhancements in regions of phase space where the SM is almost vanishing. Benchmark 1 in Fig. 6.4 serves as an example for such a behaviour, as it entails an enhanced low $m_{hh}$ region. Here the statistical uncertainty in the first bin estimated by the Monte Carlo integration in the POWHEG-BOX-V2 cannot be trusted, as an additional statistical uncertainty should be associated for the sparsely populated grid. In Ref. [201] this statistical uncertainty in the first bin of benchmark 1 has been estimated to reach 75% (as compared to 12% for the SM). For a general scenario, it cannot be assessed a priori, therefore a binning choice that spreads this uncertainty over a larger range might be appropriate.

# The structure of dimensional $\gamma_5$ schemes in SMEFT for the Higgs-gluon coupling

As has been explained in Sec. 3.6, chirality of fermions is a concept that is intimately connected to the 4-dimensional spacetime we observe. If calculations are done in terms of Dirac spinors, chirality enters in the form of projectors involving the $\gamma_5$ chirality operator. $\bar{\gamma}_5$ together with all its properties Eqs. (3.18) and (3.20) and the usual definition of cyclic traces is confined to 4-dimensional spacetime [89], thus its continuation to $D$ dimensions in DimReg poses some difficulties. Different schemes have been developed to make consistent predictions where two versions have been briefly discussed in Sec. 3.6.1 and Sec. 3.6.2. In UV complete theories a lot of experience has been gained in the application of those techniques. This lead to the expectation that calculations at intermediate steps differ depending on the scheme, but after taking into account all relevant renormalisation terms, including symmetry restoration for BMHV, the NDR scheme and BMHV scheme should coincide, see e.g. Ref. [220] for a recent example. There are also 4-dimensional regularisation schemes that avoid the $D$-dimensional continuation of $\gamma_5$, see e.g. Refs. [34]. These schemes, however, still face similar technical difficulties in the consistent treatment of $\gamma_5$ in practical calculations [31, 221, 222].

In the framework of EFTs, the relation between different dimensional $\gamma_5$ scheme choices is more subtle than for UV complete theories. It is well established from observations in flavor physics calculations [223–225] that the anomalous dimension matrix governing the scale dependence of Wilson coefficients at two loop order involving 4-fermion operators turns out to be scheme dependent if only the dependence on individual parameters Wilson coefficients is considered. In Refs. [223, 224] this scheme dependence has been absorbed in a redefinition of other parameters of the theory in order to demonstrate the scheme-independence of the anomalous dimension, thus leading to consistent results.

In this chapter, we revisit these investigations on the $\gamma_5$ scheme structure of 4-fermion operators and apply a similar logic as Refs. [223, 224] in the context of the Higgs-gluon coupling. We are mainly interested in the contribution of 4-top interactions entering the Higgs-gluon coupling indirectly at two-loop, since their Wilson coefficients are barely constrained by current global fits of the $\mathcal{O}\left(\Lambda^{-2}\right)$ interference terms [153].[19] In the process $gg \to h$, the contribution

---

[19]The prime channel to study 4-top Wilson coefficients directly is the production of four top-quarks at the LHC. Although the cross section of four top-quark production is very limited at current collider energies [226] and the

of the fixed order amplitude can be of the same order as the RGE evolution effects [229], hence the structure of the $\gamma_5$ scheme in the renormalised two-loop amplitude has to be considered. Even though the 4-top operators enter at two-loop level, the appearing Feynman integrals factorise in two one-loop parts which makes the calculation well feasible.

The discussion in this chapter is mainly based on the work of Ref. [6][20] and stuctured as follows: We first recapitulate the operator selection and set up all the ingredients that enter the calculation in Sec. 7.1. In Sec. 7.2 we discuss the one-loop subdiagrams entering the Higgs-gluon coupling and derive the $\gamma_5$ scheme dependent structure at one-loop order. We present in Sec. 7.3 the full two-loop calculation and summarise the translation table relating the parameters between NDR and BMHV. Sec. 7.4 is dedicated for a validation in the unbroken phase of the EW symmetry, first with a recomputation of the one-loop $\gamma_5$ scheme structure and subsequently with an explicit matching calculation using simplified UV models. Finally, in Sec. 7.5, the $\gamma_5$ scheme structure involving operators of the class $\psi^2 \phi^2 D$ of Ref. [111] on the one-loop subamplitudes is demonstrated in order to highlight the need for a more exhaustive study in the future.

## 7.1. Operator selection

We briefly setup the selection of contributing operators in this section. As mentioned, our primary focus lies on the effect of 4-top operators in this chapter. The relevant list is given by

$$
\begin{aligned}
\mathcal{L}_{4\mathrm{t}} = {} & \frac{\mathcal{C}_{Qt}^{(1)}}{\Lambda^2} \left( \bar{Q}_L \gamma^\mu Q_L \right) \bar{t}_R \gamma_\mu t_R + \frac{\mathcal{C}_{Qt}^{(8)}}{\Lambda^2} \left( \bar{Q}_L \gamma^\mu T^a Q_L \right) \bar{t}_R \gamma_\mu T^a t_R \\
& + \frac{\mathcal{C}_{QQ}^{(1)}}{\Lambda^2} \left( \bar{Q}_L \gamma^\mu Q_L \right) \left( \bar{Q}_L \gamma_\mu Q_L \right) + \frac{\mathcal{C}_{QQ}^{(8)}}{\Lambda^2} \left( \bar{Q}_L \gamma^\mu T^a Q_L \right) \left( \bar{Q}_L \gamma_\mu T^a Q_L \right) \\
& + \frac{\mathcal{C}_{tt}}{\Lambda^2} \bar{t}_R \gamma^\mu t_R \, \bar{t}_R \gamma_\mu t_R \,,
\end{aligned}
\tag{7.1}
$$

which enter as a two-loop correction to the Higgs-gluon coupling. The operator $\mathcal{O}_{qq,\,\mathrm{Warsaw}}^{(3)\,3333}$ of the Warsaw basis [111] has been replaced by $\mathcal{O}_{QQ}^{(8)}$ which in terms of the Wilson coefficients leads to the relation [230]

$$
\begin{aligned}
\mathcal{C}_{QQ}^{(1)} &= 2 C_{qq,\,\mathrm{Warsaw}}^{(1)\,3333} - \frac{2}{3} C_{qq,\,\mathrm{Warsaw}}^{(3)\,3333} \\
\mathcal{C}_{QQ}^{(8)} &= 8 C_{qq,\,\mathrm{Warsaw}}^{(3)\,3333} \,.
\end{aligned}
\tag{7.2}
$$

All other 4-top operators are represented in the Warsaw basis.

The 4-top operators cannot be considered in isolation, as their Wilson coefficients are connected to other parameters through renormalisation and the $\gamma_5$ scheme structure. Hence, we also need to include the chromomagnetic operator

$$
\mathcal{L}_{tG} = \frac{\mathcal{C}_{tG}}{\Lambda^2} \left( \left( \bar{Q}_L \sigma^{\mu\nu} T^a t_R \tilde{\phi} \right) G_{\mu\nu}^a + \mathrm{H.c.} \right) \,,
\tag{7.3}
$$

and a subset of the leading operators from Eq. (6.14) without the pure scalar operators, i.e.

$$
\Delta \mathcal{L}_{\mathrm{SMEFT}}^{\mathrm{lead}} \supset \frac{\mathcal{C}_{tH}}{\Lambda^2} \left( \left( \phi^\dagger \phi \right) \left( \bar{Q}_L t_R \tilde{\phi} \right) + \mathrm{H.c.} \right) + \frac{\mathcal{C}_{HG}}{\Lambda^2} \phi^\dagger \phi \, G_{\mu\nu}^a G^{\mu\nu,a} \,.
\tag{7.4}
$$

---

process just recently has been observed [227, 228], the potential to scrutinize the 4-top Wilson coefficients only including the $\mathcal{O}\left(\Lambda^{-2}\right)$ interference terms may be much better in that channel than for indirect processes [227], like $gg \to h(h)$. Nevertheless, it is relevant to investigate different channels in parallel.

[20]Notice that we follow the sign convention introduced in Eq. (2.2), such that results involving odd powers of $g_s$ have the opposite sign compared to the equations of Ref. [6].

Since we relate calculations in the broken phase of the EW symmetry in Secs. 7.2 and 7.3 with calculations in the unbroken phase in Secs. 7.4 and 7.5 we remind ourselves about the connection between the full mass parameter $m_t$ and the Yukawa parameter $y_t$ of the dimension-4 Lagrangian in Eq. (6.15).

For all calculations in this chapter, we employed QGRAF [64] for the generation of all relevant diagrams and FEYNCALC [60–62] for analytic manipulations.

## 7.2. $\gamma_5$ scheme structure at one-loop

In this section we demonstrate the $\gamma_5$ scheme dependent structure of pure 4-top operator contributions to the one-loop subamplitudes entering the calculation of the Higgs-gluon coupling of Sec. 7.3. The origin of the $\gamma_5$ scheme dependence is related to differences in the evanescent $(D-4)$-dimensional parts of the Dirac algebra between NDR (cf. property (1) of Eq. (3.22)) and BMHV (cf. Eq. (3.24) together with Eq. (3.25)). Therefore, there are already finite effects observable at one-loop order where the $\epsilon$ parts of the Dirac algebra multiply a pole of the loop integrals. As mentioned in Sec. 3.5, appearing one-loop Feynman integrals will be expressed in terms of the master integrals of the form of Passarino-Veltman scalar functions $N_0$ with $N \in \{A, B, C, \ldots\}$ in the convention of `FeynCalc` [60–62], such that loop factors are kept manifest in the formulas.

We begin considering the contribution to the gauge interaction for an on-shell gluon. An explicit calculation reveals



$$\frac{\mathcal{C}_{Qt}^{(1)} + \left(c_F - \frac{c_A}{2}\right)\mathcal{C}_{Qt}^{(8)}}{\mathcal{C}_{tG}} K_{tG} \times \qquad (7.5)$$

i.e. the contribution is proportional to an insertion of $\mathcal{C}_{tG}$. However, this depends on the constant, but scheme dependent factor

$$K_{tG} = \begin{cases} -\dfrac{\sqrt{2}m_t g_s}{16\pi^2 v} & \text{(NDR)} \\ 0 & \text{(BMHV)} . \end{cases} \qquad (7.6)$$

If the gluon is allowed to be off-shell, the structure of the correction in Eq. (7.5) has more contributions which are, however, not relevant for our investigation.

At this point it is useful to clarify the possible structures of 4-top operator contributions: In general the operator insertion leads to two possible contractions of fermion lines which are demonstrated in Fig. 7.1. The two possible contractions come with opposite relative sign. In the considered contributions the overall sign is conveniently determined by assigning a $-1$ per trace in the Dirac space whereas no additional sign is associated with open Dirac structures. For the one-loop corrections investigated in this project, however, only the contribution with an open fermion line, i.e. Fig. 7.1 (b), survives after contracting the gamma matrices. Thus, the observed scheme dependence in Eq. (7.6) is not related to a trace ambiguity [96].

Subsequently, we consider the contribution to the propagator and the Yukawa interaction. We start with the propagator correction, as the resulting factor can be identified in the Yukawa correction. Since the explicit propagator correction does not depend on the propagator momentum, its contribution is proportional to a mass insertion. Pictorially, we write



$$\frac{\mathcal{C}_{Qt}^{(1)} + c_F \mathcal{C}_{Qt}^{(8)}}{\Lambda^2} \left(B_{m_t} + K_{m_t}\right) \times \qquad (7.7)$$

**(a)**                                                                    **(b)**

**Figure 7.1.:** Visualisation of the possible contractions of closed fermion loop diagrams with 4-top operators (which holds in general for 4-fermion operators of equal fermion species): (a) closed Dirac structure yielding a trace; (b) open Dirac structure without any traces.

where we split the contribution to make the scheme dependent part

$$K_{m_t} = \begin{cases} -\dfrac{m_t^2}{8\pi^2} & \text{(NDR)} \\ 0 & \text{(BMHV)} , \end{cases} \tag{7.8}$$

obvious. The part that does not depend on the scheme, $B_{m_t}$, is given by

$$B_{m_t} = \frac{1}{4\pi^2} A_0(m_t^2) . \tag{7.9}$$

Subsequently, we consider the contribution of 4-top operators to the Yukawa interaction. Here we express the $h \to \bar{t}t$ subamplitude in terms of the Yukawa coupling with on-shell external Higgs boson

 $$= \left( \frac{\mathcal{C}_{Qt}^{(1)} + c_F \mathcal{C}_{Qt}^{(8)}}{\Lambda^2} \right) \left( B_{h\bar{t}t} + K_{m_t} - \frac{v^3}{\sqrt{2} m_t} K_{tH} \right)$$

$$\tag{7.10}$$

$$\times \quad h \text{---} \  \quad .$$

Again, we split into scheme dependent part

$$K_{tH} = \begin{cases} \dfrac{\sqrt{2} m_t \left( 4m_t^2 - m_h^2 \right)}{16\pi^2 v^3} & \text{(NDR)} \\ 0 & \text{(BMHV)} , \end{cases} \tag{7.11}$$

and scheme independent part

$$B_{h\bar{t}t} = \frac{1}{8\pi^2} \left( 2A_0(m_t^2) - \left( m_h^2 - 4m_t^2 \right) B_0(m_h^2, m_t^2, m_t^2) \right) . \tag{7.12}$$

At this point it is instructive to already try to better understand the meaning of Eqs. (7.5), (7.7) and (7.10). As has been illustrated by the pictorial representation of the one-loop corrections on the right-hand side of Eqs. (7.5), (7.7) and (7.10), the 4-top operators effectively induce a contribution to the parameters $m_t$, $\mathcal{C}_{tH}$ and $\mathcal{C}_{tG}$ which is scheme-dependent. We can, however, recast the full EFT contribution in a scheme-independent form by an effective parameter redefinition, finite renormalisation in the language of Refs. [100, 224], of the form

$$\tilde{m}_t = m_t \left[ 1 + \frac{\mathcal{C}_{Qt}^{(1)} + c_F \mathcal{C}_{Qt}^{(8)}}{\Lambda^2} K_{m_t} \right]$$

$$\tilde{\mathcal{C}}_{tH} = \mathcal{C}_{tH} + \left( \mathcal{C}_{Qt}^{(1)} + c_F \mathcal{C}_{Qt}^{(8)} \right) K_{tH} \tag{7.13}$$

$$\tilde{\mathcal{C}}_{tG} = \mathcal{C}_{tG} + \left( \mathcal{C}_{Qt}^{(1)} + \left( c_F - \frac{c_A}{2} \right) \mathcal{C}_{Qt}^{(8)} \right) K_{tG} .$$

This procedure was introduced by Refs. [100, 224, 225] in the context of the anomalous dimension matrix of Wilson coefficient mixing in flavour physics. In this way, the scheme-independence of the considered one-loop contributions is made manifest and $\tilde{m}_t$, $\tilde{\mathcal{C}}_{tH}$ and $\tilde{\mathcal{C}}_{tG}$ form scheme-independent coefficients. This form of redefinition using finite shifts obtained at one-loop will be challenged at two-loop level in Sec. 7.3.

It is important to note that the definition of the splitting into scheme-independent $B_i$ and scheme-dependent $K_i$ structures of Eqs. (7.5), 7.7 and (7.10) can be defined in different ways (there are, in principle, infinitely many options to do so), leading to an arbitrariness in finding a scheme-independent redefinition of the form in Eq. (7.13). For our investigation we choose to define the $K_i$ as the terms in $D \to 4$ dimensions that are not multiplied by the Passarino-Veltman master integrals, i.e. the *rational parts*. This choice is especially convenient, since the $K_i$ vanish for the BMHV scheme in the case of 4-top operators, such that the definitions in Eq. (7.13) coincide with the original parameters in the BMHV scheme. For other operator classes, however, this is not the case anymore, as we will see in Sec. 7.5. From a practical point of view, instead of defining scheme-independent coefficients, we will learn to appreciate these relations of Eq. (7.13) more in the form of $\gamma_5$ scheme dependent values of $m_t$, $\mathcal{C}_{tH}$ and $\mathcal{C}_{tG}$, that conspire with the scheme dependent amplitude contributions of the 4-top operators to remove the scheme dependence from the physical prediction. This allows to consistently embrace a scheme choice and still being able to translate to the other schemes, after the necessary translation relations have been derived once.

The relations of Eqs. (7.5), (7.7) and (7.10) deserve also further explanation from the power counting point of view, since they establish a close connection between parameters of the theory. In the form Eq. (7.13) is written, the relations seem to have a hierarchy of importance, such that the contributions induced by $K_i$ are suppressed by $\mathcal{O}\left(\Lambda^{-2}\mathbf{L}\right)$ in case of $m_t$ and $\mathcal{O}\left(\mathbf{L}\right)$ for the affected Wilson coefficients. If we apply the the power counting arguments of Sec. 4.3 for the assumption of a weakly coupling and renormalisable UV completion, however, the Wilson coefficient $\mathcal{C}_{tG}$ itself is expected to contain a loop suppression factor as well [147, 148]. Following this consideration the contribution of $\mathcal{C}_{Qt}^{(1)}$ and $\mathcal{C}_{Qt}^{(8)}$ to $\tilde{\mathcal{C}}_{tG}$ in Eq. (7.13) can be of the same importance as the contribution of $\mathcal{C}_{tG}$ requiring that both contributions should not be considered in isolation.

Notice that the contributions of $\mathcal{C}_{QQ}^{(1)}$, $\mathcal{C}_{QQ}^{(8)}$ and $\mathcal{C}_{tt}$ identically vanish in all subamplitudes needed for the Higgs-gluon coupling.[21]

## 7.3.  Calculation of the Higgs-gluon coupling

In this section, we investigate the full effect of our operator selection on the Higgs-gluon coupling, inserting the subdiagrams of the previous section into two-loop diagrams.

The amplitude for Higgs-gluon coupling in the presence of SMEFT operators is expanded in the form

$$\mathcal{M}_{\text{TOT}} = \mathcal{M}_{\text{SM}} + \mathcal{M}_{\text{EFT}} \,. \tag{7.14}$$

Since the 4-top operators do not enter independently we split the dimension-6 part into contributions of all operators mentioned in Sec. 7.1, such that

$$\mathcal{M}_{\text{EFT}} = \left\{ \frac{\mathcal{C}_{4t}}{\Lambda^2}\mathcal{M}_{4t} + \frac{\mathcal{C}_{tG}}{\Lambda^2}\mathcal{M}_{tG} + \frac{\mathcal{C}_{HG}}{\Lambda^2}\mathcal{M}_{HG} + \frac{\mathcal{C}_{tH}}{\Lambda^2}\mathcal{M}_{tH} + \mathcal{M}_{\text{C.T.}} \right\} \,, \tag{7.15}$$

---

[21]If we had chosen a different $D$-dimensional extension of the chiral vertex for BMHV than Eq. (3.25), we would have to deal with additional contributions from $\mathcal{C}_{QQ}^{(1)}$, $\mathcal{C}_{QQ}^{(8)}$ and $\mathcal{C}_{tt}$. These could violate symmetry relations of the theory at intermediate steps of the calculation that eventually would have to be removed by finite symmetry restoring counterterms. In addition, different choices of the chiral vertex can also lead to different parameterisations of new physics effects which are related to each other similar to Eq. (7.33).
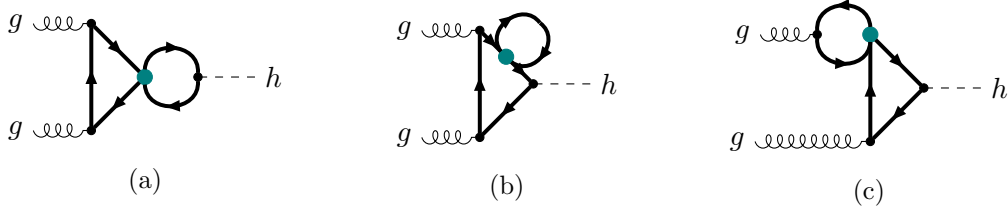
**Figure 7.2.:** Topologies of contributions from insertions of four-top quark operators (teal dot) to $gg \to h$ at two-loop level.



**Figure 7.3.:** Contribution to $gg \to h$ with a single insertion of the chromomagnetic operator (orange square dot). There are triangle topologies (left) and bubble topologies (right).

where $\frac{\mathcal{C}_{4t}}{\Lambda^2}\mathcal{M}_{4t}$ is a short-hand notation for all contributions of the 4-top operators of Eq. (7.1) and $\mathcal{M}_{\mathrm{C.T.}}$ entails the contribution from counterterms. As the coefficient $\mathcal{C}_{tH}$ effectively only leads to a redefinition of $m_t$ and modification of the Yukawa interaction, its contribution will be combined with the $\mathcal{M}_{\mathrm{SM}}$ part using the replacement

$$\mathcal{M}_{\mathrm{SM}}\left(y_t\right) + \frac{\mathcal{C}_{tH}}{\Lambda^2}\mathcal{M}_{tH} \to \left[1 - \frac{v^3}{\sqrt{2}m_t}\frac{\mathcal{C}_{tH}}{\Lambda^2}\right]\mathcal{M}_{\mathrm{SM}}\left(m_t\right) \ , \tag{7.16}$$

in the following.

In line with the reasoning in Ref. [229], we split the contribution of 4-top operators according to the corrections including the subamplitudes of Sec. 7.2. This leads to the following classes, which are also shown in Fig. 7.2:

(a) correction to the Yukawa interaction,

(b) correction to the top-quark propagator,

(c) correction to the gluon-top interaction.

On the level of the amplitude, we split into linear combinations of $\mathcal{C}_{Qt}^{(1)}$ and $\mathcal{C}_{Qt}^{(8)}$ originating from the color algebra obtained by one-loop subdiagrams as follows

$$\frac{\mathcal{C}_{4t}}{\Lambda^2}\mathcal{M}_{4t} = \frac{\mathcal{C}_{Qt}^{(1)} + c_F\mathcal{C}_{Qt}^{(8)}}{\Lambda^2}\mathcal{A}_{m_t+h\bar{t}t} + \frac{\mathcal{C}_{Qt}^{(1)} + \left(c_F - \frac{c_A}{2}\right)\mathcal{C}_{Qt}^{(8)}}{\Lambda^2}\mathcal{A}_{g\bar{t}t} \ , \tag{7.17}$$

where $\mathcal{A}_{m_t+h\bar{t}t}$ includes the contributions of type (a) and (b) of Fig. 7.2 and $\mathcal{A}_{g\bar{t}t}$ the contributions of type (c).

As already indicated in Eq. (7.5), the contribution involving a correction to the gluon-top vertex can be expressed in terms of the amplitude involving an insertion of the chromomagnetic operator which diagrams are demonstrated in Fig. 7.3. Thus we write

$$\mathcal{A}_{g\bar{t}t} = \left(4\pi e^{-\gamma_E}\right)^\epsilon \left[\frac{1}{2}K_{tG}\,\mathcal{M}_{tG}|_{\mathrm{DIV}} + K_{tG}\,\mathcal{M}_{tG}|_{\mathrm{FIN}}\right] \ , \tag{7.18}$$

where the factor of $\left(4\pi e^{-\gamma_E}\right)^\epsilon$ explicitly appears in Eq. (7.18) in order to compensate the difference of the diagrammatic loop order between $\mathcal{C}_{tG}$ and $\mathcal{C}_{Qt}^{(1/8)}$ contributions. The explicit

form of the divergent and finite piece of the amplitude involving the chromomagnetic operator $\mathcal{M}_{tG}|_{\text{DIV}}$ and $\mathcal{M}_{tG}|_{\text{FIN}}$ is given by

$$\mathcal{M}_{tG}|_{\text{DIV}} = \frac{(4\pi e^{-\gamma_E})^\epsilon}{16\pi^2\epsilon} 4\sqrt{2} m_t g_s m_h^2 T^{\mu_1\mu_2} \epsilon_{\mu_1}(p_1)\epsilon_{\mu_2}(p_2)\delta^{A_1 A_2} \ , \tag{7.19}$$

and

$$\mathcal{M}_{tG}|_{\text{FIN}} = \frac{\sqrt{2} m_t m_h^2 g_s}{8\pi^2} T^{\mu_1\mu_2} \epsilon_{\mu_1}(p_1)\epsilon_{\mu_2}(p_2)\delta^{A_1 A_2}$$
$$\times \left( \frac{A_0^{\text{fin}}(m_t^2)}{m_t^2} + B_0^{\text{fin}}(m_h^2, m_t^2, m_t^2) + 2m_t^2 C_0(0,0,m_h^2,m_t^2,m_t^2,m_t^2) - 2 \right) \ , \tag{7.20}$$

where $A_0^{\text{fin}}$ and $B_0^{\text{fin}}$ are the finite pieces of the respective Passarino-Veltman scalar functions and we use the tensor structure

$$T^{\mu_1\mu_2} = \left( g^{\mu_1\mu_2} - 2\frac{p_1^{\mu_2} p_2^{\mu_1}}{m_h^2} \right) \ . \tag{7.21}$$

Since $K_{tG}$ appearing in Eq. (7.18) is defined by Eq. (7.6), we observe that the contribution from a gauge vertex correction can be factored in the form of Eq. (7.18), such that the scheme dependence is explicitly contained in $K_{tG}$. In addition, the form of Eq. (7.18) implies that the pole structure originating from $\mathcal{C}_{Qt}^{(1/8)}$ differs depending on the scheme. This is not unexpected, since $K_{tG}$ is already obtained from rational parts of a one-loop Feynman integral, thus the second loop integration can lead to a pole.

### 7.3.1. Structure of the renormalisation

For the purpose of the discussion in this chapter, we employ $\overline{\text{MS}}$ renormalisation for the parameters of the theory. In particular, we choose to renormalise $m_t$ in the $\overline{\text{MS}}$ scheme as well, which is in contrast to the usual choice of an on-shell scheme for $m_t$ in phenomenological calculations of gluon-fusion processes. The $\overline{\text{MS}}$ scheme makes the point of $\gamma_5$ scheme independence of the final result considering scheme dependent parameters more general, since an on-shell scheme for $m_t$ completely removes contributions from diagrams of type (b) in Fig. 7.2. We postpone the structure of the on-shell $m_t$ scheme choice to Chapter 8.

Collecting all counter term contributions we identify the structures represented by the following diagrams



$$\mathcal{M}_{\text{C.T.}} = \quad \text{— — } h \quad + \quad \text{— — } h \quad + \quad \text{— — } h \ . \tag{7.22}$$

The $\overline{\text{MS}}$ renormalised top mass $m_t$ is defined by[22]

$$m_t^b = m_t + \delta_{\overline{m}_t} \ , \tag{7.23}$$

with

$$\delta_{\overline{m}_t} = -\frac{(4\pi e^{-\gamma_E})^\epsilon}{\epsilon} \frac{m_t^3}{4\pi^2} \frac{\mathcal{C}_{Qt}^{(1)} + c_F \mathcal{C}_{Qt}^{(8)}}{\Lambda^2} \ . \tag{7.24}$$

[22]Note that $m_t$ is understood as the $\overline{\text{MS}}$ mass throughout this chapter, whereas in Chapters 6 and 8 $m_t$ refers to the on-shell mass.

In order to remove the UV divergence of the diagrams of type (a) in Fig. 7.2, also the Wilson coefficient $\mathcal{C}_{tH}$ needs a renormalisation. Expanding its bare value into $\mathcal{C}_{tH}^b = \mu^{3\epsilon}\left(\mathcal{C}_{tH} + \delta_{\mathcal{C}_{tH}}^{\mathcal{C}_i}\mathcal{C}_i\right)$ in the $\overline{\text{MS}}$ scheme therefore leads to

$$\delta_{\mathcal{C}_{tH}}^{\mathcal{C}_{4t}}\mathcal{C}_{4t} = \frac{(4\pi e^{-\gamma_E})^\epsilon}{16\pi^2\epsilon}\frac{2\sqrt{2}m_t\left(4m_t^2 - m_h^2\right)}{v^3}\left(\mathcal{C}_{Qt}^{(1)} + c_F\mathcal{C}_{Qt}^{(8)}\right) , \tag{7.25}$$

which coincides with $\delta_{\mathcal{C}_i}^{\mathcal{C}_j} = \frac{(4\pi e^{-\gamma_E})^\epsilon}{16\pi^2\epsilon}\frac{\gamma_{\mathcal{C}_i\mathcal{C}_j}}{2}$ using the respective part of the anomalous dimension matrix $\gamma_{\mathcal{C}_i\mathcal{C}_j}$ of Refs. [156, 158]. The relation between $\delta_{\mathcal{C}_i}^{\mathcal{C}_j}$ and the anomalous dimension matrix is derived in Sec. 4.4.

With the counter term diagrams corresponding to the one-loop counterterms in Eqs. (7.24) and (7.25) the diagrams of classes (a) and (b) in Fig. 7.2 are made finite, i.e. $\mathcal{A}_{g_{h\bar{t}t}+m_t}$ is fully renormalised.

The diagrams of the chromomagnetic operator insertion in Fig. 7.3 are UV divergent even though they constitute the leading order contribution of $\mathcal{C}_{tG}$ to the Higgs-gluon coupling. This behaviour is well understood and leads to a renormalisation of $\mathcal{C}_{HG}^0 = \mu^{2\epsilon}\left(\mathcal{C}_{HG} + \delta_{\mathcal{C}_{HG}}^{\mathcal{C}_i}\mathcal{C}_i\right)$ [156, 231,232]. Since the 4-top contributions of type (c) in Fig. 7.2 lead to a divergence proportional to the one of the chromomagnetic operator, i.e. Eq. (7.18), we need to choose

$$\delta_{\mathcal{C}_{HG}}^{\mathcal{C}_{tG}}\mathcal{C}_{tG} + \delta_{\mathcal{C}_{HG}}^{\mathcal{C}_{4t}}\mathcal{C}_{4t} =$$
$$\frac{(4\pi e^{-\gamma_E})^\epsilon}{16\pi^2\epsilon}\frac{4\sqrt{2}m_t g_s}{v}T_F\left(\mathcal{C}_{tG} + \left(4\pi e^{-\gamma_E}\right)^\epsilon\frac{K_{tG}}{2}\left(\mathcal{C}_{Qt}^{(1)} + \left(c_F - \frac{c_A}{2}\right)\mathcal{C}_{Qt}^{(8)}\right)\right) , \tag{7.26}$$

to remove all remaining divergences.

As is apparent by the appearance of $K_{tG}$ in Eq. (7.26), the counter term for $\mathcal{C}_{HG}$ is indeed scheme dependent. This implies that also the anomalous dimension matrix contains scheme dependent contributions. Using $\frac{\mathrm{d}\mathcal{C}_{tG}^b}{\mathrm{d}\mu} = 0$ we derive

$$16\pi^2\mu\frac{\mathrm{d}\mathcal{C}_{HG}}{\mathrm{d}\mu} = \frac{8\sqrt{2}m_t g_s}{v}T_F\left(\mathcal{C}_{tG} + K_{tG}\left(\mathcal{C}_{Qt}^{(1)} - \frac{1}{6}\mathcal{C}_{Qt}^{(8)}\right)\right). \tag{7.27}$$

The combination of $\mathcal{C}_{tG}$ and $\mathcal{C}_{Qt}^{(1/8)}$ in Eq. (7.27) differs by a relative factor of 2 w.r.t. the combination in Eq. (7.26). The origin is traced back to the different orders of SM couplings that enter in the one-loop diagrams of $\mathcal{C}_{tG}$ compared with the two-loop diagrams of $\mathcal{C}_{Qt}^{(1/8)}$. The compensation of this relative factor of 2 is crucial in the need to define $\gamma_5$ scheme independent observables.

The appearance of scheme differences in the anomalous dimension originating from 4-fermion operators with chiral structure $(\bar{L}L)(\bar{R}R)$ contributing to the structure of the chromomagnetic operator has been observed in the context of flavour physics already a while ago [223–225]. Following the strategy proposed in Refs. [100,224,225], the definition of the combined parameter $\tilde{\mathcal{C}}_{tG}$ of Eq. (7.13) precisely ensures a scheme-independent anomalous dimension matrix.

### 7.3.2. Renormalised amplitude at fixed order

So far we investigated the $\gamma_5$ scheme dependent structure of 4-top operator contributions at one-loop level and the two-loop anomalous dimension. We identified a combination of Wilson coefficients (see Eq. (7.13)) that simultaneously brings the one-loop corrections and the

anomalous dimension into a manifestly scheme independent form. In this section, we investigate the $\gamma_5$ scheme dependence of the two-loop renormalised amplitude and, in particular, check if a redefinition of the form in Eq. (7.13) derived at one-loop level is sufficient to find a scheme independent combination of Wilson coefficients. Thus, we need to reorganise the $\gamma_5$ scheme dependence of the 4-top operator insertions at two-loop level which is parameterised in terms of $K_{tG}$, $K_{tH}$ and $K_{m_t}$.

The contributions of diagrams (a) and (b) of Fig. 7.2 to the renormalised amplitude can be expressed as

$$\mathcal{A}^{\text{Ren}}_{m_t+h\bar{t}t} = \mathcal{M}^{\text{S.I.}}_{m_t+h\bar{t}t} - \frac{v^3}{\sqrt{2}m_t} K_{tH} \mathcal{M}^{\text{SM}} + K_{m_t} \frac{\partial \mathcal{M}^{\text{SM}}}{\partial m_t} \times m_t \, , \qquad (7.28)$$

where $\mathcal{M}^{\text{SM}}$ and $\mathcal{M}^{\text{S.I.}}_{m_t+h\bar{t}t}$ are scheme-independent. Note that the derivative in $\dfrac{\partial \mathcal{M}^{\text{SM}}}{\partial m_t}$ also includes the $m_t$ part of the Yukawa interaction. Collecting all partial results of Eqs. (7.17), (7.18) and (7.28) we find for the full renormalised matrix element

$$
\begin{aligned}
\mathcal{M}^{\text{Ren}}_{\text{TOT}} = {} & \frac{\mathcal{C}^{(1)}_{Qt} + c_F \mathcal{C}^{(8)}_{Qt}}{\Lambda^2} \mathcal{M}^{\text{S.I.}}_{m_t+h\bar{t}t} \\
& + \left[ \frac{\mathcal{C}_{tG}}{\Lambda^2} + K_{tG} \frac{\mathcal{C}^{(1)}_{Qt} + \left(c_F - \frac{c_A}{2}\right)\mathcal{C}^{(8)}_{Qt}}{\Lambda^2} \right] \mathcal{M}_{tG}|_{\text{FIN}} \\
& + \left[ 1 - \frac{v^3}{\sqrt{2}m_t} \left( \frac{\mathcal{C}_{tH}}{\Lambda^2} + K_{tH} \frac{\mathcal{C}^{(1)}_{Qt} + c_F \mathcal{C}^{(8)}_{Qt}}{\Lambda^2} \right) \right] \mathcal{M}_{\text{SM}} \\
& + \frac{\mathcal{C}^{(1)}_{Qt} + c_F \mathcal{C}^{(8)}_{Qt}}{\Lambda^2} K_{m_t} m_t \times \frac{\partial \mathcal{M}_{\text{SM}}}{\partial m_t} \\
& + \frac{\mathcal{C}_{HG}}{\Lambda^2} \mathcal{M}_{HG} \, .
\end{aligned}
\qquad (7.29)
$$

It is important to clarify that $\mathcal{M}^{\text{Ren}}_{\text{TOT}}$ represents a physical on-shell scattering amplitude which is required to be $\gamma_5$ scheme independent. This statement is best understood in the top-down perspective considering the EFT theory as the low energy limit of a UV complete theory.[23] Thus, the scheme dependence of the $K_i$-terms has to be compensated by a scheme dependence of the parameters. In order to make the scheme independence of the amplitude manifest, we redefine the parameters using the relations of Eq. (7.13). With the form of a perturbative expansion of the mass parameter in the SM amplitude

$$\mathcal{M}_{\text{SM}}(\tilde{m}_t) = \mathcal{M}_{\text{SM}}(m_t) + \frac{\mathcal{C}^{(1)}_{Qt} + c_F \mathcal{C}^{(8)}_{Qt}}{\Lambda^2} K_{m_t} m_t \times \frac{\partial \mathcal{M}_{\text{SM}}}{\partial m_t} + \mathcal{O}\left(\Lambda^{-4}\right) \, , \qquad (7.30)$$

the parameter redefinition allows us to obtain a more compact representation of the full matrix element

$$
\begin{aligned}
\mathcal{M}^{\text{Ren}}_{\text{TOT}} = {} & \frac{\mathcal{C}^{(1)}_{Qt} + c_F \mathcal{C}^{(8)}_{Qt}}{\Lambda^2} \mathcal{M}^{\text{S.I.}}_{m_t+h\bar{t}t} + \frac{\tilde{\mathcal{C}}_{tG}}{\Lambda^2} \mathcal{M}_{tG}|_{\text{FIN}} \\
& + \left[ 1 - \frac{v^3}{\sqrt{2}m_t} \frac{\tilde{\mathcal{C}}_{tH}}{\Lambda^2} \right] \mathcal{M}_{\text{SM}}(\tilde{m}_t) + \frac{\mathcal{C}_{HG}}{\Lambda^2} \mathcal{M}_{HG} \, ,
\end{aligned}
\qquad (7.31)
$$

---

[23]SMEFT is built upon the assumption that the degrees of freedom of the UV theory manifest beyond the energy scale of the EW phase transition. Therefore, the matching calculation we refer to happens in the unbroken phase. As will be explicitly checked in Sec. 7.4, the structure of scheme dependence persists in the unbroken phase and the UV matching will be exemplified with simplified models.

which is valid at $\mathcal{O}\left(\Lambda^{-2}\right)$. Since the individual amplitude structures $\mathcal{M}_{m_t+h\bar{t}t}^{\mathrm{S.I.}}$, $\mathcal{M}_{tG}$, $\mathcal{M}_{\mathrm{SM}}$ and $\mathcal{M}_{HG}$ are scheme-independent, it follows that the combinations in Eq. (7.13) must be scheme-independent also at two-loop for the Higgs-gluon coupling.

We want to emphasize again that the redefined parameters in Eq. (7.13) derived from the necessity of overall scheme-independence at the level of one-loop are precisely the same combination that make the anomalous dimension in Eq. (7.27) and the renormalised two-loop amplitude scheme-independent.

### 7.3.3. Translation of $\gamma_5$ scheme dependent Wilson coefficients

As was already mentioned in Sec. 7.2, the prescription to split $K$-terms and $B$-terms is quite arbitrary, hence, there are a priory many possibilities to define scheme-independent combinations of the form Eq. (7.13). In particular, the choice of deriving it from the rational terms of the loop calculation is convenient, however, depends on the choice of master integrals, i.e. choosing $B_0(0, m_t^2, m_t^2)$ instead of $A_0(m_t^2)$ would introduce a finite difference in $K$, as

$$A_0(m_t^2) = m_t^2 \left( B_0(0, m_t^2, m_t^2) - 1 \right) + \mathcal{O}\left(\epsilon\right) , \tag{7.32}$$

in the limit $D \to 4$. On the other hand, the difference of the scheme dependent terms $\Delta K_i = K_i^{\mathrm{BMHV}} - K_i^{\mathrm{NDR}}$ does not depend on the chosen prescription. There is the possibility to choose a 'canonical scheme' which defines parameter combinations for the other schemes as in Eq. (7.13). In case of the 4-top operators BMHV provides the most convenient option and was therefore suggested in Ref. [223]. However, as calculations in BMHV are computationally more involved than in NDR and the $\gamma_5$ scheme dependent structure differs in other classes of operators (cf. Sec. 7.5), the choice of defining the 'canonical scheme' again relies on subjective arguments.

Therefore, instead of redefining the parameters to restore the form of the 'canonical scheme', we allow the Wilson coefficients to acquire scheme dependent values in the presence of $\mathcal{C}_{Qt}^{(1/8)}$. With the condition of a scheme independent scattering amplitude we thus require $\tilde{X}_i^{\mathrm{NDR}} = \tilde{X}_i^{\mathrm{BMHV}}$ for the parameters in Eq. (7.13). This leads to

$$m_t^{\mathrm{BMHV}} = m_t^{\mathrm{NDR}} - \frac{m_t^3}{8\pi^2\Lambda^2}\left(\mathcal{C}_{Qt}^{(1)} + c_F\mathcal{C}_{Qt}^{(8)}\right)$$

$$\mathcal{C}_{tH}^{\mathrm{BMHV}} = \mathcal{C}_{tH}^{\mathrm{NDR}} + \frac{\sqrt{2}m_t\left(4m_t^2 - m_h^2\right)}{16\pi^2 v^3}\left(\mathcal{C}_{Qt}^{(1)} + c_F\mathcal{C}_{Qt}^{(8)}\right) \tag{7.33}$$

$$\mathcal{C}_{tG}^{\mathrm{BMHV}} = \mathcal{C}_{tG}^{\mathrm{NDR}} - \frac{\sqrt{2}m_t g_s}{16\pi^2 v}\left(\mathcal{C}_{Qt}^{(1)} + \left(c_F - \frac{c_A}{2}\right)\mathcal{C}_{Qt}^{(8)}\right) .$$

With Eq. (7.33) we found a relation between the parameters of the two schemes in terms of shifts induced by $\mathcal{C}_{Qt}^{(1/8)}$. If the scheme difference of the parameters is considered, the two schemes lead to the same anomalous dimension and renormalised amplitude. The information provided by Eq. (7.13) and Eq. (7.33) is in principle the same, yet the interpretation in terms of scheme dependent parameters is much more flexible, as it does not rely on a reference scheme. Moreover, the scheme dependence of single Wilson coefficients could question the meaning of measurements of individual parameters, which implies that in the future combined parameter fits will be of relevance. A minimal requirement to find relevant sets of parameters could be that the scheme dependence should be resolvable at the considered order of power counting. Let the reader be reminded, that if we consider the loop-suppression of $\mathcal{C}_{tG}$ in the scenario of a weakly coupling and renormalisable UV completion, the contribution of $\mathcal{C}_{Qt}^{(1/8)}$ in the translation between the schemes for $\mathcal{C}_{tG}$ is expected to be of the same order as the original Wilson coefficient. Thus, $\mathcal{C}_{tG}$ should not be considered in isolation of $\mathcal{C}_{Qt}^{(1/8)}$ for such a scenario, whereas the hierarchy for $m_t$ and $\mathcal{C}_{tH}$ allows to define a leading contribution for which $\mathcal{C}_{Qt}^{(1/8)}$ provides only a subleading correction.

## 7.4. A cross-check in the top-down perspective: Matching with UV-models

We have already investigated the $\gamma_5$ scheme differences that can be understood by finite shifts on parameters of the theory in the EW broken phase. In this section, we want to validate this approach in the unbroken phase of the EW sector. We first consider one-loop amplitudes involving the 4-top operators that appear in a one-loop matching for $\mathcal{C}_{tG}$, $\mathcal{C}_{tH}$ and the dimension-4 top-Yukawa parameter $y_t$. This provides already a solid cross check, since the calculations between the two phases differ significantly. On top of that, we want to explicitly demonstrate with simplified models that the interpretation to understand the scheme dependence in amplitudes with 4-top operators as a shift of the parameters $\mathcal{C}_{tG}$, $\mathcal{C}_{tH}$ and $y_t$ naturally arises in a top-down matching.

Since the quarks are massless in the unbroken theory, it is reasonable to work with the interaction eigenstates $Q_L$ and $t_R$ for the diagrammatic representation in order to specify the relevant contributions. Throughout this section, a thicker fermion line denotes the LH iso-doublet $Q_L$, a thinner fermion line the RH iso-singlet $t_R$. The analytic calculations using FEYNCALC were performed for Dirac fields and the real scalar component of the Higgs doublet $\phi$.

### 7.4.1. $\gamma_5$ scheme structure at one-loop in the unbroken phase

In this subsection, we consider one-loop diagrams of 4-top operators of Eq. (7.1) contributing to the matching of $y_t$, $\mathcal{C}_{tG}$ and $\mathcal{C}_{tH}$. These calculations represent the EFT counter part of the matching calculation in the following subsections. If expansion by regions [233, 234] were used in the matching, this one-loop EFT contribution would correspond to the soft region, whereas the hard region defines the value of the Wilson coefficients derived in the one-loop matching. In order not to switch to an off-shell EFT basis (which is also called a Green's basis) of operators that has to be translated to the on-shell Warsaw basis, we compute the matching calculation for quasi on-shell states, allowing the SM Higgs doublet to have a 'mass' $m_\phi^2 = -\lambda v^2$. We refrain from showing the full analytic structure of the vertex corrections, since they have no direct correspondence to contributions in the unbroken theory. Hence, we rather focus on the rational parts of the loop integration to derive the scheme difference.

We start with the contribution to the Yukawa parameter for an on-shell vertex correction and project out only the rational terms

$$
\left. \text{} \right|_{\text{rat. part}} = \left( \frac{\mathcal{C}_{Qt}^{(1)} + c_F \mathcal{C}_{Qt}^{(8)}}{\Lambda^2} \right) \mathcal{K}_{\phi\bar{Q}t} \times \text{} \quad . \tag{7.34}
$$

The finite, scheme-dependent factor has the form

$$
\mathcal{K}_{\phi\bar{Q}t} = \begin{cases} -\dfrac{\lambda v^2}{16\pi^2} & \text{(NDR)} \\ 0 & \text{(BMHV)} . \end{cases} \tag{7.35}
$$

For the evaluation of the $\mathcal{C}_{tH}$ shift, it is convenient to define the off-shell Yukawa vertex

$$
\text{} := \text{} - \left( \frac{\mathcal{C}_{Qt}^{(1)} + c_F \mathcal{C}_{Qt}^{(8)}}{\Lambda^2} \right) \mathcal{K}_{\phi\bar{Q}t} \times \text{} \quad , \tag{7.36}
$$

in order to have a compact form for the one particle reducible contribution. Hence, we obtain for the on-shell $\bar{t}_R Q_L \phi^\dagger \phi \phi^\dagger$ vertex



$$\left.\phantom{x}\right|_{\text{rat. part}} = \left( \frac{\mathcal{C}_{Qt}^{(1)} + c_F \mathcal{C}_{Qt}^{(8)}}{\mathcal{C}_{tH}} \right) \mathcal{K}_{tH} \times \qquad , \tag{7.37}$$

with

$$\mathcal{K}_{tH} = \begin{cases} \dfrac{y_t(y_t^2 - \lambda)}{8\pi^2} & \text{(NDR)} \\ 0 & \text{(BMHV)} \,. \end{cases} \tag{7.38}$$

In case of on-shell $\bar{t}_R Q_L \phi^\dagger g$ the one particle reducible contribution to the rational terms is already absorbed in $K_{\phi \bar{Q} t}$ such that we only need to consider



$$= \frac{\mathcal{C}_{Qt}^{(1)} + \left(c_F + \frac{c_A}{2}\right) \mathcal{C}_{Qt}^{(8)}}{\mathcal{C}_{tG}} \mathcal{K}_{tG} \qquad . \tag{7.39}$$

Finally, we obtain the scheme dependent factor

$$\mathcal{K}_{tG} = \begin{cases} -\dfrac{g_s y_t}{16\pi^2} & \text{(NDR)} \\ 0 & \text{(BMHV)} \,. \end{cases} \tag{7.40}$$

which precisely coincides with Eq. (7.6).

In summary, using the difference $\Delta \mathcal{K}_i = \mathcal{K}_i^{\text{BMHV}} - \mathcal{K}_i^{\text{NDR}}$ we obtain the relations to translate between the parameters of the two $\gamma_5$ schemes in terms of finite shifts. This has the form

$$
\begin{aligned}
y_t^{\text{BMHV}} &= y_t^{\text{NDR}} \left( 1 - \frac{\lambda v^2}{16\pi^2} \frac{\mathcal{C}_{Qt}^{(1)} + c_F \mathcal{C}_{Qt}^{(8)}}{\Lambda^2} \right) \\
\mathcal{C}_{tH}^{\text{BMHV}} &= \mathcal{C}_{tH}^{\text{NDR}} + \frac{y_t(y_t^2 - \lambda)}{8\pi^2} \left( \mathcal{C}_{Qt}^{(1)} + c_F \mathcal{C}_{Qt}^{(8)} \right) \\
\mathcal{C}_{tG}^{\text{BMHV}} &= \mathcal{C}_{tG}^{\text{NDR}} - \frac{g_s y_t}{16\pi^2} \left( \mathcal{C}_{Qt}^{(1)} + \left(c_F - \frac{c_A}{2}\right) \mathcal{C}_{Qt}^{(8)} \right) \,,
\end{aligned}
\tag{7.41}
$$

which is equivalent to the relations in Eq. (7.33).

In the following, we validate the result by means of a top-down matching calculation with two simplified scalar models. The notation follows Ref. [235] for the scalar fields as defined by their representation of the SM gauge group. The scalar models are specified by their representations $(r_{SU(3)_{QCD}}, r_{SU(2)_L})_Y$.

### 7.4.2. New scalar: $\varphi \sim (1,2)_{\frac{1}{2}}$

This UV model extends the SM particle content by a new heavy scalar which is defined by its mass $M_\varphi \gg v$ and representation under SM gauge group $\varphi \sim (1,2)_{\frac{1}{2}}$. The relevant Lagrangian terms can be written as

$$\mathcal{L}_\varphi = (D_\mu \varphi)^\dagger D^\mu \varphi - M_\varphi^2 \varphi^\dagger \varphi - Y_\varphi \left( \varphi^\dagger \varepsilon \bar{Q}_L^T t_R + \text{H.c.} \right) \,, \tag{7.42}$$

(a)



(b)

**Figure 7.4.:** One-loop diagrams contributing to the matching to the Yukawa coupling (left) and to $\mathcal{C}_{t\phi}$ (right).

with the Levi-Civita pseudotensor $\varepsilon$ and transposition $T$ which both refer to isospin space only. Via tree-level matching we immediately obtain

$$\mathcal{L} = \frac{Y_\varphi^2}{M_\varphi^2}(\bar{Q}_L t_R)(\bar{t}_R Q_L) \,. \tag{7.43}$$

In the Warsaw basis, this operator is replaced in favor of $\mathcal{O}_{Qt}^{(1)}$ and $\mathcal{O}_{Qt}^{(8)}$, since it does not contribute independently from the present operators in $D \to 4$ dimensions. Thus, we label it as $\mathcal{R}_{Qt}^{(1)}$ in the following. In order to translate to the Warsaw basis we apply the 4-dimensional Fierz identities and $T_{ij}^a T_{kl}^a = T_F \left( \delta_{il}\delta_{kj} - \frac{1}{N_c}\delta_{ij}\delta_{kl} \right)$ which yields [235]

$$\frac{\mathcal{C}_{Qt}^{(1)}}{\Lambda^2} = -\frac{1}{2N_c}\frac{Y_\varphi^2}{M_\varphi^2}, \quad \frac{\mathcal{C}_{Qt}^{(8)}}{\Lambda^2} = -\frac{1}{2T_F}\frac{Y_\varphi^2}{M_\varphi^2} \,. \tag{7.44}$$

It is important to note that the Fierz identities are not valid in $D$-dimensions anymore, hence, we need to consider the evanescent operator explicitly in the one-loop matching calculation

$$\mathcal{E}^{(1)} = \mathcal{R}_{Qt}^{(1)} - \left( -\frac{1}{2N_c}\mathcal{O}_{Qt}^{(1)} - \frac{1}{2T_F}\mathcal{O}_{Qt}^{(8)} \right) \,, \tag{7.45}$$

which leads to $\mathcal{O}(\epsilon)$ contributions.

Now we compute the one-loop matching calculation to the Yukawa coupling $y_t$ and $\mathcal{C}_{tH}$ Wilson coefficient where we have to consider the contributions sketched in Fig. 7.4. Since the propagators of the new scalar field carry no loop momentum, they can be directly expanded for large $M_\varphi$, such that only the soft region which precisely coincides with the structure of Eq. (7.43) contributes. For the derivation of the $y_t$ ($\mathcal{C}_{tH}$) matching coefficient, all that is left is to calculate the contribution of the evanescent operator defined in Eq. (7.45). This yields for NDR

$$
\frac{Y_\varphi^2}{M_\varphi^2}\mathcal{R}_{Qt}^{(1)} = \overbrace{-\frac{1}{2N_c}\frac{Y_\varphi^2}{M_\varphi^2}}^{\mathcal{C}_{Qt}^{(1)}/\Lambda^2}\mathcal{O}_{Qt}^{(1)} \overbrace{-\frac{1}{2T_F}\frac{Y_\varphi^2}{M_\varphi^2}}^{\mathcal{C}_{Qt}^{(8)}/\Lambda^2}\mathcal{O}_{Qt}^{(8)} 
$$
$$
+ \underbrace{\frac{N_c}{2}\frac{y_t\left(y_t^2-\lambda\right)}{8\pi^2}\frac{Y_\varphi^2}{M_\varphi^2}}_{\mathcal{C}_{tH}^{\text{NDR}}/\Lambda^2}\mathcal{O}_{tH} + \left( \underbrace{-\frac{N_c}{2}\frac{\lambda v^2}{16\pi^2}\frac{Y_\varphi^2}{M_\varphi^2}}_{\Delta y_t^{\text{NDR}}}\left(\bar{Q}_L\tilde{\phi}t_R\right) + \text{H.c.} \right), \tag{7.46}
$$

which coincides with Ref. [114] upon adjustment of notation $\frac{\lambda}{2} \to \lambda$ and $\mu^2 \to \lambda v^2$. In specifying the coefficients, we introduced $\Delta y_t$ which appears as a modification of the already present four-dimensional Yukawa coupling $y_t$.

In BMHV we define the chiral vertex in the form Eq. (3.25), such that

$$\mathbb{P}_{L/R}\gamma^\mu\mathbb{P}_{R/L} = \bar{\gamma}^\mu\mathbb{P}_{R/L} \,, \tag{7.47}$$

i.e. effectively only the 4-dimensional Dirac structure is retained in the vertex. Therefore, the Fierz identity to translate $\mathcal{R}_{Qt}^{(1)}$ to $\mathcal{O}_{Qt}^{(1)}$ and $\mathcal{O}_{Qt}^{(8)}$ turns out to be exact. The redundant operator is then translated as

$$\frac{Y_\varphi^2}{M_\varphi^2}\mathcal{R}_{Qt}^{(1)} = \underbrace{-\frac{1}{2N_c}\frac{Y_\varphi^2}{M_\varphi^2}}_{\mathcal{C}_{Qt}^{(1)}/\Lambda^2}\mathcal{O}_{Qt}^{(1)} \underbrace{-\frac{1}{2T_F}\frac{Y_\varphi^2}{M_\varphi^2}}_{\mathcal{C}_{Qt}^{(8)}/\Lambda^2}\mathcal{O}_{Qt}^{(8)} \,, \tag{7.48}$$

such that $\mathcal{C}_{tH}^{\text{BMHV}} = 0$ and $\Delta y_t^{\text{BMHV}} = 0$.

Due to the colour structure, there are no one-loop diagrams involving the new scalar that may contribute to the chromomagnetic operator. Also the color structures of the Wilson coefficients obtained in Eq. (7.44) exactly cancels the linear combination that appears in one-loop calculations of the 4-top operators, i.e. $\mathcal{C}_{Qt}^{(1)} + \left(c_F - \frac{c_A}{2}\right)\mathcal{C}_{Qt}^{(8)} = 0$.

Summing up all the results, we find perfect agreement with Eq. (7.41).

### 7.4.3. New scalar: $\Phi \sim (8,2)_{\frac{1}{2}}$

In this part we want to extend the matching calculation for an additional scalar that transforms non-trivially under $SU(3)_{QCD}$. The new heavy scalar has quantum numbers $\Phi \sim (8,2)_{\frac{1}{2}}$ and its mass is defined with $M_\Phi \gg v$. The Lagrangian in this case has the form

$$\mathcal{L}_\Phi = (D_\mu\Phi)^\dagger D^\mu\Phi - M_\Phi^2\Phi^\dagger\Phi - Y_\Phi\left(\Phi^{A,\dagger}\varepsilon\bar{Q}_L^T T^A t_R + \text{H.c.}\right) \,. \tag{7.49}$$

A tree-level matching leads to

$$\mathcal{L} = \frac{Y_\Phi^2}{M_\Phi^2}(\bar{Q}_L T^A t_R)(\bar{t}_R T^A Q_L) \,. \tag{7.50}$$

Again, this is not an operator present in the Warsaw basis and we translate via Fierz identity. Applying this we have

$$\frac{\mathcal{C}_{Qt}^{(1)}}{\Lambda^2} = -\frac{c_F}{2N_c}\frac{Y_\Phi^2}{M_\Phi^2}, \quad \frac{\mathcal{C}_{Qt}^{(8)}}{\Lambda^2} = \frac{1}{2N_c}\frac{Y_\Phi^2}{M_\Phi^2} \,. \tag{7.51}$$

Following the reasoning of the previous section, we define the evanescent operator

$$\mathcal{E}^{(8)} = \mathcal{R}_{Qt}^{(8)} - \left(-\frac{c_F}{2N_c}\mathcal{O}_{Qt}^{(1)} + \frac{1}{2N_c}\mathcal{O}_{Qt}^{(8)}\right) \,, \tag{7.52}$$

which enters the one-loop matching calculation in the Warsaw basis.

In contrast to the case for the QCD singlet scalar in the previous section, it is impossible to construct one-loop corrections to $\bar{Q}_L t_R \to \phi^\dagger$ and $\bar{Q}_L t_R \to \phi^\dagger\phi\phi^\dagger$ with the current scalar model due to conservation of hypercharge or the color structure of the diagrams. This is in agreement with the contribution of the 4-top operators in the Warsaw basis with coefficients in Eq. (7.51), since the linear combination of Wilson coefficients appearing in the translation relation Eq. (7.41) for $y_t$ and $\mathcal{C}_{tH}$ vanishes, i.e. $\mathcal{C}_{Qt}^{(1)} + c_F\mathcal{C}_{Qt}^{(8)} = 0$.

We find, however, diagrams contributing to the matching of the chromomagnetic operator which are demonstrated in Fig. 7.5. There are no contributions from $t$-channel type diagrams

**Figure 7.5.:** One-loop diagrams contributing to the matching with the chromomagnetic operator.

since they would violate the conservation of hypercharge. Evaluating the diagrams in Fig. 7.5 we find identically 0. Therefore, we only have to evaluate the evanescent contribution as a remnant of the basis translation. In NDR, this leads to

$$\mathcal{C}_{Qt}^{(8),R}\mathcal{R}_{Qt}^{(8)} = \underbrace{-\frac{c_F}{2N_c}\frac{Y_\Phi^2}{M_\Phi^2}\mathcal{O}_{Qt}^{(1)}}_{\mathcal{C}_{Qt}^{(1)}/\Lambda^2} + \underbrace{\frac{1}{2N_c}\frac{Y_\Phi^2}{M_\Phi^2}\mathcal{O}_{Qt}^{(8)}}_{\mathcal{C}_{Qt}^{(8)}/\Lambda^2} + \underbrace{\frac{1}{16\pi^2}\frac{Y_\Phi^2}{M_\Phi^2}\frac{g_s y_t}{4}\mathcal{O}_{tG}}_{\mathcal{C}_{tG}^{\mathrm{NDR}}/\Lambda^2} . \tag{7.53}$$

In BMHV, on the other hand, the Fierz identity is exact and we have

$$\mathcal{C}_{Qt}^{(8),R}\mathcal{R}_{Qt}^{(8)} = \underbrace{-\frac{c_F}{2N_c}\frac{Y_\Phi^2}{M_\Phi^2}\mathcal{O}_{Qt}^{(1)}}_{\mathcal{C}_{Qt}^{(1)}/\Lambda^2} + \underbrace{\frac{1}{2N_c}\frac{Y_\Phi^2}{M_\Phi^2}\mathcal{O}_{Qt}^{(8)}}_{\mathcal{C}_{Qt}^{(8)}/\Lambda^2} , \tag{7.54}$$

leading to $\mathcal{C}_{tG}^{\mathrm{BMHV}} = 0$. Identifying $c_A = N_c$, the difference of the matching coefficients exactly resemble the scheme difference obtained by the finite shifts in Eq. (7.41).

We conclude this section with the observation that the exercise of explicitly computing the one-loop matching calculation of the simplified scalar models naturally lead to the finite shifts we derived for the scheme independence of the scattering amplitude.

## 7.5. Outlook: $\gamma_5$ scheme dependent structure introduced by the $\phi^2\psi^2 D$ operator class

The main focus of this project is to investigate the $\gamma_5$ scheme differences on the example of four-top operators, since they provide the basic principles of a two-loop calculation while being structurally simple due to a convenient factorisation into one-loop integrals. However, since there are more operator classes in the SMEFT with an explicit chiral structure, we try to point out the necessity of a more exhaustive study in the following.

Therefore, we investigate the scheme dependent parameter shifts at one-loop order induced by operators in the class of $\psi^2\phi^2 D$ of Ref. [111]. Since we want to provide only a primary observation, we limit the investigation to the two representative operators

$$\mathcal{L}_{2t2\phi} = \frac{\mathcal{C}_{\phi Q}^{(1)}}{\Lambda^2}\bar{Q}_L\gamma_\mu Q_L\left(\phi^\dagger i\overleftrightarrow{D}^\mu\phi\right) + \frac{\mathcal{C}_{\phi t}}{\Lambda^2}\bar{t}_R\gamma_\mu t_R\left(\phi^\dagger i\overleftrightarrow{D}^\mu\phi\right) , \tag{7.55}$$

where we introduced the short-hand notation

$$i\overleftrightarrow{D}^\mu = iD^\mu - i\overleftarrow{D}^\mu . \tag{7.56}$$

The main feature the operators in Eq. (7.55) have in common with the 4-top operators in Eq. (7.1) is that they are composed of current-current interaction including chiral vector

currents. Those are possibly generated by integrating out a new heavy vector particle at tree-level that couples to the SM currents for which a concrete example would be given by the Third Family Hypercharge Model [236, 237].

As has been checked in Sec. 7.4.1 for the 4-top operators, the finite shifts induced by the scheme choice coincide for the broken and unbroken phase of the EW symmetry. Thus, it is sufficient to derive the scheme dependence of the parameters in the unbroken phase considering matrix elements of (quasi) on-shell states for the derivation of the finite shifts. In addition, since the scheme dependence manifests itself in the difference of rational terms of the loop integrals, i.e. the residues in $D \to 4$ dimensions that are not multiplied by Passarino-Veltman master integrals, we only retain those rational terms in the presentation of the one-loop correction.

We start by the contribution to the $y_t$ shift, as it enters the evaluation of the $\mathcal{C}_{tG}$ and $\mathcal{C}_{tH}$ scheme dependence as well. The explicit contribution of the one-loop diagrams we need to take into account is given by



$$\tag{7.57}$$

where the scheme dependence is captured by

$$\mathcal{K}_{y_t}^{2t2\phi} = \begin{cases} 0 & \text{NDR} \\ \dfrac{\lambda v^2}{32\pi^2} & \text{BMHV} \,. \end{cases} \tag{7.58}$$

In accordance with the procedure in Sec. 7.4.1, we define a compact representation for the one-loop diagrams involving an off-shell Yukawa interaction with the short-hand notation



$$\tag{7.59}$$

Hence, we write for the one-loop contributions responsible for the $\mathcal{C}_{tG}$ shifts



$$\tag{7.60}$$

where we obtain the rational terms

$$\mathcal{K}_{tG}^{2t2\phi} = \frac{g_s y_t}{32\pi^2} \times \begin{cases} 1 & \text{NDR} \\ \dfrac{2}{3} & \text{BMHV} \,. \end{cases} \tag{7.61}$$

The evaluation of one-loop contributions to $\mathcal{C}_{tH}$ will be restricted to the gaugeless limit of the SM[24] in the following. This drastically reduces the number of diagrams, but the derived result still fully entails the scheme dependence proportional to the Yukawa interaction $y_t$ and Higgs self interaction $\lambda$.

Applying the gaugeless limit to the scheme dependent one-loop correction of $\mathcal{C}_{tH}$ yields



$$= \frac{\mathcal{C}_{HQ}^{(1)} - \mathcal{C}_{Ht}}{\mathcal{C}_{tH}} \mathcal{K}_{tH}^{2t2\phi} \times$$



and we obtain the scheme dependent part

$$\mathcal{K}_{tH}^{2t2\phi} = \begin{cases} 0 & \text{NDR} \\ \dfrac{y_t \left( y_t^2 + 3\lambda \right)}{48\pi^2} & \text{BMHV} . \end{cases} \tag{7.63}$$

Since the difference of the rational terms $\Delta\mathcal{K}_i = \mathcal{K}_i^{\text{BMHV}} - \mathcal{K}_i^{\text{NDR}}$ between the schemes leads to a shift of the parameters, we can summarise the above calculations with the translation table only retaining the contributions derived in this section as

$$
\begin{aligned}
y_t^{\text{BMHV}} &= y_t^{\text{NDR}} \left( 1 - \frac{\lambda v^2}{32\pi^2} \frac{\mathcal{C}_{HQ}^{(1)} - \mathcal{C}_{Ht}}{\Lambda^2} \right) \\
\mathcal{C}_{tH}^{\text{BMHV}} &= \mathcal{C}_{tH}^{\text{NDR}} - \frac{y_t(y_t^2 + 3\lambda)}{48\pi^2} \left( \mathcal{C}_{HQ}^{(1)} - \mathcal{C}_{Ht} \right) \\
\mathcal{C}_{tG}^{\text{BMHV}} &= \mathcal{C}_{tG}^{\text{NDR}} + \frac{g_s y_t}{48\pi^2} \left( \mathcal{C}_{HQ}^{(1)} - \mathcal{C}_{Ht} \right) ,
\end{aligned}
\tag{7.64}
$$

We want to clarify again that we assumed the gaugeless limit in order to derive the shift for $\mathcal{C}_{tH}$, thus there are potential missing contributions proportional to $g_1$ and $g_2$. For the shifts in the translation of $y_t$ and $\mathcal{C}_{tG}$, however, no restrictions on the SM field content were made and they are valid in full generality of the SM fields and parameters.

In order to exemplify that the induced shifts by the $\psi^2 \phi^2 D$ operators persist in the broken phase in the same form as derived above, we explicitly validate the form of the contribution to the chromomagnetic operator in Eq. (7.60) in the broken phase for the gaugeless theory. A concrete evaluation of the one-loop correction to $g \to \bar{t}t$ then leads to



$$= \frac{\mathcal{C}_{HQ}^{(1)} - \mathcal{C}_{Ht}}{\mathcal{C}_{tG}} K_{tG}^{2t2\phi} \times \quad g \text{~} \quad + \dots \tag{7.65}$$

---

[24]In the gaugeless limit, the gauge bosons are decoupled from the theory by carefully taking the limit $g_1 \to 0$ and $g_2 \to 0$. After symmetry breaking in the Higgs sector, this leads to a theory with massless Goldstone bosons that are physical degrees of freedom.

where the gluon and top quarks are taken on-shell and the Gordon identity for on-shell fermions is applied to arrive at this result. This configuration is kinematically not allowed, however, it simplifies the extraction of the finite shift. The $(\dots)$ in Eq. (7.65) represent contributions to vector and axial form factors that are completely removed using on-shell renormalisation of the external top fields. The scheme dependent factor is found to be

$$K_{tG}^{2t2\phi} = \frac{g_s m_t}{16\sqrt{2}v\pi^2} \times \begin{cases} 1 & \text{(NDR)} \\ \frac{2}{3} & \text{(BMHV)} \,, \end{cases} \tag{7.66}$$

where the same value as in the unbroken theory Eq. (7.61) is obtained. Although the same value separately for BMHV and NDR is mere coincidence, the important property is the difference between both schemes, since the mapping of $\mathcal{C}_{tG}$ between BMHV and NDR in the presence of the operators of Eq. (7.55) can be expressed by

$$\Delta\mathcal{K}_{tG}^{2t2\phi} = \mathcal{K}_{tG}^{2t2\phi,\text{NDR}} - \mathcal{K}_{tG}^{2t2\phi,\text{BMHV}} = K_{tG}^{2t2\phi,\text{NDR}} - K_{tG}^{2t2\phi,\text{BMHV}} = \frac{g_s m_t}{48\sqrt{2}v\pi^2} \,, \tag{7.67}$$

which was done to derive Eq. (7.64).

The result of Eq. (7.64) clearly demonstrates that there is a $\gamma_5$ scheme dependent amplitude structure induced by the $\psi^2\phi^2 D$ operators that, similar to the case of the 4-top operators in Eq. (7.41), leads to a compensating scheme dependence of other parameters of the theory. We also have the same hierarchy in the shifts: as the $\psi^2\phi^2 D$ operators are potentially tree-level induced, the finite scheme dependent shift of the Wilson coefficient of the chromomagnetic operator in Eq. (7.64) responsible for the translation between schemes can be of the same order as the coefficient value in the original scheme considering a weakly coupling and renormalisable UV completion.

For the effect on the Higgs-gluon coupling, we expect similar compensations between explicit scheme dependent contributions and scheme dependent parameter shifts that has to hold for physical observables. Since $\mathcal{C}_{tG}$ is affected by the induced scheme dependence, the anomalous dimension of $\mathcal{C}_{HG}$ has to get a scheme dependent contribution of the $\psi^2\phi^2 D$ operators at two-loop, accordingly. In addition, the renormalised two-loop amplitude of $\psi^2\phi^2 D$ insertions is expected to be scheme dependent. However, in the case of $\psi^2\phi^2 D$ operators, the contribution to the amplitude does not factorise in two one-loop structures, but will lead to genuine two-loop structures. Therefore, it is not guaranteed that the scheme dependence relations obtained at one-loop level Eq. (7.64) are sufficient for a full compensation. It might well be necessary to derive scheme dependent shifts at two-loop as well. This, however, is beyond the scope of the present work.

We may conclude that a full subleading contribution to $gg \to h(h)$ consistent with the power counting of Sec. 4.3 cannot be obtained using the chromomagnetic and 4-top operators alone. Since operators of class $\psi^2\phi^2 D$ enter the gluon-fusion processes in the broken phase also as modifications of EW couplings, it is not possible to define a 'QCD'- or 'non-EW'-subleading SMEFT contribution, thus EW corrections should, in principle, be considered alongside.

# Effects of chromomagnetic and 4-top operators in $gg \to hh$

In Chapter 6 the leading EFT contributions in $hh$ production has been thoroughly discussed. In this chapter, we include the effect of the chromomagnetic and 4-top operators which comprise a part of the subleading SMEFT contribution considering a renormalisable and weakly coupling UV completion. Therefore, their contribution enters with a suppression of an extra loop factor w.r.t. the Born contribution of Sec. 6.3, according to the power counting formula of Eq. (4.12).

The evaluation of 4-top operators in $gg \to hh$ in combination with the study in single Higgs production [229] may potentially contribute to find better constraints on the $\mathcal{O}\left(\Lambda^{-2}\right)$ interference effects as compared to recent global fits [153]. Even though the four top-quark production channel is likely more sensitive through direct observation in the long term, as indicated by upper limits on the absolute values obtained from the interference contribution in Ref. [227], the derivation will be based on very low statistics [226] and just recently the observation of four top-quark production was reported [227, 228]. Hence, it is still useful to study many channels with potential sensitivity in parallel. Since the 4-top operators consist of chiral currents, the understanding of the $\gamma_5$ scheme structure derived in Chapter 7 provides essential insight on the connection between operators which we will make use throughout the chapter. In particular, the shifts for the translation between the $\gamma_5$ schemes provides a close relationship between $\mathcal{C}_{tG}$ and the Wilson coefficients of 4-top operators following the power counting of Sec. 4.3.

The chapter presents the work of Ref. [7] and proceeds as follows. In Sec. 8.1, the full set of relevant operators is summarised and subsequently the structure of the new contributions of chromomagnetic and 4-top operators is discussed. Particularly, the dependence of $\gamma_5$ scheme choice on the structure of the 4-top amplitude is highlighted with reference to the results in Chapter 7. Thereafter, in Sec. 8.2 the potential sensitivity of $gg \to hh$ on the level of total cross section and $m_{hh}$ differential distributions is investigated and the naive consideration of independent single Wilson coefficients is demonstrated. This points out the importance of being inclusive enough in the selection of Wilson coefficients for scheme independent results.

## 8.1. Amplitude structure of subleading operators

As specified in the introduction of this chapter we combine the chromomagnetic and 4-top operator contributions with the calculation of the leading SMEFT contribution of Chapter 6.

We therefore consider the Lagrangian terms in Eq. (6.14) together with Eq. (7.1) and Eq. (7.3). For convenience we list all relevant Lagrangian terms in the following

$$
\begin{aligned}
\Delta \mathcal{L}_{\mathrm{SMEFT}} = {} & \Delta \mathcal{L}_{\mathrm{SMEFT}}^{\mathrm{lead}} + \mathcal{L}_{4t} + \mathcal{L}_{tG} \\
= {} & \frac{\mathcal{C}_{H\Box}}{\Lambda^2} \left( \phi^\dagger \phi \right) \Box \left( \phi^\dagger \phi \right) + \frac{\mathcal{C}_{HD}}{\Lambda^2} \left( \phi^\dagger D_\mu \phi \right)^* \left( \phi^\dagger D^\mu \phi \right) + \frac{\mathcal{C}_H}{\Lambda^2} \left( \phi^\dagger \phi \right)^3 \\
& + \frac{\mathcal{C}_{tH}}{\Lambda^2} \left( \left( \phi^\dagger \phi \right) \left( \bar{Q}_L t_R \tilde{\phi} \right) + \mathrm{H.c.} \right) + \frac{\mathcal{C}_{HG}}{\Lambda^2} \phi^\dagger \phi \, G^a_{\mu\nu} G^{\mu\nu,a} \\
& + \frac{\mathcal{C}_{tG}}{\Lambda^2} \left( \left( \bar{Q}_L \sigma^{\mu\nu} T^a t_R \tilde{\phi} \right) G^a_{\mu\nu} + \mathrm{H.c.} \right) \\
& + \frac{\mathcal{C}_{Qt}^{(1)}}{\Lambda^2} \left( \bar{Q}_L \gamma^\mu Q_L \right) \bar{t}_R \gamma_\mu t_R + \frac{\mathcal{C}_{Qt}^{(8)}}{\Lambda^2} \left( \bar{Q}_L \gamma^\mu T^a Q_L \right) \bar{t}_R \gamma_\mu T^a t_R \\
& + \frac{\mathcal{C}_{QQ}^{(1)}}{\Lambda^2} \left( \bar{Q}_L \gamma^\mu Q_L \right) \left( \bar{Q}_L \gamma_\mu Q_L \right) + \frac{\mathcal{C}_{QQ}^{(8)}}{\Lambda^2} \left( \bar{Q}_L \gamma^\mu T^a Q_L \right) \left( \bar{Q}_L \gamma_\mu T^a Q_L \right) \\
& + \frac{\mathcal{C}_{tt}}{\Lambda^2} \bar{t}_R \gamma^\mu t_R \, \bar{t}_R \gamma_\mu t_R \, .
\end{aligned}
\tag{8.1}
$$

The first two lines after the second equality entail the part of the leading SMEFT contribution while the third line contains the chromomagnetic operator and lines 4-6 show the relevant 4-top operators.

The leading SMEFT contributions were thoroughly studied in Chapter 6, hence we focus on the subleading contributions including the chromomagnetic operator and 4-top operators. For the final combination only truncation options (a) and (b) defined in Eq. (6.21) can be associated meaningfully in the presence of the subleading operators. As the chromomagnetic and 4-top operator contribution will be considered at LO QCD, we have for the cross section

$$
\sigma_{\mathrm{EFT}} \sim \sigma_{\mathrm{EFT}}^{\mathrm{Born}} + \sigma_{\mathrm{EFT}}^{\mathrm{NLO}} \, ,
\tag{8.2}
$$

where the Born part is given by

$$
\begin{aligned}
\sigma_{\mathrm{EFT}}^{\mathrm{Born}} \sim {} & \sigma_{\mathrm{SM}} \left[ (g_s^2 L)^2 \right] + \sigma_{\mathrm{SM}\times\mathrm{dim6}}^{\mathrm{lead}} \left[ (g_s^2 L)^2 \Lambda^{-2} \right] + \sigma_{\mathrm{SM}\times\mathrm{dim6}}^{\mathcal{C}_{tG},\mathcal{C}_{4t}} \left[ (g_s^2 L)^2 \mathbf{L} \, \Lambda^{-2} \right] \\
& \left\{ + \sigma_{\mathrm{dim6}\times\mathrm{dim6}}^{\mathrm{lead}} \left[ (g_s^2 L)^2 \Lambda^{-4} \right] + \sigma_{\mathrm{dim6}\times\mathrm{dim6}}^{\mathcal{C}_{tG},\mathcal{C}_{4t}} \left[ (g_s^2 L)^2 \mathbf{L} \, \Lambda^{-4} \right] \right\} \, ,
\end{aligned}
\tag{8.3}
$$

and the NLO QCD contribution has the form

$$
\sigma_{\mathrm{EFT}}^{\mathrm{NLO}} \sim \sigma_{\mathrm{SM}} \left[ (g_s^2 L)^3 \right] + \sigma_{\mathrm{SM}\times\mathrm{dim6}}^{\mathrm{lead}} \left[ (g_s^2 L)^3 \Lambda^{-2} \right] \quad \left\{ + \sigma_{\mathrm{dim6}\times\mathrm{dim6}}^{\mathrm{lead}} \left[ (g_s^2 L)^3 \Lambda^{-4} \right] \right\} \, .
\tag{8.4}
$$

Inspired by the notation of Eq. (6.21), $\sigma_{\mathrm{SM}\times\mathrm{dim6}}^{(\ldots)}$ corresponds to the part of linear interference of dimension-6 amplitude with the SM (i.e. $\sim 2\mathrm{Re}\left(\mathcal{M}_{\mathrm{dim6}}\mathcal{M}_{\mathrm{SM}}^*\right)$), $\sigma_{\mathrm{dim6}\times\mathrm{dim6}}^{(\ldots)}$ corresponds to the part of anomalous amplitude squared (i.e. $\sim |\mathcal{M}_{\mathrm{dim6}}|^2$). Hence, the parts inside the curly brackets $\{\ldots\}$ denote the contribution entering only for truncation option (b). $\sigma_{(\ldots)}^{\mathrm{lead}}$ involves the parts where the dimension-6 contributions are given by the leading operators of Eq. (6.14) only, $\sigma_{(\ldots)}^{\mathcal{C}_{tG},\mathcal{C}_{4t}}$ contains contributions with single insertion of the chromomagnetic or 4-top operatos. The values inside the square brackets in Eqs. (8.3) and (8.4) denote the order in power counting using the formula in Eq. (4.12).

The chromomagnetic and 4-top interactions do not provide the full subleading SMEFT contribution following the power counting rule Eq. (4.12), as we neglect contributions involving EW particles in the loop. Even though they comprise the subleading contributions of the Warsaw basis involving only coloured particles in the loop, it is in general not possible to

retain a subset based on this criteria. In particular, Eq. (7.64) demonstrated that the chromomagnetic Wilson coefficient $\mathcal{C}_{tG}$ would suffer from an unresolved ambiguity due to the $\gamma_5$ scheme choice if the operators of class $\psi^2\phi^2 D$ are not considered. We refrain from including these as we would have to include EW corrections as well which is beyond the scope of this work. Full EW corrections for $gg \to hh$ in the SM have become available very recently [183], yet the calculation of EW corrections in the SMEFT scenario is much more challenging. Nevertheless, we consider the study of chromomagnetic and 4-top operators to be still useful, as their potential impact may be relevant. In addition, it provides a starting point to advocate for the importance of $\gamma_5$ scheme independence in the consideration of global fits.

In the subsequent parts, we present the structure of the amplitude involving single insertions of the chromomagnetic operator or the 4-top operators of Eq. (8.1). The diagrams were first generated with QGRAF [64] and afterwards calculated analytically with the use of FEYNCALC [60–62]. The mass of the top quark is renormalised on-shell, whereas coupling parameters and Wilson coefficients are renormalised in the $\overline{\text{MS}}$ renormalisation scheme. The analytic results of the chromomagnetic operator have been checked against a private version of GoSam [65, 66]; the unrenormalised amplitude of the 4-top operators in $D$ dimensions has been checked against ALIBRARY [74] where the reduction has been performed with KIRA [77, 78]. In addition, the analytic version of the renormalised amplitude involving 4-top operator insertions implemented in the POWHEG-BOX-V2 [202–204] has been tested numerically for several phase space points by a comparison with the amplitude obtained in ALIBRARY which has been evaluated with pySECDEC [79–82].

### 8.1.1.  The amplitude with an insertion of the chromomagnetic operator

The amplitude contribution of insertions of the chromomagnetic operator leads to classes of diagrams that are depicted in Fig. 8.1. Even though their diagrams are of one-loop order, the
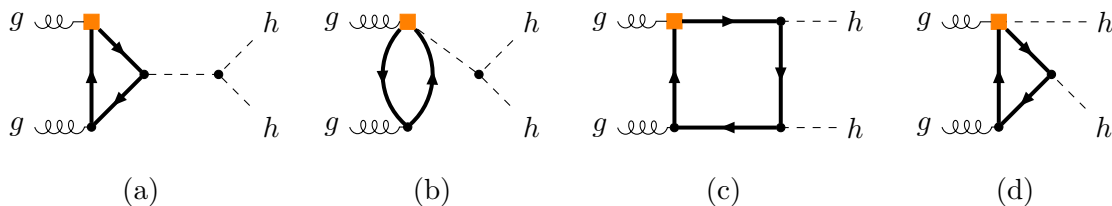


**Figure 8.1.:** Feynman diagrams involving insertions of the chromomagnetic operator. The orange squares denote insertions of the (loop-suppressed) chromomagnetic operator.

chromomagnetic operator itself can only be generated at loop level assuming a renormalisable QFT [147, 148]. Thus, following the nomenclature of the power counting formula Eq. (4.12), we find that the amplitude including $\mathcal{C}_{tG}$ contributes at the order $\mathcal{M}_{tG} \sim \mathcal{O}\left((g_s^2 L)\mathbf{L}\Lambda^{-2}\right)$. Note that this contribution is therefore suppressed by one loop factor w.r.t. the born contribution of the leading SMEFT operators, which have been investigated in Chapter 6.

As is well known [156, 231, 232] and also has been discussed in Sec. 7.3, one-loop diagrams with chromomagnetic operator insertions can lead to UV divergences that are removed by the renormalisation of $\mathcal{C}_{HG}$ in Eq. (7.26). This affects the diagram classes (a), (b) and (d) of Fig. 8.1, whereas diagram class (c) is finite.

Since the evaluation of the one-loop diagrams is straight-forward and can be performed using standard integral libraries, we refrain from showing the details of the amplitude structure here.

## 8.1.2. The amplitude with an insertion of 4-top operators

Similar to the case of the Higgs-gluon coupling of Chapter 7 the 4-top operators enter in $gg \to hh$ starting at the two-loop level. The contribution has been split into different diagram classes presented in Fig. 8.2 that follow and extend the classification in Sec. 7.3 (and Ref. [229]) for the Higgs-gluon coupling. Since 4-top operators fall in the category of operators that are
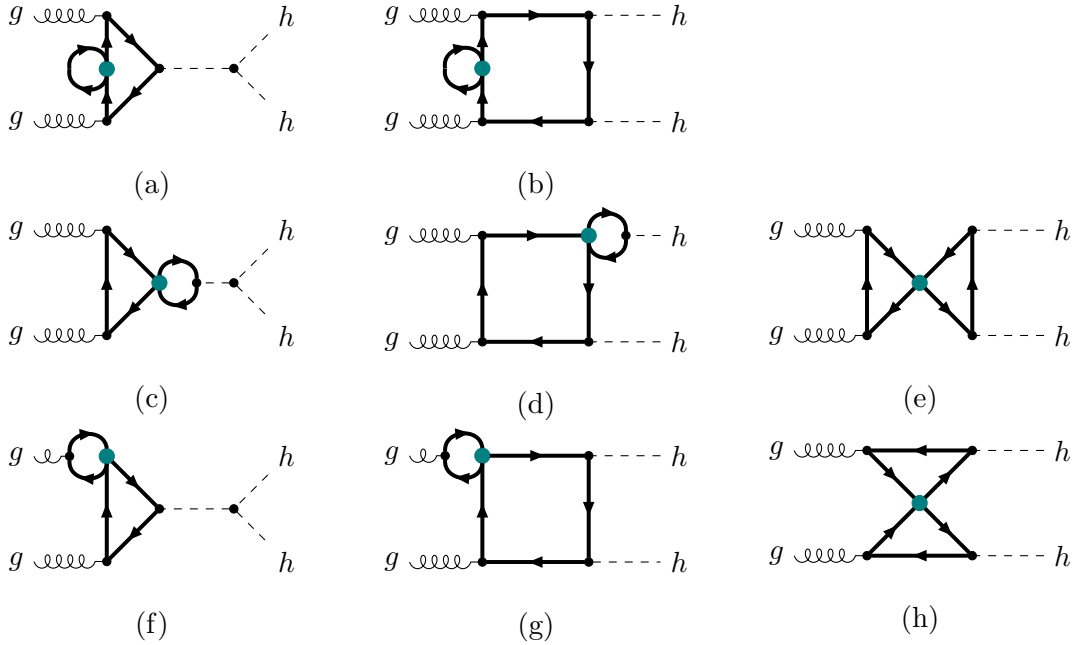


**Figure 8.2.:** Feynman diagrams involving insertions of 4-top operators. The teal dots denote insertions of 4-top operators.

potentially tree-level generated their contribution to $gg \to hh$ enters at the same order in the power counting of Eq. (4.12) as the chromomagnetic operator contribution, i.e. $\mathcal{M}_{4t} \sim \mathcal{O}\left((g_s^2 L)\mathbf{L}\Lambda^{-2}\right)$.

The diagram classes in Fig. 8.2 are grouped in rows resembling the type of one-loop sub-amplitude (propagator or vertex correction) and columns following the underlying SM born topology (triangles, boxes or no correspondence). Thus, the diagram classes are understood as follows: (a) and (b) are loop corrections to top propagators, (c) and (d) are loop corrections to the Yukawa interaction, (e) is a loop correction to the $tthh$ vertex, (f) and (g) are loop corrections to the gauge interaction (more precisely, a contraction of a one-loop subdiagram of (f) leads to the topologies of Fig. 8.1 (a) or (b)), and (h) has no clear correspondence to a vertex correction of a Born structure (but related to type (d) diagrams of Fig. 8.1 after contraction of a one-loop subdiagram). Note that the diagrams (a), (c) and (f) are completely analogous to the case of the Higgs-gluon coupling in Fig. 7.2 with the outgoing Higgs decaying into a pair of Higgs bosons.

Since many one-loop subamplitudes are very similar to the case of Sec. 7.2, we are going to refer to the details obtained in this section and point out different calculational choices if applicable.

We begin considering the propagator corrections that enter diagram classes (a) and (b) of Fig. 8.2. In contrast to what was done in Chapter 7 we choose to renormalise $m_t$ on-shell.[25] Using the expansion $m_t^b = m_t + \delta_{m_t}^{\mathrm{OS}}$ we have

$$\delta_{m_t}^{\mathrm{OS}} = -\frac{\mathcal{C}_{Qt}^{(1)} + c_F \mathcal{C}_{Qt}^{(8)}}{\Lambda^2} \left( B_{m_t} + K_{m_t} \right) , \tag{8.5}$$

where the precise form of $B_{m_t}$ and $K_{m_t}$ is given in Eqs. (7.8) and (7.9). The combination of propagator correction with mass counter term leads to

 $= 0 , \tag{8.6}$

such that the contribution of classes (a) and (b) of Fig. 8.2 to the final amplitude is completely removed.

We continue with the one-loop contribution to the Yukawa interaction. Since we use an on-shell renormalisation for $m_t$ and need the structure for an off-shell external Higgs for the amplitude class (c) of Fig. 8.2, it is more convenient to represent the vertex correction in the following way

$$h \text{---} \includegraphics{} = \left( \frac{\mathcal{C}_{Qt}^{(1)} + c_F \mathcal{C}_{Qt}^{(8)}}{\Lambda^2} \left( 2 \frac{4m_t^2 - q^2}{16\pi^2} B_0(q^2, m_t^2, m_t^2) \right. \right.$$

$$\left. \left. - \frac{v^3}{\sqrt{2}m_t} K_{tH} \frac{4m_t^2 - q^2}{4m_t^2 - m_h^2} \right) - \frac{\delta_{m_t}^{\mathrm{OS}}}{m_t} \right) \times h \text{---} \includegraphics{} , \tag{8.7}$$

where $q$ is the momentum of the Higgs, $K_{tH}$ is the $\gamma_5$ scheme dependent part given in Eq. (7.11) and $\frac{\delta_{m_t}^{\mathrm{OS}}}{m_t}$ indicates the part that is compensated by on-shell renormalisation of $m_t$. Using the counter term vertices following from Eq. (7.25), we are able to write down the amplitude contribution of diagram classes (c)–(e) of Fig. 8.2 as follows



$$= \frac{\mathcal{C}_{Qt}^{(1)} + c_F \mathcal{C}_{Qt}^{(8)}}{\Lambda^2} \mathcal{F}_{tt \to hh}^{\mathrm{4t}} \mathcal{M}_{\mathrm{LO\ SM}}^{gg \to h}$$

$$= 2 \frac{\mathcal{C}_{Qt}^{(1)} + c_F \mathcal{C}_{Qt}^{(8)}}{\Lambda^2} \mathcal{F}_{tt \to h}^{\mathrm{4t}} \mathcal{M}_{\square}^{\mathrm{LO}} , \tag{8.8}$$

---

[25] This is necessary in order to be consistent with the numerical implementation of NLO QCD corrections of the leading operators, as is explained in Chapter 6.

with

$$\mathcal{F}_{\bar{t}t \to h}^{4t} = 2 \frac{4m_t^2 - m_h^2}{16\pi^2} B_0^{\text{fin}}(m_h^2, m_t^2, m_t^2) - \frac{v^3}{\sqrt{2}m_t} K_{tH} \ ,$$

$$\mathcal{F}_{\bar{t}t \to hh}^{4t} = \frac{1}{16\pi^2 v} \left( 2 \frac{4m_t^2 s + 8m_h^2 m_t^2 - 3m_h^2 s}{\hat{s} - m_h^2} B_0^{\text{fin}}(\hat{s}, m_t^2, m_t^2) + 16m_t^2 B_0^{\text{fin}}(m_h^2, m_t^2, m_t^2) \right. \quad (8.9)$$

$$\left. + 4m_t^2 \left( 8m_t^2 - 2m_h^2 - \hat{s} \right) C_0(m_h^2, m_h^2, \hat{s}, m_t^2, m_t^2, m_t^2) \right) + \frac{3v^2}{\sqrt{2}} \frac{\hat{s}}{\hat{s} - m_h^2} K_{tH} \ ,$$

and $\mathcal{M}_{\text{LO SM}}^{gg \to h}$ denotes the LO SM amplitude of $gg \to h$ and $\mathcal{M}_{\square}^{\text{LO}}$ denotes the SM box-type contribution to the $gg \to hh$ amplitude at LO according to the splitting of Eq. (6.4).

The gauge vertex corrections are the same as for the Higgs-gluon coupling, thus, using Eq. (7.5), the $\gamma_5$ scheme dependent part $K_{tG}$ defined in Eq. (7.6) and the renormalisation of $\mathcal{C}_{HG}$ in Eq. (7.26) we immediately find



$$(8.10)$$

$\mathcal{M}_{tG}^{(a/b/c/d)}$ refer to the amplitude structures according to the contributions of the chromomagnetic operator classes in Fig. 8.1, respectively.

Lastly, we are left to describe the contributions of class (h) in Fig. 8.2. They turn out to be UV divergent, but the poles are removed by exactly the four particle counter term vertex defined by the $\delta_{\mathcal{C}_{HG}}^{\mathcal{C}_{4t}} \mathcal{C}_{4t}$ part in Eq. (7.26). Hence, we find



$$(8.11)$$

where $\mathcal{M}_{\Delta QQ,tt,(8)}^{4t}$ is a left-over amplitude structure for which we could not identify one-loop subamplitudes to decompose into. Note this is the only amplitude part where the 4-top operators of the type $(\bar{L}L)(\bar{L}L)$ and $(\bar{R}R)(\bar{R}R)$ operators enter in $gg \to hh$. In addition, the part with coefficient $T_F \frac{\mathcal{C}_{QQ}^{(8)} + \mathcal{C}_{Qt}^{(8)}}{\Lambda^2}$ is the only contribution from the contraction of 4-top operators which leads to two Dirac-traces (cf. Fig. 7.1 which demonstrates the two contraction possibilities).

The amplitude structure of the 4-top operators is now fully described and the $\gamma_5$ scheme dependent parts are explicitly highlighted by the $K$-terms defined in Sec. 7.2. Let the reader be reminded that the scheme-dependent amplitude structures in the previous formulas lead to shifts of other parameters of the theory, as is apparent from a top-down perspective, thus leading to an overall scheme-independent matrix element. In the case of 4-top operators the

shifts sufficient for $gg \rightarrow hh$ can be already fully determined at the level of the one-loop substructures which is the main result of Chapter 7 and is summarised by the translation relations in Eq. (7.33) for the case of $\overline{\text{MS}}$ scheme renormalisation of all parameters. For the on-shell renormalisation of $m_t$ these translation relations have the form

$$
\begin{aligned}
\delta_{m_t}^{\text{OS; BMHV}} &= \delta_{m_t}^{\text{OS; NDR}} - \frac{m_t^3}{8\pi^2 \Lambda^2} \left( \mathcal{C}_{Qt}^{(1)} + c_F \mathcal{C}_{Qt}^{(8)} \right) \\
\mathcal{C}_{tH}^{\text{BMHV}} &= \mathcal{C}_{tH}^{\text{NDR}} + \frac{\sqrt{2} m_t \left( 4m_t^2 - m_h^2 \right)}{16\pi^2 v^3} \left( \mathcal{C}_{Qt}^{(1)} + c_F \mathcal{C}_{Qt}^{(8)} \right) \\
\mathcal{C}_{tG}^{\text{BMHV}} &= \mathcal{C}_{tG}^{\text{NDR}} - \frac{\sqrt{2} m_t g_s}{16\pi^2 v} \left( \mathcal{C}_{Qt}^{(1)} + \left( c_F - \frac{c_A}{2} \right) \mathcal{C}_{Qt}^{(8)} \right) ,
\end{aligned}
\tag{8.12}
$$

where the scheme dependence of the $\overline{\text{MS}}$ mass in Eq. (7.33) is now shifted to the on-shell counter term $\delta_{m_t}^{\text{OS}}$.

## 8.2. Phenomenological results of chromomagnetic and 4-top operators

The contributions to the cross section of the chromomagnetic and the 4-top operators have been added as an update to the GGHH_SMEFT process files in the form of Eq. (8.4). The details about implementation and usage can be found in App. B.

In this section, we want to investigate the effect of those subleading operators on the cross section and invariant mass distributions of $gg \rightarrow hh$. The setup for the runs is equal to Sec. 6.4 apart the from the center-of-mass energy which has been changed to $\sqrt{s} = 13.6$ TeV.

In order to estimate the potential effect of the chromomagnetic and 4-top operators in $gg \rightarrow hh$ we vary single values or pairs of Wilson coefficients in the following subsections. The ranges for the variation are based on the limits of Ref. [153] derived from $\mathcal{O}\left(\Lambda^{-2}\right)$ individual bounds or $\mathcal{O}\left(\Lambda^{-2}\right)$ marginalised fits over the other Wilson coefficients, except for $\mathcal{C}_H$ which is oriented at a translation of $\kappa_\lambda$ bounds of Ref. [24]. It is important to note, however, that (besides the same flavour assumption Eq. (4.10) for the baseline scenario in Ref. [153]) the references do not apply the generic assumptions on possible UV extensions that define our power counting. Therefore, ranges based on their limits include values where the truncation at $\mathcal{O}\left(\Lambda^{-2}\right)$ and our counting of loop factors may not be valid, in particular the value of $\mathcal{C}_{tG}$ is not suppressed by a loop factor and the fairly unconstrained values for the 4-top Wilson coefficients of $\mathcal{O}\left(100 \text{ TeV}^{-2}\right)$ may be too large. However, for our first demonstration we still use those values in order to investigate the effect over a conservative parameter range.

Note that $\mathcal{C}_{tG}$ and $\mathcal{C}_{tH}$ without specification of the scheme denotes single Wilson coefficients neglecting the scheme dependence of Eq. (8.12) in the following.

### 8.2.1. Total cross sections and heat maps

In this subsection we study the changes on the total cross section based on the variation of the subleading operators. In the first part, we investigate the effect of the variation of pairs of Wilson coefficients on the total cross section in the form of heatmaps, where all contributions enter at LO QCD. Afterwards, the total cross section values for the SM and benchmark point 6 of Table 6.2 are shown together with the relative change due to a variation of a single subleading Wilson coefficient of the chromomagnetic and 4-top operators.

We begin in Fig. 8.3 with the simultaneous variation of $\mathcal{C}_{tG}$, $\mathcal{C}_{tH}$ (left) and $\mathcal{C}_{tG}$, $\mathcal{C}_H$ (right), respectively. Since all contributions are taken at LO QCD, these diagrams serve as a comparison of $\mathcal{C}_{tG}$ with the leading operators at equal footing. We note that a sizable part of the shown parameter space leads to negative total cross section values, as observable by the
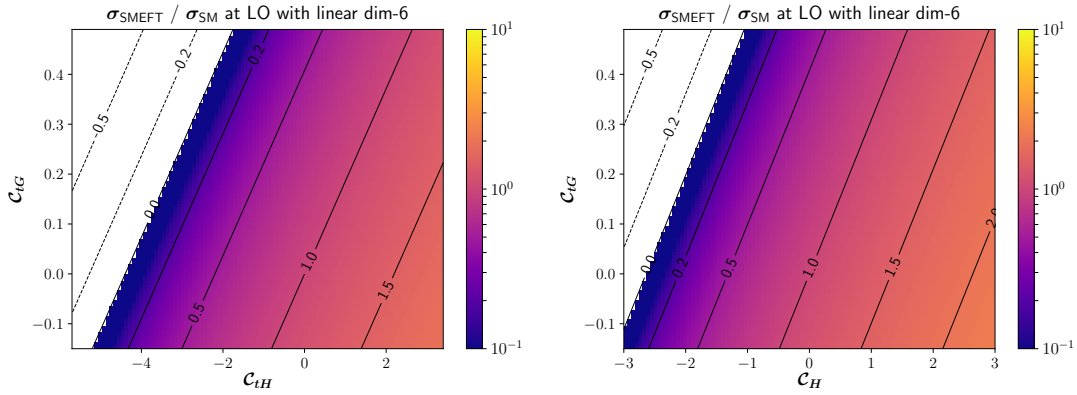
**Figure 8.3.:** Dependence of the LO cross section on the pair of Wilson coefficients $\mathcal{C}_{tG}$, $\mathcal{C}_{tH}$ (left) and $\mathcal{C}_{tG}$, $\mathcal{C}_H$ (left), respectively, with $\Lambda = 1$ TeV for the linear dimension-6 truncation. The values of the heat maps are normalised to the SM cross section. The value range of $\mathcal{C}_H$ is oriented at a translation of recent limits on $\kappa_\lambda$ [24], the ranges for the other Wilson coefficients are obtained at $\mathcal{O}\left(\Lambda^{-2}\right)$ constraints from Ref. [153] (marginalised over the other coefficients). The white areas denote regions in parameter space where the corresponding cross section would be negative.

white areas, which is clearly an unphysical configuration. Within the observed range of values for the Wilson coefficients the effect of $\mathcal{C}_{tG}$ is less dominant than $\mathcal{C}_{tH}$ and $\mathcal{C}_H$ which is the expected behaviour. However, following the power counting arguments the range of $\mathcal{C}_{tG}$ should be suppressed by a loop factor which would lead to a much weaker effect on the cross section.

In Fig. 8.4 we demonstrate the effect of pairs of 4-top Wilson coefficients on the total cross section. As is apparent from the right plot, the $(\bar{L}L)(\bar{L}L)$ operators $\mathcal{C}_{QQ}^{(8)}$ and $\mathcal{C}_{QQ}^{(1)}$ and
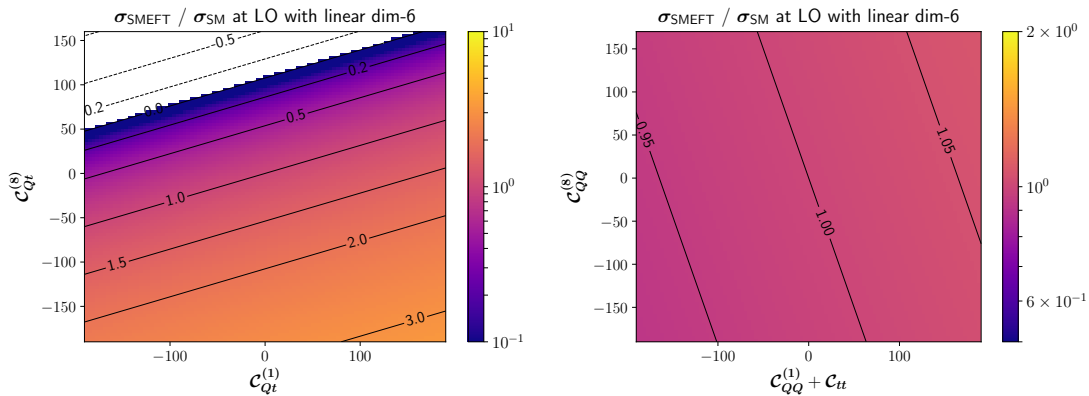


**Figure 8.4.:** Dependence of the normalised LO cross section on the couplings $\mathcal{C}_{Qt}^{(1)}$ and $\mathcal{C}_{Qt}^{(8)}$ in NDR (left) and $\mathcal{C}_{QQ}^{(1)} + \mathcal{C}_{tt}$ and $\mathcal{C}_{QQ}^{(8)}$ (right) with $\Lambda = 1$ TeV. The ranges are taken from Ref. [153] based on an $\mathcal{O}(\Lambda^{-2})$ fit marginalised over the other Wilson coefficients.

the $(\bar{R}R)(\bar{R}R)$ operator $\mathcal{C}_{tt}$ hardly contribute to the cross section. This indicates that the amplitude part in which they enter, i.e. $\mathcal{M}_{\Delta QQ, tt, (8)}^{4t}$ of Eq. (8.11), does only marginally contribute to the amplitude. Contrary to this, the $(\bar{L}L)(\bar{R}R)$ operators $\mathcal{C}_{Qt}^{(1)}$ and $\mathcal{C}_{Qt}^{(8)}$ have a sizable impact on the total cross section leading to $> 100\%$ differences w.r.t. the SM value.

The contribution of $\mathcal{C}_{Qt}^{(8)}$ is more prominent than for $\mathcal{C}_{Qt}^{(1)}$ which is related to a large cancellation between the low $m_{hh}$ and high $m_{hh}$ contributions due to a sign change of the interference of $\mathcal{C}_{Qt}^{(1)}$ with the underlying scenario. This will further be addressed in the discussion of Fig. 8.8 with the additional observation that this large cancellation does not persist if the calculation is performed in the BMHV scheme.

Fig. 8.5 compares the effect of $\mathcal{C}_{Qt}^{(1)}$ with $\mathcal{C}_{tG}$ on the total cross section, which by power counting arguments should be of equal magnitude. The heatmaps are presented for the calculation in the NDR scheme (left) and in the BMHV scheme (right), but using the same ranges for the parameter variation. Note we introduced the short-hand notation $\mathcal{C}_{Qt;\,\mathrm{BMHV}}^{(1/8)}$ to specify that the *amplitude* is calculated in the BMHV scheme, which does not mean that the value of the Wilson coefficient $\mathcal{C}_{Qt}^{(1/8)}$ itself is changed. Since the selected pair of coefficients is closely related by the $\gamma_5$ scheme choice through the relation in Eq. (8.12), this serves as an interesting showcase that demonstrates the potential difference in predictions if Eq. (8.12) is not taken into account. We observe that the gradient of the total cross section for a change
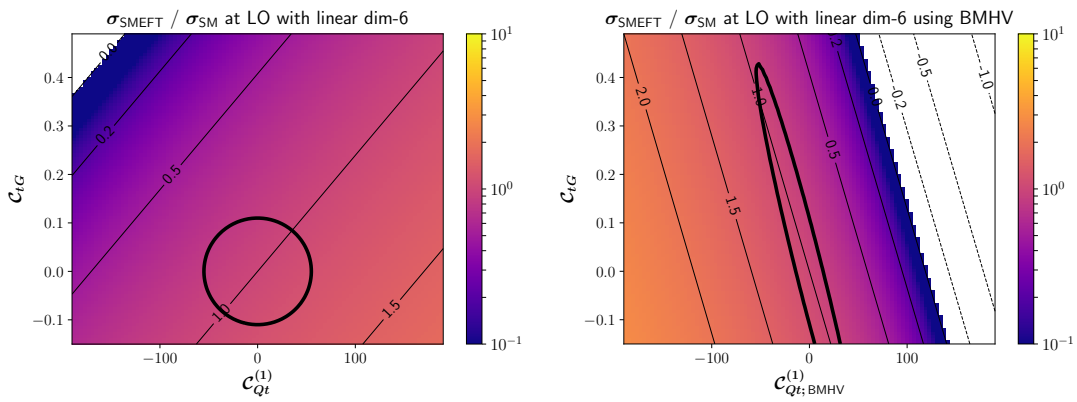


**Figure 8.5.:** Heat maps demonstrating the effect of $\gamma_5$ scheme choice on the LO cross section normalised to the SM for a variation of the couplings $\mathcal{C}_{tG}$ and $\mathcal{C}_{Qt}^{(1)}$ with $\Lambda = 1$ TeV. Left plot NDR, right plot BMHV. The ranges are taken from Ref. [153] based on an $\mathcal{O}(\Lambda^{-2})$ fit marginalised over the other Wilson coefficients. The area surrounded by the black circle (left) and the area within the ellipsis (right) demonstrate value pairs of Wilson coefficients that would be mapped into each other by using the relation for $\mathcal{C}_{tG}$ in Eq. (8.12).

of the Wilson coefficients points into a very different direction depending on the $\gamma_5$ scheme chosen for the calculation of the $\mathcal{C}_{Qt}^{(1)}$ amplitude and also the modulus of the gradient is more pronounced when calculating in BMHV scheme. The effect of the translation of $\mathcal{C}_{tG}$ in Eq. (8.12) is visualised by the areas surrounded by the black circle (left) and black ellipsis (right), respectively: The relation for the scheme translation would map coefficient value pairs $(\mathcal{C}_{Qt}^{(1)}, \mathcal{C}_{tG}^{\mathrm{NDR}})$ from within the circle onto value pairs $(\mathcal{C}_{Qt}^{(1)}, \mathcal{C}_{tG}^{\mathrm{BMHV}})$ within the ellipsis and vice versa. Note that this does not describe the full scheme translation, as the shift in $\mathcal{C}_{tH}$ of Eq. (8.12) is not considered. In addition, the shift of $\mathcal{C}_{tG}$ depends on a scale dependent coupling $g_s$ which was set to a constant, thus the areas should be only understood as an approximation for a qualitative visualisation. This clearly highlights, that the prediction using just one of the operators $\mathcal{C}_{Qt}^{(1)}$ or $\mathcal{C}_{tG}$ would suffer from significant ambiguity if they are not considered in combination, since the scheme differences can only be resolved if shifts of the form in Eq. (8.12) are considered. In principle, this also holds for other operators entering at the same order that are connected by similar relations.

Subsequently, in Table 8.1 we present values for the total cross section for the SM and benchmark point 6 of Table 6.2 using truncation (a) and (b) at NLO QCD. In addition, the relative change due to a variation of a single subleading Wilson coefficient is shown. The relative effect of the variation is larger for the SM than for benchmark 6, since the base value for the cross section is significantly larger.

The range for $\mathcal{C}_{tG}$ is very asymmetric, hence the largest possible contribution leads to a damping of the cross section of about 36% for the SM. Moreover, the relative effect on truncation (a) appears to be a bit larger than the effect on truncation (b).

For the 4-top operators, the contribution to truncation (b) is more pronounced than for truncation (a). The variation of $\mathcal{C}_{Qt}^{(1)}$ has a maximal impact of 34% on the total cross section if its contribution is evaluated in the NDR scheme, whereas in the BMHV scheme it ranges up to $\sim 100\%$. The impact of $\mathcal{C}_{Qt}^{(8)}$ is also more pronounced if calculated in the BMHV scheme compared with a calculation in NDR, however, in both cases the the scheme difference is much smaller than for $\mathcal{C}_{Qt}^{(1)}$, reaching to $\gtrsim 100\%$. The origin of the difference between $\mathcal{C}_{Qt}^{(1)}$ and $\mathcal{C}_{Qt}^{(8)}$ in the NDR scheme will be examined in the context of Fig. 8.10 for their individual contribution to $\Delta \mathcal{C}_{tG} = \mathcal{C}_{tG}^{\mathrm{BMHV}} - \mathcal{C}_{tG}^{\mathrm{NDR}}$ and $\Delta \mathcal{C}_{tH} = \mathcal{C}_{tH}^{\mathrm{BMHV}} - \mathcal{C}_{tH}^{\mathrm{NDR}}$

As has already been seen in Fig. 8.4, the variation of $\mathcal{C}_{tt}$, $\mathcal{C}_{QQ}^{(1)}$, and $\mathcal{C}_{QQ}^{(8)}$ has only marginal effect with $\leq 3.5\%$ which is only a fraction of the size of the 3-point scale uncertainty about 15-20%.

| BM | SM | 6 (a) | 6 (b) |
|---|---|---|---|
| $\sigma_{\mathrm{NLO}}[\mathrm{fb}]$ | $30.9^{+14\%}_{-13\%}$ | $56.5^{+22\%}_{-19\%}$ | $78.7^{+18\%}_{-15\%}$ |
| $\mathcal{C}_{tG}$ <br> [0.0085 , 0.14] <br> [−0.15 , 0.49] | [−0.63% −10%] <br> [+11% −36%] | [−0.34% −5.6%] <br> [+6.0% −20%] | [−0.26% −4.3%] <br> [+4.6% −15%] |
| $\mathcal{C}_{Qt}^{(1)}$ <br> [−200 , 160] <br> [−190 , 190] | [−35% +28%] <br> [−34% +34%] | [−19% +15%] <br> [−18% +18%] | [+31% −25%] <br> [+30% −30%] |
| $\mathcal{C}_{Qt;\mathrm{BMHV}}^{(1)}$ <br> [−200 , 160] <br> [−190 , 190] | [+101% −81%] <br> [+96% −96%] | [+55% −44%] <br> [+53% −53%] | [+88% −71%] <br> [+84% −84%] |
| $\mathcal{C}_{Qt}^{(8)}$ <br> [−5.6 , 20] <br> [−190 , 160] | [+3.2% −11%] <br> [+106% −89%] | [+1.7% −6.1%] <br> [+58% −49%] | [+3.1% −11%] <br> [+105% −88%] |
| $\mathcal{C}_{Qt;\mathrm{BMHV}}^{(8)}$ <br> [−5.6 , 20] <br> [−190 , 160] | [+3.8% −13%] <br> [+127% −107%] | [+2.1% −7.3%] <br> [+69% −58%] | [+3.4% −12%] <br> [+114% −96%] |
| $\mathcal{C}_{QQ}^{(1)} + \mathcal{C}_{tt}$ <br> [−6.1 , 23] <br> [−190 , 190] | [−0.11% +0.42%] <br> [−3.5% +3.5%] | [−0.061% +0.23%] <br> [−1.9% +1.9%] | [+0.094% −0.36%] <br> [+2.9% −2.9%] |
| $\mathcal{C}_{QQ}^{(8)}$ <br> [−26 , 58] <br> [−190 , 170] | [−0.16% +0.35%] <br> [−1.2% +1.0%] | [−0.087% +0.19%] <br> [−0.63% +0.57%] | [+0.13% −0.30%] <br> [+0.98% −0.87%] |

**Table 8.1.:** Total cross sections at 13.6 TeV for $gg \rightarrow hh$ at NLO QCD for the SM and benchmark point 6 with truncation option (a) or (b). Absolute values for the total cross section are presented in the second row together with scale uncertainties based on 3-point scale variations. The change due to individual variations of subleading Wilson coefficients is presented as a relative change to the base value in the second row. The ranges of the variations are oriented at $\mathcal{O}\left(\Lambda^{-2}\right)$ constraints from Ref. [153] (Upper values: individual bounds, lower values: marginalised over the other coefficients). The effect of the Wilson coefficients $\mathcal{C}_{Qt}^{(1)}$ and $\mathcal{C}_{Qt}^{(8)}$ is also demonstrated for a calculation in the BMHV scheme, which is denoted by $\mathcal{C}_{Qt;\mathrm{BMHV}}^{(1)}$ and $\mathcal{C}_{Qt;\mathrm{BMHV}}^{(8)}$.

### 8.2.2. Higgs boson pair invariant mass distributions

In this section we investigate the effect of a single subleading Wilson coefficient on the distribution of the invariant mass of the Higgs boson pair. We therefore choose the SM and benchmark point 6 with truncation (a) and (b) at NLO QCD as the baseline scenario.

In Fig. 8.6 the potential effect of the chromomagnetic operator alone within the range of $\mathcal{C}_{tG} \in [-0.15, 0.49]$ is demonstrated. As has already been observed on the level of total
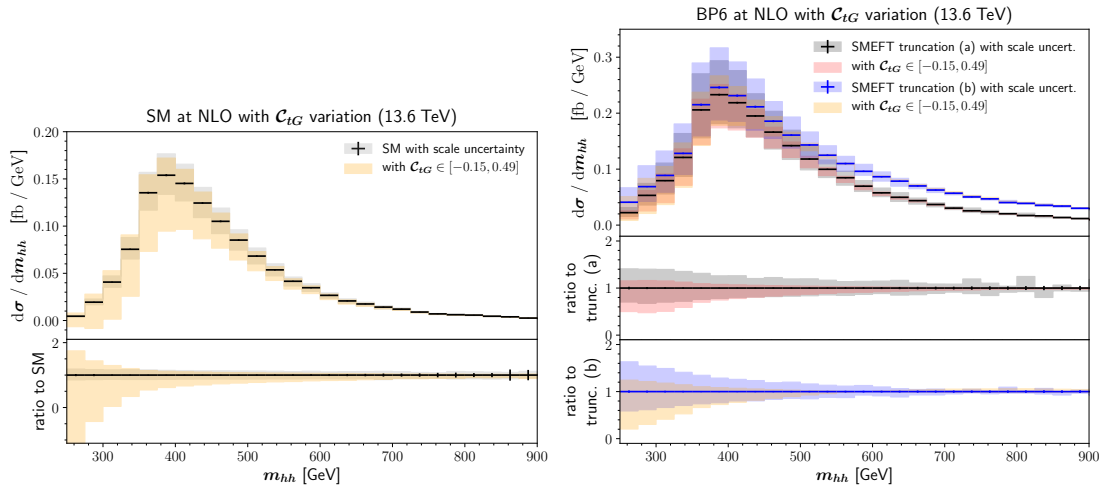


**Figure 8.6.:** Demonstration of the effect of $\mathcal{C}_{tG}$-variations on $m_{hh}$-distributions. Left: variation w.r.t. the SM scenario, right: variation w.r.t. benchmark point 6 for truncation options (a) and (b).

cross section, the asymmetric range of the chromomagnetic operator allows only for a small enhancement of the distribution but for a sizable damping which exceeds the 3-point scale uncertainty band in the low to intermediate $m_{hh}$ range.

We present in Fig. 8.7 the variation of $\mathcal{C}_{QQ}^{(1)} + \mathcal{C}_{tt}$ (left) and $\mathcal{C}_{QQ}^{(8)}$ (right), respectively. The effect on the distribution again verifies, that we cannot see a significant effect of these operators. Only in the case for the singlet operators $\mathcal{C}_{QQ}^{(1)}$ and $\mathcal{C}_{tt}$ the high $m_{hh}$ tails show a deviation beyond the uncertainty associated with the 3-point scale variation. Since the variation is done for values in $[-190, 190]$ which are beyond realistic scenarios, $gg \to hh$ is clearly not sensitive for these operators.

Subsequently, we present the effect of an individual variation of the Wilson coefficients $\mathcal{C}_{Qt}^{(1)}$ and $\mathcal{C}_{Qt}^{(8)}$ for which we expect a sizable impact. Since the structure of the amplitude involving these 4-top operators depends on the chosen $\gamma_5$ scheme, we will provide the result in both schemes.

Fig. 8.8 demonstrates the change in the distribution due to a single variation of $\mathcal{C}_{Qt}^{(1)}$. In NDR (left) we see a drastic effect in the low to intermediate $m_{hh}$ region which even leads to negative cross section values up to $m_{hh} \sim 360$ GeV. We observe a sign change in the contribution around $m_{hh} \sim 460$ GeV after which there is again a sizable effect in the large $m_{hh}$ region. In the BMHV scheme (right) there is a visible effect in the low $m_{hh}$ region for the SM which is, however, much less pronounced than in NDR. For the case of benchmark point 6 with both truncations the deviation barely exceeds the uncertainty band of the 3-point scale variation. The sign change occurs around $m_{hh} \sim 360$ GeV after which a large deviation from the underlying distribution becomes visible.
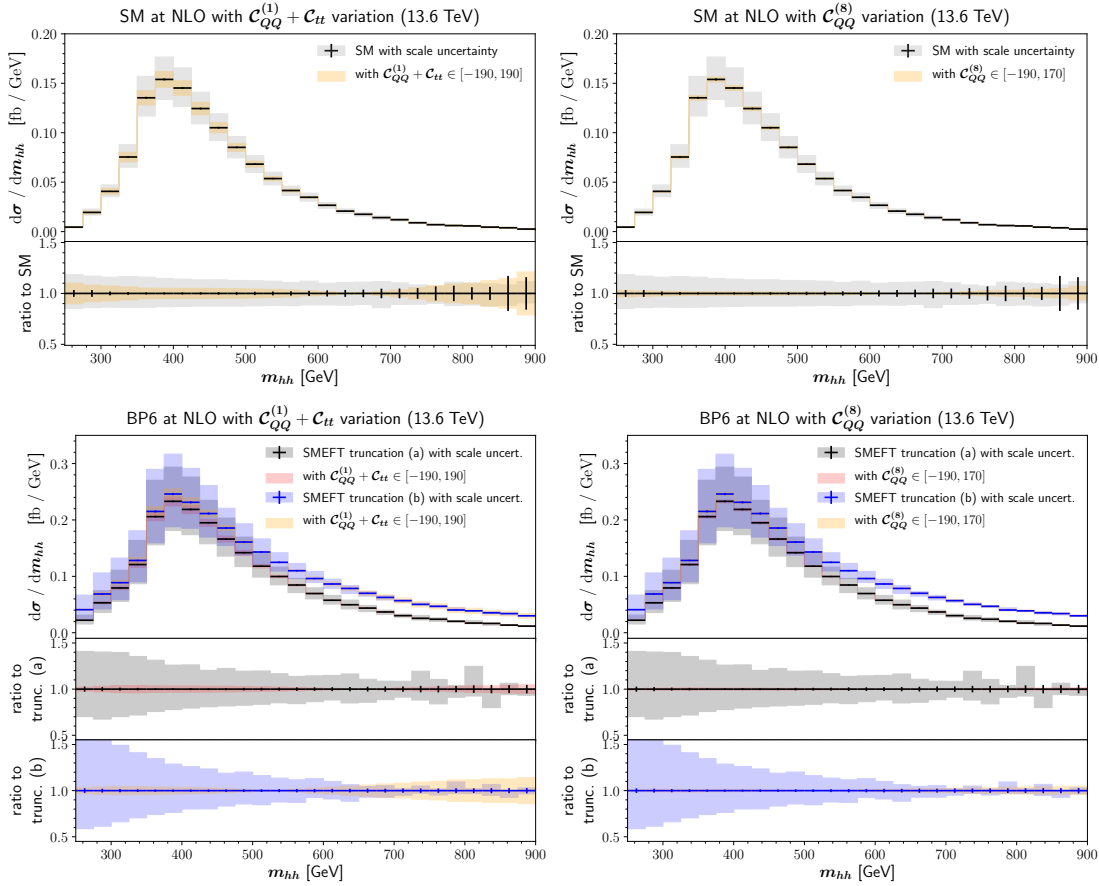
**Figure 8.7.:** Demonstration of the effect of $\mathcal{C}_{QQ}^{(1)} + \mathcal{C}_{tt}$ or $\mathcal{C}_{QQ}^{(8)}$-variations on different baseline scenarios of $m_{hh}$-distributions. Left: variation of $\mathcal{C}_{QQ}^{(1)} + \mathcal{C}_{tt}$, right: variation of $\mathcal{C}_{QQ}^{(8)}$; upper: SM baseline scenario, lower: benchmark point 6 for truncation options (a) and (b).

The dependence of the $\mathcal{C}_{Qt}^{(8)}$ contribution on the chosen $\gamma_5$ scheme is expected to be less important, as is conceived through observation on the level of total cross section in Table 8.1. This is confirmed in the distributions of Fig. 8.9. In both schemes, NDR (left) and BMHV (right), there is a sign change of the contribution around $m_{hh} \sim 360$ GeV. The effect in the low $m_{hh}$ regime is in both cases not very strong, but in the intermediate to high $m_{hh}$ regime there is a large effect. The impact on the distribution in the high $m_{hh}$ regime is a bit more pronounced for the BMHV scheme. Overall, the effect on the distribution in both schemes is qualitatively very similar to the $\mathcal{C}_{Qt}^{(1)}$ in the BMHV calculation.

It is worth investigating the origin of the large qualitative difference between $\mathcal{C}_{Qt}^{(1)}$ and $\mathcal{C}_{Qt}^{(8)}$ which only appears in the NDR and not in BMHV scheme. Therefore, we study in the following the impact of the variation of $\mathcal{C}_{Qt}^{(1)}$ and $\mathcal{C}_{Qt}^{(8)}$ separately in the scheme dependent rational parts of the amplitude structure only or, equivalently, the effect on the finite shifts $\Delta\mathcal{C}_{tG} := \mathcal{C}_{tG}^{\text{BMHV}} - \mathcal{C}_{tG}^{\text{NDR}}$ and $\Delta\mathcal{C}_{tH} := \mathcal{C}_{tH}^{\text{BMHV}} - \mathcal{C}_{tH}^{\text{NDR}}$ using the relations in Eq. (8.12) that are understood to compensate for the scheme dependence of the amplitude structure. In Fig. 8.10 we demonstrate the effect of the finite shifts on the SM distribution using the SM itself as an offset, such that only the difference of the distribution in absolute values is shown. The variation of $\mathcal{C}_{Qt}^{(1)}$ in the combined contribution of $\Delta\mathcal{C}_{tG}$ and $\Delta\mathcal{C}_{tH}$ (upper left) demonstrates a large effect on the distribution, as the yellow area is a multiple of the scale uncertainty band of the SM for the full visible range of $m_{hh}$. For the individual contributions of $\Delta\mathcal{C}_{tG}$ (middle
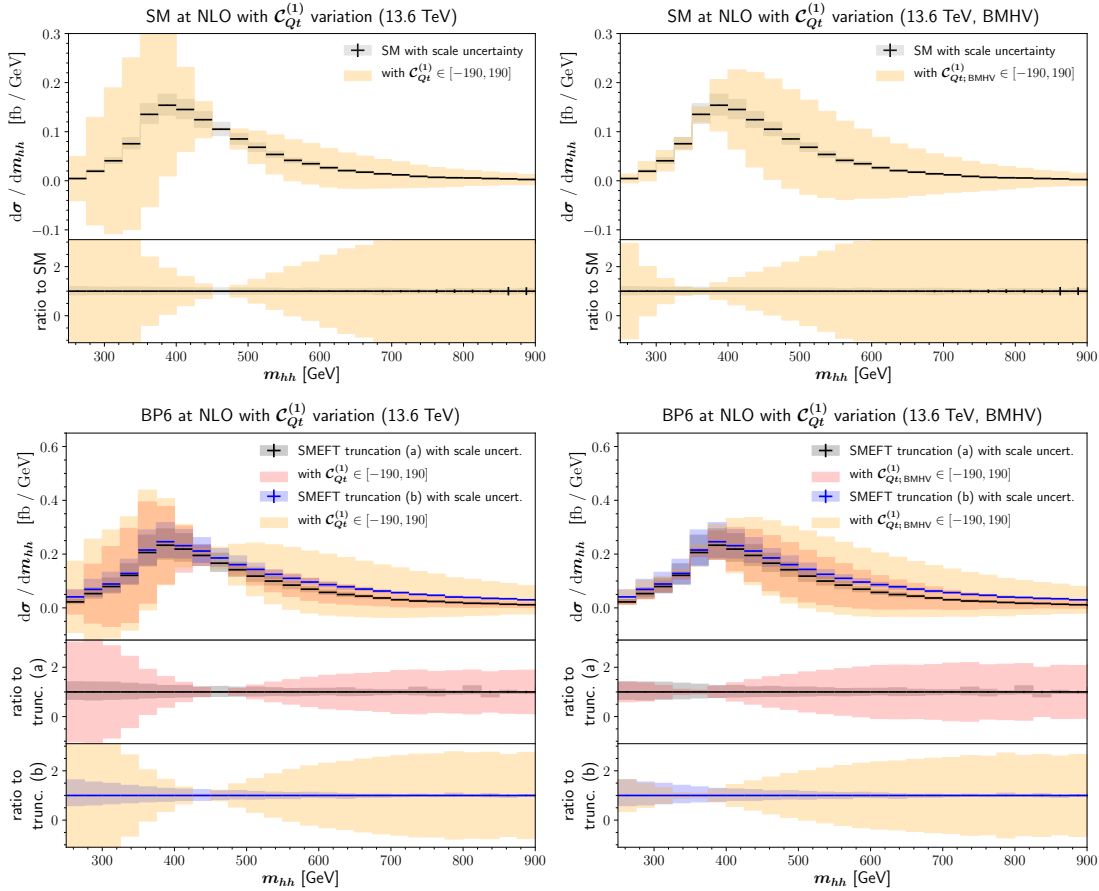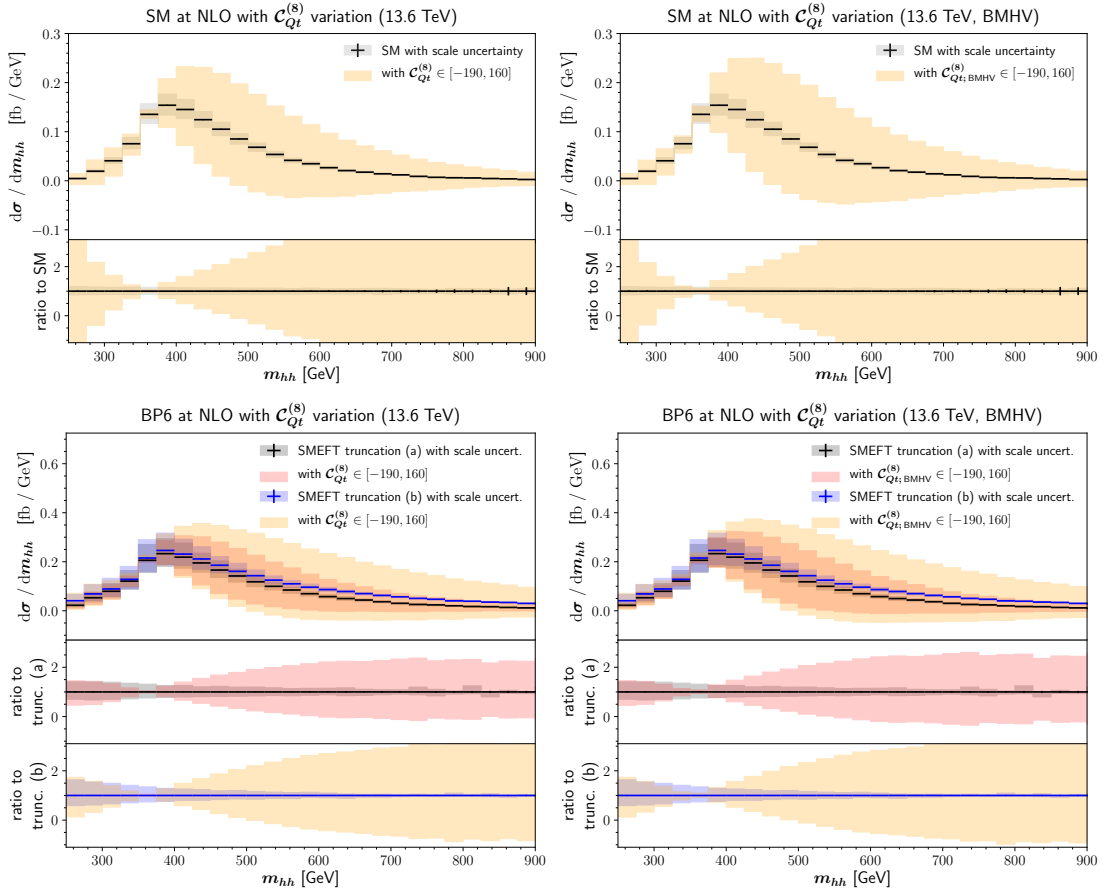
**Figure 8.8.:** Demonstration of the effect of $\mathcal{C}_{Qt}^{(1)}$-variations on different baseline scenarios of $m_{hh}$-distributions comparing $\gamma_5$ schemes. Left: NDR scheme, right: BMHV scheme; upper: SM baseline scenario, lower: benchmark point 6 for truncation options (a) and (b).

left) and $\Delta\mathcal{C}_{tH}$ (bottom left) it is clear that the effect of $\Delta\mathcal{C}_{tG}$ is more dominant than the $\Delta\mathcal{C}_{tH}$ effect. In addition, comparing the impact of $\Delta\mathcal{C}_{tG}$ (middle left) and $\Delta\mathcal{C}_{tH}$ (bottom left) separately with their combined contribution (upper left), we observe an enhancement of the individual constituents. The picture changes when considering only $\mathcal{C}_{Qt}^{(8)}$ variations. The individual contribution of $\Delta\mathcal{C}_{tH}$ (bottom right) is larger than the one of $\Delta\mathcal{C}_{tG}$ (middle right). Moreover, the combined contribution (upper right) now suffers from a cancellation between the individual parts of $\Delta\mathcal{C}_{tH}$ (bottom right) and $\Delta\mathcal{C}_{tG}$ (middle right), which is best visible in the almost vanishing contribution of the low $m_{hh}$ regime. Though also the sum of absolute areas in the low to intermediate $m_{hh}$ range of $\Delta\mathcal{C}_{tH}$ (bottom right) and $\Delta\mathcal{C}_{tG}$ (middle right) would be smaller than the envelope of combined contribution in the case of $\mathcal{C}_{Qt}^{(1)}$ (upper left).

Overall, the combined effect of the finite shifts in the presence of $\mathcal{C}_{Qt}^{(8)}$ (upper right) is hidden within the 3-point scale uncertainty approximately until $m_{hh} \sim 420$ GeV.

This different behaviour for $\mathcal{C}_{Qt}^{(1)}$ versus $\mathcal{C}_{Qt}^{(8)}$ variations can be understood when the linear combinations entering the shifts $\Delta\mathcal{C}_{tG}$ and $\Delta\mathcal{C}_{tH}$ are considered inserting explicit values for the $c_F$ and $c_A$ Casimir invariants of $SU(3)_{QCD}$. Since $\Delta\mathcal{C}_{tH} \sim \left( \mathcal{C}_{Qt}^{(1)} + \frac{4}{3}\mathcal{C}_{Qt}^{(8)} \right)$, the effect of $\mathcal{C}_{Qt}^{(1)}$ and $\mathcal{C}_{Qt}^{(8)}$ on $\Delta\mathcal{C}_{tH}$ in the bottom row of Fig. 8.10 are structurally the same up to a slight enhancement for $\mathcal{C}_{Qt}^{(8)}$ over $\mathcal{C}_{Qt}^{(1)}$. The shift in $\mathcal{C}_{tG}$, on the other hand, is proportional

**Figure 8.9.:** Demonstration of the effect of $\mathcal{C}_{Qt}^{(8)}$-variations on different baseline scenarios of $m_{hh}$-distributions comparing $\gamma_5$ schemes. Left: NDR scheme, right: BMHV scheme; upper: SM baseline scenario, lower: benchmark point 6 for truncation options (a) and (b).

to $\Delta\mathcal{C}_{tG} \sim \left(\mathcal{C}_{Qt}^{(1)} - \frac{1}{6}\mathcal{C}_{Qt}^{(8)}\right)$, thus the contribution for the $\mathcal{C}_{Qt}^{(8)}$ variation (middle right) is suppressed and with opposite sign compared to $\mathcal{C}_{Qt}^{(1)}$ (middle left). In summary, we observe an overall large effect of the $\gamma_5$ scheme choice through accumulation in the case in $\mathcal{C}_{Qt}^{(1)}$ (upper left), and relatively small effect in the low $m_{hh}$ regime through cancellation in the case of $\mathcal{C}_{Qt}^{(8)}$ (upper right).
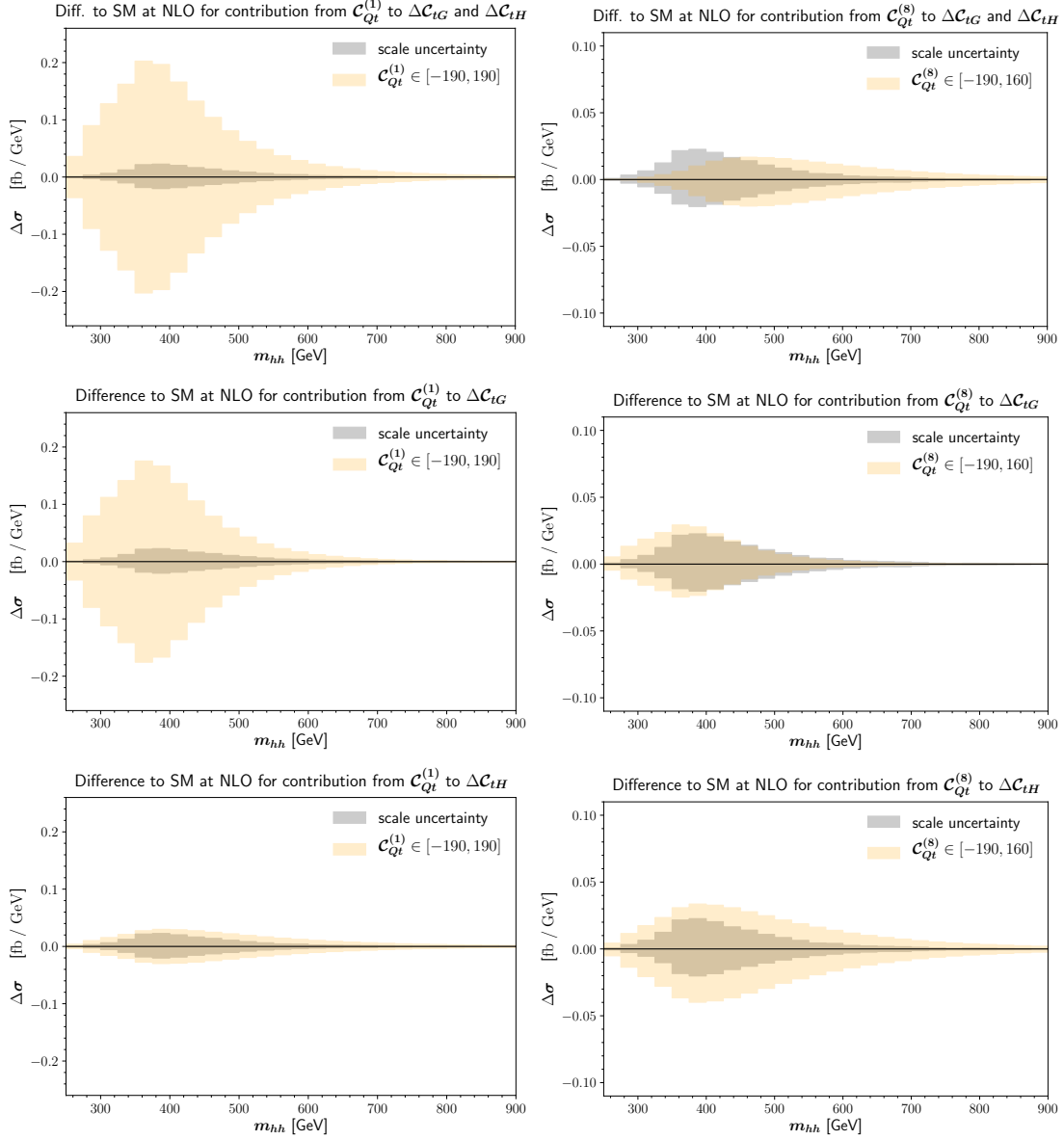
**Figure 8.10.:** Diagrams presenting the difference $\Delta\sigma = \dfrac{d\sigma}{dm_{hh}} - \dfrac{d\sigma_{\mathrm{SM}}}{dm_{hh}}$ to the $m_{hh}$-distribution of the SM only including contributions of the scheme dependent terms, $\Delta\mathcal{C}_{tG} = \mathcal{C}_{tG}^{\mathrm{BMHV}} - \mathcal{C}_{tG}^{\mathrm{NDR}}$ and $\Delta\mathcal{C}_{tH} = \mathcal{C}_{tH}^{\mathrm{BMHV}} - \mathcal{C}_{tH}^{\mathrm{NDR}}$, for individual variations of $\mathcal{C}_{Qt}^{(1)}$ and $\mathcal{C}_{Qt}^{(8)}$, respectively. Left: contribution from a $\mathcal{C}_{Qt}^{(1)}$ variation, right: contribution from a $\mathcal{C}_{Qt}^{(8)}$ variation. Upper: sum of scheme dependent terms ($\Delta\mathcal{C}_{tG}$ and $\Delta\mathcal{C}_{tH}$), middle: only $\Delta\mathcal{C}_{tG}$, lower: only $\Delta\mathcal{C}_{tH}$. SM 3-point scale uncertainty is depicted for reference.

Final Conclusion and Outlook

It is well established that the SM is not the full answer of what nature offers at the highest energies. This is certainly true when approaching the Planck scale as special relativity will not be sufficient anymore, but an extension of the SM is also expected to be relevant at intermediate energy scales. Nevertheless, up to now the SM has been proven to provide a consistent description of particle physics in the collider environment. As collider experiments at higher center-of-mass regimes will not be realised in the near future, and no prominent deviation from SM prediction has been found so far, the imprints of new physics are to be searched for in the precision domain.

Thus, precision calculations within the SM are necessary for the comparison with experiments, but also a machinery for the precise description of new physics effects is indispensable for reliable predictions. The lack of clear signals indicates an energy gap between the EW scale and new physics scale, which motivates the usage of bottom-up EFTs for a consistent and fairly universal parameterisation of low energy perturbations caused by BSM physics.

EFT techniques are widely applied nowadays, however there are still some technical difficulties which lead to potential pitfalls in a naive treatment. This is especially true considering higher order predictions where no automatised tools are available. Moreover, the selection of coupling coefficients in combined parameter determinations is usually limited, often even to single parameter studies. The interpretation of such values can become questionable, not only as new physics imprints could lead to a multitude of effects with potential cancellations or enhancements, but also due to the consistency of the EFT prediction itself. Some aspects concerning these points have been touched over the course of this thesis.

In Part I of this thesis the relevant content of the SM and the basic principles of higher order calculations have been reviewed. In addition, the two canonical bottom-up EFTs for Higgs physics, HEFT and SMEFT, were introduced and their differences in underlying assumptions and power counting determined. For the SMEFT, we also employed an implicit loop power counting in order to categorise the expected importance of contributions of Wilson coefficients according to the rather general assumption of a weakly coupling and renormalisable UV completion. This procedure is considered to be controversial in the literature, however in our view it can be useful despite not being fully general, as it allows us to focus on subsets that can be pushed to reach higher precision due to the reduction of parameters and amplitude structures.

Subsequently, in Part II recent contributions to precision calculations within EFT frameworks, mainly in the not yet precisely measured $gg \to hh$ process, were discussed.

In Chapter 6, we presented the calculation of the leading contributions of the HEFT and SMEFT framework to Higgs pair production at full NLO QCD which has been implemented in GGHH_SMEFT as part of the POWHEG-BOX-V2 framework. The effects of the two EFTs have been investigated starting from benchmark configurations in the HEFT parameter space which exhibit characteristic shapes in $m_{hh}$ distributions. In principle, HEFT and SMEFT are in some regions of parameter space mutually translatable, but HEFT generally allows for larger deviations from the SM due to the different power counting which is consistent with a potentially non-decoupling UV completion. Hence, it is advisable to study both theories in practical applications independently. The importance of that statement has been demonstrated using the benchmark points defined in HEFT, as a naive translation from perfectly valid HEFT points to SMEFT in some cases clearly lead to SMEFT configurations that are incompatible with the truncated expansion. This also extends to the interpretation of $gg \to hh$ measurements which are predominantly available in the $\kappa$- or HEFT-framework of which a translation to SMEFT should only be considered with care if at all, thus we stress the importance to perform genuine SMEFT interpretations of $gg \to hh$ as well.

In addition, we compared different truncation options for dimension-6 Wilson coefficients in the SMEFT scenario. The expansions at $\mathcal{O}\left(\Lambda^{-2}\right)$ of the cross section (option (a)) and of the amplitude (option (b)) are both common choices for fits to experimental data, whereas the other options include subsets which, despite being renormalisable in the particular case, do not comprise a consistent order of the SMEFT expansion. Differences between truncation option (a) and option (b) could provide a proxy to obtain a qualitative picture of the uncertainty due to the SMEFT truncation. Considering the Wilson coefficients as functions of the new physics scale $\Lambda$, we illustrated that the shapes of the distributions of the different truncations approach each other and the SM curve when the parameters are transported to the SM configuration. The reduction of the shape differences of the truncation options is compatible with the expected reduction of truncation uncertainty of the SMEFT expansion, however the SMEFT dimension-6 truncation options are not expected to be robust enough to derive quantitative uncertainties.

Chapter 7 was dedicated to an investigation of the structure of dimensional $\gamma_5$ schemes in $gg \to h$. We calculated the 4-top contributions appearing at the two-loop level in both the NDR and BMHV scheme which can be conveniently factorised into two one-loop structures. We demonstrated that the observed structural difference of the 4-top contribution in the two schemes has to be compensated by different values of the other parameters in order to derive consistent results. This leads to the identification of the translation of Eq. (7.33) (or equivalently Eq. (7.41)), relating the parameters of the two schemes, which was validated in the unbroken phase of EW theory and in explicit matching calculations of simplified models. Remarkably, in the case of 4-top operators the scheme dependence of the parameters could be already fully derived considering relevant one-loop subamplitudes.

Subsequently, we performed a primary investigation of the $\gamma_5$ scheme structure induced by the operator class $\psi^2\phi^2D$ of Ref. [111] using the two operators in Eq. (7.55). Following the derivation in the unbroken phase of EW theory, the calculation of one-loop subamplitudes involving insertions of the two operators lead to the translation relations in Eq. (7.64). Though, we cannot expect the relations in Eq. (7.64) to be sufficient for the full two-loop contribution to $gg \to h$, as differences of the Dirac algebra may also lead to shifts appearing at higher loop level in general.

The discussion of the two operators in the class $\psi^2\phi^2D$ leads to a generalisation of the observation of the calculation involving 4-top operators: Differences due to choices of $\gamma_5$ schemes

in the calculation of loop contributions of chiral current-current operators can be related to each other by shifts of other Wilson coefficients (and dimension-4 parameters) leading to $\gamma_5$ scheme independent results. However, we have not yet proven that chiral current-current operators are a sufficient classification of all operators inducing such a scheme dependence. This points to the necessity of a more exhaustive study to get a better understanding of the $\gamma_5$ scheme structure in SMEFT and also to have instructions to relate results based on different $\gamma_5$ schemes. We note that the $\gamma_5$ scheme choice is only one part of many calculational choices that affect interpretations in the bottom-up SMEFT framework, see for instance the discussions in Refs. [131, 133, 238].

The scheme dependent values of Wilson coefficients also bear important consequences on the selection of operators in EFT calculations and fits. As soon as the calculation is performed at an order where loop contributions of chiral current-current operators should be included, the structure of dimensional $\gamma_5$ schemes connects different Wilson coefficients. Hence, results derived only for subsets of parameters or single Wilson coefficients are scheme dependent if the selection is not sufficiently inclusive for a resolution. In particular, if a measurement of chiral current-current Wilson coefficients is based on a process where it enters at loop level, $\gamma_5$ scheme independent results require the simultaneous inclusion of Wilson coefficients entering at lower loop order. The consequences of the scheme dependence of Wilson coefficients are even more profound when the power counting based on tree-loop classification for the assumption of a weakly coupling and renormalisable UV completion is considered. In case of a clear hierarchy, e.g. by the loop factor suppression in the shift of $\mathcal{C}_{tH}$ in Eqs. (7.33) and (7.64), the shifts induced by the 4-top Wilson coefficients would only be a higher order effect. For loop generated Wilson coefficients (like $\mathcal{C}_{tG}$), however, the shifts can be of the same order of magnitude as the base value of the Wilson coefficients themselves. Therefore, the derivation of constraints for loop generated Wilson coefficients could be interpreted to suffer from large uncertainties if $\gamma_5$ scheme dependent contributions of (potentially) tree-level generated chiral current-current operators at higher explicit loop order are not considered.

If different observables are calculated in the same scheme (which is currently the case as NDR is almost exclusively used in high energy SMEFT calculations), the scheme dependent values of Wilson coefficient can, in principle, be directly compared. Hence, it may still be pragmatic to investigating single Wilson coefficients or small subsets neglecting the $\gamma_5$ dependence as primary investigations, since global fits are an immense task by themselves. Yet, the physical interpretation of such scheme dependent results would be unclear. As a consequence, we consider the requirement of $\gamma_5$ scheme independence, consistent with the systematics of the employed power counting in the EFT, to be an important component in the selection of contributions to a physical process for future research and global fits.

The above considerations also imply that once the power counting of Eq. (4.12) based on a tree-loop classification is adapted, it consequently may require the inclusion of EW corrections if loop generated Wilson coefficients of a subleading contribution are present. This can be understood by the shift of $\mathcal{C}_{tG}$ induced by $\mathcal{C}_{HQ}^{(1)}$ and $\mathcal{C}_{Ht}$ in Eq. (7.64), as diagrams with the insertion of operators of the class $\psi^2\phi^2 D$ necessarily involve EW particles.

In Chapter 8 we investigated the contributions of chromomagnetic and 4-top operators with Wilson coefficients $\mathcal{C}_{tG}$ and $\mathcal{C}_{Qt}^{(1)}$, $\mathcal{C}_{Qt}^{(8)}$, $\mathcal{C}_{QQ}^{(1)}$, $\mathcal{C}_{QQ}^{(8)}$, $\mathcal{C}_{tt}$, respectively, to $gg \to hh$ which enter at the same subleading order applying Eq. (4.12). Even though they are not a subleading contribution consistent with the above considerations of $\gamma_5$ scheme independence, the study of their potential impact to the process is nevertheless useful. The calculation of the matrix elements involving 4-top operator insertions were performed in NDR and BMHV, thus providing a showcase of the importance of differences due to $\gamma_5$ scheme choices in cross sections and distributions. The considered contributions of chromomagnetic and 4-top operators enter at

LO QCD to the cross section of $gg \to hh$ and were combined with the NLO QCD calculation of the leading contribution of SMEFT discussed in Chapter 6. The combination has entered the updated version of GGHH_SMEFT.

The effect of the selected subleading operator contributions have been studied on the total cross section and in $m_{hh}$ distributions w.r.t. the SM and benchmark point 6. The observations clearly showed that the coefficients $\mathcal{C}_{QQ}^{(1)}, \mathcal{C}_{QQ}^{(8)}, \mathcal{C}_{tt}$ lead only to a negligible contribution, hence the channel $gg \to hh$ cannot contribute to a derivation of better constraints on these values. Using current conservative limits provided in the literature, the variation of $\mathcal{C}_{tG}$ leads to noticeable effects on the cross section which is mainly visible as a damping of the distribution in the low $m_{hh}$ region. Yet, the largest impact is found by the Wilson coefficients $\mathcal{C}_{Qt}^{(1)}$ and $\mathcal{C}_{Qt}^{(8)}$ using the marginalised fits including only the $\mathcal{O}\left(\Lambda^{-2}\right)$ interference with the SM in the cross section which are up to now not well constrained. Therefore, Higgs data of $gg \to hh$ and single Higgs together with GGHH_SMEFT and the investigation of Ref. [229], respectively, can potentially improve future global fits by disentangling redundancies present in the current selection of channels.

Moreover, we highlighted the effect of the $\gamma_5$ scheme choice treating $\mathcal{C}_{Qt}^{(1)}$ and $\mathcal{C}_{Qt}^{(8)}$ independently on the total cross section and distributions. It turned out that especially the contribution of $\mathcal{C}_{Qt}^{(1)}$ is vastly different comparing the calculation of NDR and BMHV which is mainly related to the close connection with $\mathcal{C}_{tG}$ induced by Eq. (8.12). The effect is not as prominent for the octet coefficient $\mathcal{C}_{Qt}^{(8)}$, as the colour combination of the shift is suppressed for that case using the generators of $SU(3)$. These observations demonstrate the relevance of combined fits in order to derive results that are $\gamma_5$ scheme independent considering the translation relations of the form of Eq. (8.12). This has been best visualised by the shape distortion of the combined variation in $\mathcal{C}_{tG}, \mathcal{C}_{Qt}^{(1)}$ of Fig. 8.5 which in the extension to a power counting consistent multi-parameter case could be disentangled by a complete translation relation.

Finally, we outline several potential directions for future research building on the presented work.

The inclusion of subsets of dimension-8 operator contributions in the SMEFT calculation of $gg \to hh$ could lead to a better understanding of the uncertainty estimation due to the SMEFT truncation. This would be also more in line with the SMEFT expansion of observables than comparing different truncation options as in Chapter 6.

For the $\gamma_5$ scheme structure in SMEFT there are many interesting directions that could be pursued. As was mentioned beforehand, an exhaustive list at one-loop order considering all parameters in the Warsaw basis between NDR and BMHV is yet to be derived. The investigation of these scheme dependent structures could be also extended to higher orders in the loops as well as in canonical dimension. Moreover, it would be fascinating to relate the previous results in NDR and BMHV to similar calculations in different regularisation schemes that potentially avoid the introduction of $D$-dimensional spacetime, see e.g. Ref. [34]. This might potentially lead to the observation of a general criterion of chiral EFTs which hints to parameter sectors that are connected through $\gamma_5$ scheme dependent parameter shifts appearing at loop order.

After EW corrections for di-Higgs production in the SM have been obtained recently, their generalisation to the SMEFT case would be valuable for the reduction of the uncertainty related to missing EW corrections and for the completion of the subleading SMEFT contributions consistent with Eq. (4.12). Moreover, it would be interesting to compare the importance of the missing EW effects and operators with the subleading contribution of Chapter 8. In addition, a study including NLO QCD corrections in the subleading contributions of Chapter 8

would also be interesting in order to compare on an equal footing with the leading SMEFT contributions.

The projects on $hh$ production in this thesis only consider fixed order calculations. Since recent results [160, 239] suggest that the RGE evolution of Wilson coefficients lead to important effects in interpretations of LHC data, the inclusion of the parameter running in $gg \rightarrow hh$ would be a relevant future step in order to be compatible with different scale choices applied to other observables.

Feynman rules

In this appendix we summarize all relevant Feynman rules used in the thesis. We begin with the vertices in the broken phase of EW theory for unitary gauge and then briefly describe how the calculations in the unbroken phase are performed.

## A.1. Propagator and vertex rules in the broken phase

In the broken phase of EW theory, the relevant propagators are given by

$$
\begin{aligned}
t \xrightarrow{\quad p \quad} t &= \frac{i}{\not{p} - m_t} \, , \\
g^a_\mu \xrightarrow{\quad p \quad} g^b_\nu &= \frac{-i}{p^2} \left( \eta^{\mu\nu} - (1-\xi) \frac{p^\mu p^\nu}{p^2} \right) \delta^{ab} \, , \\
h \xrightarrow{\quad p \quad} h &= \frac{i}{p^2 - m_h^2} \, ,
\end{aligned}
\tag{A.1}
$$

and the relevant vertices of the SM have the form

$$
g^a_\mu \overset{t}{\underset{t}{\big\langle}} = ig_s T^a \gamma_\mu \, , \qquad h \overset{t}{\underset{t}{\big\langle}} = -i\frac{m_t}{v} \, ,
$$

$$
h \overset{h}{\underset{h}{\big\langle}} = -i\frac{3m_h^2}{v} \, .
\tag{A.2}
$$

The HEFT vertices of the Lagrangian terms in Eq. (6.5) are given by

$$
\begin{aligned}
h \cdots t t &= -ic_{tth}\frac{m_t}{v} \ , 
& h, t; h, t &= -2ic_{tthh}\frac{m_t}{v} \ ,
\end{aligned}
$$

$$
h \cdots h\,h = -ic_{hhh}\frac{3m_h^2}{v} \ ,
$$

(A.3)

$$
g^a_\mu\, p_1,\ g^b_\nu\, p_2 \cdots h = -ic_{ggh}\frac{\alpha_s}{2\pi v}p_1\cdot p_2\left(\eta^{\mu\nu}-\frac{p_2^\mu p_1^\nu}{p_1\cdot p_2}\right)\delta^{ab} \ ,
$$

$$
g^a_\mu\, p_1\, h,\ g^b_\nu\, p_2\, h = -ic_{gghh}\frac{\alpha_s}{\pi}p_1\cdot p_2\left(\eta^{\mu\nu}-\frac{p_2^\mu p_1^\nu}{p_1\cdot p_2}\right)\delta^{ab} \ .
$$

The SMEFT vertices of the leading contribution covered in Chapter 6 are obtained applying the translation Table 6.1 to the respective HEFT vertices. The SMEFT vertex rules for the chromomagnetic operator (Eq. (7.3)) are given by

$$
g^a_\mu\, p\, t\, t = -\sqrt{2}v T^a \mathcal{C}_{tG}\sigma^{\mu\nu}p_\nu \ ,
$$

(A.4)

$$
g^a_\mu\, p\, t\, h\, t = -\sqrt{2}T^a \mathcal{C}_{tG}\sigma^{\mu\nu}p_\nu \ .
$$

The 4-top vertex rule is provided with additional information for the combined spinor and colour indices $i_1$, $i_2$, $i_3$, $i_4$ of the interacting top-quarks according to
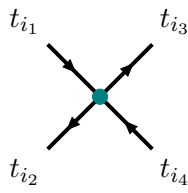
$$
\begin{aligned}
&2i\,\mathcal{C}_{QQ}^{(1)}\left[(\mathbb{P}_R\gamma^\mu\mathbb{P}_L)_{i_2i_1}(\mathbb{P}_R\gamma_\mu\mathbb{P}_L)_{i_3i_4} - (\mathbb{P}_R\gamma^\mu\mathbb{P}_L)_{i_2i_4}(\mathbb{P}_R\gamma_\mu\mathbb{P}_L)_{i_3i_1}\right]\\
&+2i\,\mathcal{C}_{tt}\left[(\mathbb{P}_L\gamma^\mu\mathbb{P}_R)_{i_2i_1}(\mathbb{P}_L\gamma_\mu\mathbb{P}_R)_{i_3i_4} - (\mathbb{P}_L\gamma^\mu\mathbb{P}_R)_{i_2i_4}(\mathbb{P}_L\gamma_\mu\mathbb{P}_R)_{i_3i_1}\right]\\
&+i\,\mathcal{C}_{Qt}^{(1)}\left[(\mathbb{P}_R\gamma^\mu\mathbb{P}_L)_{i_2i_1}(\mathbb{P}_L\gamma_\mu\mathbb{P}_R)_{i_3i_4} + (\mathbb{P}_L\gamma^\mu\mathbb{P}_R)_{i_2i_1}(\mathbb{P}_R\gamma_\mu\mathbb{P}_L)_{i_3i_4}\right.\\
&\qquad\quad\left. - (\mathbb{P}_R\gamma^\mu\mathbb{P}_L)_{i_2i_4}(\mathbb{P}_L\gamma_\mu\mathbb{P}_R)_{i_3i_1} - (\mathbb{P}_L\gamma^\mu\mathbb{P}_R)_{i_2i_4}(\mathbb{P}_R\gamma_\mu\mathbb{P}_L)_{i_3i_1}\right]\\
&+2i\,\mathcal{C}_{QQ}^{(8)}\left[(\mathbb{P}_R\gamma^\mu\mathbb{P}_L\,T^a)_{i_2i_1}(\mathbb{P}_R\gamma_\mu\mathbb{P}_L\,T^a)_{i_3i_4}\right.\\
&\qquad\quad\left. - (\mathbb{P}_R\gamma^\mu\mathbb{P}_L\,T^a)_{i_2i_4}(\mathbb{P}_R\gamma_\mu\mathbb{P}_L\,T^a)_{i_3i_1}\right]\\
&+i\,\mathcal{C}_{Qt}^{(8)}\left[(\mathbb{P}_R\gamma^\mu\mathbb{P}_L\,T^a)_{i_2i_1}(\mathbb{P}_L\gamma_\mu\mathbb{P}_R\,T^a)_{i_3i_4}\right.\\
&\qquad\quad + (\mathbb{P}_L\gamma^\mu\mathbb{P}_R\,T^a)_{i_2i_1}(\mathbb{P}_R\gamma_\mu\mathbb{P}_L\,T^a)_{i_3i_4}\\
&\qquad\quad - (\mathbb{P}_R\gamma^\mu\mathbb{P}_L\,T^a)_{i_2i_4}(\mathbb{P}_L\gamma_\mu\mathbb{P}_R\,T^a)_{i_3i_1}\\
&\qquad\quad\left. - (\mathbb{P}_L\gamma^\mu\mathbb{P}_R\,T^a)_{i_2i_4}(\mathbb{P}_R\gamma_\mu\mathbb{P}_L\,T^a)_{i_3i_1}\right]\ .
\end{aligned}
\tag{A.5}
$$

The calculation of Eq. (7.65) in the gaugeless limit is incompatible with unitary gauge, as it requires the presence of physical Goldstone bosons. The additional propagator rule is given by
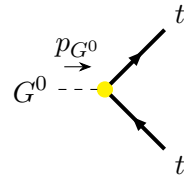
$$
G^0 \overset{p}{\dashrightarrow} G^0 \;=\; \frac{i}{p^2}\ ,
\tag{A.6}
$$

the vertex rule for the SM is given by
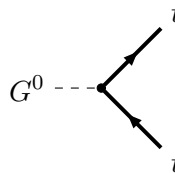
$$
G^0 \dashrightarrow\!\!\big\langle{}^t_t \;=\; -i\frac{m_t}{v}\ ,
\tag{A.7}
$$

and the relevant rule for the terms in Eq. (7.55) has the form

$$
G^0 \overset{p_{G^0}}{\dashrightarrow}\!\!\big\langle{}^t_t \;=\; -v\,\mathcal{C}_{HQ}^{(1)}\mathbb{P}_R\,\slashed{p}_{G^0}\mathbb{P}_L - v\,\mathcal{C}_{Ht}\mathbb{P}_L\,\slashed{p}_{G^0}\mathbb{P}_R\ .
\tag{A.8}
$$

## A.2. Propagator and vertex rules in the unbroken phase

Despite the depiction of the diagrams in terms of iso-doublet $Q_L$, iso-singlet $t_R$ and Higgs doublet $\phi$ we evaluate the contributions componentwise which leads to equivalent results for the derivation of the scheme-dependent shifts. We therefore quantise for massless top quarks in the Dirac representation, expand the Higgs doublet as

$$
\phi = \begin{pmatrix} \phi^+ \\ \dfrac{\phi^s + i\phi^0}{\sqrt{2}} \end{pmatrix}\ ,
\tag{A.9}
$$

and always calculate the diagrams for an external real scalar component $\phi^s$. In the following we present the Feynman rules which are different to their counter part in the broken phase.

The Feynman rules for the propagators are therefore

$$
\begin{aligned}
t \xrightarrow{\quad p \quad} t &= \frac{i}{\not{p}} \,, \\
\phi^i \text{ - - -} \xrightarrow{\quad p \quad} \text{- - - } \phi^i &= \frac{i}{p^2 - m_\phi^2} \,,
\end{aligned} \tag{A.10}
$$

where $m_\phi^2 = -\lambda v^2$ is the effective 'mass' of the Higgs doublet. The relevant vertex rules dictated by the SM Lagrangian are



$$
\tag{A.11}
$$

Finally, the relevant new SMEFT vertices for $\mathcal{C}_{tH}$ in Eq. (6.14) and the terms in Eqs. (7.3) and (7.55) are



$$
\tag{A.12}
$$

To exemplify the evaluation of Feynman diagrams in the unbroken phase, we consider the calculation of $\mathcal{K}_{y_t}^{2t2\phi}$ which enters in Eq. (7.57). Instead of the shown Feynman diagrams we equivalently calculate



$$
\tag{A.13}
$$

for massless top quarks in order to derive the value of $\mathcal{K}_{y_t}^{2t2\phi}$.

Implementation of ggHH_SMEFT

The code GGHH_SMEFT is implemented in the Monte Carlo event generator framework of the POWHEG-BOX-V2 [202–204]. The process files are mainly build upon the code GGHH [163, 199, 200] for calculations of $gg \to hh$ at NLO QCD in the HEFT which in turn relies on previous results of calculations in the SM [164, 165] for the two-loop virtual contributions. The anomalous couplings in GGHH_SMEFT are included in a modular way allowing to choose between the inherited NLO QCD HEFT calculation or NLO QCD of the leading SMEFT contribution with additional possibility to combine with insertions of the chromomagnetic and 4-top operators at LO QCD which constitute parts of the subleading SMEFT contributions according to Sec. 4.3. The SMEFT routines also allow the user to choose between different truncation options defined in Eq. (6.21).

In the following, we describe some details about the implementation. We first briefly recall the main principle of the POWHEG-BOX-V2 framework. Afterwards, the process dependent ingredients of the Born, virtual and real radiation contribution are discussed with particular focus on details that have been omitted in the main body of the thesis. Subsequently, instructions for the usage of the code are given collecting the descriptions in Refs. [5, 7].

## B.1. Basic principles of the POWHEG-BOX-V2

The POWHEG-BOX-V2 provides a general framework to combine NLO calculations with shower Monte Carlo programs which is based on the POWHEG method described in Refs. [202, 203, 240]. The core principle of POWHEG (which is short-hand for **PO**sitive **W**eight **H**ardest **E**mission **G**enerator) is to generate events for the hardest emission first (i.e. with largest transverse momentum) which can be described at NLO by the formula [240]

$$d\sigma = \bar{\mathcal{B}}(\Phi_n)\mathrm{d}\Phi_n \left[\Delta(p_T^{\min}) + \Delta(p_T)\frac{\mathcal{R}^S(\Phi_{n+1})}{\mathcal{B}(\Phi_n)}\mathrm{d}\Phi_r\right] + \mathcal{R}^F(\Phi_{n+1})\mathrm{d}\Phi_{n+1} \ , \qquad (\mathrm{B.1})$$

with the underlying Born configuration

$$\bar{\mathcal{B}}(\Phi_n) = \mathcal{B}(\Phi_n) + \mathcal{V}_{\mathrm{fin}}(\Phi_n) + \int \mathcal{R}_{\mathrm{fin}}^S(\Phi_{n+1})\mathrm{d}\Phi_r \ . \qquad (\mathrm{B.2})$$

In the above formulas, $\mathcal{B}$ denotes the Born squared matrix element with corresponding Born phase space $\Phi_n$. The real radiation contribution $\mathcal{R}$ can be split into singular part $\mathcal{R}^S$ and finite part $\mathcal{R}^F$ in the framework of the POWHEG-BOX-V2 using an implemented distribution $F(p_T)$ which can be written as $\mathcal{R}^S = F(p_T)\mathcal{R}$ and $\mathcal{R}^F = (1 - F(p_T))\,\mathcal{R}$ with default setting $\mathcal{R}^S = \mathcal{R}$. $\Phi_{n+1} = \Phi_n\Phi_r$ is the combination of Born phase space and radiation phase space $\Phi_r$. $\mathcal{V}_{\text{fin}}$ denotes the UV renormalised and IR subtracted virtual contribution and $\mathcal{R}^S_{\text{fin}}$ the IR subtracted singular part of the real radiation. The lower cutoff value $p_T^{\min}$ describes the generation of events without radiation when the threshold value is not reached. Finally, $\Delta(x)$ denotes the POWHEG Sudakov form factor for transverse momentum ordering

$$\Delta(x) = \exp\left[-\int \mathrm{d}\Phi_r\, \frac{\mathcal{R}^S(\Phi_{n+1})}{\mathcal{B}(\Phi_n)}\Theta\left(p_T(\Phi_r) - x\right)\right] \ . \tag{B.3}$$

Events that are generated according to Eq. (B.1) can subsequently be fed to shower Monte Carlo generators under the requirement that subsequent showering happens for transverse momenta which are below the $p_T$ of the event. This can be achieved setting the starting scale of momentum ordered showers or by defining vetoing procedures in showers with other ordering principles. The combination of events generated by the POWHEG-BOX-V2 with shower Monte Carlo generators is facilitated by the interface of Les Houches event files.

For the application of the POWHEG-BOX-V2 framework to specific processes, some process dependent files need to be provided. These comprise, in particular, routines for a parameterisation of the Born phase space and the squared matrix elements for the Born, virtual and real radiation contribution.

## B.2. Infos about the ggHH_SMEFT process files

In this section we discuss the process files of GGHH_SMEFT, beginning with a brief description for the Born and real radiation contribution, then followed by a detailed account on the modification of the virtual contribution necessary to comply with the SMEFT truncations and subsequently the handling of the subleading chromomagnetic and 4-top contributions at LO QCD.

The Born matrix elements are implemented analytically building on the original calculation of Ref. [162] in terms of Passarino-Veltman integrals. The addition of anomalous couplings and tree level diagrams involving Higgs-gluon couplings together with the splitting of the amplitude of the form in Eq. (6.17) is straight forward.

The $2 \to 3$ matrix elements at one-loop and tree level for the real emission part have been generated using a modified version of GoSam [65, 66] that splits the amplitude according to Eq. (6.17) together with a model file in the UFO [207, 208] format which specifies the relevant anomalous couplings. The GoSam routines are called by the existing interface [209] to the POWHEG-BOX-V2 which has been adjusted to allow the setting of the truncation options.

The evaluation of the virtual contribution in terms of a grid interpolation and the necessary modifications for SMEFT deserve a dedicated subsection in the following.

### B.2.1. Grids for the virtual contribution in the SMEFT scenario

As was described in Sec. 6.2 and Sec. 6.3, the evaluation of the virtual contribution mainly relies on the combination of 23 pre-sampled grids generated for different HEFT couplings with subsequent interpolation. Both steps are performed using the same PYTHON script `creategrids.py`. In the current version of GGHH_SMEFT the combination of the grids

depending on the settings for coupling values and truncation option is performed before calling the compiled program. Details about the interpolation can be found in Ref. [199].

In the following, we assume the 23 grids are already rotated to the form of Eq. (6.12) and describe the adjustment of Eq. (6.12) for SMEFT in the different truncation options defined by Eq. (6.21). In particular, we derive the necessary shift for truncation (b) which was introduced in Eq. (6.22) as $\delta_\mathcal{V}^{(b)}$. For convenience, we recall Eq. (6.12):

$$
\begin{aligned}
\mathcal{V}_{\text{fin}}^{\text{HEFT}} =\ & a_1 \cdot c_{tth}^4 + a_2 \cdot c_{tthh}^2 + a_3 \cdot c_{tth}^2 c_{hhh}^2 + a_4 \cdot c_{ggh}^2 c_{hhh}^2 + a_5 \cdot c_{gghh}^2 + a_6 \cdot c_{tthh} c_{tth}^2 \\
& + a_7 \cdot c_{tth}^3 c_{hhh} + a_8 \cdot c_{tthh} c_{tth} c_{hhh} + a_9 \cdot c_{tthh} c_{ggh} c_{hhh} + a_{10} \cdot c_{tthh} c_{gghh} \\
& + a_{11} \cdot c_{tth}^2 c_{ggh} c_{hhh} + a_{12} \cdot c_{tth}^2 c_{gghh} + a_{13} \cdot c_{tth} c_{hhh}^2 c_{ggh} + a_{14} \cdot c_{tth} c_{hhh} c_{gghh} \\
& + a_{15} \cdot c_{ggh} c_{hhh} c_{gghh} + a_{16} \cdot c_{tth}^3 c_{ggh} + a_{17} \cdot c_{tth} c_{tthh} c_{ggh} + a_{18} \cdot c_{tth} c_{ggh}^2 c_{hhh} \\
& + a_{19} \cdot c_{tth} c_{ggh} c_{gghh} + a_{20} \cdot c_{tth}^2 c_{ggh}^2 + a_{21} \cdot c_{tthh} c_{ggh}^2 \\
& + a_{22} \cdot c_{ggh}^3 c_{hhh} + a_{23} \cdot c_{ggh}^2 c_{gghh} \ .
\end{aligned}
\tag{B.4}
$$

The relevant combinations for truncation options (a), (c) and (d) can be easily obtained applying the coupling translation of Table 6.1 with subsequent truncation at $\mathcal{O}\left(\Lambda^{-2}\right)$, $\mathcal{O}\left(\Lambda^{-4}\right)$ or no truncation, respectively. In case of truncation option (b), the need for additional terms can be best understood considering the combinatorics of a decomposition of the matrix elements in terms of HEFT couplings, as the truncation is defined on the level of the matrix element. We therefore split the LO and NLO matrix elements similar to Eq. (6.12) into polynomials of the HEFT couplings with kinematic dependent coefficients $m_i$ and $M_i$, respectively. This yields

$$
\begin{aligned}
\mathcal{M}_{\text{HEFT}}^{\text{LO}} =\ & m_1 \cdot c_{tth}^2 + m_2 \cdot c_{tth} c_{hhh} + m_3 \cdot c_{tthh} + m_4 \cdot c_{ggh} c_{hhh} + m_5 \cdot c_{gghh} \\
\mathcal{M}_{\text{HEFT}}^{\text{NLO}} =\ & M_1 \cdot c_{tth}^2 + M_2 \cdot c_{tth} c_{hhh} + M_3 \cdot c_{tthh} + M_4 \cdot c_{ggh} c_{hhh} + M_5 \cdot c_{gghh} \\
& + M_6 \cdot c_{ggh}^2 + M_7 \cdot c_{ggh} c_{tth} \ .
\end{aligned}
\tag{B.5}
$$

Since there are no double insertions on the level of matrix elements for truncation (b), it is obvious that $M_6$ is multiplied by 0 in that case.

The grids $a_i$ of Eq. (6.12) can be thought of as combinations of the kinematic dependent coefficients of the matrix elements, i.e. we have schematically

$$
a_i = \sum m_{i_{\text{LO}}} \times M_{i_{\text{NLO}}} \ ,
\tag{B.6}
$$

with $m_{i_{\text{LO}}} \times M_{i_{\text{NLO}}} \sim 2\text{Re}\left(m_{i_{\text{LO}}} \cdot (M_{i_{\text{NLO}}})^*\right)$. Thus, those $a_i$ of Eq. (6.12) which comprise a combination with $M_6$ and other combinations cannot be straight forwardly reused for truncation (b). After all non-ambiguous combinations for truncation (b) are associated with the corresponding $a_i$ the only residuals for the squared matrix parts are

$$
\begin{aligned}
& (m_1 \times M_4 + m_4 \times M_1) \cdot \bar{\mathcal{C}}_{ggh} \left(1 + 2\bar{\mathcal{C}}_{tth}\right) + m_2 \times M_7 \cdot \bar{\mathcal{C}}_{ggh} \left(1 + \bar{\mathcal{C}}_{hhh} + \bar{\mathcal{C}}_{tth}\right) + m_4 \times \mathcal{M}_7 \cdot \bar{\mathcal{C}}_{ggh}^2 \\
& = a_{11} \cdot \bar{\mathcal{C}}_{ggh} \left(1 + 2\bar{\mathcal{C}}_{tth}\right) + m_2 \times M_7 \cdot \bar{\mathcal{C}}_{ggh} \left(\bar{\mathcal{C}}_{hhh} - \bar{\mathcal{C}}_{tth}\right) + m_4 \times \mathcal{M}_7 \cdot \bar{\mathcal{C}}_{ggh}^2 \ ,
\end{aligned}
\tag{B.7}
$$

with $a_{11} = m_1 \times M_4 + m_4 \times M_1 + m_2 \times M_7$. In the above equation we introduced the short-hand notation $\bar{\mathcal{C}}_i$ to describe the dimension-6 part of the anomalous couplings defined by Table 6.1. Hence, with Eq. (B.7) we find

$$
\delta_\mathcal{V}^{(b)} = m_2 \times M_7 \cdot \bar{\mathcal{C}}_{ggh} \left(\bar{\mathcal{C}}_{hhh} - \bar{\mathcal{C}}_{tth}\right) + m_4 \times \mathcal{M}_7 \cdot \bar{\mathcal{C}}_{ggh}^2 \ ,
\tag{B.8}
$$

which can be implemented analytically, as the amplitude parts contain only tree-level and one-loop contributions.

For completeness, we list the coefficients of the $a_i$ in the SMEFT truncated version of Eq. (6.12) in Table B.1.

**Table B.1.:** The coefficients for the virtual contribution of the SMEFT truncated version of Eq. (6.12). Elements marked by $^{*}$ denote the coefficients which are determined by Eq. (B.7).

| SMEFT truncation Coefficient of | (a) | (b) | (c) | (d) |
|---|---|---|---|---|
| $a_1$ | $1+4\bar{C}_{tth}$ | $1+4\bar{C}_{tth}+4\bar{C}_{tth}^{2}$ | $1+4\bar{C}_{tth}+6\bar{C}_{tth}^{2}$ | $(1+\bar{C}_{tth})^{4}$ |
| $a_2$ | 0 | $\bar{C}_{tth}^{2}$ | $\bar{C}_{tth}^{2}$ | $\bar{C}_{tth}^{2}$ |
| $a_3$ | $1+2(\bar{C}_{hhh}+\bar{C}_{tth})$ | $(1+\bar{C}_{hhh}+\bar{C}_{tth})^{2}$ | $(1+\bar{C}_{hhh}+\bar{C}_{tth})^{2}+2\bar{C}_{hhh}\bar{C}_{tth}$ | $(1+\bar{C}_{tth})^{2}(1+\bar{C}_{hhh})^{2}$ |
| $a_4$ | 0 | $\bar{C}_{ggh}^{2}$ | $\bar{C}_{ggh}^{2}$ | $\bar{C}_{ggh}^{2}(1+\bar{C}_{tth})^{2}$ |
| $a_5$ | 0 | $\bar{C}_{ggh}^{2}$ | $\bar{C}_{ggh}^{2}$ | $\bar{C}_{ggh}^{2}$ |
| $a_6$ | $\bar{C}_{tth}$ | $\bar{C}_{tth}(1+2\bar{C}_{tth})$ | $\bar{C}_{tth}(1+2\bar{C}_{tth})$ | $\bar{C}_{tth}(1+\bar{C}_{tth})^{2}$ |
| $a_7$ | $1+\bar{C}_{hhh}+3\bar{C}_{tth}$ | $(1+\bar{C}_{hhh}+\bar{C}_{tth})(1+2\bar{C}_{tth})$ | $1+\bar{C}_{hhh}+3\bar{C}_{tth}(1+\bar{C}_{hhh}+\bar{C}_{tth})$ | $(1+\bar{C}_{tth})^{3}(1+\bar{C}_{hhh})$ |
| $a_8$ | $\bar{C}_{tthh}$ | $\bar{C}_{tthh}(1+\bar{C}_{tth}+\bar{C}_{hhh})$ | $\bar{C}_{tthh}(1+\bar{C}_{tth}+\bar{C}_{hhh})$ | $\bar{C}_{tthh}(1+\bar{C}_{tth})(1+\bar{C}_{hhh})$ |
| $a_9$ | 0 | $\bar{C}_{ggh}\bar{C}_{tthh}$ | $\bar{C}_{ggh}\bar{C}_{tthh}$ | $\bar{C}_{tthh}\bar{C}_{ggh}(1+\bar{C}_{hhh})$ |
| $a_{10}$ | 0 | $\bar{C}_{gghh}\bar{C}_{tthh}$ | $\bar{C}_{gghh}\bar{C}_{tthh}$ | $\bar{C}_{tthh}\bar{C}_{gghh}$ |
| $a_{11}$ | $\bar{C}_{ggh}$ | $\bar{C}_{ggh}(1+2\bar{C}_{tth})^{*}$ | $\bar{C}_{ggh}(1+2\bar{C}_{tth}+\bar{C}_{hhh})$ | $(1+\bar{C}_{tth})^{2}\bar{C}_{ggh}(1+\bar{C}_{hhh})$ |
| $a_{12}$ | $\bar{C}_{ggh}$ | $\bar{C}_{ggh}(1+2\bar{C}_{tth})$ | $\bar{C}_{ggh}(1+2\bar{C}_{tth})$ | $(1+\bar{C}_{tth})^{3}\bar{C}_{ggh}$ |
| $a_{13}$ | $\bar{C}_{ggh}$ | $\bar{C}_{ggh}(1+2\bar{C}_{tth})$ | $\bar{C}_{ggh}(1+2\bar{C}_{tth}+\bar{C}_{tth})$ | $(1+\bar{C}_{tth})\bar{C}_{tthh}\bar{C}_{ggh}$ |
| $a_{14}$ | $\bar{C}_{gghh}$ | $\bar{C}_{gghh}(1+\bar{C}_{hhh}+\bar{C}_{tth})$ | $\bar{C}_{gghh}(1+\bar{C}_{hhh}+\bar{C}_{tth})$ | $(1+\bar{C}_{tth})(1+\bar{C}_{hhh})\bar{C}_{gghh}$ |
| $a_{15}$ | 0 | $\bar{C}_{ggh}\bar{C}_{gghh}$ | $\bar{C}_{ggh}\bar{C}_{gghh}$ | $\bar{C}_{ggh}(1+\bar{C}_{hhh})\bar{C}_{gghh}$ |
| $a_{16}$ | $\bar{C}_{ggh}$ | $\bar{C}_{ggh}(1+2\bar{C}_{tth})$ | $\bar{C}_{ggh}(1+3\bar{C}_{tth})$ | $(1+\bar{C}_{tth})^{3}\bar{C}_{ggh}$ |
| $a_{17}$ | 0 | $\bar{C}_{ggh}\bar{C}_{tthh}$ | $\bar{C}_{ggh}\bar{C}_{tthh}$ | $(1+\bar{C}_{tth})\bar{C}_{tthh}\bar{C}_{ggh}$ |
| $a_{18}$ | 0 | $0^{*}$ | $\bar{C}_{ggh}^{2}$ | $(1+\bar{C}_{tth})\bar{C}_{ggh}^{2}(1+\bar{C}_{hhh})$ |
| $a_{19}$ | 0 | $\bar{C}_{ggh}\bar{C}_{gghh}$ | $\bar{C}_{ggh}\bar{C}_{gghh}$ | $(1+\bar{C}_{tth})\bar{C}_{ggh}\bar{C}_{gghh}$ |
| $a_{20}$ | 0 | 0 | $\bar{C}_{ggh}^{2}$ | $(1+\bar{C}_{tth})^{2}\bar{C}_{ggh}^{2}$ |
| $a_{21}$ | 0 | 0 | 0 | $\bar{C}_{tthh}\bar{C}_{ggh}^{2}$ |
| $a_{22}$ | 0 | 0 | 0 | $\bar{C}_{ggh}^{3}(1+\bar{C}_{hhh})$ |
| $a_{23}$ | 0 | 0 | 0 | $\bar{C}_{ggh}^{2}\bar{C}_{gghh}$ |

### B.2.2. Implementation of chromomagnetic and 4-top operators

The analytic structure of the subleading SMEFT contributions involving insertions of chromomagnetic and 4-top operators at LO QCD have been described in Sec. 8.1. The combination with the leading SMEFT contribution can be schematically expressed according to Eqs. (8.2) – (8.4), however, they enter differently within the framework of the POWHEG-BOX-V2. The implementation of the subleading contribution has been performed analytically in separate subroutines which are found in `Subleading.f` with calls of the subroutines of the matrix elements in `MEchromo.f90`, `ME4top.f90` and `MEborn.f90`. If NLO corrections are included in the run, the subroutines for the subleading contribution are called in the routines for the virtual contribution in the POWHEG-BOX-V2, whereas if the code is run in `bornonly` mode, they enter in the Born routines.

## B.3. Usage of ggHH_SMEFT

The code is provided within the `POWHEG-BOX-V2` [204] and can be obtained from the web page `https://powhegbox.mib.infn.it/` as part of the `User-Processes-V2`. The usage has already been fully described in Refs. [5, 7] together with the parts which are inherited from GGHH and described in Ref. [200]. For convenience, this section serves as a collection of the instructions in the aforementioned references to the EFT related settings.

An example input card `powheg.input-save` and a run script `run.sh` are provided in the folder `testrun`. The EFT parameters are directly defined in the input card. We first describe the usage for the leading contribution discussed in Chapter 6 and subsequently the subleading contributions of chromomagnetic and 4-top operators considered in Chapter 8 for the SMEFT case.

For the HEFT case, the couplings are set by:

| | |
|---|---|
| `chhh:` | the ratio of the Higgs trilinear coupling to its SM value ($c_{hhh}$ in Chapter 6), |
| `ct:` | the ratio of the Higgs Yukawa coupling to the top quark to its SM value ($c_{tth}$ in Chapter 6), |
| `ctt:` | the effective coupling of two Higgs bosons to a top quark pair ($c_{tthh}$ in Chapter 6), |
| `cggh:` | the effective coupling of two gluons to the Higgs boson ($c_{ggh}$ in Chapter 6), |
| `cgghh:` | the effective coupling of two gluons to two Higgs bosons ($c_{gghh}$ in Chapter 6). |

For the SMEFT case, the mass scale of new physics is set by:

`Lambda=1.0:` the input value of the SMEFT heavy mass scale $\Lambda$ (in TeV),

and the value of the SMEFT coefficients in the Warsaw basis is set by the following keywords:

| | |
|---|---|
| `CHbox:` | the Higgs kinetic term coefficient $\mathcal{C}_{H\square}$, |
| `CHD:` | the Higgs kinetic term coefficient $\mathcal{C}_{HD}$, |
| `CH:` | the Higgs trilinear coupling term $\mathcal{C}_H$, |
| `CuH:` | the Higgs Yukawa coupling to up-type quarks term $\mathcal{C}_{tH}$, |
| `CHG:` | the effective coupling of gluons to Higgs bosons $\mathcal{C}_{HG}$. |

The input keyword `usesmeft` defines which EFT is used and takes the values `0` or `1`. `usesmeft=1` denotes the SMEFT case in which the parameters for `CHbox`, `CHD`, `CH`, `CuH`, `CHG` are taken from the input card and translated internally by means of Table 6.1 (the values of `chhh`, `ct`, `ctt`, `cggh`, `cgghh` in the input card are ignored). When `usesmeft=0` is chosen, the calculation is performed for the HEFT case for the parameter values set by `chhh`, `ct`, `ctt`, `cggh`, `cgghh` (the values of `CHbox`, `CHD`, `CH`, `CuH`, `CHG`, `Lambda` in the input card are ignored).

The different SMEFT truncation options defined by Eq. (6.21) are selected via the keyword `multiple-insertion`, where the values 0–3 of this flag denote the respective options (a)–(d).

The leading SMEFT calculation has been extended by the subleading contributions of chromomagnetic and 4-top operators which have been considered in Chapter 8. The amplitudes have been implemented analytically and the combination with the fixed order NLO QCD corrections of the leading SMEFT contribution is accomplished according to the formulas of Eqs. (8.2) – (8.4), however the internal splitting of contributions follows the description of Sec. B.2.2. Since the subleading contributions have Born kinematics and are expressed in terms of one-loop Feynman integrals, the time spent for their evaluation per phase-space point is of the order of the existing Born contribution, hence the run-time of the code is not significantly affected.

The Wilson coefficients of the chromomagnetic and 4-top operators in Eq. (8.1) are set by:

    `CtG:`            Wilson coefficient of chromomagnetic operator $\mathcal{C}_{tG}$,

    `CQt:`            Wilson coefficient of 4-top operator $\mathcal{C}_{Qt}^{(1)}$,

    `CQt8:`          Wilson coefficient of 4-top operator $\mathcal{C}_{Qt}^{(8)}$,

    `CQQtt:`        sum of Wilson coefficients of 4-top operators $\mathcal{C}_{QQ}^{(1)} + \mathcal{C}_{tt}$,

    `CQQ8:`         Wilson coefficient of 4-top operator $\mathcal{C}_{QQ}^{(8)}$.

If the combination with subleading contributions is used, only truncation options (a) and (b) are retained, as the other options are not meaningful for this case. Therefore, the available setting for the selection of cross section contributions from SMEFT operators are visualized in Table B.2. The keyword `includesubleading` activates the inclusion of the subleading contribution and can be set to `0`, `1` or `2`. For `includesubleading=0` the subleading contributions are omitted and the program behaves as the previous `ggHH_SMEFT` version, i.e. the values for `CtG`, `CQt`, `CQt8`, `CQQtt` and `CQQ8` are ignored and all truncation options as well as the HEFT scenario are available. When `includesubleading=1` the subleading contributions follow the power counting of Eq. (4.12) and only enter in the interference with the leading LO matrix elements according to Eqs. (8.2) – (8.4). In `bornonly` mode, also the setting `includesubleading=2` is available which does not follow the power counting formula applied in this thesis. In this case, the user remains completely agnostic about possible UV extensions meaning that $\mathcal{C}_{tG}$ is treated as part of the leading SMEFT contribution which allows squared $\mathcal{C}_{tG}$-contributions to $|\mathcal{M}_{\text{dim-6}}|^2$ in truncation option (b). However, no NLO QCD corrections to the amplitude with insertions of $\mathcal{C}_{tG}$ are available, thus restricting the evaluation to the LO QCD case.

Finally, the 4-top contributions are available in the two considered $\gamma_5$ schemes which can be chosen by `GAMMA5BMHV`: With `GAMMA5BMHV=0` the NDR scheme is chosen, `GAMMA5BMHV=1` switches to the BMHV scheme with the definition of chiral vertices according to Eq. (3.25). This choice only affects the dependence on `CQt` and `CQt8`.

| truncation | (a) | (b) |
|---|---|---|
| $\sigma_{\mathrm{EFT}}^{\mathrm{Born}}$ | | |
| includesubleading | | |
| 0 | $\sigma_{\mathrm{SM}\times\mathrm{dim6}}^{\mathrm{lead}}\left[(g_s^2 L)^2 \Lambda^{-2}\right]$ | $\sigma_{\mathrm{dim6}\times\mathrm{dim6}}^{\mathrm{lead}}\left[(g_s^2 L)^2 \Lambda^{-4}\right]$ |
| 1 | $\sigma_{\mathrm{SM}\times\mathrm{dim6}}^{\mathcal{C}_{tG},\mathcal{C}_{4t}}\left[(g_s^2 L)^2 \mathbf{L}\,\Lambda^{-2}\right]$ | $\sigma_{\mathrm{dim6}\times\mathrm{dim6}}^{\mathcal{C}_{tG},\mathcal{C}_{4t}}\left[(g_s^2 L)^2 \mathbf{L}\,\Lambda^{-4}\right]$ |
| 2 | | $\sigma_{\mathrm{dim6}\times\mathrm{dim6}}^{\mathcal{C}_{tG}^2}\left[(g_s^2 L)^2 \mathbf{L}^2\,\Lambda^{-4}\right]$ |
| $\sigma_{\mathrm{EFT}}^{\mathrm{NLO}}$ | | |
| | $\sigma_{\mathrm{SM}\times\mathrm{dim6}}^{\mathrm{lead}}\left[(g_s^2 L)^3 \Lambda^{-2}\right]$ | $\sigma_{\mathrm{dim6}\times\mathrm{dim6}}^{\mathrm{lead}}\left[(g_s^2 L)^3 \Lambda^{-4}\right]$ |

**Table B.2.:** Available selection for the SMEFT contributions for the calculation of the cross section. The rows specify the selection of subleading operator contributions for the Born cross section in the upper part and the NLO cross section in the lower part which is untouched by the setting of `includesubleading`, the columns show the truncation options for the $1/\Lambda$–expansion. The higher setting for the selection always include the addition of the partial cross section contributions of previous contributions and the SM as well. Notice that `includesubleading=2` is only available in `bornonly` mode.

More details about the usage can be found in the `Docs` folder of the code, parameters common to all processes in the POWHEG-BOX-V2 are described in the manual `V2-paper.pdf` which is located in the `POWHEG-BOX-V2/Docs` directory. The generation of full-fledged Monte-Carlo events is achieved using the interface to `Pythia 8` [241, 242] and `Herwig 7` [243, 244] which is inherited from GGHH [163, 199, 200]. We like to finish this section with the reminder that the two-loop grids for the virtual contributions are only available for *fixed* values of the Higgs and the top-quark masses which are set to $m_h = 125$ GeV and $m_t = 173$ GeV. Changing these is only possible in `bornonly` mode.

# Acknowledgements (Danksagungen)

# References

[1] **ATLAS** Collaboration, G. Aad *et al.*, "Observation of a new particle in the search for the Standard Model Higgs boson with the ATLAS detector at the LHC," *Phys. Lett. B* **716** (2012) 1–29, `arXiv:1207.7214 [hep-ex]`.

[2] **CMS** Collaboration, S. Chatrchyan *et al.*, "Observation of a New Boson at a Mass of 125 GeV with the CMS Experiment at the LHC," *Phys. Lett. B* **716** (2012) 30–61, `arXiv:1207.7235 [hep-ex]`.

[3] **CMS** Collaboration, A. Tumasyan *et al.*, "A portrait of the Higgs boson by the CMS experiment ten years after the discovery.," *Nature* **607** no. 7917, (2022) 60–68, `arXiv:2207.00043 [hep-ex]`.

[4] **ATLAS** Collaboration, G. Aad *et al.*, "A detailed map of Higgs boson interactions by the ATLAS experiment ten years after the discovery," *Nature* **607** no. 7917, (2022) 52–59, `arXiv:2207.00092 [hep-ex]`. [Erratum: Nature 612, E24 (2022)].

[5] G. Heinrich, J. Lang, and L. Scyboz, "SMEFT predictions for $gg \to hh$ at full NLO QCD and truncation uncertainties," *JHEP* **08** (2022) 079, `arXiv:2204.13045 [hep-ph]`.

[6] S. Di Noi, R. Gröber, G. Heinrich, J. Lang, and M. Vitti, "On $\gamma_5$ schemes and the interplay of SMEFT operators in the Higgs-gluon coupling," `arXiv:2310.18221 [hep-ph]`.

[7] G. Heinrich and J. Lang, "Combining chromomagnetic and four-fermion operators with leading SMEFT operators for $gg \to hh$ at NLO QCD," `arXiv:2311.15004 [hep-ph]`.

[8] P. W. Higgs, "Broken Symmetries and the Masses of Gauge Bosons," *Phys. Rev. Lett.* **13** (1964) 508–509.

[9] F. Englert and R. Brout, "Broken Symmetry and the Mass of Gauge Vector Mesons," *Phys. Rev. Lett.* **13** (1964) 321–323.

[10] G. S. Guralnik, C. R. Hagen, and T. W. B. Kibble, "Global Conservation Laws and Massless Particles," *Phys. Rev. Lett.* **13** (1964) 585–587.

[11] T. W. B. Kibble, "Symmetry breaking in nonAbelian gauge theories," *Phys. Rev.* **155** (1967) 1554–1561.

[12] S. L. Glashow, "Partial Symmetries of Weak Interactions," *Nucl. Phys.* **22** (1961) 579–588.

[13] A. Salam, "Weak and Electromagnetic Interactions," *Conf. Proc. C* **680519** (1968) 367–377.

[14] S. Weinberg, "A Model of Leptons," *Phys. Rev. Lett.* **19** (1967) 1264–1266.

[15] D. J. Gross and F. Wilczek, "Ultraviolet Behavior of Nonabelian Gauge Theories," *Phys. Rev. Lett.* **30** (1973) 1343–1346.

[16] H. D. Politzer, "Reliable Perturbative Results for Strong Interactions?," *Phys. Rev. Lett.* **30** (1973) 1346–1349.

[17] L. D. Faddeev and V. N. Popov, "Feynman Diagrams for the Yang-Mills Field," *Phys. Lett. B* **25** (1967) 29–30.

[18] M. D. Schwartz, *Quantum Field Theory and the Standard Model.* Cambridge University Press, 3, 2014.

[19] N. Cabibbo, "Unitary Symmetry and Leptonic Decays," *Phys. Rev. Lett.* **10** (1963) 531–533.

[20] M. Kobayashi and T. Maskawa, "CP Violation in the Renormalizable Theory of Weak Interaction," *Prog. Theor. Phys.* **49** (1973) 652–657.

[21] A. Denner and S. Dittmaier, "Electroweak Radiative Corrections for Collider Physics," *Phys. Rept.* **864** (2020) 1–163, `arXiv:1912.06823 [hep-ph]`.

[22] **LHC Higgs Cross Section Working Group** Collaboration, A. David, A. Denner, M. Duehrssen, M. Grazzini, C. Grojean, G. Passarino, M. Schumacher, M. Spira, G. Weiglein, and M. Zanetti, "LHC HXSWG interim recommendations to explore the coupling structure of a Higgs-like particle," `arXiv:1209.0040 [hep-ph]`.

[23] **LHC Higgs Cross Section Working Group** Collaboration, J. R. Andersen *et al.*, "Handbook of LHC Higgs Cross Sections: 3. Higgs Properties," `arXiv:1307.1347 [hep-ph]`.

[24] **ATLAS** Collaboration, G. Aad *et al.*, "Constraints on the Higgs boson self-coupling from single- and double-Higgs production with the ATLAS detector using pp collisions at s=13 TeV," *Phys. Lett. B* **843** (2023) 137745, `arXiv:2211.01216 [hep-ex]`.

[25] A. D. Sakharov, "Violation of CP Invariance, C asymmetry, and baryon asymmetry of the universe," *Pisma Zh. Eksp. Teor. Fiz.* **5** (1967) 32–35.

[26] **Super-Kamiokande** Collaboration, Y. Fukuda *et al.*, "Evidence for oscillation of atmospheric neutrinos," *Phys. Rev. Lett.* **81** (1998) 1562–1567, `arXiv:hep-ex/9807003`.

[27] **SNO** Collaboration, Q. R. Ahmad *et al.*, "Measurement of the rate of $\nu_e + d \rightarrow p + p + e^-$ interactions produced by $^8$B solar neutrinos at the Sudbury Neutrino Observatory," *Phys. Rev. Lett.* **87** (2001) 071301, `arXiv:nucl-ex/0106015`.

[28] **SNO** Collaboration, Q. R. Ahmad *et al.*, "Direct evidence for neutrino flavor transformation from neutral current interactions in the Sudbury Neutrino Observatory," *Phys. Rev. Lett.* **89** (2002) 011301, `arXiv:nucl-ex/0204008`.

[29] J. Ellis, "TikZ-Feynman: Feynman diagrams with TikZ," *Comput. Phys. Commun.* **210** (2017) 103–123, `arXiv:1601.05437 [hep-ph]`.

[30] R. K. Ellis and G. Zanderighi, "Scalar one-loop integrals for QCD," *JHEP* **02** (2008) 002, `arXiv:0712.1851 [hep-ph]`.

[31] H. Bélusca-Maïto, A. Ilakovac, P. Kühler, M. Mađor-Božinović, D. Stöckinger, and M. Weißwange, "Introduction to Renormalization Theory and Chiral Gauge Theories in Dimensional Regularization with Non-Anticommuting $\gamma_5$," *Symmetry* **15** no. 3, (2023) 622, `arXiv:2303.09120 [hep-ph]`.

[32] K. G. Wilson, "Quantum field theory models in less than four-dimensions," *Phys. Rev. D* **7** (1973) 2911–2926.

[33] J. C. Collins, *Renormalization: An Introduction to Renormalization, The Renormalization Group, and the Operator Product Expansion*, vol. 26 of *Cambridge Monographs on Mathematical Physics*. Cambridge University Press, Cambridge, 1986.

[34] C. Gnendiger *et al.*, "To $d$, or not to $d$: recent developments and comparisons of regularization schemes," *Eur. Phys. J. C* **77** no. 7, (2017) 471, `arXiv:1705.01827` `[hep-ph]`.

[35] S. Weinberg, "High-energy behavior in quantum field theory," *Phys. Rev.* **118** (1960) 838–849.

[36] Y. Hahn and W. Zimmermann, "An Elementary Proof of Dyson's Power Counting Theorem," *Commun. Math. Phys.* **10** (12, 1968) 330–342.

[37] W. Zimmermann, "The power counting theorem for minkowski metric," *Commun. Math. Phys.* **11** (1968) 1–8.

[38] G. 't Hooft, "Dimensional regularization and the renormalization group," *Nucl. Phys. B* **61** (1973) 455–468.

[39] S. Weinberg, "New approach to the renormalization group," *Phys. Rev. D* **8** (1973) 3497–3509.

[40] J. C. Collins, "Structure of Counterterms in Dimensional Regularization," *Nucl. Phys. B* **80** (1974) 341–348.

[41] W. A. Bardeen, A. J. Buras, D. W. Duke, and T. Muta, "Deep Inelastic Scattering Beyond the Leading Order in Asymptotically Free Gauge Theories," *Phys. Rev. D* **18** (1978) 3998.

[42] T. Kinoshita, "Mass singularities of Feynman amplitudes," *J. Math. Phys.* **3** (1962) 650–677.

[43] T. D. Lee and M. Nauenberg, "Degenerate Systems and Mass Singularities," *Phys. Rev.* **133** (1964) B1549–B1562.

[44] S. Catani and M. H. Seymour, "The Dipole formalism for the calculation of QCD jet cross-sections at next-to-leading order," *Phys. Lett. B* **378** (1996) 287–301, `arXiv:hep-ph/9602277`.

[45] S. Catani and M. H. Seymour, "A General algorithm for calculating jet cross-sections in NLO QCD," *Nucl. Phys. B* **485** (1997) 291–419, `arXiv:hep-ph/9605323`. [Erratum: Nucl.Phys.B 510, 503–504 (1998)].

[46] S. Catani, S. Dittmaier, M. H. Seymour, and Z. Trocsanyi, "The Dipole formalism for next-to-leading order QCD calculations with massive partons," *Nucl. Phys. B* **627** (2002) 189–265, `arXiv:hep-ph/0201036`.

[47] G. Heinrich, "Collider Physics at the Precision Frontier," *Phys. Rept.* **922** (2021) 1–69, `arXiv:2009.00516` `[hep-ph]`.

[48] S. M. Aybat, L. J. Dixon, and G. F. Sterman, "The Two-loop soft anomalous dimension matrix and resummation at next-to-next-to leading pole," *Phys. Rev. D* **74** (2006) 074004, `arXiv:hep-ph/0607309`.

[49] A. Mitov, G. F. Sterman, and I. Sung, "The Massive Soft Anomalous Dimension Matrix at Two Loops," *Phys. Rev. D* **79** (2009) 094015, `arXiv:0903.3241` `[hep-ph]`.

[50] T. Becher and M. Neubert, "On the Structure of Infrared Singularities of Gauge-Theory Amplitudes," *JHEP* **06** (2009) 081, `arXiv:0903.1126 [hep-ph]`. [Erratum: JHEP 11, 024 (2013)].

[51] T. Becher and M. Neubert, "Infrared singularities of QCD amplitudes with massive partons," *Phys. Rev. D* **79** (2009) 125004, `arXiv:0904.1021 [hep-ph]`. [Erratum: Phys.Rev.D 80, 109901 (2009)].

[52] M. Czakon, A. Mitov, and G. F. Sterman, "Threshold Resummation for Top-Pair Hadroproduction to Next-to-Next-to-Leading Log," *Phys. Rev. D* **80** (2009) 074017, `arXiv:0907.1790 [hep-ph]`.

[53] A. Ferroglia, M. Neubert, B. D. Pecjak, and L. L. Yang, "Two-loop divergences of massive scattering amplitudes in non-abelian gauge theories," *JHEP* **11** (2009) 062, `arXiv:0908.3676 [hep-ph]`.

[54] A. Mitov, G. F. Sterman, and I. Sung, "Computation of the Soft Anomalous Dimension Matrix in Coordinate Space," *Phys. Rev. D* **82** (2010) 034020, `arXiv:1005.4646 [hep-ph]`.

[55] B. Agarwal, G. Heinrich, S. P. Jones, M. Kerner, S. Y. Klein, J. Lang, V. Magerya, and A. Olsson, "Two-loop amplitudes for ttH production: the quark-initiated Nf-part," `arXiv:2402.03301 [hep-ph]`.

[56] J. C. Collins, D. E. Soper, and G. F. Sterman, "Factorization of Hard Processes in QCD," *Adv. Ser. Direct. High Energy Phys.* **5** (1989) 1–91, `arXiv:hep-ph/0409313`.

[57] **CTEQ** Collaboration, R. Brock *et al.*, "Handbook of perturbative QCD; Version 1.1: September 1994,".

[58] G. Passarino and M. J. G. Veltman, "One Loop Corrections for e+ e- Annihilation Into mu+ mu- in the Weinberg Model," *Nucl. Phys. B* **160** (1979) 151–207.

[59] G. 't Hooft and M. J. G. Veltman, "Scalar One Loop Integrals," *Nucl. Phys. B* **153** (1979) 365–401.

[60] V. Shtabovenko, R. Mertig, and F. Orellana, "FeynCalc 9.3: New features and improvements," *Comput. Phys. Commun.* **256** (2020) 107478, `arXiv:2001.04407 [hep-ph]`.

[61] V. Shtabovenko, R. Mertig, and F. Orellana, "New Developments in FeynCalc 9.0," *Comput. Phys. Commun.* **207** (2016) 432–444, `arXiv:1601.01167 [hep-ph]`.

[62] R. Mertig, M. Bohm, and A. Denner, "FEYN CALC: Computer algebraic calculation of Feynman amplitudes," *Comput. Phys. Commun.* **64** (1991) 345–359.

[63] T. Hahn and M. Perez-Victoria, "Automatized one loop calculations in four-dimensions and D-dimensions," *Comput. Phys. Commun.* **118** (1999) 153–165, `arXiv:hep-ph/9807565`.

[64] P. Nogueira, "Automatic Feynman graph generation," *J. Comput. Phys.* **105** (1993) 279–289.

[65] **GoSam** Collaboration, G. Cullen *et al.*, "GOSAM-2.0: a tool for automated one-loop calculations within the Standard Model and beyond," *Eur. Phys. J. C* **74** no. 8, (2014) 3001, `arXiv:1404.7096 [hep-ph]`.

[66] G. Cullen, N. Greiner, G. Heinrich, G. Luisoni, P. Mastrolia, G. Ossola, T. Reiter, and F. Tramontano, "Automated One-Loop Calculations with GoSam," *Eur. Phys. J. C* **72** (2012) 1889, `arXiv:1111.2034 [hep-ph]`.

[67] J. Kuipers, T. Ueda, J. A. M. Vermaseren, and J. Vollinga, "FORM version 4.0," *Comput. Phys. Commun.* **184** (2013) 1453–1467, `arXiv:1203.6543 [cs.SC]`.

[68] G. Cullen, M. Koch-Janusz, and T. Reiter, "Spinney: A Form Library for Helicity Spinors," *Comput. Phys. Commun.* **182** (2011) 2368–2387, `arXiv:1008.0803 [hep-ph]`.

[69] T. Binoth, J. P. Guillet, G. Heinrich, E. Pilon, and T. Reiter, "Golem95: A Numerical program to calculate one-loop tensor integrals with up to six external legs," *Comput. Phys. Commun.* **180** (2009) 2317–2330, `arXiv:0810.0992 [hep-ph]`.

[70] G. Cullen, J. P. Guillet, G. Heinrich, T. Kleinschmidt, E. Pilon, T. Reiter, and M. Rodgers, "Golem95C: A library for one-loop integrals with complex masses," *Comput. Phys. Commun.* **182** (2011) 2276–2284, `arXiv:1101.5595 [hep-ph]`.

[71] J. P. Guillet, G. Heinrich, and J. F. von Soden-Fraunhofen, "Tools for NLO automation: extension of the golem95C integral library," *Comput. Phys. Commun.* **185** (2014) 1828–1834, `arXiv:1312.3887 [hep-ph]`.

[72] H. van Deurzen, G. Luisoni, P. Mastrolia, E. Mirabella, G. Ossola, and T. Peraro, "Multi-leg One-loop Massive Amplitudes from Integrand Reduction via Laurent Expansion," *JHEP* **03** (2014) 115, `arXiv:1312.6678 [hep-ph]`.

[73] T. Peraro, "Ninja: Automated Integrand Reduction via Laurent Expansion for One-Loop Amplitudes," *Comput. Phys. Commun.* **185** (2014) 2771–2797, `arXiv:1403.1229 [hep-ph]`.

[74] V. Magerya, "Amplitude library (ALIBRARY): gluing all the tools needed for computing multi-loop amplitudes in QCD and beyond." `https://github.com/magv/alibrary`.

[75] S. Laporta, "High-precision calculation of multiloop Feynman integrals by difference equations," *Int. J. Mod. Phys. A* **15** (2000) 5087–5159, `arXiv:hep-ph/0102033`.

[76] A. von Manteuffel and C. Studerus, "Reduze 2 - Distributed Feynman Integral Reduction," `arXiv:1201.4330 [hep-ph]`.

[77] P. Maierhöfer, J. Usovitsch, and P. Uwer, "Kira—A Feynman integral reduction program," *Comput. Phys. Commun.* **230** (2018) 99–112, `arXiv:1705.05610 [hep-ph]`.

[78] J. Klappert, F. Lange, P. Maierhöfer, and J. Usovitsch, "Integral reduction with Kira 2.0 and finite field methods," *Comput. Phys. Commun.* **266** (2021) 108024, `arXiv:2008.06494 [hep-ph]`.

[79] S. Borowka, G. Heinrich, S. Jahn, S. P. Jones, M. Kerner, J. Schlenk, and T. Zirke, "pySecDec: a toolbox for the numerical evaluation of multi-scale integrals," *Comput. Phys. Commun.* **222** (2018) 313–326, `arXiv:1703.09692 [hep-ph]`.

[80] S. Borowka, G. Heinrich, S. Jahn, S. P. Jones, M. Kerner, and J. Schlenk, "A GPU compatible quasi-Monte Carlo integrator interfaced to pySecDec," *Comput. Phys. Commun.* **240** (2019) 120–137, `arXiv:1811.11720 [physics.comp-ph]`.

[81] G. Heinrich, S. Jahn, S. P. Jones, M. Kerner, F. Langer, V. Magerya, A. Põldaru, J. Schlenk, and E. Villa, "Expansion by regions with pySecDec," *Comput. Phys. Commun.* **273** (2022) 108267, `arXiv:2108.10807 [hep-ph]`.

[82] G. Heinrich, S. P. Jones, M. Kerner, V. Magerya, A. Olsson, and J. Schlenk, "Numerical scattering amplitudes with pySecDec," *Comput. Phys. Commun.* **295** (2024) 108956, `arXiv:2305.19768 [hep-ph]`.

[83] J. C. Ward, "An Identity in Quantum Electrodynamics," *Phys. Rev.* **78** (1950) 182.

[84] Y. Takahashi, "On the generalized Ward identity," *Nuovo Cim.* **6** (1957) 371.

[85] J. C. Taylor, "Ward Identities and Charge Renormalization of the Yang-Mills Field," *Nucl. Phys. B* **33** (1971) 436–444.

[86] A. A. Slavnov, "Ward Identities in Gauge Theories," *Theor. Math. Phys.* **10** (1972) 99–107.

[87] S. L. Adler, "Axial vector vertex in spinor electrodynamics," *Phys. Rev.* **177** (1969) 2426–2438.

[88] J. S. Bell and R. Jackiw, "A PCAC puzzle: $\pi^0 \to \gamma\gamma$ in the $\sigma$ model," *Nuovo Cim. A* **60** (1969) 47–61.

[89] F. Jegerlehner, "Facts of life with gamma(5)," *Eur. Phys. J. C* **18** (2001) 673–679, `arXiv:hep-th/0005255`.

[90] M. S. Chanowitz, M. Furman, and I. Hinchliffe, "The Axial Current in Dimensional Regularization," *Nucl. Phys. B* **159** (1979) 225–243.

[91] G. 't Hooft and M. J. G. Veltman, "Regularization and Renormalization of Gauge Fields," *Nucl. Phys. B* **44** (1972) 189–213.

[92] P. Breitenlohner and D. Maison, "Dimensional Renormalization and the Action Principle," *Commun. Math. Phys.* **52** (1977) 11–38.

[93] W. A. Bardeen, R. Gastmans, and B. E. Lautrup, "Static quantities in Weinberg's model of weak and electromagnetic interactions," *Nucl. Phys. B* **46** (1972) 319–331.

[94] A. J. Buras and P. H. Weisz, "QCD Nonleading Corrections to Weak Decays in Dimensional Regularization and 't Hooft-Veltman Schemes," *Nucl. Phys. B* **333** (1990) 66–99.

[95] D. Kreimer, "The $\gamma(5)$ Problem and Anomalies: A Clifford Algebra Approach," *Phys. Lett. B* **237** (1990) 59–62.

[96] J. G. Korner, D. Kreimer, and K. Schilcher, "A Practicable gamma(5) scheme in dimensional regularization," *Z. Phys. C* **54** (1992) 503–512.

[97] D. Kreimer, "The Role of gamma(5) in dimensional regularization," `arXiv:hep-ph/9401354`.

[98] L. Chen, "An observation on Feynman diagrams with axial anomalous subgraphs in dimensional regularization with an anticommuting $\gamma_5$," *JHEP* **2023** no. 11, (2023) 30, `arXiv:2304.13814 [hep-ph]`.

[99] S. A. Larin, "The Renormalization of the axial anomaly in dimensional regularization," *Phys. Lett. B* **303** (1993) 113–118, `arXiv:hep-ph/9302240`.

[100] M. Ciuchini, E. Franco, G. Martinelli, and L. Reina, "The Delta S = 1 effective Hamiltonian including next-to-leading order QCD and QED corrections," *Nucl. Phys. B* **415** (1994) 403–462, `arXiv:hep-ph/9304257`.

[101] C. Cornella, F. Feruglio, and L. Vecchi, "Gauge invariance and finite counterterms in chiral gauge theories," *JHEP* **02** (2023) 244, `arXiv:2205.10381 [hep-ph]`.

[102] G. Isidori, F. Wilsch, and D. Wyler, "The Standard Model effective field theory at work," `arXiv:2303.16922 [hep-ph]`.

[103] I. Brivio and M. Trott, "The Standard Model as an Effective Field Theory," *Phys. Rept.* **793** (2019) 1–98, `arXiv:1706.08945 [hep-ph]`.

[104] A. V. Manohar, "Introduction to Effective Field Theories," `arXiv:1804.05863 [hep-ph]`.

[105] J. D. Jackson, *Classical Electrodynamics*. Wiley, 1998.

[106] E. Fermi, "An attempt of a theory of beta radiation. 1.," *Z. Phys.* **88** (1934) 161–177.

[107] T. Appelquist and J. Carazzone, "Infrared Singularities and Massive Fields," *Phys. Rev. D* **11** (1975) 2856.

[108] B. A. Ovrut and H. J. Schnitzer, "Gauge Theories With Minimal Subtraction and the Decoupling Theorem," *Nucl. Phys. B* **179** (1981) 381–416.

[109] S. Weinberg, "Baryon and Lepton Nonconserving Processes," *Phys. Rev. Lett.* **43** (1979) 1566–1570.

[110] W. Buchmüller and D. Wyler, "Effective Lagrangian Analysis of New Interactions and Flavor Conservation," *Nucl. Phys. B* **268** (1986) 621–653.

[111] B. Grzadkowski, M. Iskrzynski, M. Misiak, and J. Rosiek, "Dimension-Six Terms in the Standard Model Lagrangian," *JHEP* **10** (2010) 085, `arXiv:1008.4884 [hep-ph]`.

[112] J. C. Criado and M. Pérez-Victoria, "Field redefinitions in effective theories at higher orders," *JHEP* **03** (2019) 038, `arXiv:1811.09413 [hep-ph]`.

[113] S. Herrlich and U. Nierste, "Evanescent operators, scheme dependences and double insertions," *Nucl. Phys. B* **455** (1995) 39–58, `arXiv:hep-ph/9412375`.

[114] J. Fuentes-Martín, M. König, J. Pagès, A. E. Thomsen, and F. Wilsch, "Evanescent operators in one-loop matching computations," *JHEP* **02** (2023) 031, `arXiv:2211.09144 [hep-ph]`.

[115] B. Henning, X. Lu, T. Melia, and H. Murayama, "2, 84, 30, 993, 560, 15456, 11962, 261485, ...: Higher dimension operators in the SM EFT," *JHEP* **08** (2017) 016, `arXiv:1512.03433 [hep-ph]`. [Erratum: JHEP 09, 019 (2019)].

[116] B. Henning, X. Lu, T. Melia, and H. Murayama, "Hilbert series and operator bases with derivatives in effective field theories," *Commun. Math. Phys.* **347** no. 2, (2016) 363–388, `arXiv:1507.07240 [hep-th]`.

[117] L. Lehman and A. Martin, "Low-derivative operators of the Standard Model effective field theory via Hilbert series methods," *JHEP* **02** (2016) 081, `arXiv:1510.00372 [hep-ph]`.

[118] L. Lehman and A. Martin, "Hilbert Series for Constructing Lagrangians: expanding the phenomenologist's toolbox," *Phys. Rev. D* **91** (2015) 105014, `arXiv:1503.07537 [hep-ph]`.

[119] B. Gripaios and D. Sutherland, "DEFT: A program for operators in EFT," *JHEP* **01** (2019) 128, `arXiv:1807.07546 [hep-ph]`.

[120] R. M. Fonseca, "Enumerating the operators of an effective field theory," *Phys. Rev. D* **101** no. 3, (2020) 035040, `arXiv:1907.12584 [hep-ph]`.

[121] C. W. Murphy, "Dimension-8 operators in the Standard Model Eective Field Theory," *JHEP* **10** (2020) 174, `arXiv:2005.00059 [hep-ph]`.

[122] H.-L. Li, Z. Ren, J. Shu, M.-L. Xiao, J.-H. Yu, and Y.-H. Zheng, "Complete set of dimension-eight operators in the standard model effective field theory," *Phys. Rev. D* **104** no. 1, (2021) 015026, `arXiv:2005.00008 [hep-ph]`.

[123] H.-L. Li, Z. Ren, M.-L. Xiao, J.-H. Yu, and Y.-H. Zheng, "Complete set of dimension-nine operators in the standard model effective field theory," *Phys. Rev. D* **104** no. 1, (2021) 015025, `arXiv:2007.07899 [hep-ph]`.

[124] R. V. Harlander, T. Kempkens, and M. C. Schaaf, "Standard model effective field theory up to mass dimension 12," *Phys. Rev. D* **108** no. 5, (2023) 055020, `arXiv:2305.06832 [hep-ph]`.

[125] R. V. Harlander and M. C. Schaaf, "AutoEFT: Automated Operator Construction for Effective Field Theories," `arXiv:2309.15783 [hep-ph]`.

[126] I. Brivio *et al.*, "Truncation, validity, uncertainties," `arXiv:2201.04974 [hep-ph]`.

[127] M. Trott, "Methodology for theory uncertainties in the standard model effective field theory," *Phys. Rev. D* **104** no. 9, (2021) 095023, `arXiv:2106.13794 [hep-ph]`.

[128] A. Helset, A. Martin, and M. Trott, "The Geometric Standard Model Effective Field Theory," *JHEP* **03** (2020) 163, `arXiv:2001.01453 [hep-ph]`.

[129] C. Hays, A. Helset, A. Martin, and M. Trott, "Exact SMEFT formulation and expansion to $\mathcal{O}(v^4/\Lambda^4)$," *JHEP* **11** (2020) 087, `arXiv:2007.00565 [hep-ph]`.

[130] T. Corbett, A. Helset, A. Martin, and M. Trott, "EWPD in the SMEFT to dimension eight," *JHEP* **06** (2021) 076, `arXiv:2102.02819 [hep-ph]`.

[131] T. Corbett, A. Martin, and M. Trott, "Consistent higher order $\sigma\left(\mathcal{GG} \to h\right)$, $\Gamma\left(h \to \mathcal{GG}\right)$ and $\Gamma(h \to \gamma\gamma)$ in geoSMEFT," *JHEP* **12** (2021) 147, `arXiv:2107.07470 [hep-ph]`.

[132] A. Martin and M. Trott, "*ggh* variations," *Phys. Rev. D* **105** no. 7, (2022) 076004, `arXiv:2109.05595 [hep-ph]`.

[133] A. Martin and M. Trott, "More accurate $\sigma\left(\mathcal{GG} \to h\right), \Gamma\left(h \to \mathcal{GG}, \mathcal{AA}, \overline{\Psi}\Psi\right)$ and Higgs width results via the geoSMEFT," *JHEP* **01** (2024) 170, `arXiv:2305.05879 [hep-ph]`.

[134] J. Lang, S. Liebler, H. Schäfer-Siebert, and D. Zeppenfeld, "Effective field theory versus UV-complete model: vector boson scattering as a case study," *Eur. Phys. J. C* **81** no. 7, (2021) 659, `arXiv:2103.16517 [hep-ph]`.

[135] S. Dawson, S. Homiller, and M. Sullivan, "Impact of dimension-eight SMEFT contributions: A case study," *Phys. Rev. D* **104** no. 11, (2021) 115013, `arXiv:2110.06929 [hep-ph]`.

[136] F. Feruglio, "The Chiral approach to the electroweak interactions," *Int. J. Mod. Phys. A* **8** (1993) 4937–4972, `arXiv:hep-ph/9301281`.

[137] C. P. Burgess, J. Matias, and M. Pospelov, "A Higgs or not a Higgs? What to do if you discover a new scalar particle," *Int. J. Mod. Phys. A* **17** (2002) 1841–1918, `arXiv:hep-ph/9912459`.

[138] B. Grinstein and M. Trott, "A Higgs-Higgs bound state due to new physics at a TeV," *Phys. Rev. D* **76** (2007) 073002, `arXiv:0704.1505 [hep-ph]`.

[139] R. Contino, C. Grojean, M. Moretti, F. Piccinini, and R. Rattazzi, "Strong Double Higgs Production at the LHC," *JHEP* **05** (2010) 089, `arXiv:1002.1011 [hep-ph]`.

[140] R. Alonso, M. B. Gavela, L. Merlo, S. Rigolin, and J. Yepes, "The Effective Chiral Lagrangian for a Light Dynamical "Higgs Particle"," *Phys. Lett. B* **722** (2013) 330–335, `arXiv:1212.3305 [hep-ph]`. [Erratum: Phys.Lett.B 726, 926 (2013)].

[141] G. Buchalla, O. Catà, and C. Krause, "Complete Electroweak Chiral Lagrangian with a Light Higgs at NLO," *Nucl. Phys. B* **880** (2014) 552–573, `arXiv:1307.5017 [hep-ph]`. [Erratum: Nucl.Phys.B 913, 475–478 (2016)].

[142] S. Weinberg, "Phenomenological Lagrangians," *Physica A* **96** no. 1-2, (1979) 327–340.

[143] J. Gasser and H. Leutwyler, "Chiral Perturbation Theory to One Loop," *Annals Phys.* **158** (1984) 142.

[144] G. Buchalla, O. Catà, and C. Krause, "On the Power Counting in Effective Field Theories," *Phys. Lett. B* **731** (2014) 80–86, `arXiv:1312.5624 [hep-ph]`.

[145] C. G. Krause, *Higgs Effective Field Theories - Systematics and Applications.* PhD thesis, Munich U., 2016. `arXiv:1610.08537 [hep-ph]`.

[146] C. Müller, "Top-pair production via gluon fusion in the Standard Model effective field theory," *Phys. Rev. D* **104** no. 9, (2021) 095003, `arXiv:2102.05040 [hep-ph]`.

[147] G. Buchalla, G. Heinrich, C. Müller-Salditt, and F. Pandler, "Loop counting matters in SMEFT," *SciPost Phys.* **15** (2023) 088, `arXiv:2204.11808 [hep-ph]`.

[148] C. Arzt, M. B. Einhorn, and J. Wudka, "Patterns of deviation from the standard model," *Nucl. Phys. B* **433** (1995) 41–66, `arXiv:hep-ph/9405214`.

[149] G. Buchalla, O. Cata, and C. Krause, "A Systematic Approach to the SILH Lagrangian," *Nucl. Phys. B* **894** (2015) 602–620, `arXiv:1412.6356 [hep-ph]`.

[150] G. F. Giudice, C. Grojean, A. Pomarol, and R. Rattazzi, "The Strongly-Interacting Light Higgs," *JHEP* **06** (2007) 045, `arXiv:hep-ph/0703164`.

[151] R. Contino, M. Ghezzi, C. Grojean, M. Muhlleitner, and M. Spira, "Effective Lagrangian for a light Higgs-like scalar," *JHEP* **07** (2013) 035, `arXiv:1303.3876 [hep-ph]`.

[152] A. Greljo, A. Palavrić, and A. E. Thomsen, "Adding Flavor to the SMEFT," *JHEP* **10** (2022) 010, `arXiv:2203.09561 [hep-ph]`.

[153] **SMEFiT** Collaboration, J. J. Ethier, G. Magni, F. Maltoni, L. Mantani, E. R. Nocera, J. Rojo, E. Slade, E. Vryonidou, and C. Zhang, "Combined SMEFT interpretation of Higgs, diboson, and top quark data from the LHC," *JHEP* **11** (2021) 089, `arXiv:2105.00006 [hep-ph]`.

[154] C. Degrande, G. Durieux, F. Maltoni, K. Mimasu, E. Vryonidou, and C. Zhang, "Automated one-loop computations in the standard model effective field theory," *Phys. Rev. D* **103** no. 9, (2021) 096024, `arXiv:2008.11743 [hep-ph]`.

[155] G. D'Ambrosio, G. F. Giudice, G. Isidori, and A. Strumia, "Minimal flavor violation: An Effective field theory approach," *Nucl. Phys. B* **645** (2002) 155–187, `arXiv:hep-ph/0207036`.

[156] E. E. Jenkins, A. V. Manohar, and M. Trott, "Renormalization Group Evolution of the Standard Model Dimension Six Operators II: Yukawa Dependence," *JHEP* **01** (2014) 035, `arXiv:1310.4838 [hep-ph]`.

[157] M. B. Einhorn and J. Wudka, "The Bases of Effective Field Theories," *Nucl. Phys. B* **876** (2013) 556–574, `arXiv:1307.0478 [hep-ph]`.

[158] E. E. Jenkins, A. V. Manohar, and M. Trott, "Renormalization Group Evolution of the Standard Model Dimension Six Operators I: Formalism and lambda Dependence," *JHEP* **10** (2013) 087, `arXiv:1308.2627 [hep-ph]`.

[159] R. Alonso, E. E. Jenkins, A. V. Manohar, and M. Trott, "Renormalization Group Evolution of the Standard Model Dimension Six Operators III: Gauge Coupling Dependence and Phenomenology," *JHEP* **04** (2014) 159, `arXiv:1312.2014 [hep-ph]`.

[160] M. Battaglia, M. Grazzini, M. Spira, and M. Wiesemann, "Sensitivity to BSM effects in the Higgs $p_T$ spectrum within SMEFT," *JHEP* **11** (2021) 173, `arXiv:2109.02987 [hep-ph]`.

[161] J. Alison *et al.*, "Higgs boson potential at colliders: Status and perspectives," *Rev. Phys.* **5** (2020) 100045, `arXiv:1910.00012 [hep-ph]`.

[162] E. W. N. Glover and J. J. van der Bij, "HIGGS BOSON PAIR PRODUCTION VIA GLUON FUSION," *Nucl. Phys. B* **309** (1988) 282–294.

[163] G. Heinrich, S. P. Jones, M. Kerner, G. Luisoni, and L. Scyboz, "Probing the trilinear Higgs boson coupling in di-Higgs production at NLO QCD including parton shower effects," *JHEP* **06** (2019) 066, `arXiv:1903.08137 [hep-ph]`.

[164] S. Borowka, N. Greiner, G. Heinrich, S. P. Jones, M. Kerner, J. Schlenk, U. Schubert, and T. Zirke, "Higgs Boson Pair Production in Gluon Fusion at Next-to-Leading Order with Full Top-Quark Mass Dependence," *Phys. Rev. Lett.* **117** no. 1, (2016) 012001, `arXiv:1604.06447 [hep-ph]`. [Erratum: Phys.Rev.Lett. 117, 079901 (2016)].

[165] S. Borowka, N. Greiner, G. Heinrich, S. P. Jones, M. Kerner, J. Schlenk, and T. Zirke, "Full top quark mass dependence in Higgs boson pair production at NLO," *JHEP* **10** (2016) 107, `arXiv:1608.04798 [hep-ph]`.

[166] J. Baglio, F. Campanario, S. Glaus, M. Mühlleitner, M. Spira, and J. Streicher, "Gluon fusion into Higgs pairs at NLO QCD and the top mass scheme," *Eur. Phys. J. C* **79** no. 6, (2019) 459, `arXiv:1811.05692 [hep-ph]`.

[167] J. Baglio, F. Campanario, S. Glaus, M. Mühlleitner, J. Ronca, M. Spira, and J. Streicher, "Higgs-Pair Production via Gluon Fusion at Hadron Colliders: NLO QCD Corrections," *JHEP* **04** (2020) 181, `arXiv:2003.03227 [hep-ph]`.

[168] J. Davies, G. Heinrich, S. P. Jones, M. Kerner, G. Mishima, M. Steinhauser, and D. Wellmann, "Double Higgs boson production at NLO: combining the exact numerical result and high-energy expansion," *JHEP* **11** (2019) 024, `arXiv:1907.06408 [hep-ph]`.

[169] J. Davies, G. Mishima, K. Schönwald, and M. Steinhauser, "Analytic approximations of $2 \to 2$ processes with massive internal particles," *JHEP* **06** (2023) 063, `arXiv:2302.01356 [hep-ph]`.

[170] E. Bagnaschi, G. Degrassi, and R. Gröber, "Higgs boson pair production at NLO in the POWHEG approach and the top quark mass uncertainties," *Eur. Phys. J. C* **83** no. 11, (2023) 1054, `arXiv:2309.10525 [hep-ph]`.

[171] S. Dawson, S. Dittmaier, and M. Spira, "Neutral Higgs boson pair production at hadron colliders: QCD corrections," *Phys. Rev. D* **58** (1998) 115012, `arXiv:hep-ph/9805244`.

[172] D. de Florian and J. Mazzitelli, "Two-loop virtual corrections to Higgs pair production," *Phys. Lett. B* **724** (2013) 306–309, `arXiv:1305.5206 [hep-ph]`.

[173] D. de Florian and J. Mazzitelli, "Higgs Boson Pair Production at Next-to-Next-to-Leading Order in QCD," *Phys. Rev. Lett.* **111** (2013) 201801, `arXiv:1309.6594 [hep-ph]`.

[174] J. Grigo, K. Melnikov, and M. Steinhauser, "Virtual corrections to Higgs boson pair production in the large top quark mass limit," *Nucl. Phys. B* **888** (2014) 17–29, `arXiv:1408.2422 [hep-ph]`.

[175] D. de Florian, M. Grazzini, C. Hanga, S. Kallweit, J. M. Lindert, P. Maierhöfer, J. Mazzitelli, and D. Rathlev, "Differential Higgs Boson Pair Production at Next-to-Next-to-Leading Order in QCD," *JHEP* **09** (2016) 151, `arXiv:1606.09519 [hep-ph]`.

[176] L.-B. Chen, H. T. Li, H.-S. Shao, and J. Wang, "Higgs boson pair production via gluon fusion at N$^3$LO in QCD," *Phys. Lett. B* **803** (2020) 135292, `arXiv:1909.06808 [hep-ph]`.

[177] M. Grazzini, G. Heinrich, S. Jones, S. Kallweit, M. Kerner, J. M. Lindert, and J. Mazzitelli, "Higgs boson pair production at NNLO with top quark mass effects," *JHEP* **05** (2018) 059, `arXiv:1803.02463 [hep-ph]`.

[178] L.-B. Chen, H. T. Li, H.-S. Shao, and J. Wang, "The gluon-fusion production of Higgs boson pair: N$^3$LO QCD corrections and top-quark mass effects," *JHEP* **03** (2020) 072, `arXiv:1912.13001 [hep-ph]`.

[179] J. Baglio, F. Campanario, S. Glaus, M. Mühlleitner, J. Ronca, and M. Spira, "$gg \to HH$: Combined uncertainties," *Phys. Rev. D* **103** no. 5, (2021) 056002, `arXiv:2008.11626 [hep-ph]`.

[180] M. Mühlleitner, J. Schlenk, and M. Spira, "Top-Yukawa-induced corrections to Higgs pair production," *JHEP* **10** (2022) 185, `arXiv:2207.02524 [hep-ph]`.

[181] J. Davies, G. Mishima, K. Schönwald, M. Steinhauser, and H. Zhang, "Higgs boson contribution to the leading two-loop Yukawa corrections to gg → HH," *JHEP* **08** (2022) 259, `arXiv:2207.02587 [hep-ph]`.

[182] J. Davies, K. Schönwald, M. Steinhauser, and H. Zhang, "Next-to-leading order electroweak corrections to $gg \to HH$ and $gg \to gH$ in the large-$m_t$ limit," *JHEP* **10** (2023) 033, `arXiv:2308.01355 [hep-ph]`.

[183] H.-Y. Bi, L.-H. Huang, R.-J. Huang, Y.-Q. Ma, and H.-M. Yu, "Electroweak corrections to double Higgs production at the LHC," `arXiv:2311.16963 [hep-ph]`.

[184] R. Gröber, M. Mühlleitner, M. Spira, and J. Streicher, "NLO QCD Corrections to Higgs Pair Production including Dimension-6 Operators," *JHEP* **09** (2015) 092, `arXiv:1504.06577 [hep-ph]`.

[185] R. Gröber, M. Mühlleitner, and M. Spira, "Higgs Pair Production at NLO QCD for CP-violating Higgs Sectors," *Nucl. Phys. B* **925** (2017) 1–27, `arXiv:1705.05314 [hep-ph]`.

[186] G. Buchalla, M. Capozi, A. Celis, G. Heinrich, and L. Scyboz, "Higgs boson pair production in non-linear Effective Field Theory with full $m_t$-dependence at NLO QCD," *JHEP* **09** (2018) 057, `arXiv:1806.05162 [hep-ph]`.

[187] D. de Florian, I. Fabre, and J. Mazzitelli, "Higgs boson pair production at NNLO in QCD including dimension 6 operators," *JHEP* **10** (2017) 215, `arXiv:1704.05700 [hep-ph]`.

[188] D. de Florian, I. Fabre, G. Heinrich, J. Mazzitelli, and L. Scyboz, "Anomalous couplings in Higgs-boson pair production at approximate NNLO QCD," *JHEP* **09** (2021) 161, arXiv:2106.14050 [hep-ph].

[189] A. Falkowski and R. Rattazzi, "Which EFT," *JHEP* **10** (2019) 255, arXiv:1902.05936 [hep-ph].

[190] R. Alonso, E. E. Jenkins, and A. V. Manohar, "A Geometric Formulation of Higgs Effective Field Theory: Measuring the Curvature of Scalar Field Space," *Phys. Lett. B* **754** (2016) 335–342, arXiv:1511.00724 [hep-ph].

[191] R. Alonso, E. E. Jenkins, and A. V. Manohar, "Geometry of the Scalar Sector," *JHEP* **08** (2016) 101, arXiv:1605.03602 [hep-ph].

[192] T. Cohen, N. Craig, X. Lu, and D. Sutherland, "Is SMEFT Enough?," *JHEP* **03** (2021) 237, arXiv:2008.08597 [hep-ph].

[193] T. Cohen, N. Craig, X. Lu, and D. Sutherland, "Unitarity violation and the geometry of Higgs EFTs," *JHEP* **12** (2021) 003, arXiv:2108.03240 [hep-ph].

[194] R. Gómez-Ambrosio, F. J. Llanes-Estrada, A. Salas-Bernárdez, and J. J. Sanz-Cillero, "Distinguishing electroweak EFTs with WLWL→n×h," *Phys. Rev. D* **106** no. 5, (2022) 053004, arXiv:2204.01763 [hep-ph].

[195] R. Gómez-Ambrosio, F. J. Llanes-Estrada, A. Salas-Bernárdez, and J. J. Sanz-Cillero, "SMEFT is falsifiable through multi-Higgs measurements (even in the absence of new light particles)," *Commun. Theor. Phys.* **75** no. 9, (2023) 095202, arXiv:2207.09848 [hep-ph].

[196] R. L. Delgado, R. Gómez-Ambrosio, J. Martínez-Martín, A. Salas-Bernárdez, and J. J. Sanz-Cillero, "Production of two, three, and four Higgs bosons: where SMEFT and HEFT depart," *JHEP* **03** (2024) 037, arXiv:2311.04280 [hep-ph].

[197] A. Biekötter, J. Brehmer, and T. Plehn, "Extending the limits of Higgs effective theory," *Phys. Rev. D* **94** no. 5, (2016) 055032, arXiv:1602.05202 [hep-ph].

[198] R. Aoude, E. Madge, F. Maltoni, and L. Mantani, "Quantum SMEFT tomography: Top quark pair production at the LHC," *Phys. Rev. D* **106** no. 5, (2022) 055007, arXiv:2203.05619 [hep-ph].

[199] G. Heinrich, S. P. Jones, M. Kerner, G. Luisoni, and E. Vryonidou, "NLO predictions for Higgs boson pair production with full top quark mass dependence matched to parton showers," *JHEP* **08** (2017) 088, arXiv:1703.09252 [hep-ph].

[200] G. Heinrich, S. P. Jones, M. Kerner, and L. Scyboz, "A non-linear EFT description of $gg \to HH$ at NLO interfaced to POWHEG," *JHEP* **10** (2020) 021, arXiv:2006.16877 [hep-ph].

[201] L. Alasfar *et al.*, "Effective Field Theory descriptions of Higgs boson pair production," arXiv:2304.01968 [hep-ph].

[202] P. Nason, "A New method for combining NLO QCD with shower Monte Carlo algorithms," *JHEP* **11** (2004) 040, arXiv:hep-ph/0409146.

[203] S. Frixione, P. Nason, and C. Oleari, "Matching NLO QCD computations with Parton Shower simulations: the POWHEG method," *JHEP* **11** (2007) 070, arXiv:0709.2092 [hep-ph].

[204] S. Alioli, P. Nason, C. Oleari, and E. Re, "A general framework for implementing NLO calculations in shower Monte Carlo programs: the POWHEG BOX," *JHEP* **06** (2010) 043, `arXiv:1002.2581 [hep-ph]`.

[205] G. Buchalla, O. Cata, A. Celis, and C. Krause, "Fitting Higgs Data with Nonlinear Effective Theory," *Eur. Phys. J. C* **76** no. 5, (2016) 233, `arXiv:1511.00988 [hep-ph]`.

[206] R. Frederix, S. Frixione, F. Maltoni, and T. Stelzer, "Automation of next-to-leading order computations in QCD: The FKS subtraction," *JHEP* **10** (2009) 003, `arXiv:0908.4272 [hep-ph]`.

[207] C. Degrande, C. Duhr, B. Fuks, D. Grellscheid, O. Mattelaer, and T. Reiter, "UFO - The Universal FeynRules Output," *Comput. Phys. Commun.* **183** (2012) 1201–1214, `arXiv:1108.2040 [hep-ph]`.

[208] L. Darmé *et al.*, "UFO 2.0: the 'Universal Feynman Output' format," *Eur. Phys. J. C* **83** no. 7, (2023) 631, `arXiv:2304.09883 [hep-ph]`.

[209] G. Luisoni, P. Nason, C. Oleari, and F. Tramontano, "$HW^{\pm}$/HZ + 0 and 1 jet at NLO with the POWHEG BOX interfaced to GoSam and their merging within MiNLO," *JHEP* **10** (2013) 083, `arXiv:1306.2542 [hep-ph]`.

[210] J. Butterworth *et al.*, "PDF4LHC recommendations for LHC Run II," *J. Phys.* **G43** (2016) 023001, `arXiv:1510.03865 [hep-ph]`.

[211] A. Buckley, J. Ferrando, S. Lloyd, K. Nordström, B. Page, M. Rüfenacht, M. Schönherr, and G. Watt, "LHAPDF6: parton density access in the LHC precision era," *Eur. Phys. J.* **C75** (2015) 132, `arXiv:1412.7420 [hep-ph]`.

[212] M. Cacciari, G. P. Salam, and G. Soyez, "The anti-$k_T$ jet clustering algorithm," *JHEP* **04** (2008) 063, `arXiv:0802.1189 [hep-ph]`.

[213] M. Cacciari and G. P. Salam, "Dispelling the $N^3$ myth for the $k_t$ jet-finder," *Phys.Lett.* **B641** (2006) 57–61, `arXiv:hep-ph/0512210 [hep-ph]`.

[214] M. Cacciari, G. P. Salam, and G. Soyez, "FastJet User Manual," *Eur.Phys.J.* **C72** (2012) 1896, `arXiv:1111.6097 [hep-ph]`.

[215] M. Capozi and G. Heinrich, "Exploring anomalous couplings in Higgs boson pair production through shape analysis," *JHEP* **03** (2020) 091, `arXiv:1908.08923 [hep-ph]`.

[216] **CMS** Collaboration, "Combined Higgs boson production and decay measurements with up to 137 fb$^{-1}$ of proton-proton collision data at $\sqrt{s} = 13$ TeV," tech. rep., 2020.

[217] **ATLAS** Collaboration, "Combined measurements of Higgs boson production and decay using up to 139 fb$^{-1}$ of proton-proton collision data at $\sqrt{s} = 13$ TeV collected with the ATLAS experiment," tech. rep., 2021.

[218] "LHC Higgs working group, twiki page LHC Higgs WG4 group," 2022. `https://twiki.cern.ch/twiki/bin/view/LHCPhysics/LHCHWGHH`.

[219] J. Mazzitelli, "NNLO study of top-quark mass renormalization scheme uncertainties in Higgs boson production," *JHEP* **09** (2022) 065, `arXiv:2206.14667 [hep-ph]`.

[220] M. Heller, A. von Manteuffel, R. M. Schabinger, and H. Spiesberger, "Mixed EW-QCD two-loop amplitudes for $q\bar{q} \to \ell^+\ell^-$ and $\gamma_5$ scheme independence of multi-loop corrections," *JHEP* **05** (2021) 213, `arXiv:2012.05918 [hep-ph]`.

[221] A. C. D. Viglioni, A. L. Cherchiglia, A. R. Vieira, B. Hiller, and M. Sampaio, "$\gamma_5$ algebra ambiguities in Feynman amplitudes: Momentum routing invariance and anomalies in $D = 4$ and $D = 2$," *Phys. Rev. D* **94** no. 6, (2016) 065023, `arXiv:1606.01772 [hep-th]`.

[222] A. M. Bruque, A. L. Cherchiglia, and M. Pérez-Victoria, "Dimensional regularization vs methods in fixed dimension with and without $\gamma_5$," *JHEP* **08** (2018) 109, `arXiv:1803.09764 [hep-ph]`.

[223] M. Ciuchini, E. Franco, G. Martinelli, L. Reina, and L. Silvestrini, "Scheme independence of the effective Hamiltonian for b —> s gamma and b —> s g decays," *Phys. Lett. B* **316** (1993) 127–136, `arXiv:hep-ph/9307364`.

[224] M. Ciuchini, E. Franco, L. Reina, and L. Silvestrini, "Leading order QCD corrections to b —> s gamma and b —> s g decays in three regularization schemes," *Nucl. Phys. B* **421** (1994) 41–64, `arXiv:hep-ph/9311357`.

[225] A. J. Buras, M. Misiak, M. Munz, and S. Pokorski, "Theoretical uncertainties and phenomenological aspects of B —> X(s) gamma decay," *Nucl. Phys. B* **424** (1994) 374–398, `arXiv:hep-ph/9311345`.

[226] R. Frederix, D. Pagani, and M. Zaro, "Large NLO corrections in $t\bar{t}W^{\pm}$ and $t\bar{t}t\bar{t}$ hadroproduction from supposedly subleading EW contributions," *JHEP* **02** (2018) 031, `arXiv:1711.02116 [hep-ph]`.

[227] **ATLAS** Collaboration, G. Aad *et al.*, "Observation of four-top-quark production in the multilepton final state with the ATLAS detector," *Eur. Phys. J. C* **83** no. 6, (2023) 496, `arXiv:2303.15061 [hep-ex]`.

[228] **CMS** Collaboration, A. Hayrapetyan *et al.*, "Observation of four top quark production in proton-proton collisions at s=13TeV," *Phys. Lett. B* **847** (2023) 138290, `arXiv:2305.13439 [hep-ex]`.

[229] L. Alasfar, J. de Blas, and R. Gröber, "Higgs probes of top quark contact interactions and their interplay with the Higgs self-coupling," *JHEP* **05** (2022) 111, `arXiv:2202.02333 [hep-ph]`.

[230] D. Barducci *et al.*, "Interpreting top-quark LHC measurements in the standard-model effective field theory," `arXiv:1802.07237 [hep-ph]`.

[231] M. Grazzini, A. Ilnicka, and M. Spira, "Higgs boson production at large transverse momentum within the SMEFT: analytical results," *Eur. Phys. J. C* **78** no. 10, (2018) 808, `arXiv:1806.08832 [hep-ph]`.

[232] N. Deutschmann, C. Duhr, F. Maltoni, and E. Vryonidou, "Gluon-fusion Higgs production in the Standard Model Effective Field Theory," *JHEP* **12** (2017) 063, `arXiv:1708.00460 [hep-ph]`. [Erratum: JHEP 02, 159 (2018)].

[233] M. Beneke and V. A. Smirnov, "Asymptotic expansion of Feynman integrals near threshold," *Nucl. Phys. B* **522** (1998) 321–344, `arXiv:hep-ph/9711391`.

[234] B. Jantzen, "Foundation and generalization of the expansion by regions," *JHEP* **12** (2011) 076, `arXiv:1111.2589 [hep-ph]`.

[235] J. de Blas, J. C. Criado, M. Perez-Victoria, and J. Santiago, "Effective description of general extensions of the Standard Model: the complete tree-level dictionary," *JHEP* **03** (2018) 109, `arXiv:1711.10391 [hep-ph]`.

[236] B. C. Allanach and J. Davighi, "Third family hypercharge model for $R_{K^{(*)}}$ and aspects of the fermion mass problem," *JHEP* **12** (2018) 075, `arXiv:1809.01158 [hep-ph]`.

[237] B. C. Allanach and H. Banks, "Hide and seek with the third family hypercharge model's $Z'$ at the large hadron collider," *Eur. Phys. J. C* **82** no. 3, (2022) 279, `arXiv:2111.06691 [hep-ph]`.

[238] J. Aebischer, M. Pesut, and Z. Polonsky, "Renormalization scheme factorization of one-loop Fierz identities," *JHEP* **01** (2024) 060, `arXiv:2306.16449 [hep-ph]`.

[239] R. Aoude, F. Maltoni, O. Mattelaer, C. Severi, and E. Vryonidou, "Renormalisation group effects on SMEFT interpretations of LHC data," *JHEP* **09** (2023) 191, `arXiv:2212.05067 [hep-ph]`.

[240] P. Nason and B. Webber, "Next-to-Leading-Order Event Generators," *Ann. Rev. Nucl. Part. Sci.* **62** (2012) 187–213, `arXiv:1202.1251 [hep-ph]`.

[241] T. Sjostrand and P. Z. Skands, "Transverse-momentum-ordered showers and interleaved multiple interactions," *Eur. Phys. J.* **C39** (2005) 129–154, `arXiv:hep-ph/0408302 [hep-ph]`.

[242] T. Sjöstrand, S. Ask, J. R. Christiansen, R. Corke, N. Desai, P. Ilten, S. Mrenna, S. Prestel, C. O. Rasmussen, and P. Z. Skands, "An Introduction to PYTHIA 8.2," *Comput. Phys. Commun.* **191** (2015) 159–177, `arXiv:1410.3012 [hep-ph]`.

[243] G. Marchesini and B. R. Webber, "Monte Carlo Simulation of General Hard Processes with Coherent QCD Radiation," *Nucl. Phys.* **B310** (1988) 461–526.

[244] J. Bellm *et al.*, "Herwig 7.0/Herwig++ 3.0 release note," *Eur. Phys. J. C* **76** no. 4, (2016) 196, `arXiv:1512.01178 [hep-ph]`.